TECHNICAL REPORT NO. 11758 (LL141)

AN APPLICATION OF PLASTICITY THEORY TO THE SOLUTION OF THE RIGID WHEEL-SOIL INTERACTION PROBLEM

March 1973

U.S. ARMY
TANK-AUTOMOTIVE
COMMAND
CONTRACT
DAAE07-72-C-0033

by LESLIE L. KARAFIATH*
EDWARD A. NOWATZKI*
I. ROBERT EHRLICH**
JOHN CAPIN**

GRUMMAN AEROSPACE CORPORATION*
STEVENS INSTITUTE OF TECHNOLOGY**

TACOM
MOBILITY SYSTEMS LABORATORY
U.S. ARMY TANK AUTOMOTIVE COMMAND Warren, Michigan

Technical Report No.11758 (LL141)

AN APPLICATION OF PLASTICITY THEORY TO THE SOLUTION OF THE RIGID WHEEL - SOIL INTERACTION PROBLEM

MARCH 1973

FINAL REPORT

by

Leslie L. Karafiath*
Edward A. Nowatzki*
I. Robert Ehrlich**
John Capin**

Prepared for the
United States Army Tank-Automotive Command
Mobility Systems Laboratory

Prepared by
Research Department
Grumman Aerospace Corporation
Bethpage, New York 11714

Under Contract No. DAAE07-72-C-0033

* Grumman Aerospace Corporation
** Stevens Institute of Technology

FOREWORD

One of the most urgent needs in land mobility technology is for a valid comprehensive methodology to (1) evaluate new potentials and guide their exploitation; (2) support complex decision processes throughout the military material development cycle with analyses which incorporate the effect of land mobility capabilities; (3) reduce the time and cost required to develop land mobility systems, in particular vehicles, responsive to perceived or actual needs.

A component of paramount importance of the required land mobility technology is modeling or simulating the interaction of the terrain-vehicle-man system.

In 1971, the U.S. Army Tank-Automotive Command (TACOM) and the U.S. Army Corps of Engineers, Waterways Experiment Station (WES) completed a first generation terrain-vehicle-man interaction simulation called the "AMC '71 Vehicle Mobility Model."

Further research effort is needed, however, to improve the accuracy and range of applicability of this model. One of the sub-models to be perfected is the analysis and simulation of a wheeled vehicle moving in soft soil.

With this in mind, TACOM has contracted with Grumman Aerospace Corporation to develop a rigorous computerized scheme for calculating rigid wheel slip, sinkage, torque requirements, motion resistance and drawbar pull from vehicle and soil inputs, such as, wheel load, width, diameter, soil cohesion, friction and bulk density.

This was conceived to be the first step (the second being a similar scheme for pneumatic tires) toward the establishment of a rigorous method for predicting the maximum speed that a wheeled vehicle can attain in soft soil as well as for the accurate assessment of performance of fuel consumption requirements in performing specific missions.

ABSTRACT

Plasticity theory is applied to the analysis of soil-wheel interaction. The problem is reduced to the determination of stresses at the interface of the rigid wheel and the soil. Once these stresses are known, the wheel load, torque, pull and drag are obtained by integrating the stresses along the wheel perimeter. To find the distribution of interface stresses, the basic differential equations of equilibrium are combined with the Coulomb - Mohr yield criterion for soils and the equations are solved by a numerical procedure. The numerical solution scheme and the computer program which accomplishes the solution are described in detail.

Tests performed with the soil bin dynamometer facilities of Stevens Institute of Technology are discussed. Test results show good agreement with prediction. The validity of assumptions introduced in the computational scheme is examined. It is found that refinement in the assumptions regarding the distribution of interface friction and the magnitude of the "separation angle" would further improve the accuracy of the method.

Finally, it is concluded that the proposed theory for predicting rigid wheel performance is fundamentally correct and is practical from the viewpoint of required computer time.

This report represents an essential first step toward the establishment of a rigorous simulation of the soft soil performance of wheeled vehicles.

ACKNOWLEDGMENTS

The work reported here was performed for the Mobility Systems Laboratory of the U.S. Army Tank-Automotive Command (TACOM), Warren, Michigan under the general supervision of Mr. Robert T. Otto, Chief of the Surface Mobility Division and Dr. Howard Dugoff, Supervisor, Research and Analysis Branch. Technical Monitor was Mr. Zoltan J. Janosi, Supervisor, Vehicle Locomotion Function. Their help and valuable suggestions in carrying out this research work is gratefully acknowledged.

The major part of the experimental program reported herein was performed under subcontract from Grumman Aerospace Corporation at Stevens Institute of Technology under the direction of Dr. Robert I. Ehrlich, Manager, Transportation Research Group. Mr. John Capin performed the experiments with the help of Messrs. Daniel Meyers and Nicholas Bibitch. Data processing was done by Mr. Frederick Behrens.

Laboratory soil and wheel performance tests at Grumman were performed by Mr. George Homfeld, under the direction of Dr. Edward A. Nowatzki.

NOTATION

A	= singular point
c	= cohesion
C_{1-5}	= constants
DB	= drawbar pull, drag
f	= function
j	= slip
j_0	= constant defining threshold slip
k	= constant in plate sinkage equation
K	= constant in slip equation
L	= load
n	= exponent in plate sinkage equation
$Nq\delta$	= bearing capacity factor
p	= pressure in plate sinkage equation
p_0	= constant in plate sinkage equation
q	= normal stress
q_{mf}	= normal stress in forward field at α_m
q_{mr}	= normal stress in rear field at α_m
q_t	= normal stress at the edge of the wheel corresponding to transverse failure
R	= radius of wheel
s	= $(\sigma_1 + \sigma_3)/2$, reference stress
x, z	= geometric coordinates

α = central angle (measured from vertical)

α_e = entry angle

α_m = angle of separation

α_r = rear angle

γ = unit weight of soil

δ = angle of inclination of resultant stress to normal, angle of shear mobilization

δ_c = interface friction factor for cohesive soils

ϵ = slope angle

θ = angle between x axis and major principal stress

λ = load coefficient (L/L_o)

μ = $\pi/4 - \varphi/2$

ξ = tolerance limit

σ = $(\sigma_1 + \sigma_3)/2 + \psi$

σ_n = normal stress

$\sigma_{1,\ 3}$ = principal stresses

τ = shear stress/shear strength

τ_{max} = maximum available shear strength

τ_{mob} = mobilized shear strength

φ = angle of internal friction

ψ = c cot φ

ω = pull coefficient. (DB/L_o)

SUBSCRIPTS

a = active

i, j = designation for slip line numerals

K = designation for iteration numerals

m = model

max = maximum

min = minimum

mob = mobilized

o = input (design) values

CONTENTS

I. SCOPE OF WORK

The scope of work as described in the Request for (Contract) Proposal work statement was to conduct theoretical and experimental investigations on the application of plasticity theory to the solution of wheel soil interaction problems. Emphasis was placed on the following items:

- Development of a computer program for the prediction of performance of rigid wheels
- Performance of validation tests to compare theoretical and experimental results

Presentation of the results of the research work is arranged in the above order with an introductory section on theoretical background.

II. THEORETICAL BACKGROUND

A. Basic Assumptions and Definitions

In the application of plasticity theory to the solution of the soil-wheel interaction problem, the following basic assumptions are made:

- The soil is semiinfinite, homogeneous, and isotropic.
- Strength properties of the soil are characterized by the cohesion and internal angle of friction.
- Soil failure is governed by the Mohr-Coulomb yield (failure) criterion.
- Stresses are the same in all planes parallel to the plane of notion of the wheel (the problem is assumed to be two dimensional).
- Wheel velocity is constant.
- Soil inertia forces are negligible.
- Pore water pressures are negligible.

Some of the terms frequently used in the following discussions are defined below:

- Plastic state of stress, plastic equilibrium conditions, or failure conditions are used interchangeably to define a stress state at any point in the soil where the Mohr-Coulomb yield criterion is satisfied.
- Slip line is a line along which failure conditions obtain.
- Slip zone, slip line field, or failure zone is a finite area where the Mohr-Coulomb yield criterion is satisfied.
- Angle of interface friction is the angle that determines the shear stress in a Mohr-Coulomb plot (Fig. 1) according to the following relationship

$$\tau = (\sigma_n + c.\cot\varphi)\tan\delta \qquad (1)$$

If $\delta = \varphi$, Eq. (1) reverts to the Mohr-Coulomb yield criterion.

B. Soil-Wheel Interaction Concept

The application of plasticity theory to the analysis of soil-wheel interaction is based on the concept that failure conditions develop in the soil beneath towed or driven wheels, and that they control the interface stresses. The validity of this concept is supported by experimental observations as well as by the good agreement between measured interface stresses and those predicted by the theory. The concept and its practical application for wheel performance calculations is dealt with in detail in References 1 and 2 and is discussed here only briefly for the convenience of reference.

Any soil-wheel interaction problem can be reduced to the determination of interface stresses. Once these are known, the wheel can be considered as a free body and the computation of load, torque, and drag or drawbar pull consists of a simple integration of normal and shear stresses along the wheel perimeter.

In soft soils, the interface stresses are controlled by the inability of the soil to carry loads higher than those causing failure in the soil. Failure in the soil occurs in zones along slip lines. There are generally two failure zones beneath loaded wheels, as shown in Fig. 2, a forward and a rear one. Each failure zone is comprised of three different types of failure states, as described in Fig. 2. The adjectives denote both the location of these zones and the direction in which failure occurs. One requirement is that the two zones must meet and that at their common point the interface stresses be the same. In certain cases, there is only a single failure zone, as shown in Fig. 3. This occurs when the interface stress for the single zone is less than that which would cause failure in the other direction as, for example, at point B in Fig. 3.

C. Interface Stresses and Wheel-Soil Interaction

The role of the wheel in soil-wheel interaction is twofold. First, the entry and rear angles are the limits of the integration of interface stresses that yield the load, torque, and drawbar pull. The integration limits express the change in the contact area and thus affect wheel performance profoundly. Second, the applied torque on the wheel generates shear stresses at the interface that influence the magnitude and distribution of normal stresses

that the soil can carry. The entry and exit angles also affect the failure stresses in the soil. These interaction effects are illustrated in Figs. 4 and 5. The method of calculation of slip line field geometries and interface stresses is described in Section III; here the results are anticipated for the purpose of realistic illustration.

Rear slip line fields for various angles of interface friction angle are shown in Fig. 4. The rear field was selected for illustration because of the drastic effect of the interface friction angle on the geometry of the rear slip line field. For comparison, all parameters but the angle of interface friction are the same in Fig. 4. The diminishing of the extent of the rear slip line field with the increase of the interface friction angle is evident from Fig. 4. With the change in the geometry, the associated normal interface stresses also change as shown on the right side of Fig. 4. The effect of the angle of interface friction (generated by the applied torque) on the normal stresses is very pronounced as seen in the illustration.

The effect of the entry and exit angles on the interface stresses is less pronounced. Slip line field geometries for various entry angles are compared in Fig. 5, all other variables being the same. The change in the extent of slip line fields is due mostly to the condition that they all were made to end at the angle of 15 degrees. The corresponding normal stresses shown on the right side of the illustration appear to rise along parallel lines; however, there is a significant difference in the rate of the rise as a comparison of the dashed line with the solid one at 60° shows. The dashed line is the normal stress for 30°-entry angle but plotted at 60° so that a comparison with the solid line for 60°-entry angle be facilitated. This comparison shows that the entry angle influences the normal stresses but to a lesser degree than the angle of interface friction.

D. Application of Plasticity Theory to the Determination of the Geometry of Soil Failure Zones and Associated Interface Stresses

In plasticity theory, the differential equations of equilibrium are combined with a yield criterion for the material. For soils, the failure criterion that is generally recognized to give the best agreement with experiments is the Mohr-Coulomb yield criterion, which expresses the following linear relationship between yield shear strength and normal stress (for notations see page vi):

$$\tau = c + \sigma_n \tan \varphi \tag{2}$$

This failure criterion, when combined with the differential equations of equilibrium, yields, after some manipulations (Refs. 3 - 5), the following set of differential equations:

$$dz = dx \tan (\theta \pm \mu)$$

$$d\sigma \pm 2\sigma \tan \varphi d\theta = \frac{\gamma}{\cos \varphi} \left[\sin (\epsilon \pm \varphi)\, dx + \cos (\epsilon \pm \varphi)\, dz\right] \tag{3}$$

The cohesion term (c) in Eq. (2) does not appear explicitly in Eqs. (3); it is included, however, in the value of σ which equals

$$\sigma = 1/2\ (\sigma_1 + \sigma_3) + c \cot \varphi \tag{4}$$

Equations (3) lose their meaning if $\varphi = 0$, since σ becomes infinite. In this case, the following differential equations apply (Ref. 3):

$$dz = dx \tan (\theta \pm \mu)$$

$$ds \pm 2sd\theta = \gamma\, dz \tag{5}$$

where

$$s = 1/2\ (\sigma_1 + \sigma_3)$$

For properly defined boundary conditions, the above sets of the differential equations of plasticity for soils yield a unique solution in the form of a slip line field and associated stresses. At any point within the slip line field, the applicable differential equations set forth above are satisfied.

There are some fundamental aspects of the theory that need to be emphasized here before proceeding to the discussion of the numerical procedures applied for the solution of the above differential equations. These are:

- The Mohr-Coulomb yield criterion as applied in the above equation refers to effective stresses, i.e., for the case where pore water pressures are negligible. (Apparent cohesion due to pore water tension may be considered as effective stress.)
- Equations (3) of the plasticity theory are valid, however, for a non-linear strength envelope (Ref. 6) and may be expanded to include pore water pressures (Ref. 2) or soil inertia forces (Ref. 7).

- The Mohr-Coulomb yield criterion implies that the soil strength expressed by Eq. (2) is available regardless of the volumetric strain that is associated with the stress state expressed by Eq. (2). In soil-wheel interaction problems in soft soils, where the soil is progressively compressed as the wheel advances, the volumetric strain in the soil is generally much larger than in static problems and the shear strength, as expressed by Eq. (2), is available for a failure zone to form. However, at, and in the close vicinity of the entry angle, the volumetric strain may not be enough to mobilize the full Mohr-Coulomb strength and, consequently, the rise of normal stresses in cohesive soils, though rapid, is not instantaneous as predicted by the theory.
- In plasticity theory, solutions obtained by integration of Eqs. (3) are termed statically admissible solutions and are considered lower bound solutions. Kinematic admissibility is analyzed by constructing velocity fields for the slip zones on the basis that the material is incompressible. A kinematically admissible solution would constitute an upper bound. For soil-wheel interaction problems in soft soils, the assumption of incompressibility is inappropriate and conclusions drawn on the basis of such an assumption are inapplicable. Experimental evidence, as discussed in Section IV, shows that interface stresses predicted by the application of Eqs. (3) agree well with measured ones indicating the validity of the solutions.

E. Similitude and the Application of Plasticity Theory to Soil-Wheel Interaction

The concept that interface stresses are governed by the differential equations of plasticity for soils leads to interesting considerations regarding the use of the principles of similitude in soil-wheel interaction studies. Equations (3) can be written in dimensionless form if a characteristic length and a reference stress is introduced. For soil-wheel interaction problems, the characteristic length may be conveniently chosen as the radius of the wheel. The geometry of the slip line fields in a soil-wheel interaction problem will be similar for the same φ and δ if the following equality holds:

$$\frac{\gamma_m R_m}{s_m} = \frac{\gamma_p R_p}{s_p} \tag{6}$$

The subscripts m and p denote model and prototype, respectively. For geometrically similar slip line fields

$$\frac{\sigma_m}{\sigma_p} = \frac{s_m}{s_p} \tag{7}$$

Thus, at the interface, the distribution of σ values are the same but their magnitude changes according to relationship (7). At this point, attention is called to the definition of σ in plasticity theory [Eq. (4)]. If $c = 0$, or $\varphi = 0$, and Eqs. (5) are used, the normal and shear stresses at the interface are proportional to σ. As a consequence, dimensionless wheel performance parameters, such as pull coefficients (DB/L) will be the same for all geometrically similar slip line fields, since a constant ratio of interface stresses can be factored out in the integration for both load and drawbar pull. Thus, in the case of $c = 0$ or $\varphi = 0$ soils, the application of plasticity theory for soil-wheel interaction confirms the validity of the results obtained in similitude studies regarding the selection of dimensionless parameters, at least for wheels traveling at velocities where soil inertia effects are negligible.

In the case of $c \neq 0$, $\varphi \neq 0$ ($c - \varphi$ soils) geometrically similar slip line fields result in similar distributions of σ along the interface. However, in this case, distribution of normal stresses is no longer similar to the σ distribution, since σ contains the term $c \cot \varphi$ (Eq. 4) and σ_n does not. Thus, similarity exists between the distribution of $\sigma_n + c \cot \varphi$, the shear stresses τ, and σ. In the integration formulas for load, drawbar pull, and torque, the constant $c \cot \varphi$ can be computed separately and a correction factor for $c - \varphi$ soils in the similitude relations may be established.

It is also noted that while Eqs. (3) also apply for nonlinear yield criteria (Ref. 6), they cannot be put in dimensionless form unless the yield criterion is linear. Thus, similitude in soil-wheel interaction as expressed by Eqs (6) and (7) is restricted to soils that follow the linear Mohr-Coulomb yield criterion.

F. Slip and the Development of Interface Friction

For slip line fields to be determined uniquely by the differential equations of plasticity, it is necessary to set some of the boundary conditions at the interface. In this so-called mixed boundary value problem, two variables of the four independent ones in Eqs. (3) must be specified. In the solution for the conventional bearing capacity problem, z and θ are specified at the base of the bearing plate. In the soil-wheel interaction problem, it is not possible to specify the value a priori of any of two of the four variables at the interface. Instead, the boundary conditions take the form of a relationship between x and z given by the wheel geometry and a relationship between θ and the angle of interface friction. This relationship is (Ref. 3)

$$\theta = \frac{\pi}{2} + \frac{1}{2}(\Delta+\delta) - \alpha \tag{8}$$

where

$$\Delta = \text{arc sin}\left(\frac{\sin \delta}{\sin \varphi}\right) \tag{9}$$

Thus, the interface friction angle needs to be specified along the interface for the slip line field and the associated interface stresses to be uniquely defined. In wheel performance calculations, however, the performance parameters are related to slip rather than to the interface friction angle. The development of shear stresses at the interface is associated with slip, and mathematical formulations for the relationship between shear stress and slip have been proposed by various researchers. On the basis of direct shear tests, Janosi and Hanamoto proposed the following relationship between mobilized shear and slip for tracked vehicles (Ref. 13):

$$\tau_{mob} = \tau_{max}\left(1 - e^{-j/K}\right). \tag{10}$$

For compressible soils, which are of primary interest in off-road locomotion, this equation properly describes the relationship between shear stress and slip. When this relationship is applied to the rigid wheel, however, it is useful to include a constant, j_0, in the slip term to account for the fact that a threshold perimeter shear exists, at which movement of the wheel starts. Thus, Eq. (10) is modified as follows:

$$\tau_{mob} = \tau_{max}\left(1 - e^{-(j + j_0)/K}\right) \tag{11}$$

The following relationship holds between the shear strength mobilized at the interface and the angle δ (Fig. 1):

$$\tan \delta = \frac{\tau_{mob}}{\sigma_n + \Psi} \tag{12}$$

From Eqs. (11) and (12) comes the following relationship:

$$\tan \delta = \tan \delta_{max} \left(1 - e^{-(j+j_o)/K}\right) \tag{13}$$

The relationship between the interface friction angle and slip established by Eq. (13) allows the computation of slip for various values of δ if j_o and K are known. The concept of soil-wheel interaction, as outlined in the preceding paragraphs, has important implications regarding the value of δ_{max}. According to this concept, the soil adjoining the interface is in the active state of failure. For a given normal and shear stress at the interface, there is one Mohr circle that represents the active and another one that represents the passive state of stresses. Figure 6 shows Mohr circles for the active and passive state for the same normal stress but with increasing interface shear stress. Stress circles for the active state are shown by full lines, and by dashed lines for the passive state. The interface shear stress τ is shown to increase with the interface friction angle ($\tau_3 > \tau_2 > \tau_1$ and $\delta_3 > \delta_2 > \delta_1$). In the active state, the center of Mohr circles is to the left of the shear stress ordinate; in the passive state, it is to the right. From the construction of the Mohr circles, it is obvious that the maximum shear stress that can be mobilized in the active state is the one corresponding to a Mohr circle that has its center at σ_n (circle 3 in Fig. 6). Were the shear stress higher than this, the corresponding Mohr circle would represent a passive state. Thus, it is incorrect to assume that the full soil strength can be mobilized beneath a wheel or track. The passive state beneath a wheel or track can exist only if the soil is pushed toward the wheel or track, an obviously meaningless situation for vehicle mobility. The only possible stress state in the soil beneath a wheel or track is the active state of stresses and it follows from this state that the maximum mobilized shear stress cannot exceed that defined by Mohr circle 3 in Fig. 6. In mathematical terms

$$\tau_{max} = (\sigma_n + \psi) \tan \delta_{max} = (\sigma_n + \psi) \sin \varphi \tag{14}$$

$$\delta_{max} = \arctan (\sin \varphi) \tag{15}$$

G. Constraints Imposed on the Slip Line Fields by the Wheel

The interface friction angle degines θ at the soil-wheel interface (Eq. (8)) and, together with the geometry, defines the boundary conditions so that Eqs. (3) yield a unique solution for a particular slip line field. For the soil-wheel interaction problem, however, the boundary conditions for both the forward and rear slip line field must be defined so that the solution be unique. This involves the determination of angle α_m that defines the end point of the forward and rear field. The following considerations apply in this respect.

For dry sand it was found by Sela (Ref. 8) that the angle of separation approximately equals the developed friction angle. This finding is consistent with the concept that the forward failure zone extends over that part of the wheel perimeter where the component of the normal and shear stresses (ΔD) in the direction of motion is negative (i.e., resisting the motion), and that the backward zone extends over that part of the wheel perimeter where this component is positive. Applying this concept to soils with cohesion and pore water pressures results in the following relations:

$$\Delta D = \tau_{mob} \cos \alpha - \sigma_n \sin \alpha$$

$$\tau_{mob} = (\sigma_n + \psi) \tan \delta \text{ (Eq. (12))}$$

$$\Delta D = (\sigma_n + \psi) \tan \delta \tan \alpha = 0$$

$$\alpha_m = \text{arc tan} \left(\frac{\sigma_n + \psi}{\sigma_n} \tan \delta \right) \tag{16}$$

III. COMPUTATIONAL METHODS

A. General

The solution of differential Equations (3) yields the slip line fields and associated interface stresses for wheel performance calculations. For numerical computations, differential Equations (3) are replaced by the following finite difference Equations (Fig. 7):

$$x_{i,j} = (z_{i-1,j} - z_{i,j-1} + \alpha_1 x_{i,j-1} - \alpha_2 x_{i-1,j})/(\alpha_1 - \alpha_2)$$

$$z_{i,j} = z_{i-1,j} + \alpha_2 (x_{i,j} - x_{i-1,j}) \tag{17}$$

$$\sigma_{i,j} = \frac{\gamma(C\sigma_{i,j-1} + D\sigma_{i-1,j}) + 2\sigma_{i,j-1}\sigma_{i-1,j}\left[1 + (\theta_{i,j-1} - \theta_{i-1,j}) \tan \varphi\right]}{\sigma_{i,j-1} + \sigma_{i-1,j}}$$

$$\theta_{i,j} = \frac{\sigma_{i,j-1} - \sigma_{i-1,j} + 2 \tan \varphi(\sigma_{i,j-1}\theta_{i,j-1} + \sigma_{i-1,j}\theta_{i-1,j}) + \gamma (D-C)}{2 \tan \varphi (\sigma_{i,j-1} + \sigma_{i-1,j})}$$

where $x_{i,j}$, $z_{i,j}$ are coordinates of the subscripted nodal point

$$\alpha_1 = \tan (\theta_{i,j-1} + \mu), \quad \alpha_2 = \tan (\theta_{i-1,j} - \mu)$$

and

$$C = \frac{\sin (\epsilon-\varphi)}{\cos \varphi} (x_{i,j} - x_{i-1,j}) + \frac{\cos (\epsilon-\varphi)}{\cos \varphi} (z_{i,j} - z_{i-1,j})$$

$$D = \frac{\sin (\epsilon+\varphi)}{\cos \varphi} (x_{i,j} - x_{i-1,j}) + \frac{\cos (\epsilon+\varphi)}{\cos \varphi} (z_{i,j} - z_{i-1,j}).$$

These difference equations permit the computation of the coordinates of a nodal point (intersection of slip lines), as well as the values of σ and θ at that point, from the known values at neighboring nodal points having lesser subscripts.

The slip line field in the passive zone can be computed by equations starting with the boundary values given at the soil surface (sloping or level). In the radial shear zone, the same equations are used, but special consideration is given to the central point ("A") where the second family of slip lines converge. This point is a degenerated slip line, where θ changes from the value at the passive zone boundary to that specified at the active zone boundary. The total change in θ is divided by the number of slip lines converging at this point to result in an equal $\Delta\theta$ increment between two adjacent slip lines. The σ values for each increment are computed from the equation $\sigma = \sigma_o \, e^{2(\theta - \theta_o) \tan \varphi}$, which is the solution of the differential equations of Eqs. (3) if both dx and dz vanish. With these θ and σ values assigned to each slip line at the singular point, the coordinates as well as the σ and θ values for all other points in the radial shear zone can be computed by Eqs. (17).

In the active zone, the same equations are used except for the boundary at the interface, where $\theta_{i,j}$ is specified and x and z must lie on the circle with radius R. For numerical computations, the circle is approximated by a polygon, allowing the use of the following difference equations:

$$x_{i,j} = \frac{1}{1 + \alpha_0 F} x_{i-1,j} + \alpha_0 F \, x_{i-1,j-1} + \alpha_0 \, (z_{i-1,j-1} - z_{i-1,j})$$

$$z_{i,j} = z_{i-1,j-1} + F \, (x_{i-1,j-1} - x_{i,j})$$

$$\sigma_{i,j} = \sigma_{i-1,j} + 2 \tan \varphi \, \sigma_{i-1,j} + (\theta_{i,j} - \theta_{i-1,j}) + \gamma C \qquad (18)$$

where

$$\alpha_0 = \operatorname{cotan} \left(\frac{1}{2} \, (\theta_{i,j-1} + \theta_{i,j}) - \mu \right)$$

$$F = \tan \alpha_{i-1,j-1}$$

To improve the accuracy of calculations, an iteration is performed where $\theta_{i-1,j}$, $\theta_{i,j-1}$, $\sigma_{i-1,j}$, $\sigma_{i,j-1}$ values in the above difference equations are replaced by values averaged with the computed value of $\theta_{i,j}$ and $\sigma_{i,j}$, respectively.

B. Computation of a Single Slip Line Field

The finite difference equations given in Section III. A are suitable for the numerical computation of a single slip line field. For the problem of soil-wheel interaction, it is convenient to carry out the computations in such a way that the slip line comprising the outer boundary of the field ends at a specified location at the interface. To this end, a sequence of operations, different from that used for the conventional bearing capacity problem, is employed, as shown in the flow diagram in Fig. 8. Instead of computing the variables first in the passive, then in the radial, and finally in the active zone, the variables are computed along the first "j" line in all three zones and then along subsequent "j" lines until a "j" line exceeds the end point. Then a "j" line is interpolated so that it ends up at α_m within the limits of tolerance (ξ). This method eliminates the time consuming trial and error procedure of finding the length of passive zone that matches the arc length of the active zone. The length of the passive zone in this procedure is overestimated so that the last "j" line overshoots the α_m angle. The grid in this procedure is larger than in the conventional one (16 x 48 instead of 10 x 30), requiring a somewhat larger core, but the computing time for finding a slip line field that meets the boundary condition is much less.

The interface friction angle, as shown in the flow diagram, is assumed to be constant. However, the program can as well accommodate a δ angle that varies along the interface.

C. Computation of a Matching Set of Slip Line Fields

For the problem of soil-wheel interaction, a matching set of slip line fields must be found that meets the constraints described in Section II.C. For this purpose, it is convenient to start the computations with the rear slip line field using the subroutine outlined in Section III.B, but allowing for appropriate sign changes due to the fact that the rear field is a mirror image of the front field. The reason for starting the computation with the rear field is twofold: first, the rear angle varies within a narrow range; second, a normal stress from the rear field (q_{mr}) at α_m can be generally matched by a normal stress from the forward field. This is not true vice-versa. When q_{mr} for the assumed rear angle (α_r) and interface friction angle (δ) is determined, the front field is found by varying the entry angle (α_e)

until the normal stress from the front field (q_{mf}) matches q_{mr} within the allowed tolerance. Since the interface friction angle, δ, is assumed to be the same for both the forward and rear fields, the shear stress at α_m from both fields is the same (within the tolerance) when q_{mr} and q_{mf} are matched. The flow diagram for this procedure is shown in Fig. 9. When a matching set of rear and forward fields is found by this procedure, the load, torque, and drawbar pull are computed by appropriate numerical integration of the interface stresses for the assumed value of α_r and δ. The slip is computed from Eq. (13) and the sinkage from the entry angle.

D. Inversion Procedure

The procedure described in Section III.C yields the wheel performance parameters for an assumed rear angle and interface friction. An inversion procedure is required to solve for torque, slip, and sinkage when wheel load, drawbar pull, and soil properties are given. Such a procedure is outlined below. Load, drawbar pull, and torque are functions of the rear angle, α_r, and interface friction angle, δ, as expressed by the following relationships:

$$\begin{aligned} L &= f_1(\alpha_r, \delta) \\ DB &= f_2(\alpha_r, \delta) \\ T &= f_3(\alpha_r, \delta) \end{aligned} \tag{19}$$

The functions f_1, f_2, f_3 are, of course, not closed form functions. In the solution procedure outlined in Section III.B, one set of L, DB and T values are found for an assumed α_r and slip corresponding to an assumed δ. The procedure to find the torque for given load and drawbar pull consists of finding α_r and δ, which yield the given load and drawbar pull; once the matching set of slip line fields for these conditions is found, the torque, slip, and sinkage is also available from the computations. Even if the functions f_1 and f_2 were known, the solution for L and DB would require the solution of a system of two nonlinear equations. Since there is no generally valid theorem for the solution of this problem, and convergence criteria for iterative solutions cannot be established if the derivatives of f_1 and f_2 are

not known, it was necessary to study the general behavior of these functions and to make judicious use of some of their properties to devise an efficient and convergent iteration scheme for the solution of the problem.

There are two properties of the wheel performance relationships expressed by Eqs. (19) that are useful for the solution of the inversion problem. First, the wheel load increases monotonically with the rear angle for a constant angle of interface friction. Second, the pull coefficient DB/L, often used as a dimensionless parameter in wheel performance studies, was found to increase monotonically with the interface friction angle. Although there is no rigorous proof for this to hold true for every combination of conditions, theoretical considerations and evaluation of computations performed for a wide range of conditions indicate that this second relationship is generally valid. In the inversion procedure, these two relationships constitute the basis of the iteration procedure, which is shown schematically in Fig. 10. The iteration steps are described in greater detail in Section III.F where the comprehensive computer program is described.

E. Computation of Wheel Performance in Purely Cohesive Soils

The computational procedures described in the preceding paragraphs refer to wheel performance calculations where the numerical solution of differential Eqs. (3) is required. As it was pointed out in Section II.D, the form of the governing differential equations (Eqs. 4) is somewhat different in purely cohesive soils. The solution of these equations yields the slip line field geometry and associated stresses, just as Eqs. (3) do in the case of frictional soils. A study of the slip line fields and interface stresses obtained from the numerical solution of Eqs. (4) showed, however, that it is not necessary in this special case to perform these numerical calculations because the interface stresses can be calculated with very close approximation from the following formulas (Ref. 3):

$$\sigma_n = c\,(1 + \pi + \cos\delta_c \pm \frac{1}{2}\,\delta_c \mp \alpha)$$

$$\tau = c \sin\delta_c \qquad (20)$$

(The upper sign refers to the front, and the lower to the rear field).

In the above equations, the angle δ_c is equivalent to the interface friction angle. It is defined as

$$\delta_c = \text{arc sin} \frac{\tau_{mob}}{\tau_{max}} \tag{21}$$

The requirement that the normal stress from the forward and the rear field be equal at the angle of separation leads to the following relationship:

$$\alpha_m = \delta_{c/2} \tag{22}$$

This relationship is not consistent with Eq. (16), established for c - φ soils, and this apparent contradiction is the consequence of assuming uniform interface friction along the interface. In actuality, the interface friction is not uniform and adjusts itself in such a way that the two conditions are met at the angle of separation. Therefore, the assumption of a uniformly developed interface friction is retained for computational purposes.

In contrast to frictional soils, in the case of $\varphi = 0$, the interface stresses at any point depend only on the central angle and interface friction but not on the entry or rear angle. For this reason, further assumption regarding these angles is necessary to make the problem definite. It is assumed on the basis of experiments that the rear angle is one third of the entry angle. The computation of wheel performance parameters, based on this assumption, follows the flow chart shown in Fig. 11.

F. Description of Comprehensive Computer Program

In the following description, emphasis is laid on the user's anticipated needs rather than on details of the program. The comprehensive program consists of the following programs:

Main program	LKWH
Subroutine 1	SLIP
Subroutine 2	LKWC

Listings of the above programs are given in the Appendix.

1. Subscripted Variables and Dimension Statements

Main program LKWH:

J designates a location at the interface.

K designates the numeral assigned to consecutive iterations in the inversion procedure Section III.D.

HH(J) = α_j

QQ(J) = q_j

EE(J) = τ_j

WE(J), DRB(J), TRQ(J) = auxiliary variables

LD(K) = Load

DR(K) = Drawbar pull

TR(K) = Torque

AR(K) = Rear angle

AE(K) = Entry angle

DEL(K) = Interface friction angle

PU(K) = Pull coefficient

LC(K) = Load coefficient

Subroutine SLIP:

The variables in Eqs. (16) are designated as follows:

X(I,J) = $x_{i,j}$

Z(I,J) = $z_{i,j}$

S(I,J) = $\sigma_{i,j}$

T(I,J) = $\theta_{i,j}$

The dimension statement corresponds to a 48 x 16 grid for the computation of the geometry of slip line fields. All J locations are not necessarily used in actual computations, as indicated in Section III.B. Several hundred computations were performed satisfactorily with the above grid size and, therefore, no need for the change of the grid size is anticipated.

Variables with one subscript are as follows:

$D(J) = \delta_j$

$H(J) = \alpha_j$

$Q(J) = q_j$

$E(J) = \tau_j$

Where j designates a location at the interface. A(J), B(J), C(J) are auxiliary variables.

The dimensions of the variables with one subscript are tied to the J dimensions of the variables with two subscripts.

Subroutine LKWC:

Designation of subscripted variables are the same as in the main program.

2. Input Files

Input variables and constants that the user may want to change are read from input files so that the program need not be recompiled if these data are changed. Three input files are used in the present program; they may be combined in one if so desired. The input files contain the following data:

Input file SOL contains data on soil properties in the following order:

Cohesion (CO) in lbs/sq ft
Friction angle (FO) in degrees
Unit weight of soil (GO) in lbs/cu ft
Slope angle (SO) in degrees
Slip parameter j_o (SLJ), dimensionless number
Slip parameter K (SLK), dimensionless number

It is noted here that cohesion and friction angle are strength parameters as determined by triaxial tests at a rate of loading comparable to that obtained under a moving wheel. Strength parameters from direct shear tests may also be used. Strength parameters obtained from Bevameter shear tests, sheargraph, and other devices do not yield true internal strength parameters and are not to be used with this program.

Input file WH1 contains data on wheel geometry and wheel forces in the following order:

Wheel radius (RO) in ft
Wheel width (BO) in ft
Wheel load (LO) in lbs
Drawbar pull (DB) in lbs

Input file TOL contains tolerance limits and numerical constants that determine the magnitude of changes in the rear and interface friction angle in the inversion procedure and the maximum number of iterations with these constants. The values of limits and constants in this input file have been selected on the basis of experience with the program and they may be changed judiciously according to required accuracy, allotted computer time, etc.

Following is a list of data in this file in the order they are read with recommended values:

Tolerance limit for load	(TOL)	0.1
Tolerance limit for pull coefficient	(TOP)	0.03
Numerical constants	(B1)	1.09
for the determination	(B2)	0.95
of the size of δ and α_r	(B4)	20.0
increments	(B5)	2.0
	(B6)	2.0
	(B7)	0.9
	(B8)	0.7

Limit for the number of iterations	1st Phase (K3)	16
	2nd Phase (K5)	12

The tolerance limits define the range of accuracy desired in the inversion procedure. There are inherent inaccuracies in prediction theories due to the various assumptions, inaccuracies in the determination of soil properties and the approximations inherent in numerical methods. Thus, there is no point in performing iterations to achieve an apparent accuracy in the prediction when inaccuracies from other sources would dominate.

The recommended tolerance limit for load (TOL) is ± 10 percent, and for the pull coefficient (TOP) ± 3 percent. The numerical constants listed are consistent with these limits. Their significance is explained in the description of the inversion procedure. Because of the nature of the problem of the inversion procedure, it was not possible to establish criteria for the convergence of the iteration procedure. Instead, a limit (K3) is set for the number of iterations performed in steps as determined by one set of constants set forth in the input file. If solution is not reached within the allotted number of iterations, the program changes these constants and performs a maximum of K5 additional iterations where the steps correspond to the changed constants. The recommended limits for iterations may be changed but only within the limits of dimension statements.

3. Decisions, Assumptions and Iterations in the Main Program

The general logic of the main program is shown in the flow diagrams. There are, however, some provisions in the main program that, for clarity, have not been included in the flow diagrams. These are discussed below.

In Section III.E, the special case of $\varphi = 0$ was discussed. It was found that the simplified method applicable to this case also yielded reasonably accurate results for small φ angles if an appropriate correction in the value of cohesion was made. Therefore, a provision was made in the main program to perform calculations by the subroutine LKWC whenever $\varphi < 12$ degrees.

It is also assumed that soils that exhibit a friction angle greater than 12 degrees are only partially saturated and, therefore, are liable to change their unit volume (void ratio or porosity) under the action of the wheel. While 12 degrees were selected on the basis of judgment, it is obviously an arbitrary average value introduced in the computer program as a necessity. The consequence of the volume change of soil under the action of the wheel is that the soil in the rear field is precompressed by the stresses in the front field; therefore, generally the strength of soil is higher in the rear field than in the front.

It is desirable for prediction purposes to limit soil characterization to the strength parameters of the undisturbed ground. To improve the accuracy of predictions, however, it is necessary to consider the change in the strength

properties due to the compacting effect of the wheel. To reconcile these conflicting requirements, a crude estimate of the change in strength properties is made according to the following scheme:

	Strength Parameters of Undistrubed Ground	Qualitative Assessment of Soil	Effect of Wheel Passage on Soil Strength in Rear field	
(A)	$\phi > 40$ $C < 50$ lbs/sq.ft.	dense frictional	no change	
(B)	$\phi < 40$ $C < 50$ lbs/sq.ft.	loose and medium dense frictional	friction angle and unit weight increase due to densification	High sinkage: increase 10% Low sinkage: increase 5%
(C)	$C > 50$ lbs/sq.ft.	cohesive soil	effect of wheel passage similar to that of overconsolidation. cohesion increases, friction angle decreases	

While the determination of whether the soil is in the A, B, or C category is straightforward, further considerations are necessary to estimate the sinkage beforehand in category B and the strength properties in category C.

To this end, a measure of the maximum vertical pressure (SIM) is established by dividing the wheel load with a contact area corresponding to 0.8 arc length. This is compared to an estimate of the maximum normal stress obtained from the following formula:

$$\sigma_n = (C+0.33\ \gamma R)\ N_{q\delta} \qquad (23)$$

where $N_{q\delta}$ is a bearing capacity factor computed from the following fomula:

$$N_{q\delta} = \frac{\cos\delta + \sqrt{\cos^2\delta - \cos^2\varphi}}{\cos\delta - \sqrt{\cos^2\delta + \cos^2\varphi}}\ e^{2\tan\varphi\,(\theta_p - \theta_a)} \qquad (24)$$

If the estimated maximum normal stress is lower than the estimated maximum vertical pressure, low sinkage is anticipated and a 5 percent increase is indicated. Otherwise, the increase is 10 percent. If the strength parameters

of the undisturbed ground fall in category C, then the strength parameters in the rear field are assumed as shown in Fig. 12. In this case, the strength of soil in the rear field is higher than in the front for normal pressures lower than the estimated maximum normal stress.

The inversion procedure discussed in Section III. D requires an estimate of initial data for the first run. These were chosen as α_r = 10 degrees and

$$\delta = (0.35 + (DB/L)). \varphi \qquad (25)$$

In the inversion procedure, the values of α_r and δ are changed as shown in the flow diagram in Fig. 10. The magnitude of the changes in each step is determined by a formula of the general type, as follows:

$$\begin{aligned} \delta_{k+1} &= C_1\delta_k - C_2\,(\lambda_k - \lambda_o) + C_3 \\ \alpha_{k+1} &= C_1\alpha_k + C_4\omega_k + C_5 \end{aligned} \qquad (26)$$

The constants in the above equations are chosen appropriately to result in a change indicated in the flow chart in Fig. 10. The following list gives the options for the above constants:

C_1 = B1 , B2

C_2 = B3

C_3 = B4 , B8

C_4 = B5

C_5 = B6 , B8

The following absolute limits have been set in the computer program for the variables α_r, α_e and δ:

$\alpha_{r\,max}$ (AMAX) = 21°

$\alpha_{r\,min}$ (AMIN) = 1°

$\alpha_{e\,max}$ (AEMAX) = 60°

δ_{max} (DMAX) = 0.98 x arc tan (sin ϕ)

δ_{min} (DMIN) = 0.05 ϕ

The limits on the entry and rear angles are based on available experimental data, and are self-explanatory. A factor of 0.98 is applied to the theoretical δ_{max} value to avoid certain computations close to limit conditions where formulas become indefinite. The δ_{min} limit is arbitrary and serves to avoid computations that would not be useful in approaching the solution.

The above limits are also used as criteria for an acceptable solution. If, for any particular input condition, the flow chart in Fig. 10 indicates a need for a change in either of the variables δ and α_r, but it is not possible to execute that change because of these limits, then there is no solution for the input condition. If the iteration procedure is terminated because the maximum limits would have to be exceeded for a solution, the "no solution" condition indicates a "no go" condition, or 100 percent slip. If the iteration procedure is terminated because the minimum limits would have to be transgressed, the "no solution" condition indicates that the soil strength is so high that failure in the soil does not develop under the input load and a "hard soil" condition exists.

The results of each step in the computer program iteration are preserved as subscripted variables with the subscripts denoting the numerals assigned to the consecutive iterations. If the solution is not reached within K3 iterations, the program changes the steps so that the increments or decrements in the δ and α_r values become about half of that during the first K3 iterations and performs an additional K5 iterations with changed constants that reduce the magnitude of δ and α_r steps to about 50 percent of that in the first K3 iterations. If no solution is reached within K3 and K5 iterations, the program scans the results and computes the output data by an approximate interpolation, if appropriate.

Output - Output data in the program are in printout form that can be easily changed to other output formats if desired. Following are the output data and symbols:

Load	LD(K)
Drawbar pull	DR(K)
Torque	TR(K)
Slip	SLP
Sinkage	SNK

The load and drawbar pull values are printed out for information only since they may differ from the input load and drawbar pull values by the tolerance limits. The torque and slip values may be used in conjunction with the transmission and engine subroutines available at TACOM (Ref. 9) to determine vehicle speed, power requirements, and fuel consumption.

IV. EXPERIMENTAL PROGRAM

A. Performance of Experiments at the Davidson Laboratory of Stevens Institute of Technology

1. Test Facility and Equipment

a. Soil Bins

The soil bin of the Davidson Laboratory is 40 feet long and 7 feet wide. The bin is divided in half longitudinally to form two separate 40' x 3 1/2' bins. One bin was filled with sand, the other with loam, both to a depth of approximately 2 1/2 feet.

b. Dynamometer Carriage

The dynamometer carriage contains the test wheel, the wheel drive motor, the hydraulics required to drive the wheel, the wheel loading system, and the dynamometer balance. The dynamometer carriage is unpowered; carriage motion is supplied by connecting it to an auxiliary carriage that contains the soil processing equipment and that is propelled by an off-carriage chain drive system.

c. Test Wheel

The wheel used was made of plywood, 28 inches in diameter and 4 1/2 inches wide. The wheel was attached to the wheel drive motor by a metal faceplate. On the circumference of the wheel were mounted four sensors, each to measure the normal and tangential forces at the periphery of the wheel. These sensors were cantilevered, L-shaped arms (Figure 13). Each leg of the L had been strain-gauged and wired in such a way that the leg perpendicular to the circumference measured the tangential forces; the other leg measured the normal forces. The four sensors were mounted transversely across the face of the wheel from the center to one edge to give a record of the cross-wise distribution of the load on the wheel as it rolls through the soil. The signals from the sensors were transmitted through a slip ring mounted on the axle to overhead cables and then to the recorders.

The head of each sensor was a square plate approximately 3/8-inch on a side. Each head was tangent to the circumference of the wheel and protruded through the approximate center of a 1/2-inch metal grid. Details of the sensor configuration within the grid and the spacing of the sensors on the wheel face are

shown in Figure 14. To prevent soil from getting between the sensors and the grid, a thin rubber membrane was cemented around the circumference.

d. Wheel Drive

The wheel was driven directly from a hydraulic motor that was, in turn, connected to an electrically-driven, variable-displacement hydraulic pump. Varying the pump output, therefore, varied the wheel speed in direct proportion. Difficulty was encountered in maintaining a constantly smooth rotation of the wheel due to a porting action at the motor. This is attributed to the fact that the wheel pump was designed to operate at speeds considerably greater than those used in the testing program.

e. Dynamometer

The wheel motor was mounted directly onto a six-component dynamometer that measured all three forces (load, drawbar pull, and side-force) all three moments (yaw moment, input torque, and roll moment).

f. Wheel Loading System

The dynamometer was mounted directly to a loading device. Loads on the wheel were applied by an air-actuated belofram and servo system. Air pressure above and below the belofram controlled the load. As the wheel sank into the soil, a hydraulic servo system positioned the beloframs in response to this wheel movement so that the beloframs were always near to their center position, regardless of the sinkage experienced. The entire wheel and loading system could be raised or lowered by manually actuating the servo system, thus clearing the wheel from the soil for soil processing or wheel maintenance.

g. Wheel Speed and Sensor Position

Wheel speed was measured in two ways. A tachometer connected directly to the wheel drive motor indicated the wheel speed. Wheel speed could also be calculated from angular position indicators mounted on the wheel. These position indicators, mounted every two degrees about the wheel generated spikes on the recording traces. These spikes began when the sensors were 50° before bottom center and ended when they were 50° after bottom center.

Initially, angular position was indicated by a series of brass screws placed at 2° intervals in a 100° arc. Two separate bronze spring brushes were placed side by side so that both brushes touched each screw as it passed. This

closed a circuit that generated a spike on both strip chart records.

The speed of the wheel frequently caused the springs to bounce, and to miss a few spikes. Therefore, after the sand tests, a new position-indicating device was employed. A semicircular piece of sheet metal was slit every 2^{o} and was mounted to the side of the wheel. A photocell detected these slits as they passed by, and caused a similar spike to be recorded.

The spikes thus generated could then be used to locate accurately the position of the sensors relative to the soil and, by measuring the distance between the spikes and the chart paper speed, to compute the wheel speed while the sensors were passing through the soil.

h. Carriage Velocity

The carriage velocity was measured by signals from markers spaced one foot apart along the side of the soil bin. As the carriage travels down the bin, the markers trip a microswitch that, in turn, causes a spike to appear on the strip chart record. With this record appearing every foot of carriage travel, and a known paper speed, the carriage velocity could be easily calculated. For all tests, carriage speed was held constant; slip was controlled by changing wheel speed.

i. Sinkage

The sinkage, or vertical travel relative to the soil surface, was measured by a multiple turn potentiometer. A spring was secured at one end of the carriage and then wrapped around a pulley on the potentiometer, which was fastened to the wheel mounting apparatus. When the wheel moved in the vertical direction, the string caused the pulley to rotate, thereby giving a signal that was calibrated to wheel sinkage. Zero sinkage is established with the bottom of the wheel, just touching the undisturbed soil surface.

j. Instrumentation

The instruments used were Sanborn Models 150 and 850 multi-channel strip chart recorders. The 8-sensor signals were fed into the Sanborn 850; the Sanborn 150 recorded wheel speed, carriage speed, sinkage, torque, horizontal drawbar pull, and vertical load. Both recorders registered the sensor position spikes. Before each day's testing, a calibration was made of all sensors so that the strip charts produced a signal accurate to one part in forty.

2. Calibration Technique

a. Calibration of Sensors

Calibration of the normal load on the sensors was done by balancing 1- to 5-pound loads on the face of the sensor. A small nut was placed on top of the sensor while the sensor was in the top center position, and then weights were balanced on the nut to prevent contact of the weight with the wheel surface. This process was done for each of the four sensors.

Calibration of the tangential loads was performed by positioning the wheel so that the sensors were at 90° from the vertical. While in this position, a small pin was placed in a hole in each sensor. Then a string carrying a 1-, 2-, or 3-pound weight was hung on that pin.

b. Calibration of Dynamometer

Calibration of the drawbar pull force was done by placing a harness on the wheel and leading a wire cable horizontally over a pulley. Weights were then hung on this cable. Vertical load was obtained by placing the wheel on a pre-calibrated load cell and loading the beloframs with air with the servos in the automatic mode. Since it was difficult to maintain a steady load with the equipment, load calibration was made before and after every test. Torque was calibrated by setting the load cell one foot from the axle center under one arm of a beam that was bolted to the axle of the wheel. The sinkage was calibrated by measuring the wheel displacement with a steel rule.

3. Preparation of Soil Bed

The following three types of soil beds were prepared:

Loose sand
Dense sand
Loam

The loose sand was processed by a gyrotiller, a leveling blade, and, for dense sand tests, a plate vibrator. The gyrotiller disturbed the sand to a depth of 18 inches and produced an uniformly loose sand layer. The plate vibrator was used for compacting the sand; it was towed at a constant speed behind the carriage after tilling. It compacted the sand to about a 6-inch depth.

The loam bed was prepared at a moisture content of approximately 16 percent. The loam was processed by the gyrotiller, leveling blade, and a roller. First, the gyrotiller tilled the clay to a depth of six inches while the blade leveled and smooth the soil. Next, a lawn roller filled with water to about two-thirds capacity was used to compact the loam (Figure 15). The loam bed was protected from evaporation by a plastic cover; water was added by sprinkling whenever loss of moisture was observed.

4. Control Tests in Soil Bed

Cone penetrometer tests were performed in the soil bed to check the uniformity and condition of the soil before the wheel performance tests (Figure 16). Cone penetrometer tests were also performed for selected tests in the ruts after the passage of the wheel. Results of these tests are reported in Section V.

The moisture content of the load bed was determined during preparation at several locations and undisturbed cylinder samples were taken to determine the density of the soil bed. These data were essential for the proper duplication of soil conditions in the triaxial tests performed for the determination of shear strength properties.

5. Strength Properties of Test Soils

For the determination of strength properties of the test soils, triaxial tests were performed on them in the Soil Mechanics Laboratory at Grumman. Results of these tests are summarized below.

a. Sand

The strength properties of sand were determined by two series of triaxial tests, one performed at a low density (98 lbs/cu. ft.) and the other one at a high density (106 lbs/cu. ft.). The air dry sand was placed in one-inch layers in a 7-inch-high, 2.8-inch-diameter mold to ensure uniform density throughout the sample. During the tests, the samples were allowed to change their volume freely; volume changes were computed from circumferential gauge readings. The tests were stress controlled; load increments were applied after the stabilization of vertical displacement. The sand was found to be insensitive to the rate of loading; therefore, no attempt was made to duplicate the loading rates in the wheel tests. The sand failed at relatively low vertical strain (less than 5 percent in each test). Mohr circle representation of the triaxial test results is

shown in Figures 17 and 18. It is seen that the strength envelope is slightly curved and the friction angle at low normal stresses is relatively high. Grain size distribution of the sand is shown in Figure 19.

b. Loam

The moisture samples taken from the test bed showed a variation of moisture content from 14.7 to 16.4 percent. The dry density of the loam, determined from cylinder samples, varied from 1.29 to 1.33 g/cu. cm. For the determination of the strength properties of the soil bed, triaxial test samples were prepared in a 7-inch-high, 2.8-inch-diameter mold in 1-inch-thick layers from uniformly mixed soil kept at 16 percent moisture content. Some moisture content was lost during the preparation and the actual moisture content of the samples was somewhat lower. Preliminary tests indicated that the loam at this moisture content was moderately sensitive to the rate of loading; the final tests, therefore, were performed as rapidly as it was possible with the available stress controlled triaxial apparatus. Failure of the loam, as expected, occurred at relatively high strains, as shown in Figure 20. Mohr circle representation of the triaxial test results is shown in Figure 21. It is noted that the moisture content of Test Number 16 was slightly higher and its dry density slightly lower than that of the other tests in the series, resulting in a relatively low strength that was not considered in drawing the strength envelope.

c. Laboratory Cone Penetrometer Tests

To correlate the strength tests with the cone penetrometer tests performed in the soil bed, cone penetrometer tests were performed in laboratory soil bins under controlled conditions. Results of these tests for sand are shown in Figure 22. These tests show that penetration resistance increases with depth as expected. While the increase is approximately linear at the lower densities it is not possible at higher densities to use linear approximation for the cone penetration curve. Nevertheless, these graphs can be used as guides to estimate the in situ density of soil bed and, therefrom, its strength properties.

A typical results of a cone penetrometer test in the loam is shown in Figure 23. The cone penetration resistance reaches an approximately constant value after about two inches of penetration. Cone penetrometer tests were performed in a laboratory bin where the loam was prepared at about 15 percent moisture content at various densities. The constant value of cone penetration resistance reached after an initial increasing portion is plotted in Figure 24.

6. Performance of Test

a. Test Plan

The test plan was to obtain three different slip ranges for three different load ranges for each of three different soil conditions. The slip and load ranges were as follows:

Slip Ranges for all Tests	
Low	5% - 10%
Medium	15% - 25%
High	greater than 25%

Load Ranges for Loose Sand and Clay	
Low	200 lb - 250 lb
Medium	300 lb - 350 lb
High	400 lb - 450 lb

Load Ranges for Compacted Sand	
Low	300 lb - 350 lb
Medium	450 lb - 500 lb
High	700 lb - 750 lb

b. Test Procedure

After preparation of the soil, cone penetrometer measurements were recorded along the path where the wheel would pass. The desired load was then set up by switching to the automatic loading mode while the wheel was at the beginning of the bin. The load measured by the dynamometer was noted on the recorder; if the desired load was not obtained, air from a high pressure supply was proportioned more suitably in the two air pressure tanks of the belofram system. The slip rate was established by presetting the wheel speed at an estimated condition, conducting short pilot tests, and noting the slip obtained. Repeated trials could obtain a close approximation to the desired slip. The test was then ready to be conducted.

One person controlled the wheel and one person controlled the recorders. The person at the recorders would first start the recorders for a few seconds before the load was applied for each channel to register zero readings. Then the chart recording the sensor outputs was stopped. To start the test, the carriage was started and the turning wheel was lowered into the fresh soil.

When the sensors were about 90° from bottom center, the chart recording the sensor outputs was started; it was then turned off when all signals of the 100° sweep were completed. This was done to conserve paper due to the high paper speed required for clear and precise signals every two degrees of wheel revolution. For each revolution, the paper recording the sensors was started and stopped until the end of the run. After the run was complete, both recorders were left running for a few seconds to re-establish the zero readings. Cone penetrometer tests were taken in the rut before the soil was prepared for the next test.

7. Problems Encountered

In concept, this program appeared to be straightforward and similar to that conducted by Shamay (Reference 10) on the same equipment in 1971. However, it was soon found that many aspects of the equipment were not well suited to the data detail required by this program.

The first problem centered about the sensors. Initially, the sensors came into direct contact with the soil. Soon after tests began, it was discovered that sand entered the spaces between the sensors and their surrounding grid, thus greatly distorting the tangential readings. To overcome this difficulty, a rubber membrane was placed over the entire circumference of the wheel.

This membrane solved the sand intrusion problem but created others. There was a difficulty in obtaining a good bond between the membrane and the sensors in order to get good transmission of shearing forces. With the membrane attached to the sensors, the strain in the rubber became part of the sensor system; hence, each sensor had to be calibrated with the membrane attached. Finally, uncertainty now arose, when converting the recorded sensor force to pressure, as to what proportion of the area of the membrane suspended between the sensor and the grid should be considered as the bearing surface of the sensor.

Obtaining stable vertical loads on the wheel posed a second problem. Theoretically, the pressure in the belofram dictated the load on the wheel. Friction in the system, however, made the load vary over a range of about 20 pounds during tests.

Proper control of wheel speed was also a problem. At the extremely slow speeds required to separate the sensor data every two degrees, the hydraulic

pump/motor system experienced porting problems that resulted in a nonuniform rotational speed. Since the carriage maintained a constant forward motion, the unsteady motion of the wheel resulted in a nonuniform slip condition. This problem would be avoided by driving the wheel through a large gear reduction system so that motor irregularities will be less pronounced.

During the testing of the wheel in the loam, it was noted that an outline of the sensors was visible in the loam where the sensors had been in contact with it (Figure 25). Apparently the loam forces itself and the membrane into the area around the sensor, thus interfering with the tangential motion of the sensor. The magnitude of this influence could not be determined.

8. Data Processing

After the tests, a preliminary analysis was conducted at the Davidson Laboratory to simplify the data, convert it to digital form, and perform preparatory validity checks.

All data except cone penetrometer readings were initially recorded in analog form on paper strip charts. The major effort of data reduction centered about the eight channels of output from the four load sensors mounted on the face of the wheel.

The first step in reducing the data that was reported from the sensors was to convert the analog output of the Sanborn recorder to digital information. This conversion was done manually by a Gerber scanner at the Davidson Laboratory. After manually positioning cross hairs on the analog curve, the Gerber scanner would automatically punch out a computer card with the numbers proportional to the magnitude recorded at each of the eight channels. The digitizing was continued past bottom center until all eight channels had returned to zero. In addition to the digitized sensor data, each card contained the run number, and the span of angular positions associated with that card. One thousand digital units were assigned each channel, which spanned 50 mm of recording paper.

Another part of the preliminary data reduction scheme was the computation of the applied loads to the wheel. Using the output of the Gerber, and the calibration data acquired each day, a computer program transferred the measured sensor loads at each interval and computed the net horizontal (drawbar pull) and vertical load and torque. This computation consisted of a numerical inte-

gration of each 2-degree force measurement, appropriately modified by the sine or cosine of the angle from the vertical of the sensors at the time of the measurement. Consideration was also given to the placement of the sensors across the face of the wheel and to the fact that only one side of the wheel was instrumented.

For further analysis, a digitized data file was prepared for each run, punched on paper tape and transmitted for use with the On-line computer system at Grumman. A typical printout of such a data file is shown in Figure 26. The paper tape was read at Grumman and was stored in the computer for ready availability. Computer programs were written at Grumman to prepare reduced data files suitable for graphical display of the experimental results on the visual display terminal. The program allowed display and visual inspection of the experimental results in the following forms:

- Distribution of normal stresses across the wheel at verious central angles
- Distribution of shear stress across the wheel at various central angles
- Longitudinal distribution of normal stresses measured by individual gages
- Longitudinal distribution of shear stresses measured by individual gages
- Longitudinal distribution of interface friction coefficient measured by individual sensors
- Longitudinal distribution of average normal and shear stresses
- Longitudinal distribution of average interface friction coefficient

In the preparation of the reduced data files for the display of average stresses, the program allowed the optional elimination of one of the four sensor readings from the computation of averages. This option made it possible to use data from some runs where readings of a sensor were found defective.

Copies of the graphical presentations on the visual display terminal were made by a hard copier and used for the purposes of records and preparation of illustrations.

B. Performance of Experiments at Grumman

1. Mobility Testing Bin

The Grumman Research Department's mobility testing bin measures 1' x 0.85' x 7.5' in its present configuration. The bin is positioned in a larger container

and its width is adjusted by changing the size of the interior lateral support members (see Figure 27). This feature was incorporated into the bin design to facilitate handling of test bed materials. The bin can also be sloped up to 15 degrees, a feature unique to the Grumman bin. When the bin is sloped, the wheel assembly can be pivoted on the carriage and locked into place to allow the application of vertical loads. The carriage that contains the wheel assembly rests on teflon sliders and is driven by a recirculating ball drive. The wheel itself is driven by a variable speed motor with controls that ensure a constant torque over the range of vertical loads used in the testing program. An aluminum wheel, 8 inches in diameter and 2 inches wide, was used although the wheel assembly can accept a slightly larger diameter and width.

2. Instrumentation

Load and drawbar pull are obtained directly by load cells attached to the wheel assembly. Normal and shear stresses are measured by a sensor that consists of strain gauges on an axle-mounted cantilever beam. The sensor head (3/8-inch square) is tangent to the circumference of the wheel. It protrudes through an approximately 1/2-inch square opening in the face of the wheel. The opening is filled with a lightweight, flexible, felt cloth to prevent bed material from entering the sensor or lodging in the sensor housing. As an added precaution, a rubber membrane is stretched over the wheel so that the entire wheel face is covered. The center of the sensor may be positioned on the wheel face either at the center or 5/16-inch from one of the edges. Torque is measured directly by a Lebow torque sensor on the shaft of the wheel drive motor. On each revolution of the wheel, the position of the sensor is recorded as it passes through "12 o'clock." The travel length of the wheel per revolution is determined by measuring directly the distance between sensor imprints in the bed material. A check is obtained by comparing the computed slip to the slip corresponding to the precalibrated settings of the wheel and carriage motor controls. The output signals of all sensors and load cells are transmitted through a slip ring on the wheel axle to a six-channel Brush strip chart recorder (Model 260).

V. RESULTS OF EXPERIMENTS

A. General

The experimental data obtained from each run (one revolution of the wheel) were examined to determine whether the measurements were acceptable. The first step in this examination was a comparison of the measured load, drawbar pull, and torque values with those computed by integrating the measured interface stresses. In this comparison, differences can be expected not only due to the experimental inaccuracies, but also because of the approximations in the integration procedure. The stresses measured by the individual gauges are averaged on the assumption that the stress distribution between gauges is linear, resulting in an inherent inaccuracy in the computation whenever this is not the case. In comparing the measured and computed values, the experimental data were accepted when the load and torque values agreed reasonably well. With respect to the computed and measured drawbar pull values, the criteria for accepting the test results were liberal, mainly because the measured drawbar pull values reflected an average value over a full revolution of the wheel, while the measured stress values were valid for the short period while the instrumented portion was in contact with the soil. Due to the problem of uneven motion of the wheel, mentioned in Section IV. A.7, the difference in measured and computed drawbar pull values did not necessarily indicate inconsistency. In comparison to theoretical predictions, the drawbar pull computed from interface stress measurements was accepted as representative of that particular position of the wheel.

Another examination of the experimental data consisted of the inspection of the transverse distribution of measured stresses. In some cases, stresses measured by an individual gauge were found inconsistent with those measured by the neighboring gauges. Such defective measurements may have been caused by the malfunction of electronic circuitry, but may also have been caused by local soil conditions. Although the test sand contained only an insignificant amount of sizes greater than 1/4-inch, occasionally such a particle could have conceivably been encountered by a sensor, causing erratic signals. When such a situation was detected, the defective gauge readings were eliminated from the averaging process.

The above examination of experimental data resulted in detecting equipment malfunctions and improper operational procedures, leading to subsequent improvements in the performance of the experiments. Those experiments where the validity of data was questionable were eliminated from the comparison of experiments to theory and are not reported here. The results of valid experiments are reported below, grouped according to the type of soil in which they were performed.

B. Experiments Performed in Loose Sand

The results of experiments performed in loose sand are shown in Table 1, together with the wheel performance data predicted by the theory. The measured distribution of interface normal and shear stresses are shown in Figures 27 through 44 as indicated in the tabulation. The stress distributions for several runs that were performed in the same carriage pass are shown in the same illustration. These are:

Fig. 30	for Runs Nos. 77-78
Fig. 31	for Runs Nos. 80-81
Fig. 36	for Runs Nos. 87-88
Fig. 37	for Runs Nos. 89-91
Fig. 38	for Runs Nos. 92-94
Fig. 44	for Runs Nos. 121-123.

These illustrations show that the experiments yielded repeatable results within the accuracy of the equipment used and the limitations of preparing a uniform soil bed. It is interesting to note that stress distributions that could be called identical on visual inspection yield sometimes significant differences in drawbar pull.

The measured coefficient of interface friction was also evaluated for most of the runs. Results, where available, are shown in Figs. 45 to 55. The scatter of the points close to the entry and rear angle is the result of both the shear and normal stresses in this region being very low. The inherent inaccuracies in the measurements become magnified when the interface friction coefficient is computed as the ratio of shear stress to normal stress. Further discussion of the interface friction is presented in Section VI.

Table 1.

RESULTS OF TESTS PERFORMED IN LOOSE SAND

Run No.	τ	Load (Lbs)	Drawbar Pull (Lbs)	Torque (Ft-Lb)	Slip (%)	Sinkage (in.)	Distr. of Avg. Stresses Fig. No.	Distr. of Interf. Fr. Coeff. Fig. No.	Cone Penetrometer Tests Fig. No.
69	M	402	6	157	33	3.2	28	45	56
	P	386	0	107	13	2.5			
70	M	446	26	193	32	3.6		46	
	P	429	13	152	20	2.9			
71	M	417	6	156	17	4.0	29	47	
	P	386	1	108	13	2.5			
77	M	519	-1	199	25	3.5	30	-	
	P	469	4	125	12	2.9			
78	M	522	-5	193	26	3.5		-	
	P	474	1	123	12	2.9			
80	M	406	2	146	29	3.6	31	48	
	P	386	-1	105	12	2.5			
81	M	379	10	143	29	3.6			
	P	385	-1	105	15	2.5			
82	M	353	-8	82	22	3.2	32	-	
	P	386	-4	90	10	2.3			
83	M	457	34	122	14	3.0	33	-	
	P	482	23	199	25	3.5			
84	M	327	-20	50	4	3.5	34	-	
	P	299	-11	45	4	1.6			
85	M	319	-13	59	4	3.0	35	-	
	P	309	-5	73	8	2.0			
87	M	375	9	125	30	4.2	36	49	
	P	378	4	122	18	2.6			
89	M	409	-3	116	20	4.4	37	50	
	P	383	1	115	15	2.5			
90	M	441	-2	137	21	4.4		51	
	P	455	5	137	14	2.8			
91	M	453	-16	140	24	4.4		52	
	P	465	-3	115	9	2.9			
92	M	413	19	139	15	3.6	38	53	
	P	373	6	127	18	2.6			
93	M	411	7	123	16	3.6		54	
	P	380	4	120	16	2.6			
94	M	428	13	135	13	3.6		-	
	P	444	9	146	16	2.4			
102	M	444	25	145	34	3.0	39	-	57
	P	440	12	153	18	2.9			
105	M	532	2	164	22	3.5	40	-	
	P	480	8	148	14	3.2			
117	M	229	17	68	10	1.4	41	-	
	P	217	12	70	16	1.8			
119	M	299	37	113	9	2.0	42	55	
	P	316	34	145	32	2.6			
120	M	286	0	67	5	1.8	43	-	
	P	276	6	57	6	7.6			
121	M	250	30	96	13	1.8		-	
	P	248	30	112	28	2.4			
122	M	254	19	83	22	1.8	44	-	
	P	267	17	86	16	2.0			
123	M	247	11	75	21	1.8		-	
	P	227	10	68	14	1.7			

τ M = Measured
P = Predicted (these values may differ marginally from those predicted by the delivered program because of changes in the assumption of initial values).

Predictions shown in Table 1 are based on $\varphi = 38^{o}$ friction angle in the front field. In the rear field, 5 percent increase of the friction angle was assumed for lower loads (up to 300 pounds) and 10 percent for high loads. Slip predictions are based on the constants $j_o = 0.07$ and $K = 0.35$. Results of cone penetration tests are shown in Figs. 56 and 57. Parameters in the plate sinkage equation,

$$p = p_o + kz^n$$

were found as follows (dimensions in inches and pounds):

$$p_o = 1.8 \quad k = 4.0 \quad n = 1.28$$

C. Experiments Performed in Dense Sand

The results of experiments performed in dense sand are shown in Table 2, together with the wheel performance data predicted by the theory. Figures 58 through 69 show the distribution of average interface stresses obtained in various runs for the loading conditions indicated in Table 2. Figure 63 shows interface stress distributions for Runs 111 and 112, which were obtained in one carriage pass. It can be seen that the measured stresses were reasonably well reproduced in the two runs, indicating the validity of the measurements. The interface friction coefficients for these tests are shown in Figs. 69 through 78. While the interface friction that developed along the soil wheel interface in loose sand was reasonably uniform in most of the runs, in dense sand it decreased from the entry and rear angles toward the separation angle.

The results of cone penetrometer tests performed both before and after runs are shown in Figs. 79 through 83. It is interesting to note that cone indices measured in the rut were generally lower than those measured in the compacted soil bed before the test. This finding is consistent with soil mechanics theory that associates volume changes with the development of the shear strength of granular materials. While loosening of dense granular materials on shearing have been observed in many triaxial tests, it is the first time that such loosening has been observed in connection with wheel-soil interaction. The wheel performance predictions given in Table 1 are based on a friction angle of $\phi = 44$ degrees in both the front and rear field. Since loosening of the material

Table 2.

RESULTS OF TESTS PERFORMED IN DENSE SAND

Run No.	τ	Load (Lbs)	Drawbar Pull (Lbs)	Torque (Ft-Lb)	Slip (%)	Sinkage (in.)	Distr. of Avg. Stresses Fig. No.	Distr. of Interf. Fr. Coeff. Fig. No.	Cone Penetrometer Tests Fig. No.
98	M	426	32	138	29	1.5	58	-	79
	P	424	33	158	20	1.5			
107	M	486	57	158	26	1.9	59	69	
	P	503	45	200	22	1.9			
108	M	487	67	177	26	1.0	60	70	
	P	491	62	240	46	2.2			
109	M	561	51	127	13	0.9	61	71	
	P	530	44	205	20	1.8			80
		574	58	189					
110	M	481	10	118	24	1.3	62	72	
	P	467	22	116	9	1.2			
111	M	535	15	100	30	1.0	63	73	
	P	520	24	107	6	1.1			
112	M	552	4	105	15	1.1		74	
	P	567	21	106	6	1.0			
113	M	535	25	124	19	1.1	64	75	
	P	541	40	188	17	1.7			
114	M	576	2	127	24	1.3	65	76	
	P	542	14	78	3	0.8			
115	M	513	41	174	31	1.4	66	77	81
	P	527	43	199	20	1.8			
124	M	336	42	83	12	1.0	67	78	
	P	308	32	146	32	1.8			
126	M	550	1	79	11	0.8	68	-	
	P	544	14	77	3	0.8			

τ M = Measured
P = Predicted (these values may differ marginally from those predicted by the delivered program because of changes in the assumption of initial values).

is the end product of the shearing process, a decreased friction angle would have manifested itself only on a new application of load, as in tandem wheel arrangements of multiple pass situation. The slip predictions are based on $j_o = 0.04$ and $K = 0.35$. Plate sinkage test parameters for the compacted sand were found as follows:

$$p_o = 3.0 \quad k = 6.9 \quad n = 2$$

In some instances, the predicted torque values differ appreciably from the measured ones. The main cause of these discrepancies is that in the tests performed in dense sand the distribution of interface friction was far from the uniform one assumed in the computations. Further discussion on the effect of non uniform distribution of interface friction on wheel performance is given in Section VI.

D. Experiments Performed in Loam

The results of experiments performed in loam are summarily presented in Table 3. The measured average normal and shear stresses are presented in Figs. 82 through 89. Figures 82 through 87 show interface stresses measured in more than one run in the same pass of the carriage. The measurements indicate a reasonable repeatability of tests run under the same conditions. One inaccuracy that occurred in almost all of the tests performed in loam is a minor negative shear stress in the neighborhood of the entry angle. This could have been caused either by some stress in the rubber membrane or by soil intruding in the clearance between the sensor and wheel face. Even though these negative shear stresses were obviously erroneous, their magnitude was insignificant and the error caused by this inaccuracy negligible.

Another interesting feature of these tests is the increase of developed shear stresses toward the rear. In some instances, the shear stresses in the rear were as high as the normal stresses (e.g., Fig. 84), indicating a condition that is difficult to explain by the Mohr-Coulomb concept of shear strength. Examination of these experimental data did not reveal major inconsistencies and, therefore, they are believed to be at least approximately correct. Interface stress measurements by others (Ref. 11) show similar magnitudes of the shear stress in cohesive soils, supporting thereby the validity of the experimental results obtained at Stevens. The study of these measurements and the

Table 3

RESULTS OF TESTS PERFORMED IN LOAM

Run No.	τ	Load (Lbs)	Drawbar Pull (Lbs)	Torque (Lb-Ft)	Slip (%)	Sinkage (in.)	Distr. of Avg. Stresses Fig. No.	Distr. of Interf. Fr. Coeff. Fig. No.	Cone Penetrometer Tests Fig. No.
129	M	336	120	203	16	1.0			
	P	336	122	176	10	1.0			
130	M	322	111	185	22	1.0	82	90	
	P	322	102	167	10	1.1			
131	M	310	130	199	13	0.9			
	P	310	109	142	10	0.6			
132	M	244	24	72	?	0.9			
	P	244	28	28	-1	0.2		91	
133	M	244	14	59	?	0.9	83		97
	P	244	28	29	-1	0.2		92	
134	M	303	100	166	11	1.0			
	P	303	116	92	6	0.4		93	
135	M	340	111	185	7	1.0	84		
	P	340	103	168	9	1.1		94	
136	M	336	114	192	10	1.0			
	P	336	112	177	10	1.1		95	
137	M	401	66	157	0?	1.2			
	P	401	69	106	2	0.5		-	
138	M	404	39	125	0?	1.2			
	P	404	39	64	-1	0.4	85	-	
139	M	370	34	111	0?	1.2			
	P	370	36	55	-1	0.3		-	
140	M	490	33	141?	-5?	1.5			
	P	490	37	70	-1	0.6		-	
141	M	527	25	149?	-4?	1.5	86		
	P	508	11	64	-2	1.7			98
142	M	519	0	118?	-8?	1.5			
	P	479	3	40	-4	0.5		-	
143	M	441	158	257	10	1.5			
	P	441	148	229	10	1.5		-	
144	M	461	140	264	7	1.5	87		
	P	461	128	226	6	1.6		-	
145	M	454	20	121	0?	1.3			
	P	493	8	57	-2	0.6	88	-	
146	M	531	107	226	1?	1.3			
	P	531	101	153	3	0.8	89	96	

τ M = Measured
P = Predicted (these values may differ marginally from those predicted by the delivered program because of changes in the assumption of initial values).

soil properties lead to the tentative conclusion that the expansion of the partially saturated loam, that wheel action allows in this zone, results in special strength properties. Further research is needed in this area to confirm this tentative conclusion.

This interface friction coefficients (tan δ as defined in Fig. 1) is shown for some runs in Figs. 90 through 96. The development of interface friction is different from that observed either in the loose or dense sand; the interface friction appears to be generally increasing from the entry angle towards the rear.

The predicted values are based on a cohesion of 220 lbs/sq ft and a friction angle of ϕ = 18 degrees as found by the triaxial tests. The predicted torque values are generally lower than the measured ones for reasons explained in detail in Section VI. The slip predictions are based on the following parameters: j_o = 0.15, K = 0.15. Plate sinkage parameters were found to be p_o = 4, k = 6.6 and n = 0.62.

E. Experiments Performed in Medium Dense Jones Beach Sand

The results of experiments performed at the Grumman Soils Research Laboratory in medium dense Jones Beach sand (Long Island, New York) are shown, together with predicted wheel performance data, in Table 4. The 8-inch-diameter, 2-inch-wide wheel could accommodate only one sensor at a time across its width. Therefore, to determine the stress distribution across the wheel, one series of tests was performed with the sensor centerline at the center of the wheel face and another series with its offset 3/4 inch from the center. The equipment was calibrated prior to each series of tests. The average cone index of the material before passage of the wheel was approximately nine psi whereas the average cone index measured in the rut after passage of the wheel was approximately 15 psi. To account for this change of strength, the predictions shown in Table 4 are based on ϕ = 36 degrees in the front field and ϕ = 41 degrees in the rear.

Figures 99 and 100 show measured and computed stress distributions beneath the wheel for the level and sloped bin, respectively. In both illustrations, the data points refer to measured interface normal and shear stresses, while the solid and dashed curves correspond, respectively, to the normal and shear stress distribution computed by the theory. In all cases, agreement between measured and computed performance parameters is seen to be acceptable.

Table 4.

RESULTS OF TEST PERFORMED AT GRUMMAN IN MEDIUM DENSE JONES BEACH SAND

Run No.*	τ	Load (Lb)	Drawbar (Lbs)	Torque (ft-lb)	Slip (%)	Sinkage (in)	Dist. of Avg Str Fig No
111003 and 111401	M	10	0.8	0.9	38	0.53	-
	P	9	0.6	0.5	30	0.37	-
111005 and 111403	M	10	1.1	1.0	17	0.49	-
	P	8	1.6	0.8	16	0.30	-
110102 and 110602 (Level)	M	7.5	1.2	0.7	17	0.32	99
	P	7.2	1.8	0.8	21	0.24	99
110104 and 110604 (Slope)	M	10.7	0.8	0.8	17	0.68	100
	P	8.9	1.1	1.0	21	0.53	100

τ M = Measured
P = Predicted

* Two run numbers are given for each entry, one corresponding to the sensor position at the middle of the wheel face and the other for the sensor at the edge.

VI. EVALUATION OF TEST RESULTS AND PREDICTIONS

A. Validity of Basic Concepts

The experimental program results generally confirm the validity of the basic concept of soil-wheel interaction that the interface stresses are governed by the plastic state of stresses in the soil. Sample comparisons of interface stresses measured and computed on this basic concept are shown in Figs. 39, 40, 58 and 86 for various conditions. These illustrations show good agreement between experiments and theory. A detailed examination of all test results showed that there were three areas where evaluation of the experimental results has a bearing on the basic concept. These are discussed below.

- The predicted stress distribution curves from the front and rear field form a cusp at the angle of separation. The stress distribution curves obtained in the experiments show a rather smooth transition at this point. Whether this smoothness is due to some inertial lag in the instrumentation or some adjustment in the soil could not be ascertained. Since the observed discrepancies between predicted and measured values are limited to a small area, the question is mainly of academic interest and does not affect prediction results appreciably.
- In cohesive soils, the theory predicts an instantaneous rise of the interface stresses at the entry and rear angles. The observed stress rise, though rapid, is not instantaneous. This discrepancy between theory and experiments is the consequence of using the Mohr-Coulomb yield criterion in plasticity theory irrespective of the volumetric strain that is associated with the development of yield strength of soil. In the prediction method, a stress distribution that features instantaneous rise results in a smaller entry angle and, consequently, a lower torque value than in reality.

  If soil strength properties are determined by triaxial tests, the vertical strain associated with yield strength is available. In soil-wheel interaction, the direction of major principal stress in the front field is close to the vertical, just as it is in the triaxial test. Thus, an analogous situation exists from which approximate relationships could be developed for the strength properties applicable at central angles close to the entry angle where soil strain

is low. Further research in this area is recommended.

- One basic assemption of the theory is that the stresses in planes parallel to the plane of motion are the same, i.e., the problem is two dimensional. An evaluation of the experimental results was made to see how well the experiments conform with this basic assumption. The results of this evaluation are summarized below.

  In the tests performed in loose sand, the distribution of stresses across the wheel was reasonably uniform. A typical example of such distribution is shown in Figs. 101 and 102.

  In the tests performed in dense sand, the distribution of stresses across the wheel was found to conform with the hypothesis that there is a limiting transverse distribution governed by potential lateral failure. In granular soils, this limit is approximately linear (Fig. 103) and varies with the depth of the cross section. Stresses computed from the conditions in the plan of motion may not exceed this limit set by the transverse conditions. Figures 104 and 105 show an example where this limiting condition governs the stresses across the full width of the wheel, while Figures 106 and 107 exemplify a case where the transverse limiting conditions govern in that portion of the wheel that is close to the side and longitudinal conditions govern the stresses in the center portion.

  In the tests performed in loam, the transverse distribution of stresses was found to be influenced by the condition of the uniform vertical displacement imposed on the soil by the rigidity of the wheel. These conditions require that the stresses at the edges be higher at the edges than in the center. A typical transverse distribution of normal stresses in loam is shown in Figs. 108 and 109. This type of distribution also indicates that in the transverse direction the soil is far from failure state; although the hypothesis for a transverse limiting conditions could hold true for cohesive as well as frictional soils, in cohesive soils this condition is rarely critical as it will be seen from the discussion below.

The above typical examples show various types of transverse distribution of stresses and raise a question as to why the transverse limiting conditions govern in one case and not in another one. The answer lies in understanding the nature of the limiting conditions shown in Fig. 103. The intercept, q_t, is proportional to the depth of the cross section. For the transverse limit-

ing conditions to govern, the sinkage of the wheel must be low (depth of cross sections small) and the longitudinal stresses must be relatively high. Both of these conditions are present in the wheel tests performed in dense sand and are absent in the test performed in loose sand.

In cohesive soils, the magnitude of q_t intercept depends not only on the depth of the cross section, but also on the value of cohesion. Even a small amount of cohesion is sufficient to result in such q_t values that the transverse limiting condition ceases to be critical.

It is possible to formulate the above qualitative statements mathematically and to improve thereby the accuracy of the prediction method. A further advantage of the mathematical formulation would be in the analysis of multiple wheel performance. Adjacent wheels influence the transverse limiting conditions by hindering lateral failure; their effect would, however, be negligible when transverse limiting conditions are not critical.

B. Validity of Tentative Assumptions

In the application of the basic concept of soil-wheel interaction to the problem of wheel performance calculations, it was necessary to make certain assumptions, discussed in Section II, to define the problem completely. These assumptions were made on the basis of experimental information available at the time of the development of the program. With more information available from the validation test series performed at Stevens Institute, it is proper to reexamine these assumptions. The results of this reexamination are summarized below.

For the definition of the boundary condition at the interface, the interface friction angle δ was introduced. In the computations, this angle was assumed to be constant. This assumption, however, is not essential to the basic concept that requires only that the angle δ be defined but not necessarily constant along the interface. For the evaluation of the interface friction that developed along the interface in the experiments, a computer program was written that calculates the coefficient of interface friction ($\tan \delta$) from

the raw data file and prepares a data file suitable for viewing on the visual display terminal. The computed values are averages over the width of the wheel and are shown, where available, in the illustrations referenced in Tables 1 through 3. The following general conclusions may be drawn from these illustrations:

In loose sand, with some exceptions, the assumption of a constant interface friction coefficient appears to be a reasonable approximation (see Figs. 45 through 55). The exceptions are where the interface friction coefficient decreases from the edges toward the center, a distribution that was found typical of the tests performed in dense sand (see Figs. 69 through 78). In the loam, the distribution of the interface friction coefficient along the interafce was found to be different from either that typical of loose sand or that typical of dense sand. The typical feature of the distributions of the interface friction coefficient in loam shown in Figs. 90 through 96 is that the highest value occurs at α = 0 degree, the bottommost part of the wheel. An explanation of this feature could be that the development of interface friction in the highly compressible loam is associated with volumetric straining of the soil, which is obviously the greatest at the bottom of the wheel.

In anticipation of a nonuniform distribution of the interface friction coefficient, provisions were made in the computer program that allow a linear variation of the interface friction coefficient along the interface. However, the new experimental evidence obtained in the validation test series is not sufficient to formulate a relationship among the various types of the distributions of interface friction coefficients and soil properties and wheel loadings. For this reason, it was not possible to use that capacity of the program that allows a linear variation of δ along the interface. Further theoretical and experimental research is needed to clarify the relationships that govern the development of interface friction. This is all the more important since the traction developed by wheels is directly related to the development of interface friction.

Another reason to do further research in this area is the connection between the angle δ and the angle of separation, α_m. In Section II, a relationship between δ and α_m was established that was incorporated in the

computer program. In the development of this relationship, δ was assumed to be constant. If δ is variable along the interface, α_m may become indefinite. Another possibility that would have to be investigated is that the variation of the interface friction reflects the mutual adjustment of the angle of separation and interface friction so that the requirements set forth in Eq. (16) may be met. A review of predictions indicates that in most cases where prediction accuracy was not good, the maximum normal stress occurred at an angle that deviates from the hypothesized separation angle. Thus, a significant improvement in prediction accuracy could be obtained if the variation of the friction along the interface and the angle of separation associated with this variation could be more accurately introduced in the program.

The development of interface friction is also associated with slip and Eq. (13) was used in the program to compute slip from the value. Obviously, Eq. (13) is not defined for a variable δ and this may be one reason for the poor slip predictions shown in the tabulations. Unfortunately, the measured slip values are also somewhat uncertain because of the uneven rotation of the wheel discussed in Section IV. A. 1. For this reason, it is difficult to evaluate the validity of Eq. (13) or to draw conclusions about the influence of a variable δ on slip. An interesting concept that would evolve from the study of the variation of δ and slip is shown schematically in Fig. 110. It was found that, at lease in the front field, lines drawn perpendicular to the direction of the major prinicpal stress intersected the vertical of the wheel axle within very narrow limits presumably centering around the instantaneous center of reaction. Since the direction of principal stresses coincides with that of principal strains in isotropic soils, it is reasonable to assume that the displacement velocity vector would be directed the same way as the principal strain vector in compressible media. Could this be proven and formulated mathematically, a very important breakthrough in the somewhat nebulous relationship between slip and mobilization of interface friction could be accomplished.

To study possibilities of improving slip predictions, an analysis of measured and predicted slip values was made. Results of this analysis are shown in Figs. 111 and 112, which show measured and predicted slip values plotted against the pull coefficient for the tests performed in loose sand.

For a given soil, the points should be within a narrow band representing a unique relationship for the experimental scatter. It can be seen from Fig. 111 that the experimental results do not collapse in a narrow band, indicating that the uneven motion of wheel resulted in inaccurate slip measurements. Because of the uncertainities in the measured slip values, it was pointless to try improvements in the theoretical predictions that yield, at least qualitatively, a satisfactory pull coefficient slip relationship (Fig. 112).

VII CONCLUSIONS AND RECOMMENDATIONS

The theoretical and experimental investigations performed under the contract conclusively show that the proposed concept of soil-wheel interaction is valid and that the application of plasticity theory to wheel-tire interaction problems is a valuable tool in the mathematical formulation of the problem. The analysis of experimental results in the framework of the basic concept provided new insight into the interaction problem and essential new information was gained for the theoretical formulation of more complex interaction problems such as soil interaction with pneumatic tires, tandem and multiple wheels, and multipass interaction analysis.

The computer program developed for the numerical solution of the interaction problem yields the answers within an acceptable computer time. Predictions by the computer program were generally good. The accuracy of predictions depended on how well certain assumptions, made in the development of the program on the basis of experimental information, approximated actual conditions.

The areas where further research would result in improved prediction accuracy or in expanding the applicability of the concept and program to cases not covered in the present study are listed below.

- Theoretical and experimental research in the area of the development of the interface friction and its relationship with slip. Research in this area would lead to a significant improvement in the prediction method. Also, theoretical formulation of the development of interface friction for towed and braked wheels could be included in this research and used in the application of the present computer program for the prediction of towed and braked wheel performance. This would then be used to predict the performance of 2x4, 4x6 and other multi-axle vehicles.
- Theoretical and experimental research to develop a theory for changes in strength properties of soils due to the compacting effect of wheels. Mobility predictions are based on virgin ground soil properties, yet traction develops primarily in the rear portion of the wheel where the soil is already compacted. A study to formulate the effect of compaction would be essential not only for application in the present theory but also for use with any other predictive method. In the framework of such a study, an analysis of the volumetric strain necessary to

develop the Mohr-Coulomb yield strength could be made and improvements in the accuracy of wheel performance predictions could be achieved. Research in the strength properties would also be useful for the formulation of the analysis of tandem wheel performance and for the development of multipass criteria.

- Theoretical and experimental research to formulate criteria for lateral failure. Such research would not only improve the prediction method, but would also lay the foundations for the analysis of multiple wheel performance.
- Validation test program for slopes. All validation tests, except for one at Grumman, were performed on level soil beds. It would be desirable to perform a test series on slopes with interface stress measurements since no such information is available at present.
- An extension of the theory of rigid wheel-soil interaction to pneumatic tire-soil interaction so that the effect of tire deflection on soil response could be taken into account and a computer program for the prediction of tire performance in soft soil formulated.

VIII. REFERENCES

1. Karafiath, L., "Plasticity Theory and Stress Distribution beneath Wheels," Journal of Terramechanics, Vol. 8, No. 2, 1971.

2. Karafiath, L., "On the Effect of Pore Pressures on Soil-Wheel Interaction," Proceedings Fourth International Conference for Terrain Vehicle Systems, Stockholm, April 1972.

3. Sokolovskii, V. V., Statics of Granular Media, Pergamon Press, 1965.

4. Harr, M. E., Foundations of Theoretical Soil Mechanics, McGraw-Hill Book Company, 1966.

5. Karafiath, L. and Nowatzki, E., "Stability of Slopes Loaded over a Finite Area," Highway Research Board Record No. 323, November 1970.

6. Nowatzki, E. and Karafiath, L., "General Yield Conditions In A Plasticity Analysis of Soil-Wheel Interaction," presented at 8th U. S. National Off-Road Mobility Symposium of the ISTVS, Purdue University, October 1972.

7. Karafiath, L. and Nowatzki, E., The Effect of Speed on Wheel Drag in Soil, Grumman Research Department Memorandum RM-546, July 1972.

8. Sela, A., The Shear to Normal Stress Relationship between a Rigid Wheel and Dry Sand, U. S. ATAC Land Locomotion Laboratory Report, June 1964.

9. Wollam, J., Generalized Tracked and Wheeled Automotive Performance Model, SAE Paper No 710628, June 1971.

10. Shamay, S., Normal and Shear Stress Distribution Under a Rigid Wheel in Dry Sand, Report SIT-DL-71-1554 Davidson Laboratory, Stevens Institute of Technology, September 1971.

11. Krick, G., "Radial and Shear Stress Distribution Under Rigid Wheels and Pneumatic Tires Operating on Yielding Soils with Consideration of Tire Deformation," Journal of Terramechanics, Vol. 6, No. 3, 1969.

12. Krick, G., Die Wechselbeziehungen Zwischen Starren Rad, Luftreifen and Nachgiebigem Boden, Dissertation, Technische Universität München, 1971.

13. Janosi, Z, and Hanamoto, B., "The Analytical Determination of Drawbar Pull as a Function of Slip for Tracking Vehicles in Deformable Soils" Paper No. 44 Proceedings of the First International Conferance on Terrain - Vehicle Systems, Edizion Minerva Technica, Torino, Italy, 1961

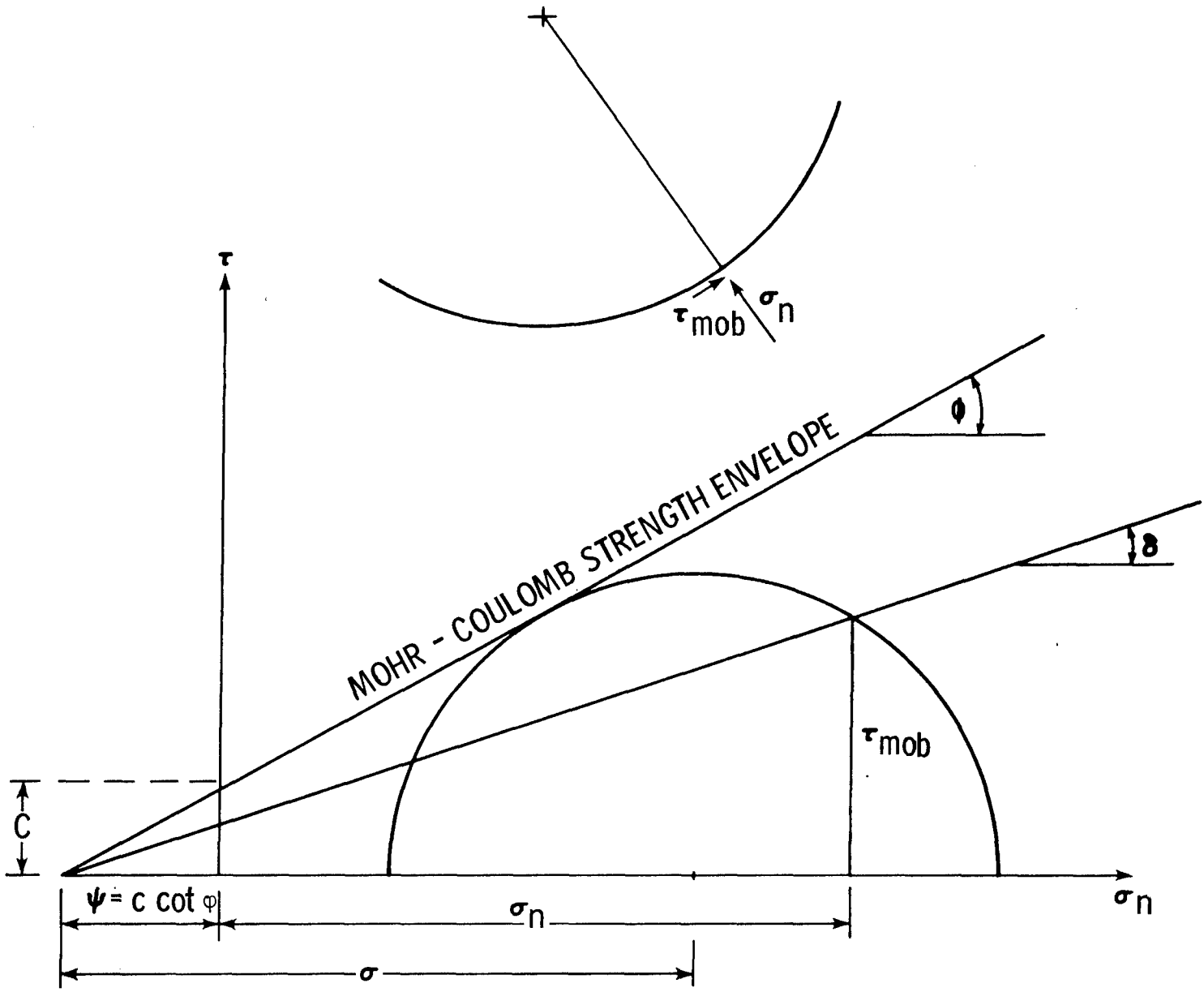

Fig. 1 Mohr Circle, Mobilized Shear Strength and Interface Friction Angle (δ)

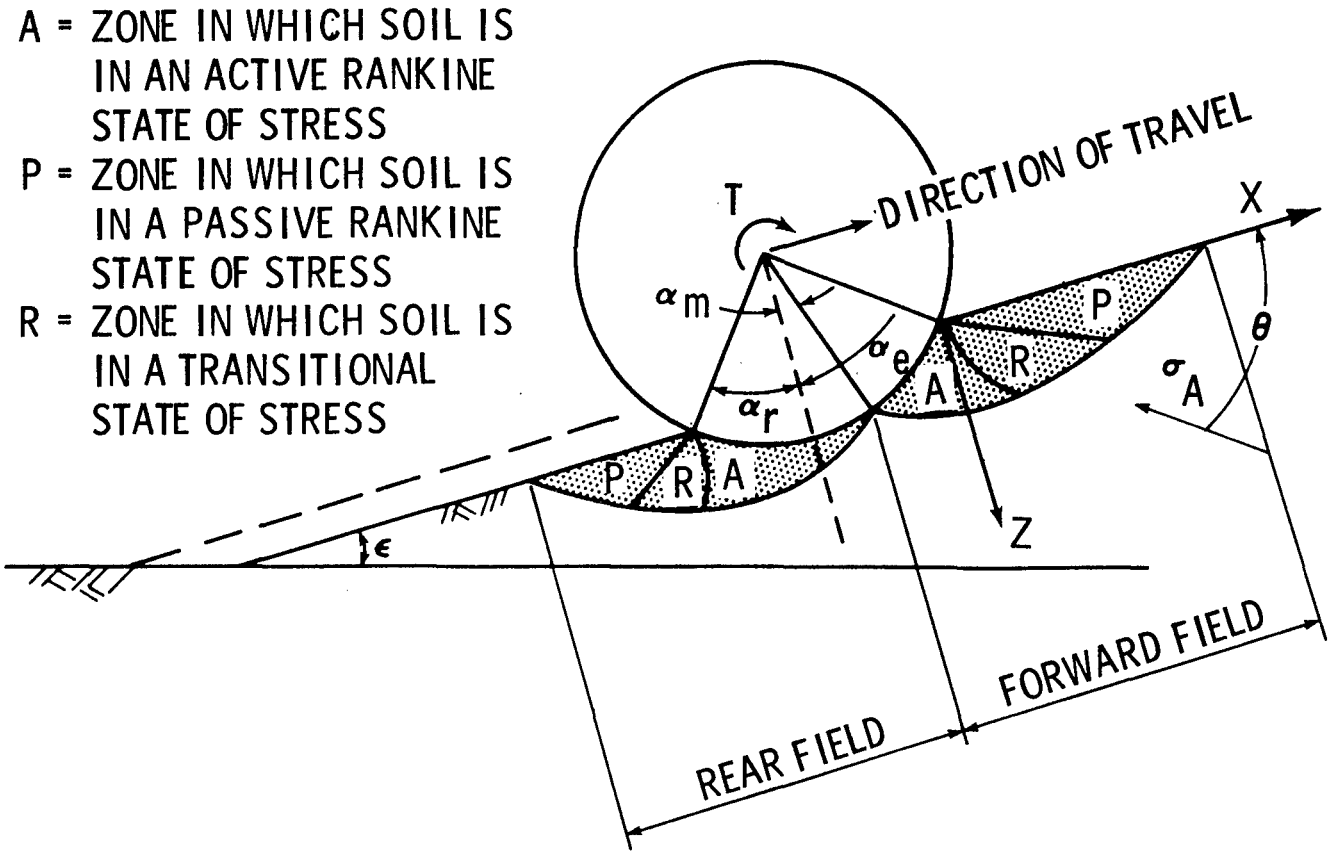

Fig. 2 Failure Zones Beneath Wheels

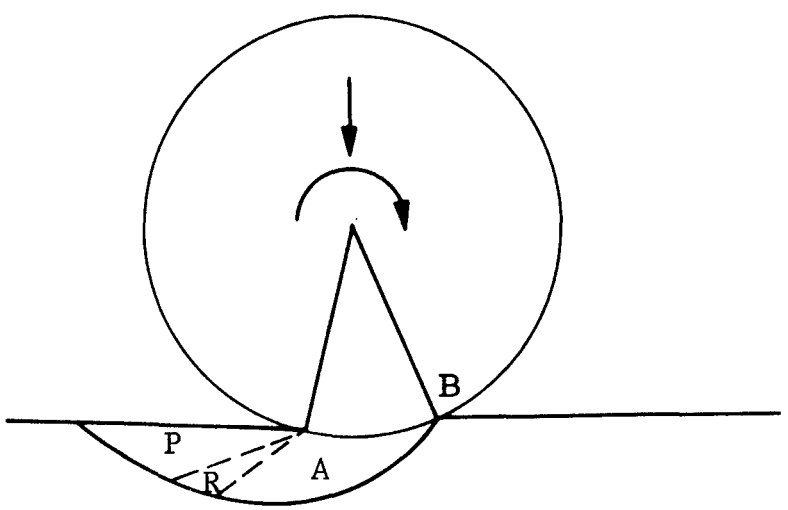

Fig. 3 Single Failure Zone in the Rear of a Driven Wheel

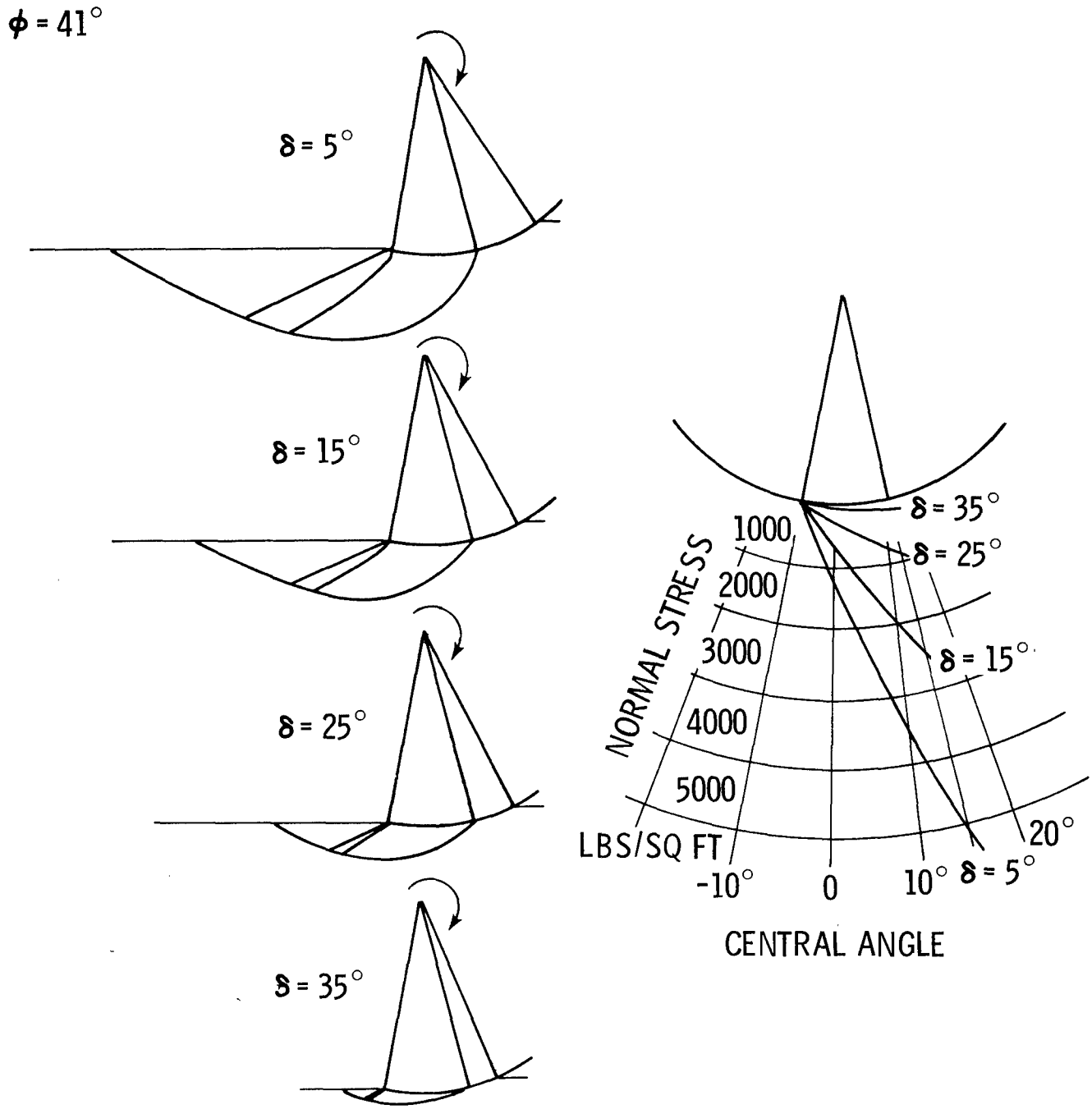

Fig. 4 Effect of the Interface Friction Angle on the Geometry of Rear Slip Line Field and Associated Normal Stresses

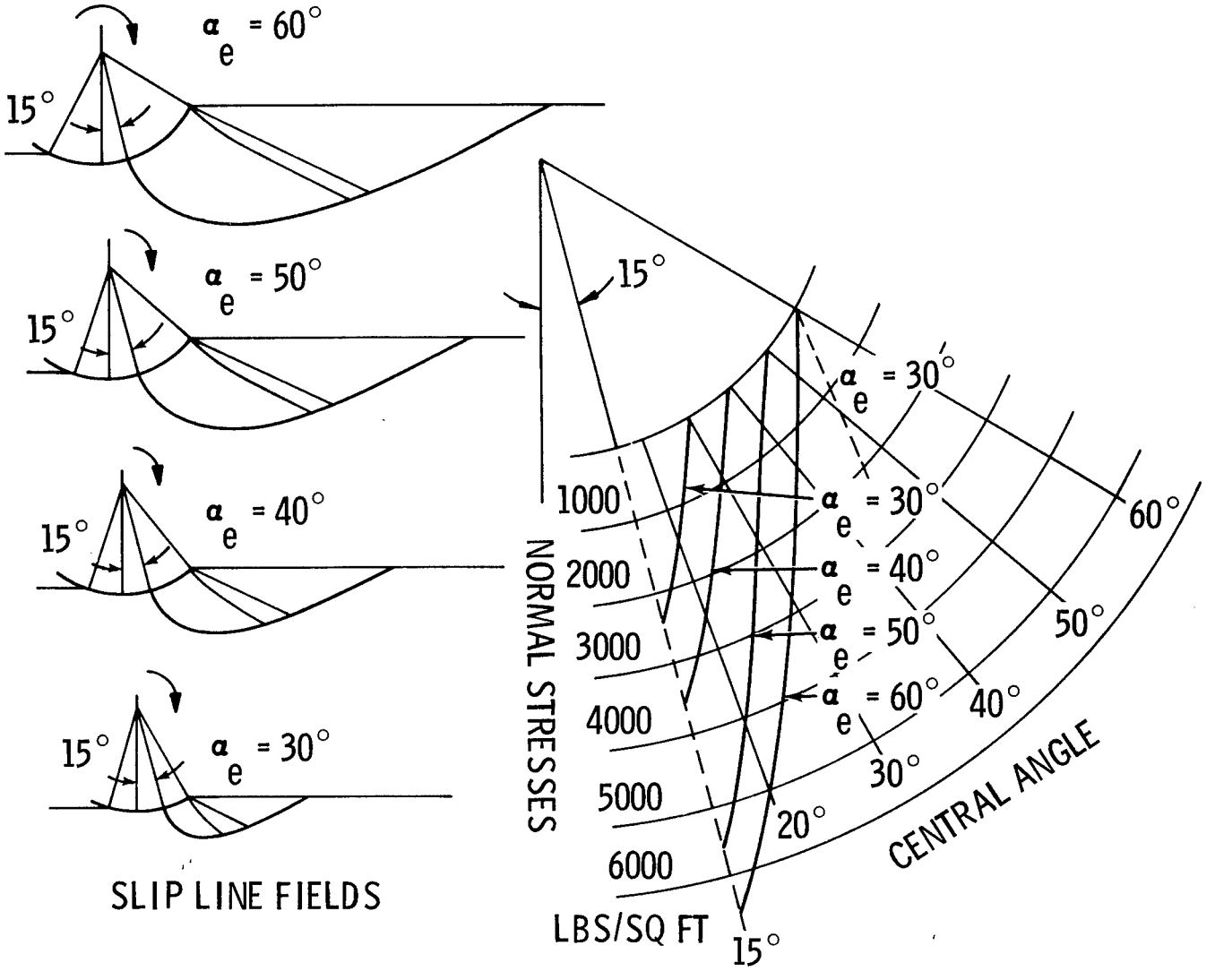

Fig. 5 Slip Line Fields and Associated Normal Stresses for Various Entry Angles

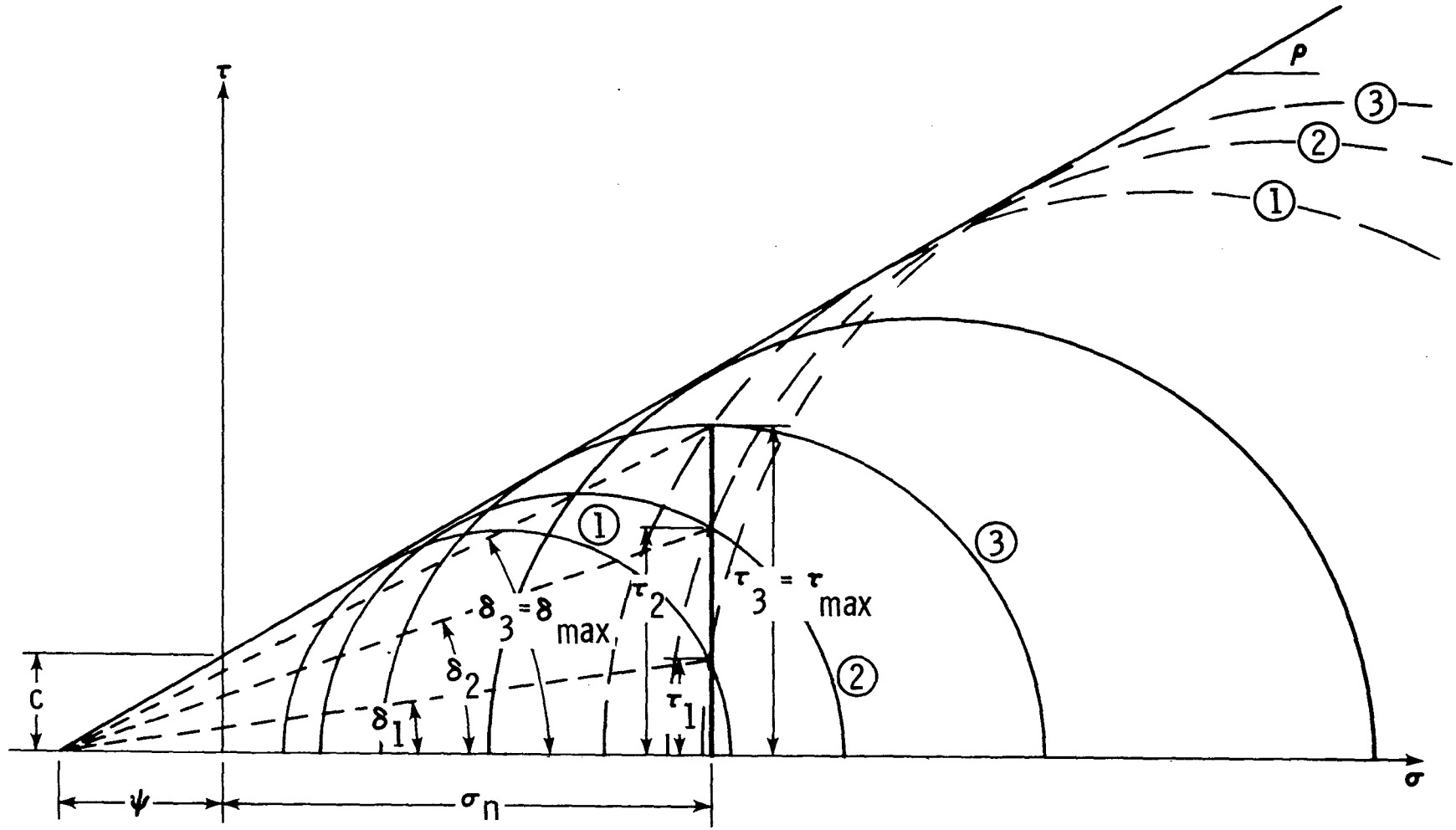

Fig. 6 Mohr Circle for the Active and Passive State of Stresses for Increasing Mobilization of Interface Friction

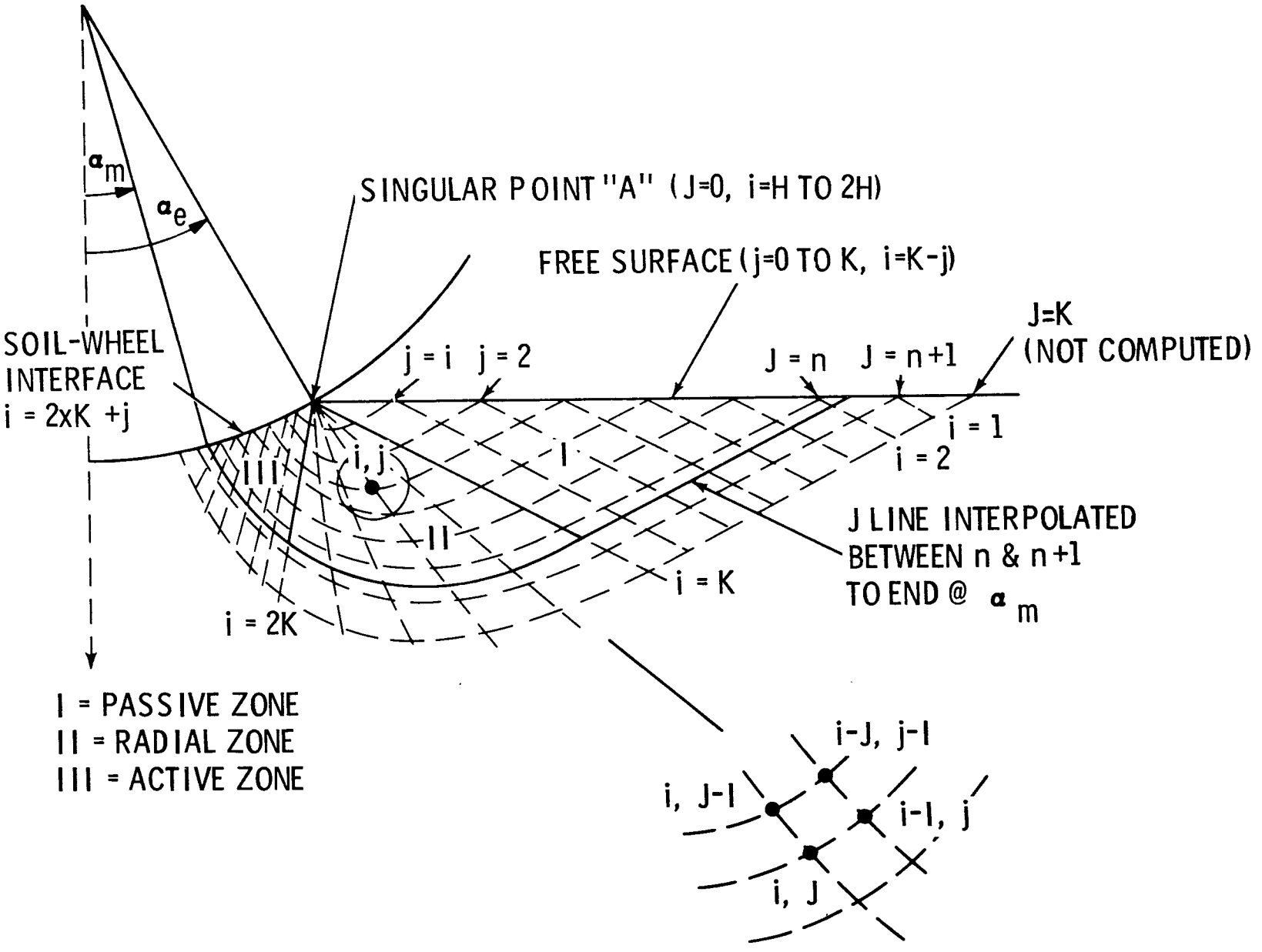

Fig. 7 Computation of Slip Line Field by Finite Differences

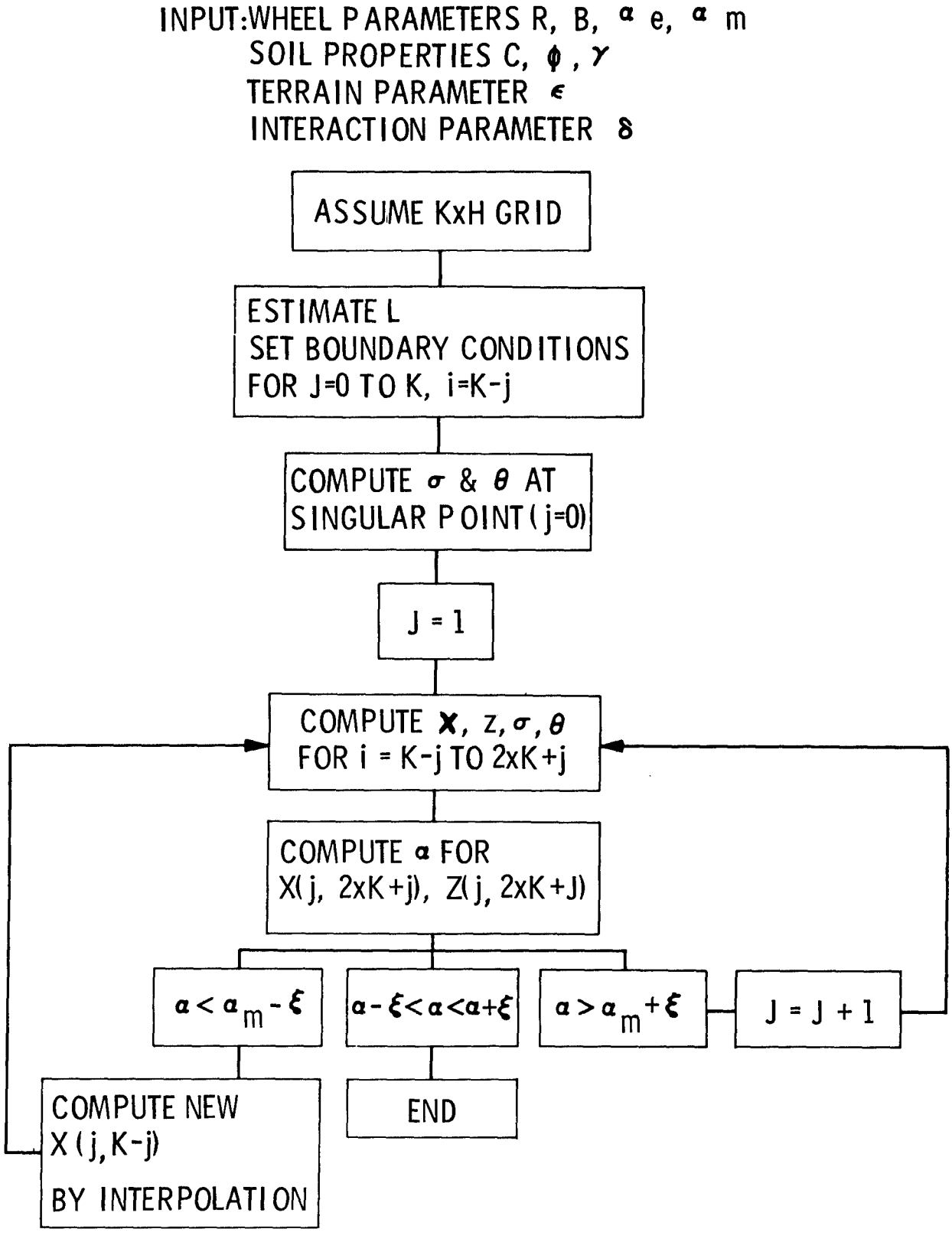

Fig. 8 Flow Diagram for the Computation of a Single Slip Line Field (Subroutine 1, SLIP)

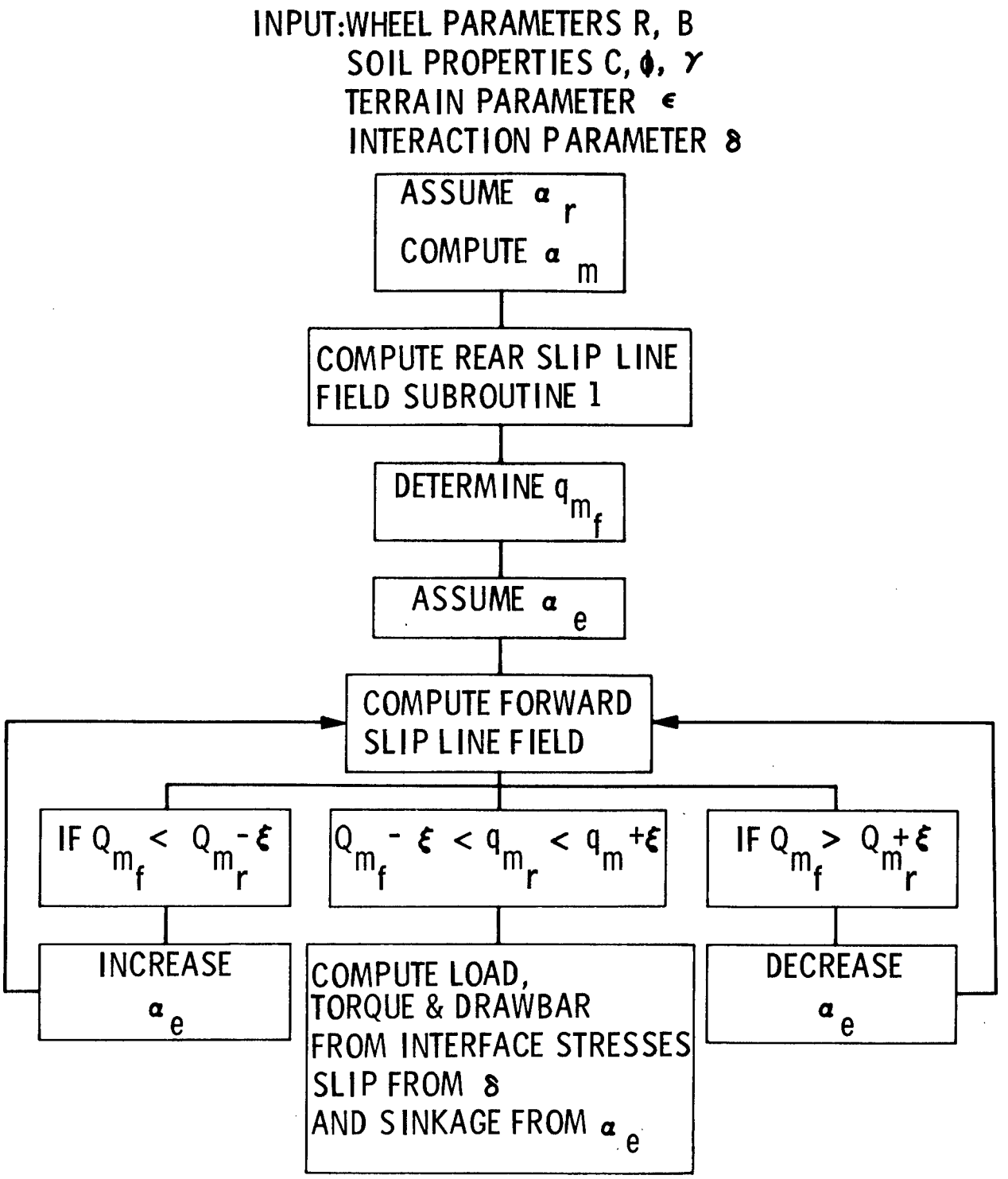

Fig. 9 Flow Diagram for the Computation of a Matching Set of Slip Line Fields and Wheel Performance Parameters

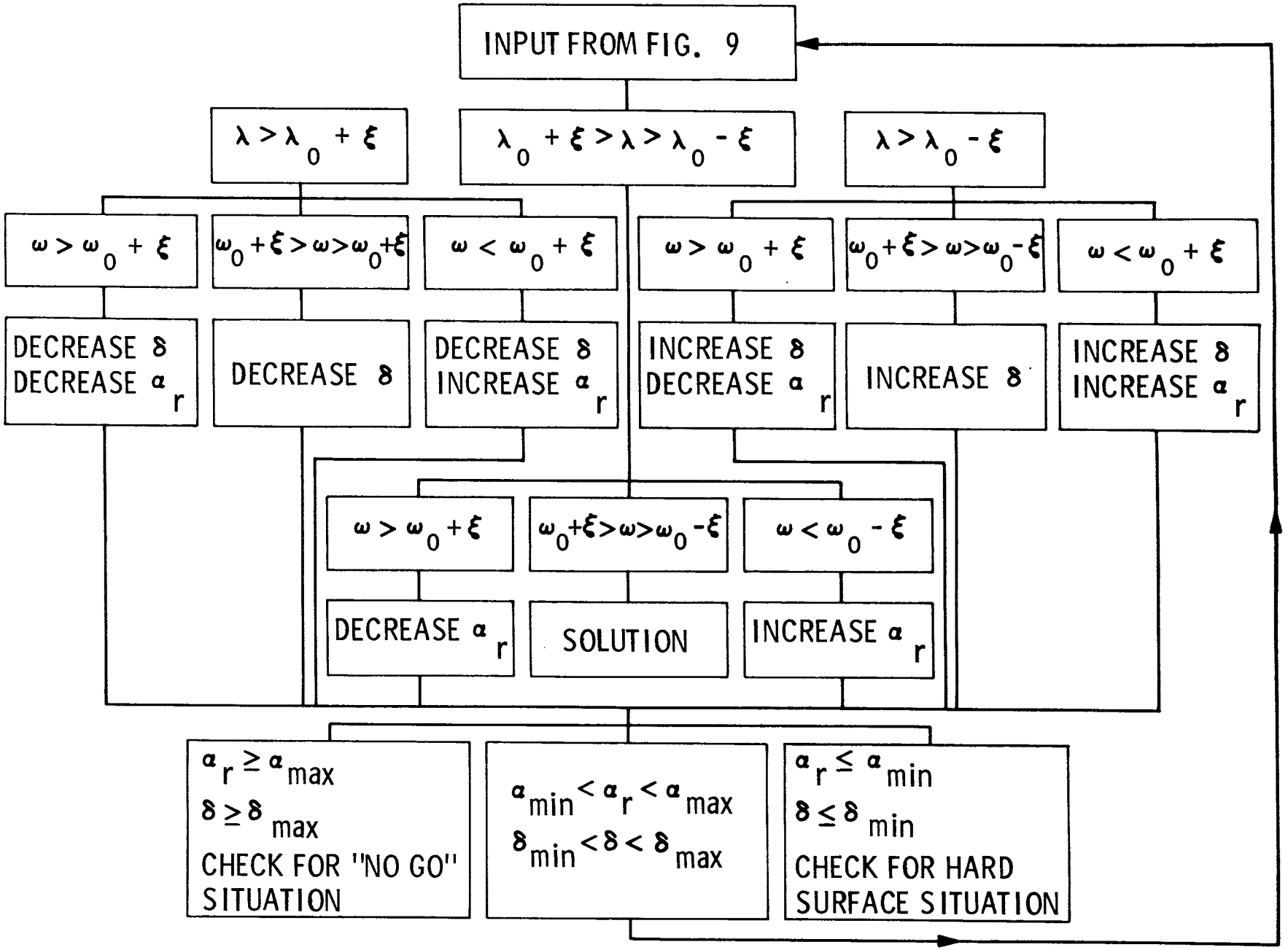

Fig 10 Flow Diagram for the Iterative Procedure for Finding α_r and δ Values for Given Load, Drawbar Pull, and Soil Properties

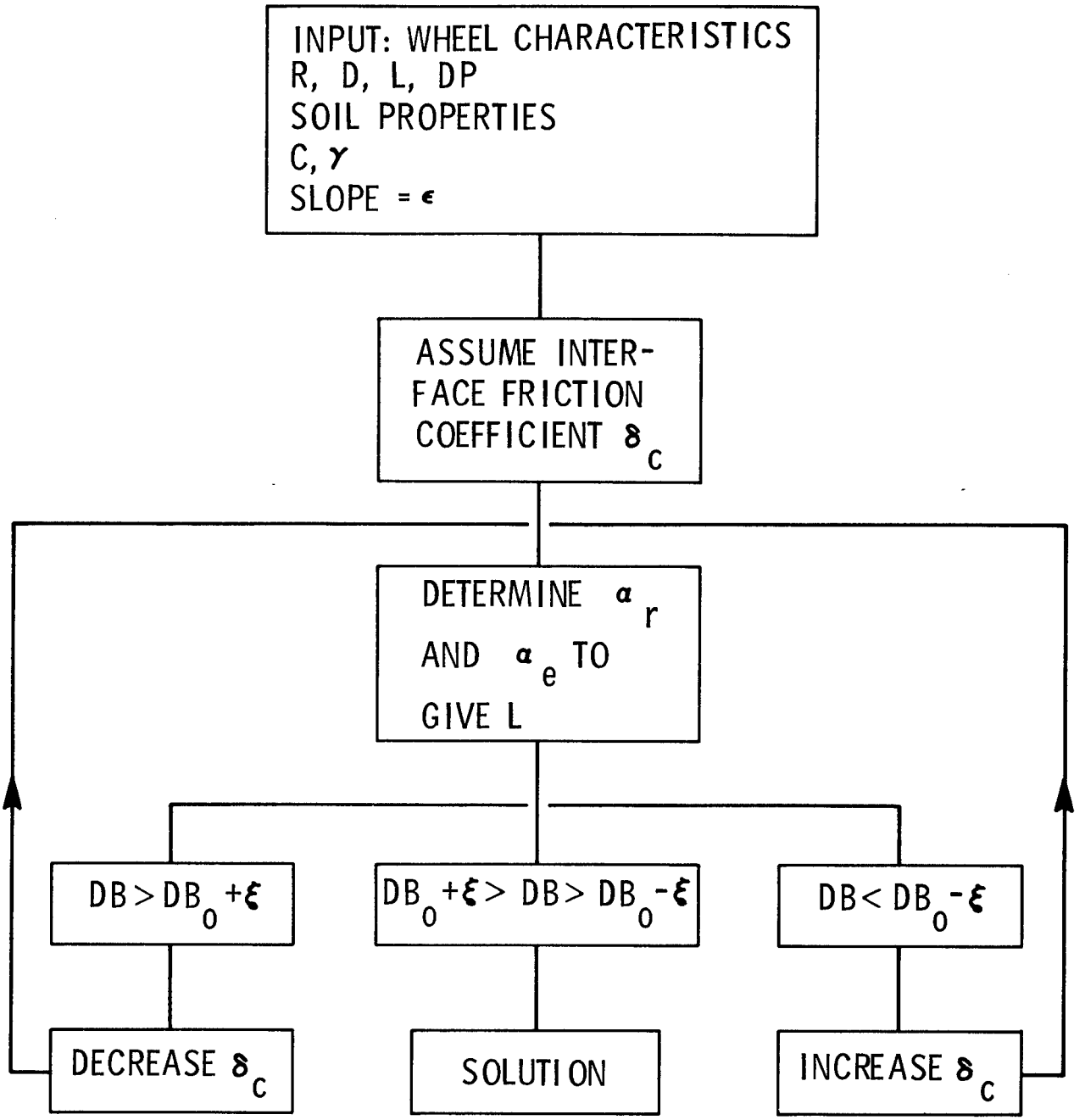

Fig. 11 Flow Diagram for the Computation of Wheel Performance in Cohesive Soils

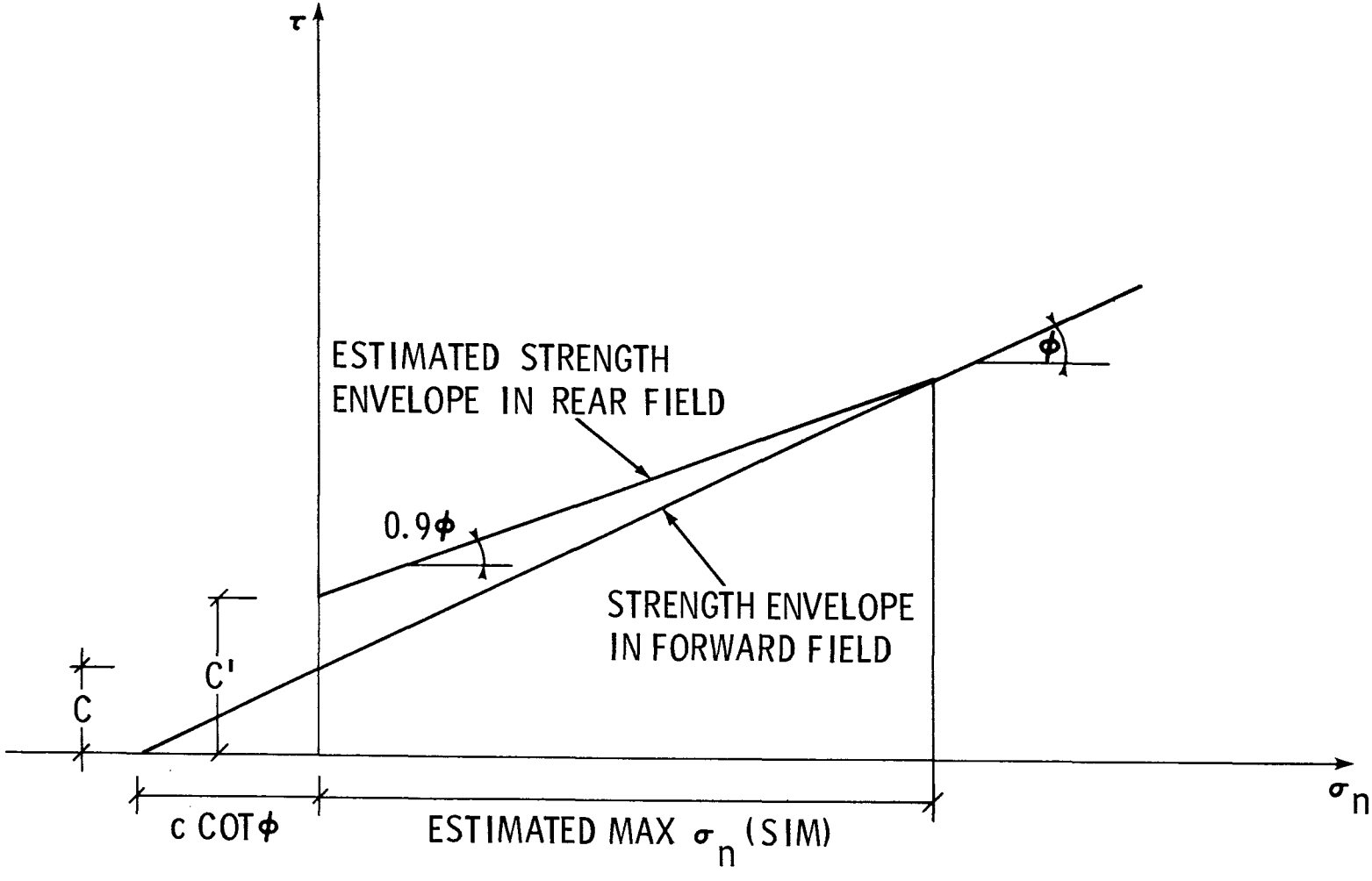

Fig. 12 Estimation of Strength Properties of Soil in the Rear Field

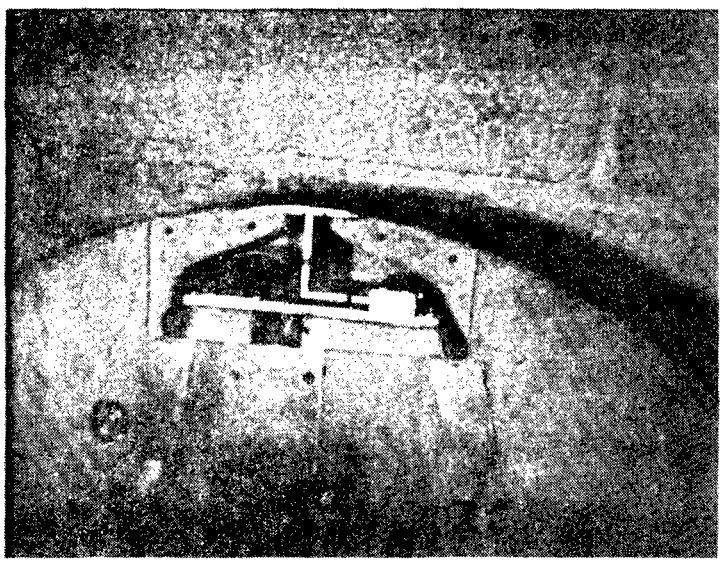

Fig. 13 L Shaped Sensors Mounted on the Circumference of the Wheel

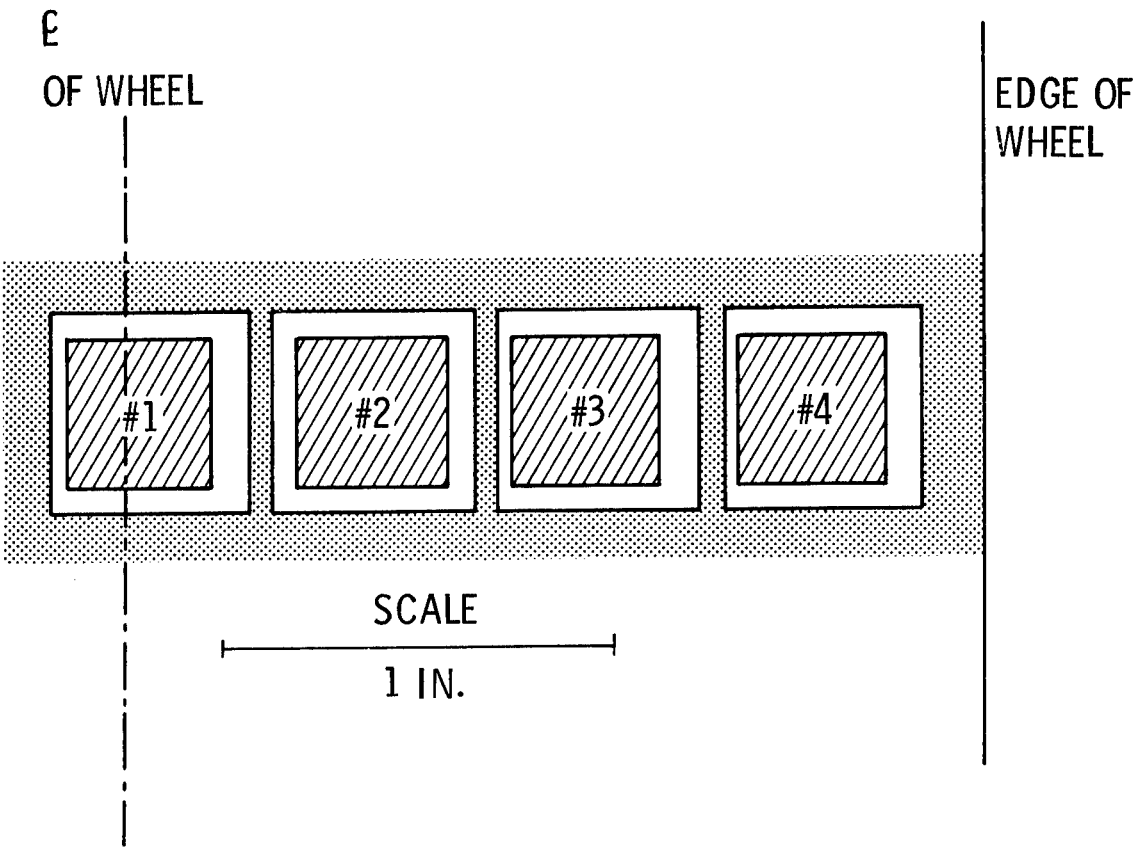

Fig. 14 Sensor Configuration at Wheel Face

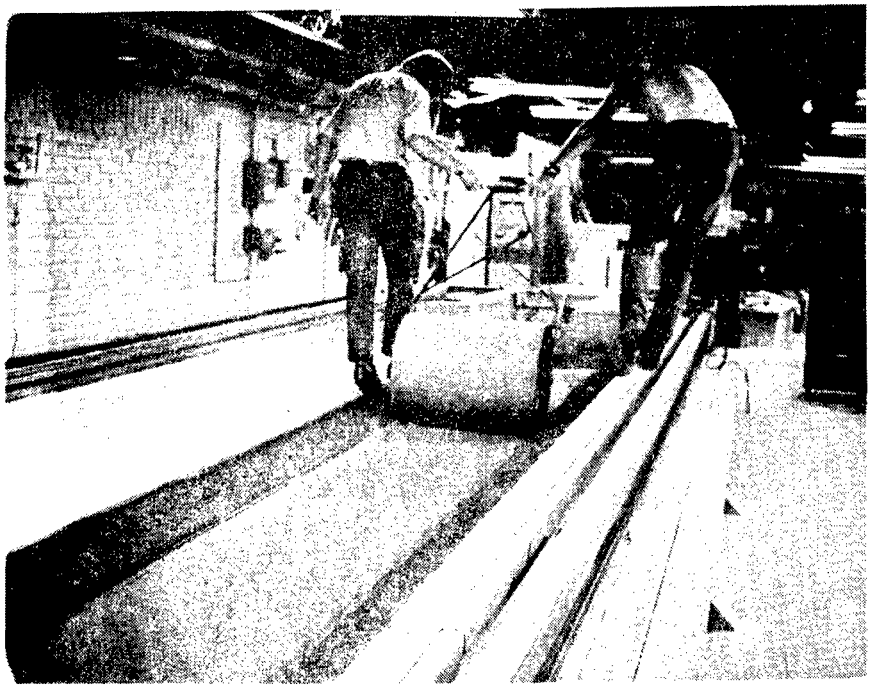

Fig. 15 Rolling of Loam Bed in Soil Bin

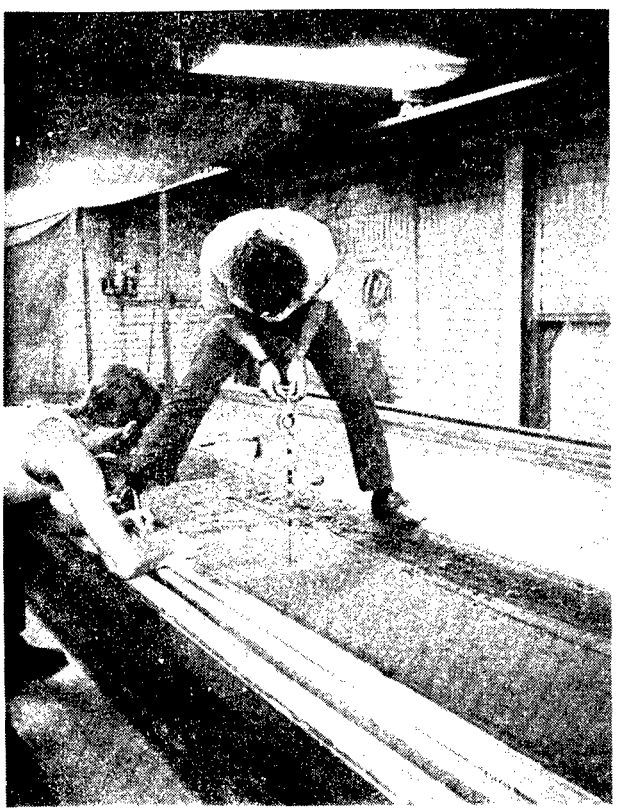

Fig. 16 Performance of Cone Penetrometer Tests in Loam Bed

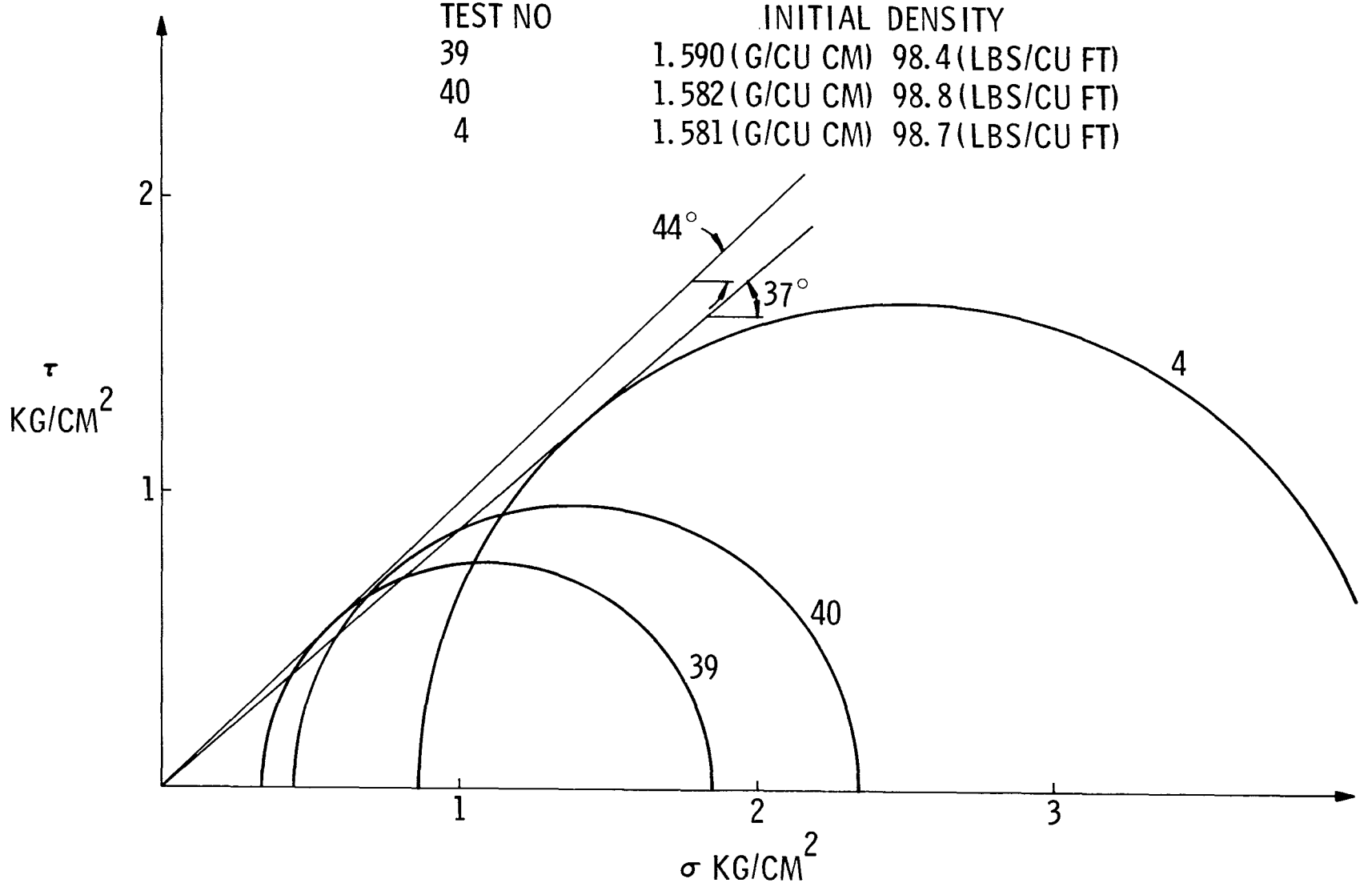

Fig. 17 Results of Triaxial Tests on Loose Sand

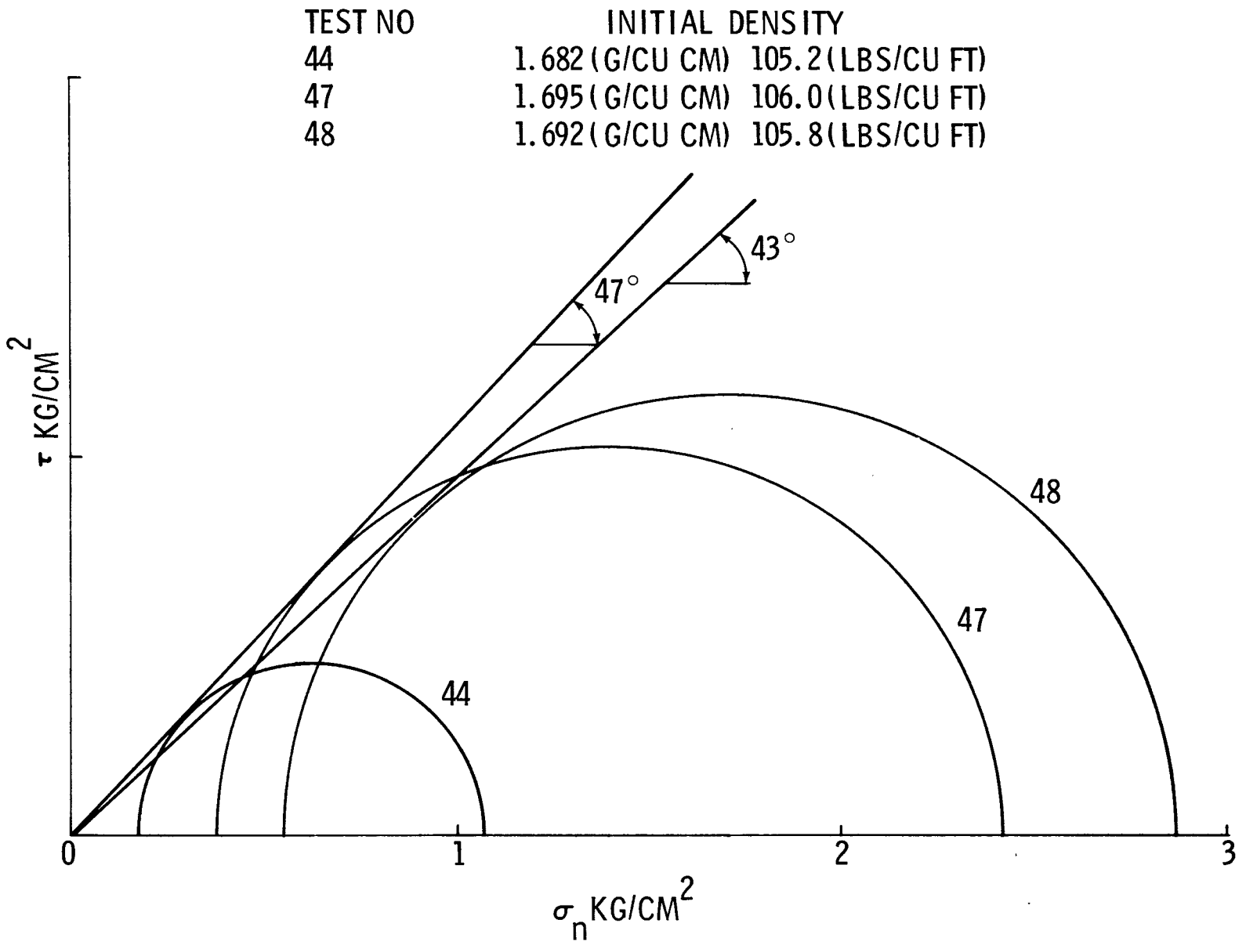

Fig. 18 Results of Triaxial Tests on Dense Sand

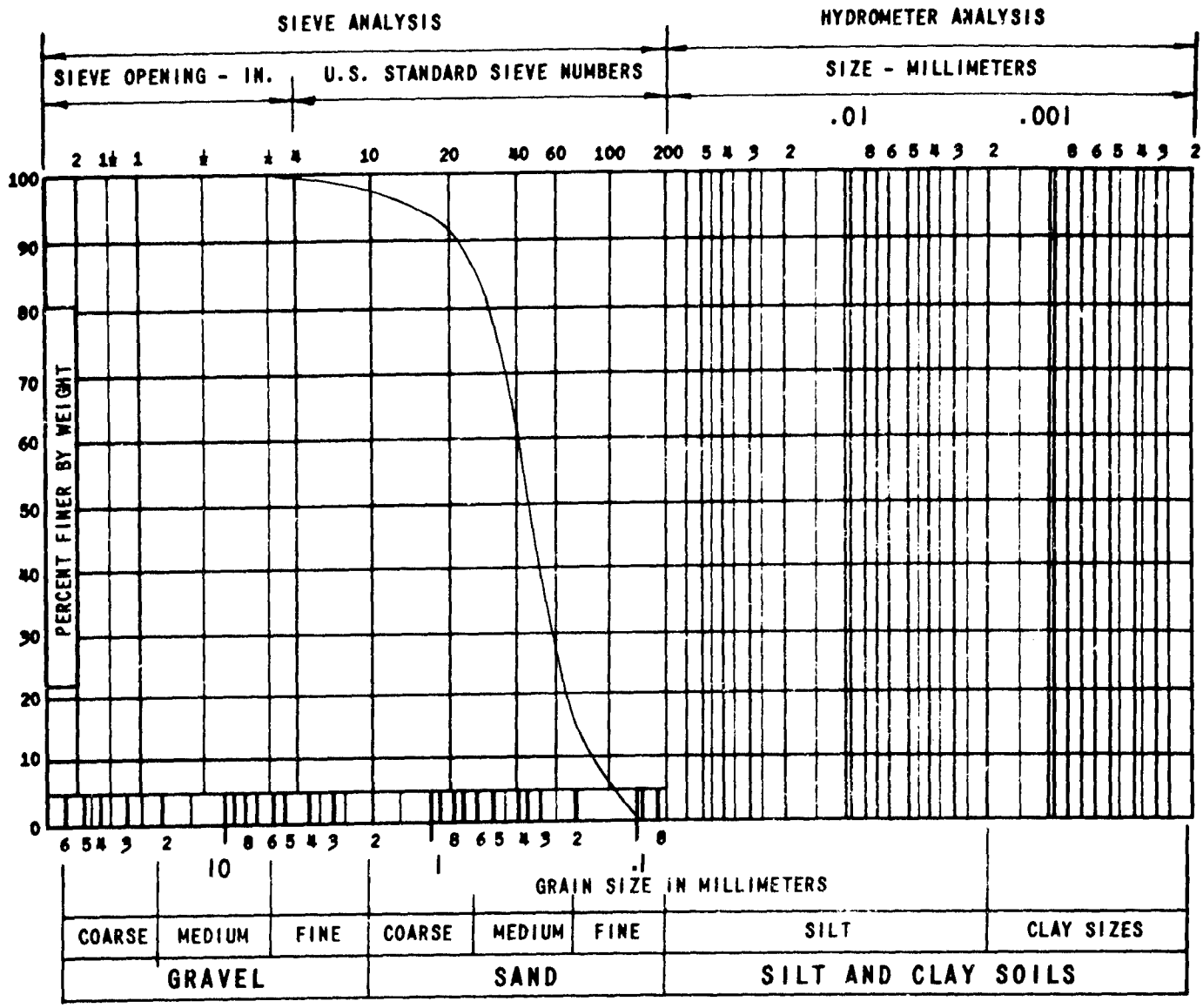

Fig. 19 Grain Size Distribution of Test Sand

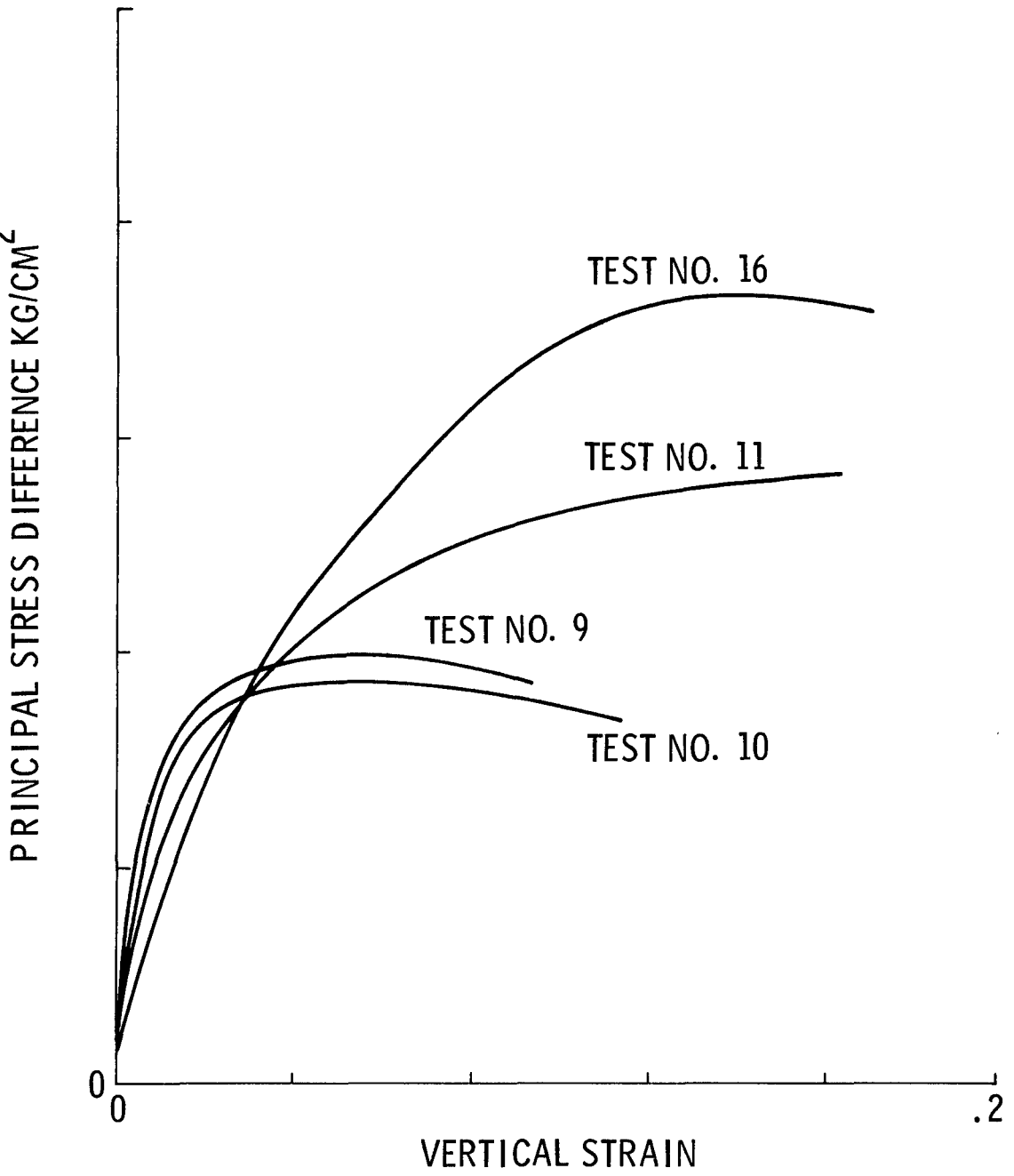

Fig. 20 Principal Stress Difference Versus Strain -- Results of Triaxial Tests in Loam

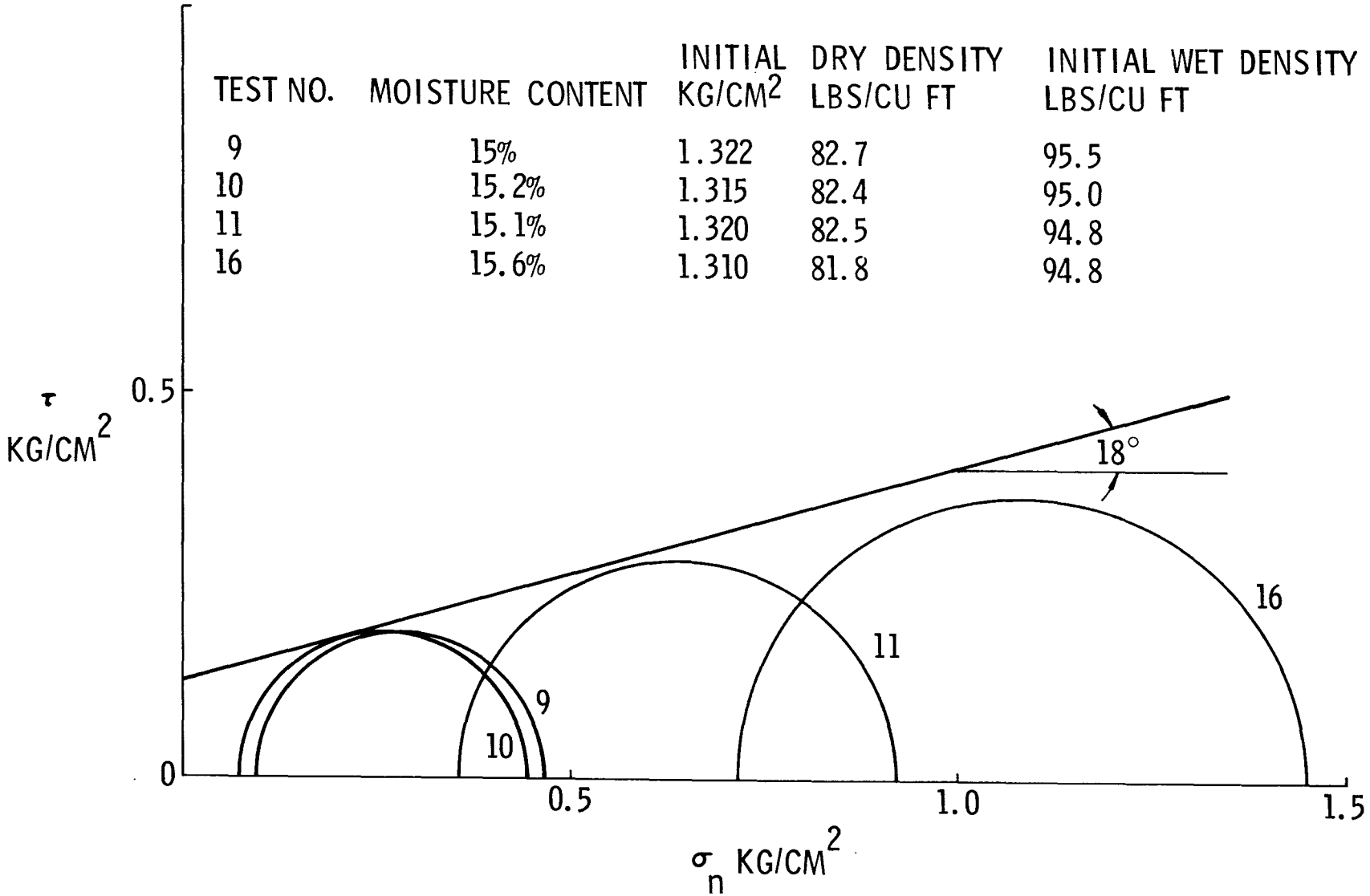

Fig. 21 Results of Triaxial Tests on Loam

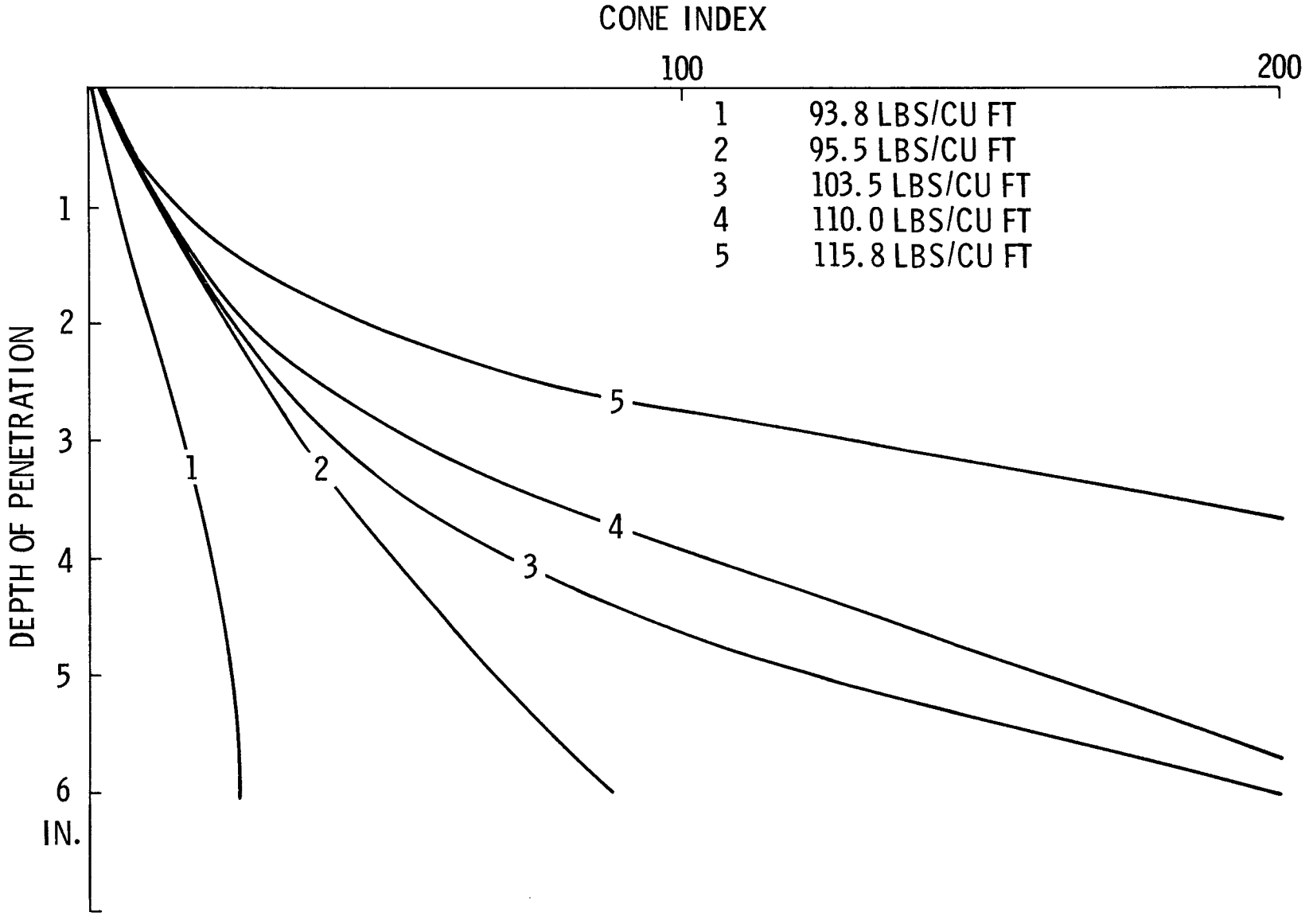

Fig. 22 Results of Cone Penetrometer Tests in Sand at Various Densities

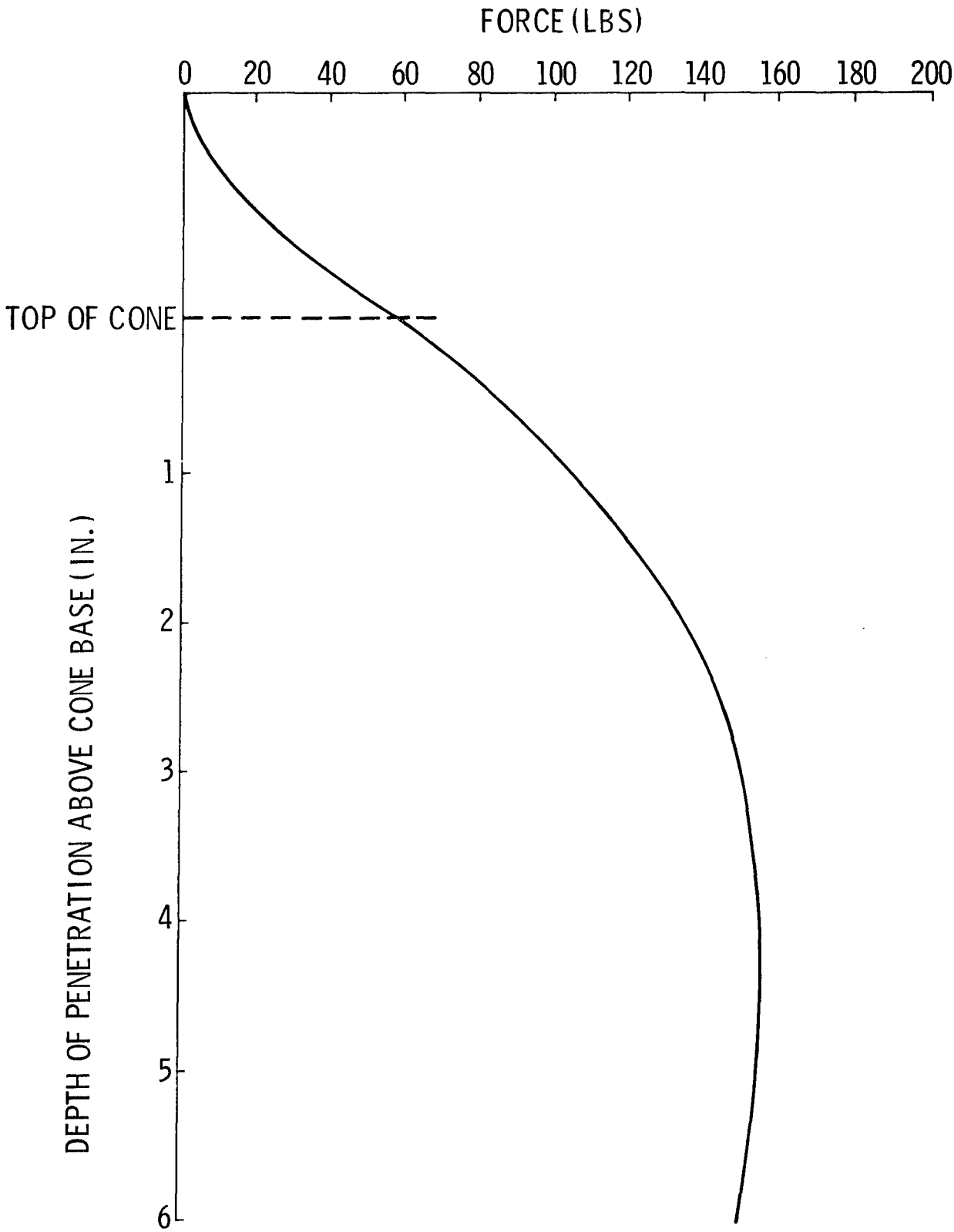

Fig. 23 Typical Variation of Cone Penetration Force with Depth in Loam

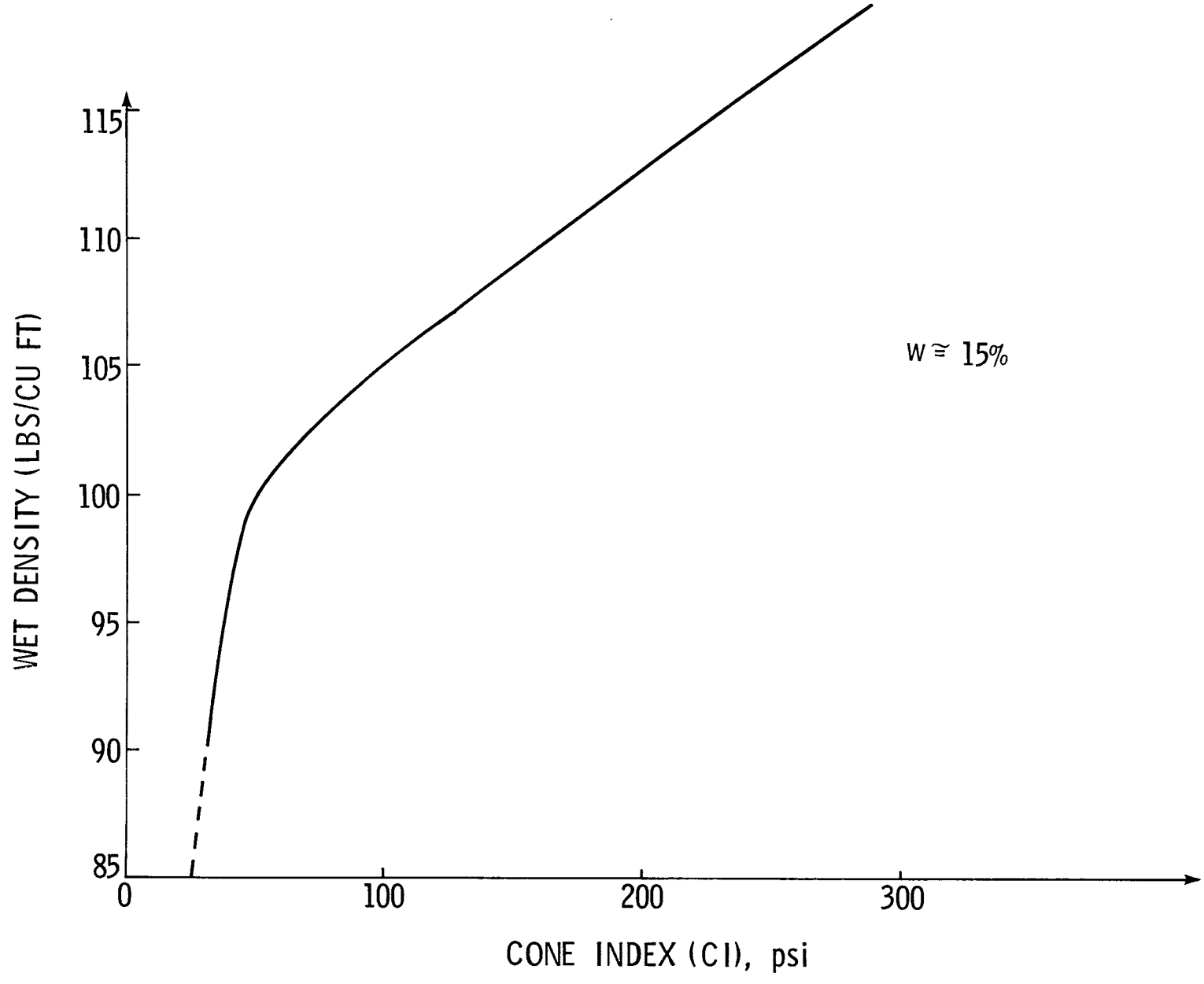

Fig. 24 Cone Index Versus Wet Density in Loam

Fig. 25 Imprint Made in Loam by the Sensors

INSTRUMENTATION SCHEME:

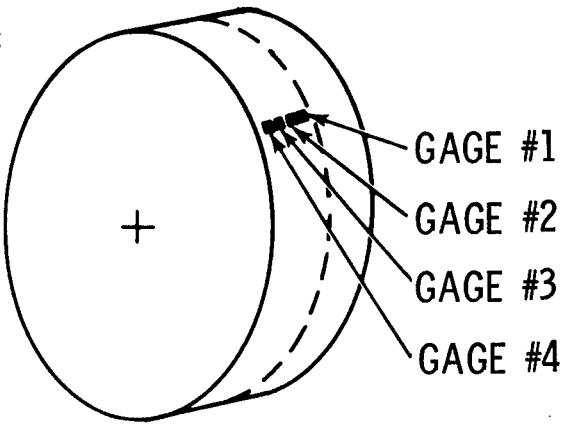

RAW DATA FILE:

RUN #	CENTRAL ANGLE	NORMAL STRESS GAGE #4	SHEAR STRESS GAGE #4	NORMAL STRESS GAGE #3	SHEAR STRESS GAGE #3	NORMAL STRESS GAGE #2	SHEAR STRESS GAGE #2	NORMAL STRESS GAGE #1	SHEAR STRESS GAGE #1	PUNCH CARD #
77	44	170	410	225	330	170	220	160	300	004
77	42	200	422	260	350	210	232	179	334	005
77	40	234	425	319	374	221	253	209	349	006
77	38	295	448	369	389	253	275	249	379	007
77	36	339	459	433	412	276	294	272	414	008
77	34	382	482	522	448	335	313	312	442	009
77	32	471	489	590	475	389	339	348	474	010
77	30	494	514	630	485	415	369	363	509	011
77	28	569	520	686	493	429	364	384	502	012
77	26	515	534	668	493	449	389	415	556	013
77	24	564	541	704	504	459	389	439	551	014
77	22	672	539	791	494	489	371	454	544	015
77	20	663	531	779	485	486	362	455	534	016P
77	18	673	524	786	489	499	359	460	540	017
77	16	636	529	719	483	479	364	409	509	018
77	14	584	529	714	490	456	375	464	492	019
77	12	599	519	711	481	441	375	459	469	020
77	10	573	513	669	469	415	371	432	479	021
77	8	457	500	551	459	383	369	369	490	022
77	6	382	499	485	459	331	389	340	479	023
77	4	323	435	419	454	285	391	305	459	024
77	2	279	461	356	401	255	345	259	399	025

Fig. 26 Typical Digitized Raw Data File

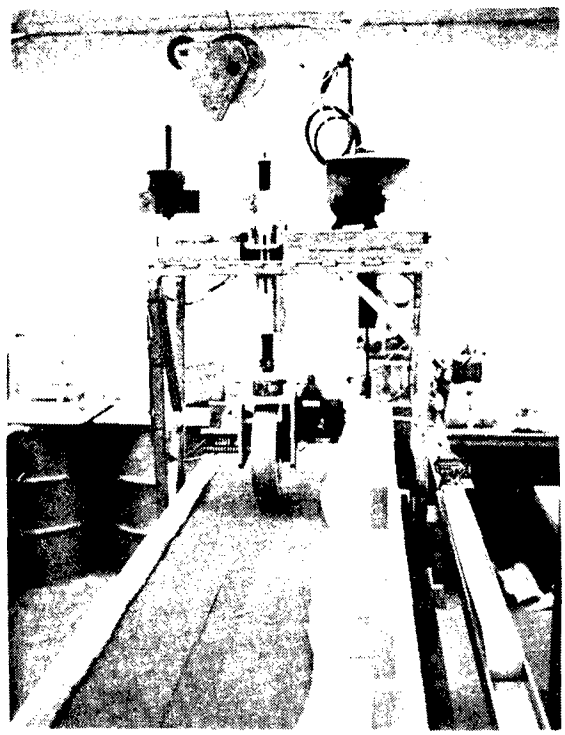

Fig. 7 Laboratory Mobility Bin at Grumman

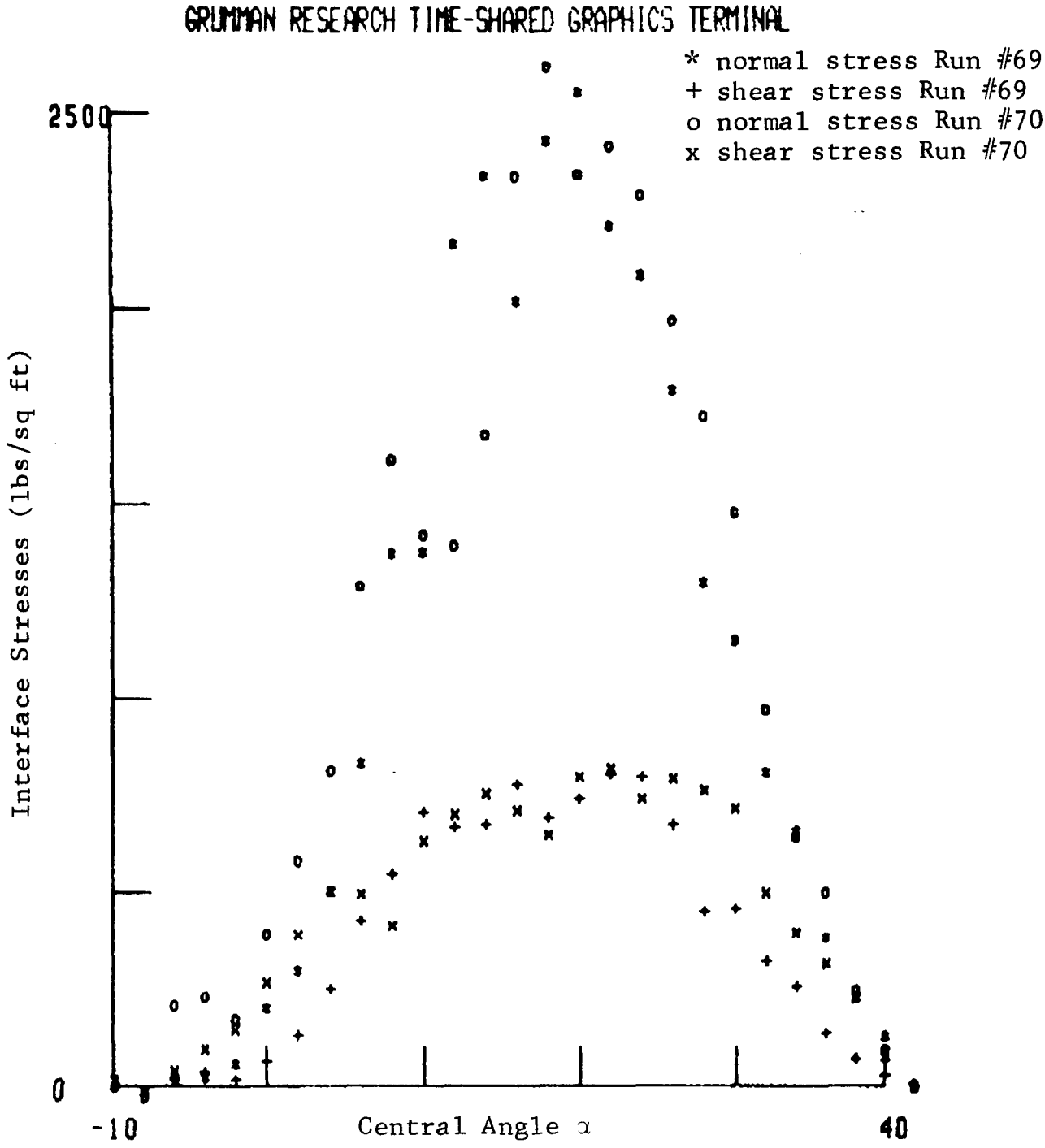

Fig. 28 Run #69 - 70 Average Interface Normal and Shear Stresses Measured in Loose Sand

Run #69 Load = 402 Lbs, Drawbar Pull = 6 lbs, Torque = 157 ft lbs

Run #70 Load = 446 lbs, Drawbar Pull = 26 lbs, Torque = 193 ft lbs

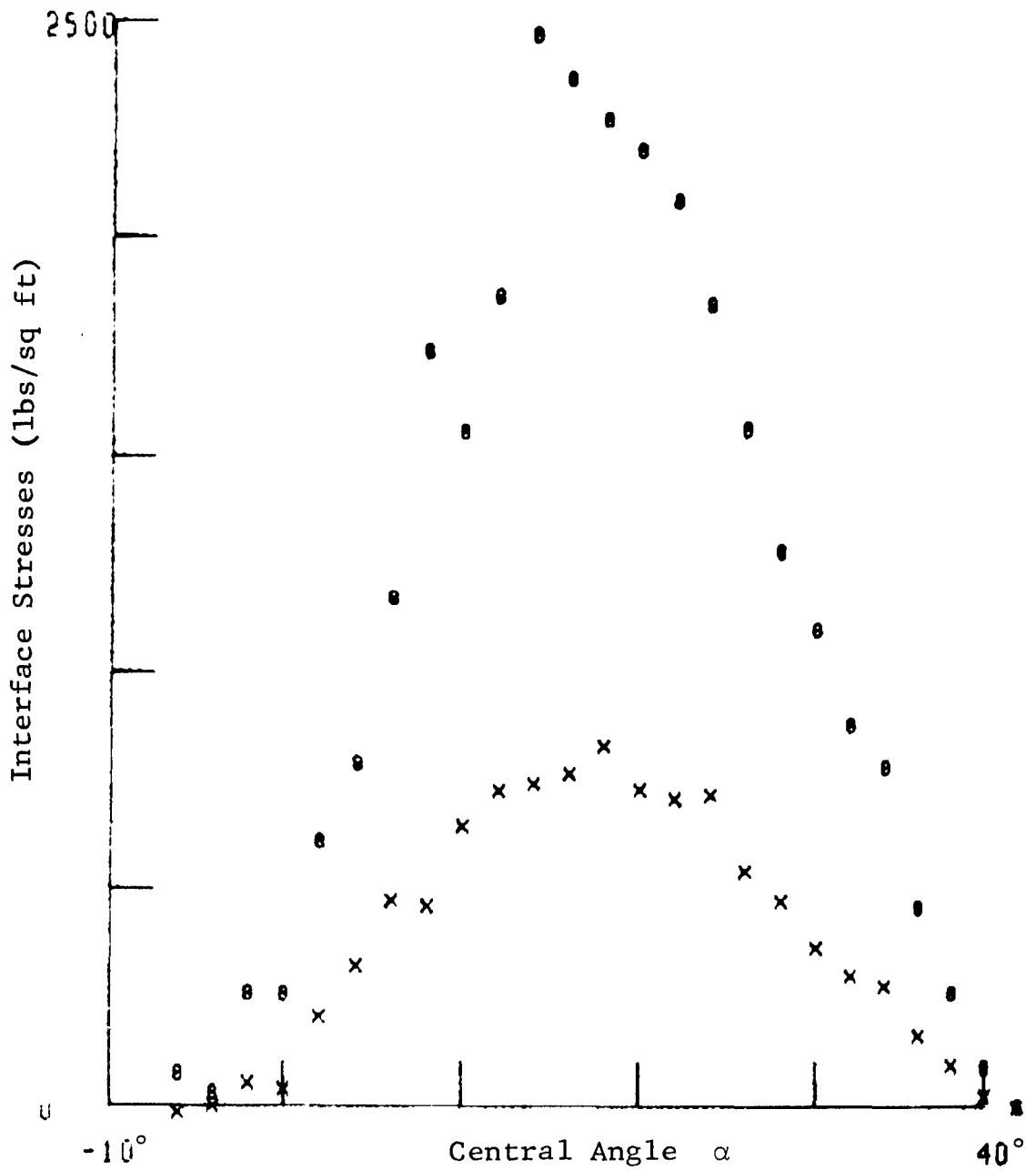

Fig. 29 Run #71 Average Interface Normal and Shear Stresses Measured in Loose Sand
Load = 417 lbs, Drawbar Pull = 6 lbs, Torque = 156 ft lbs

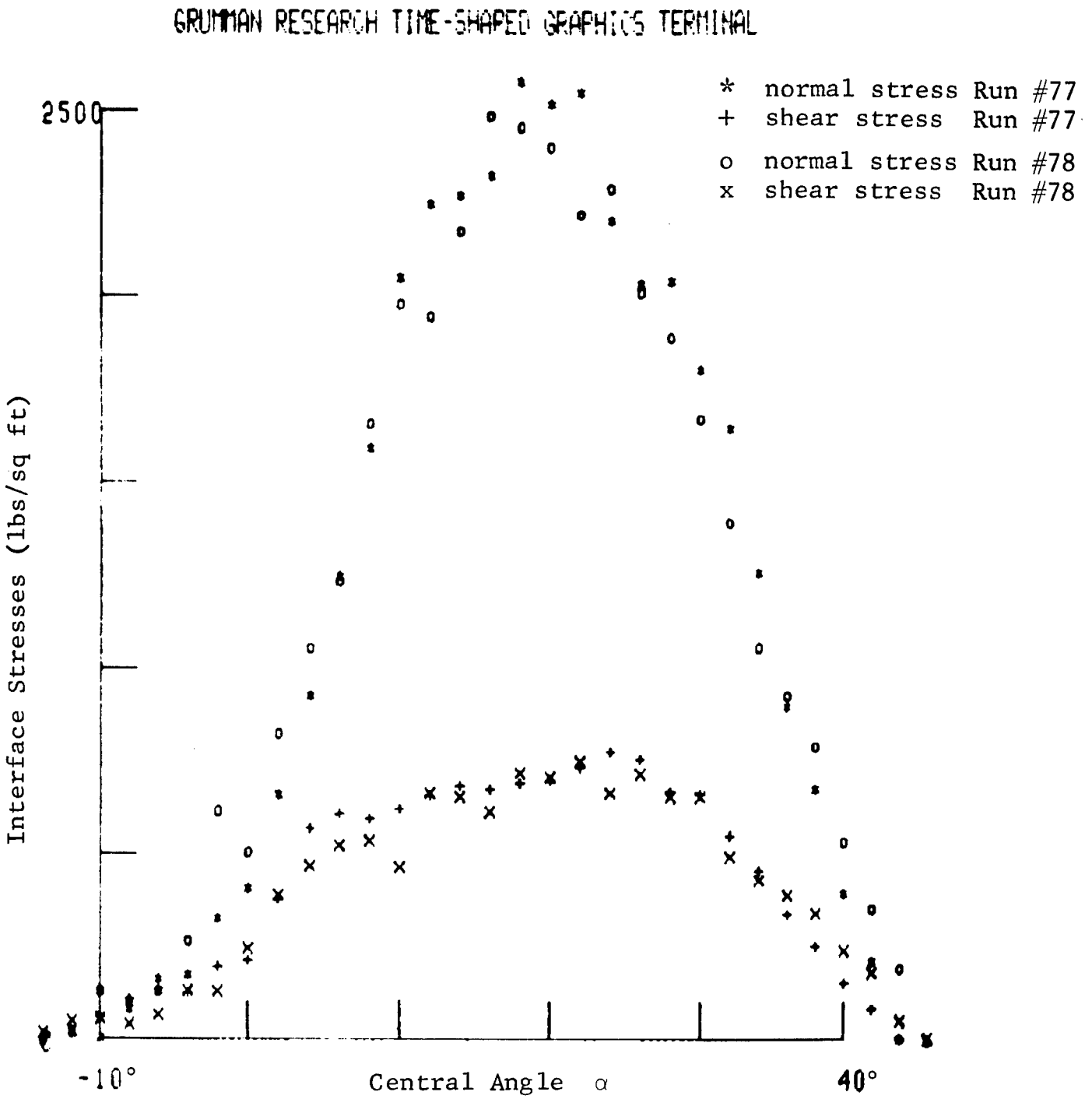

Fig. 30 Run #77-78 Average Interface Normal and Shear Stresses Measured in Loose Sand
Run #77: Load = 519 lbs, Drawbar Pull = 1 lb, Torque = 199 ft lbs
Run #78: Load = 522 lbs, Drawbar Pull = -5 lbs, Torque = 193 ft lbs

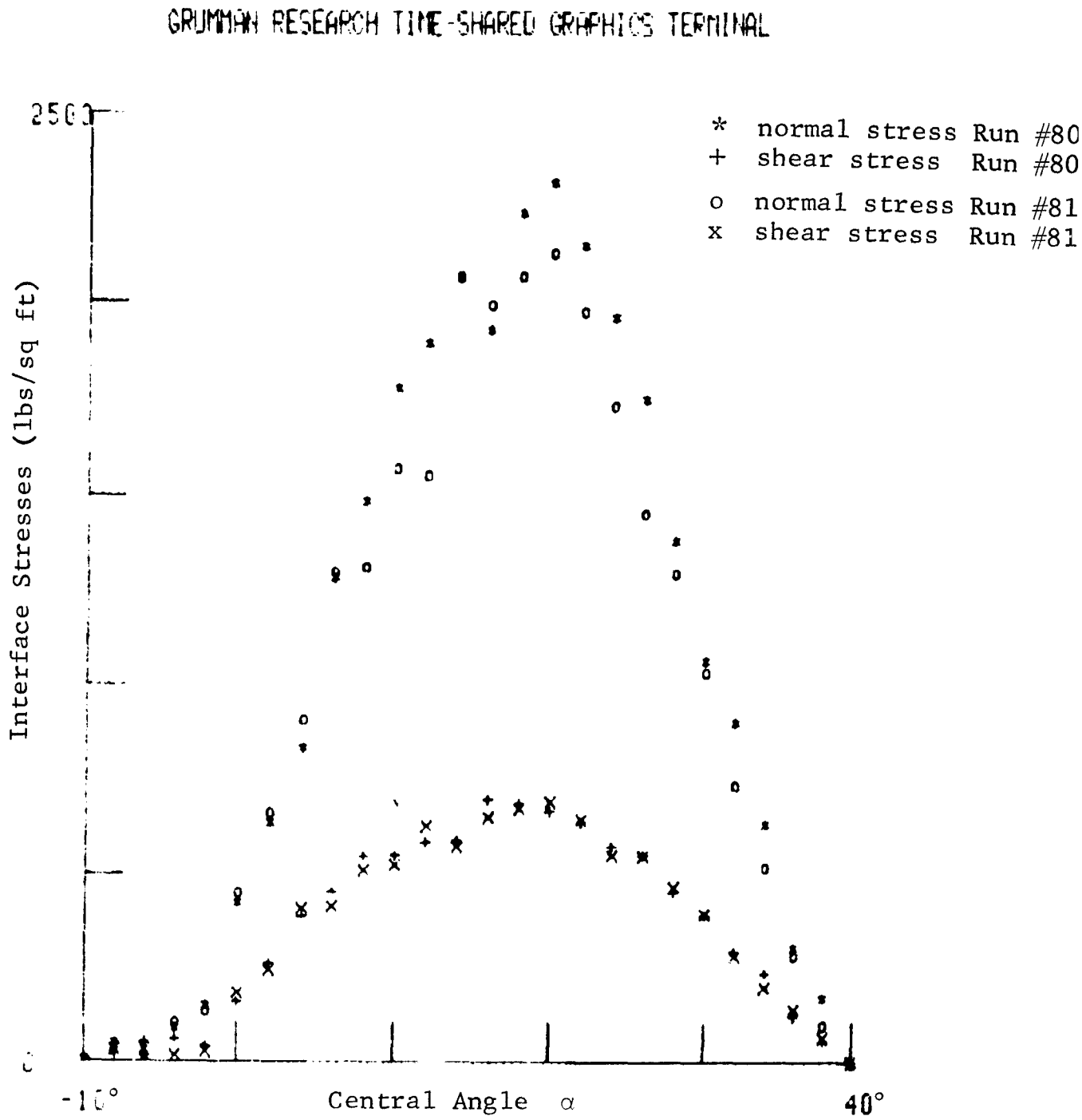

Fig. 31 Run #80-81 Average Interface Normal and Shear Stresses Measured in Loose Sand
Run #80: Load = 406 lbs, Drawbar Pull = 2 lbs, Torque = 146 ft lbs
Run #81: Load = 379 lbs. Drawbar Pull = 10 lbs, Torque = 143 ft lbs

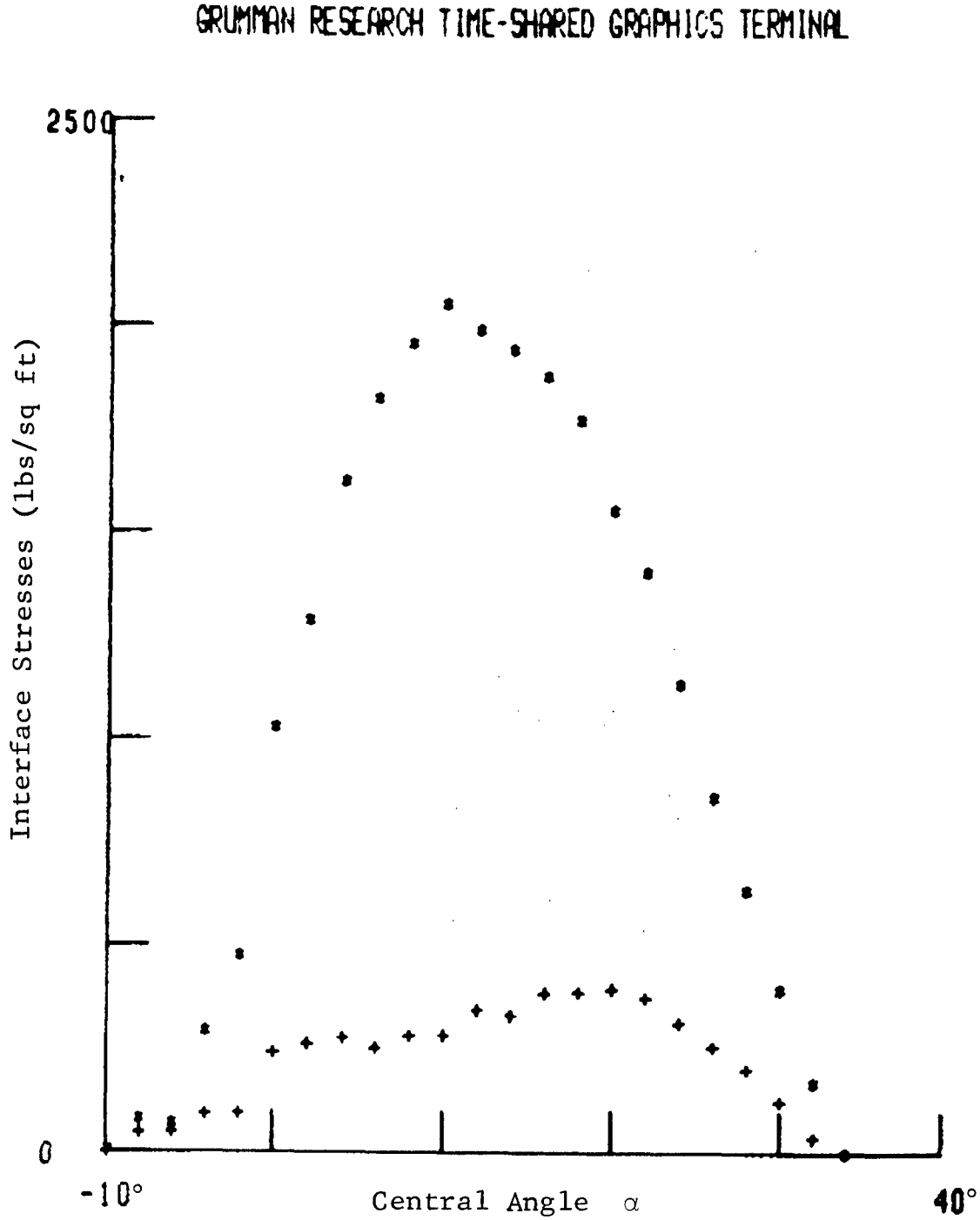

Fig. 32 Run #82 Average Interface Normal and Shear Stresses Measured in Loose Sand
Load = 353 lbs, Drawbar Pull = -8 lbs, Torque = 82 ft lbs

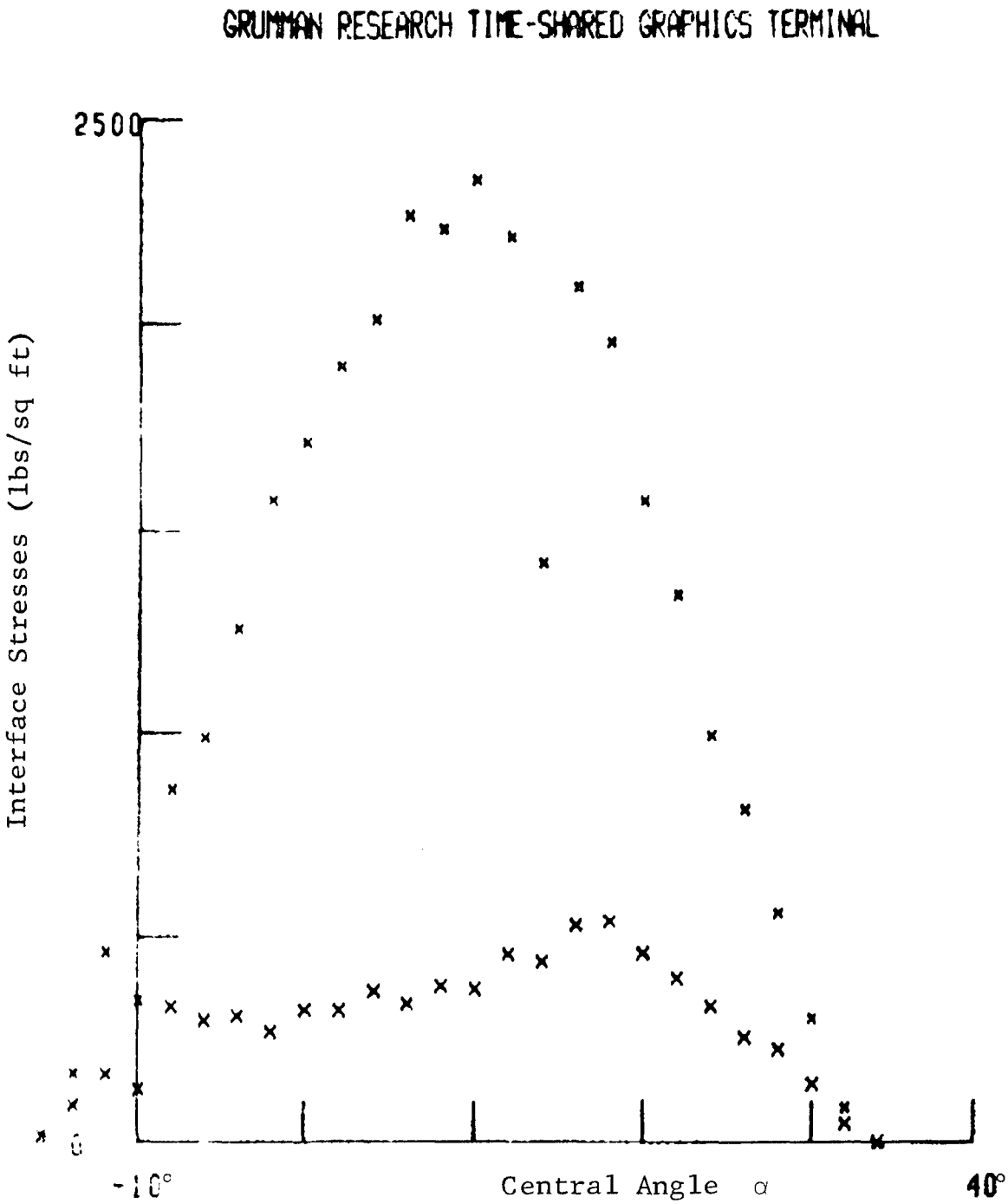

Fig. 33 Run #83 Average Interface Normal and Shear Stresses
Measured in Loose Sand
Load = 457 lbs, Drawbar Pull = 34 lbs, Torque = 122 ft lbs

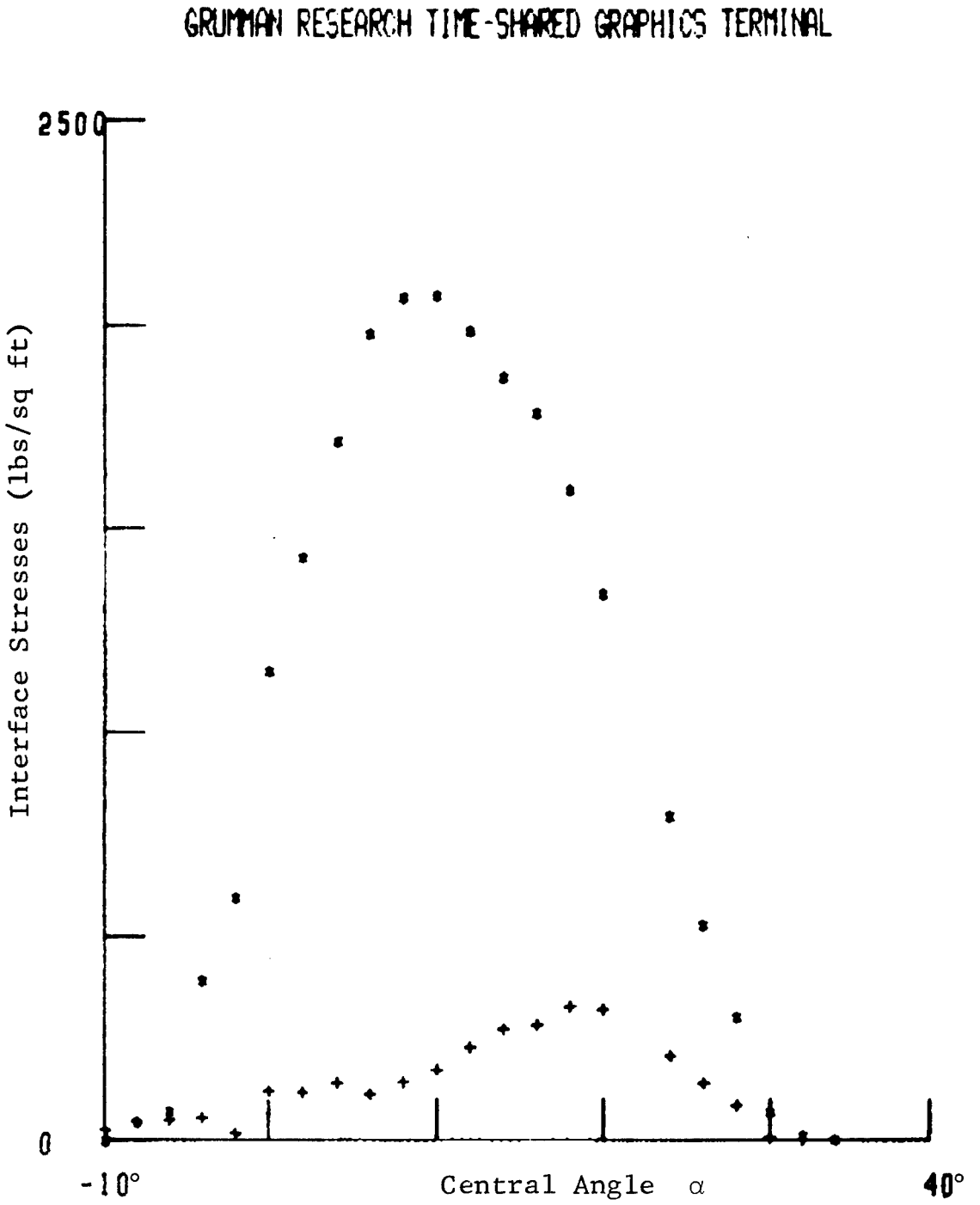

Fig. 34 Run #84 Average Interface Normal and Shear Stresses Measured in Loose Sand
Load = 327 lbs, Drawbar Pull = -20 lbs, Torque = 50 ft lbs

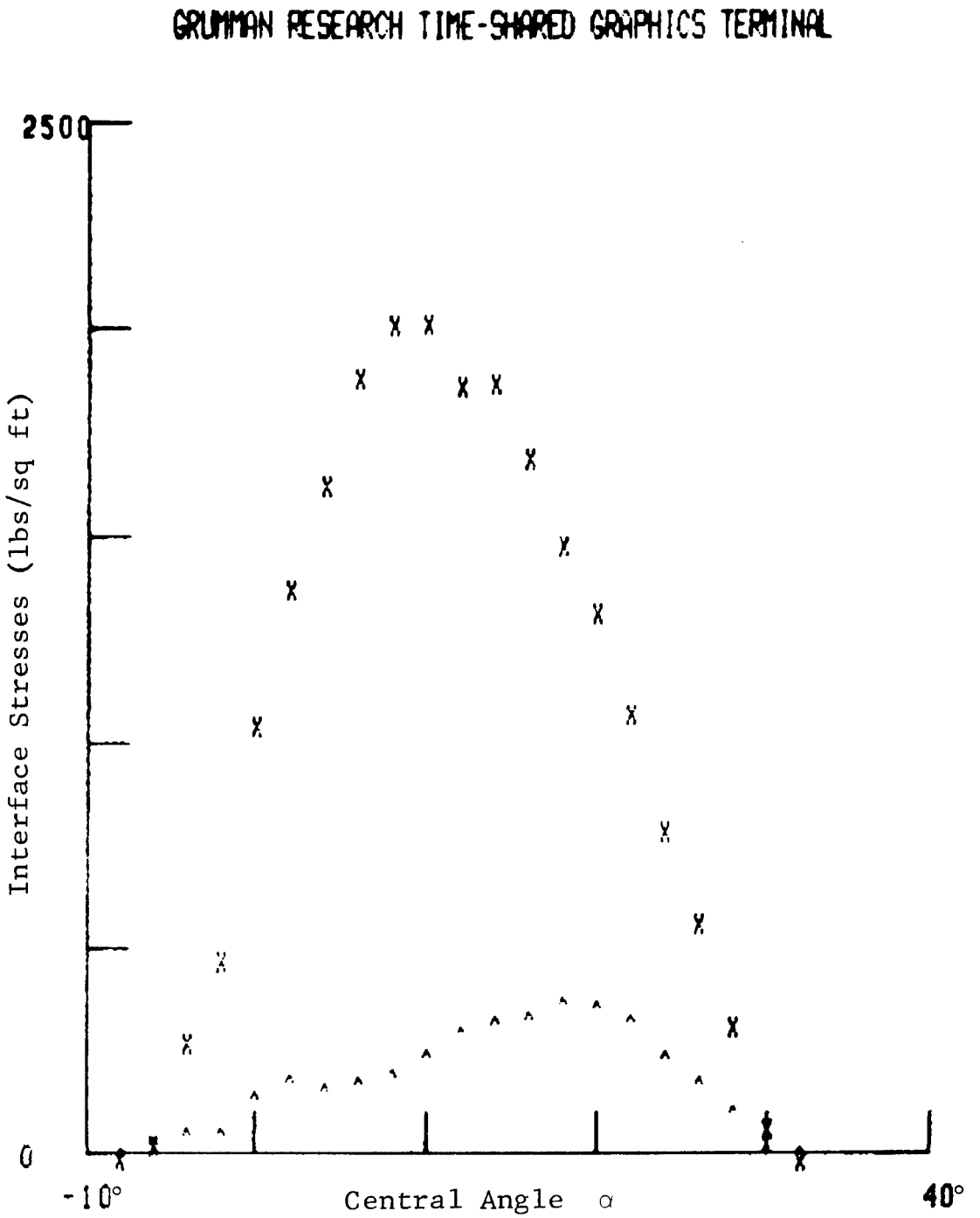

Fig. 35 Run #85 Average Interface Normal and Shear Stresses Measured in Loose Sand
Load = 319 lbs, Drawbar Pull = -13 lbs, Torque = 59 ft lbs

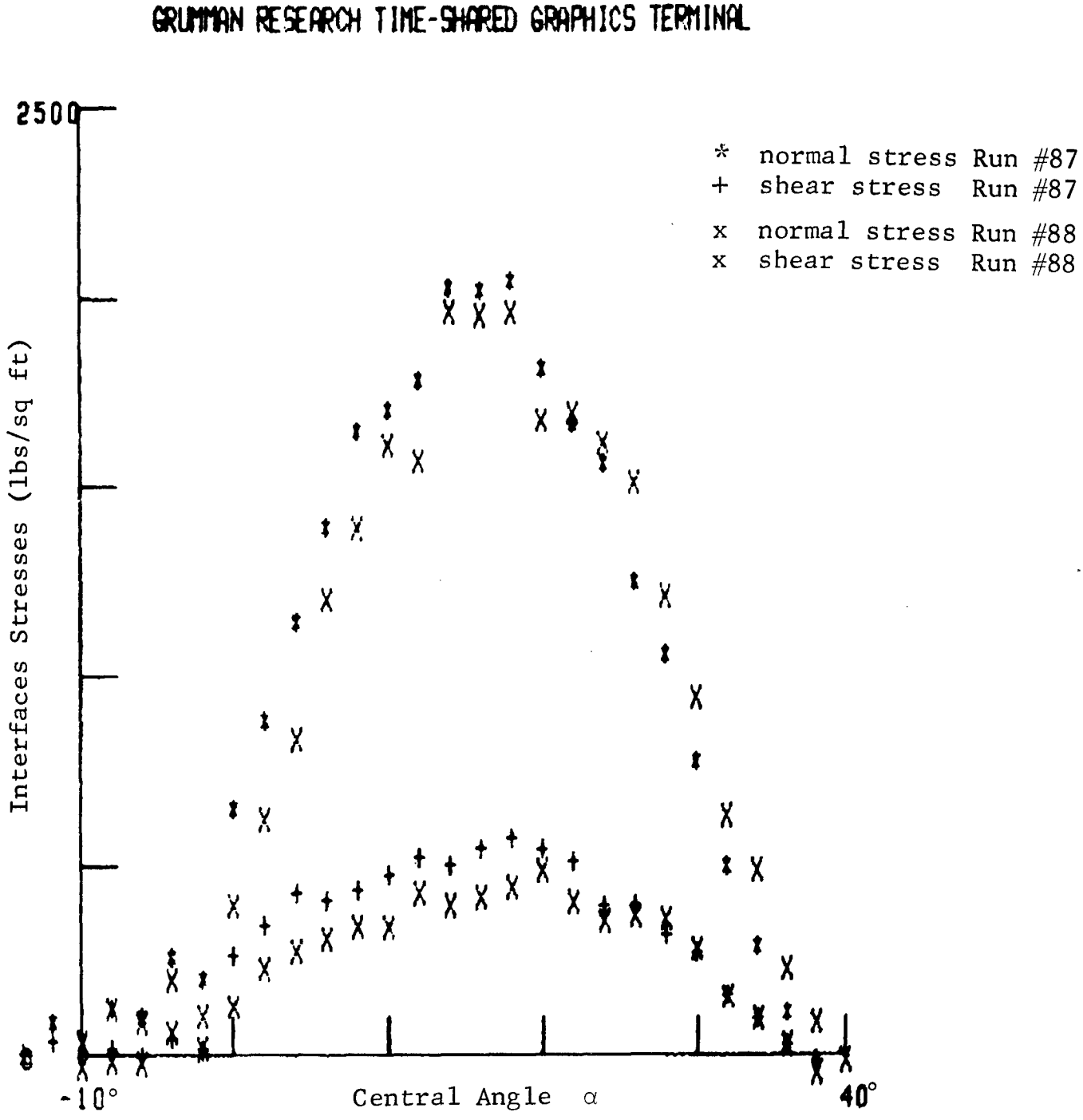

Fig. 36 Run #87-88 Average Interface Normal and Shear Stresses Measured in Loose Sand
Run #87: Load = 375 lbs, Drawbar Pull = 9 lbs, Torque = 125 ft lbs
Run #88: Load = 354 lbs, Drawbar Pull = -17 lbs, Torque = 100 ft lbs

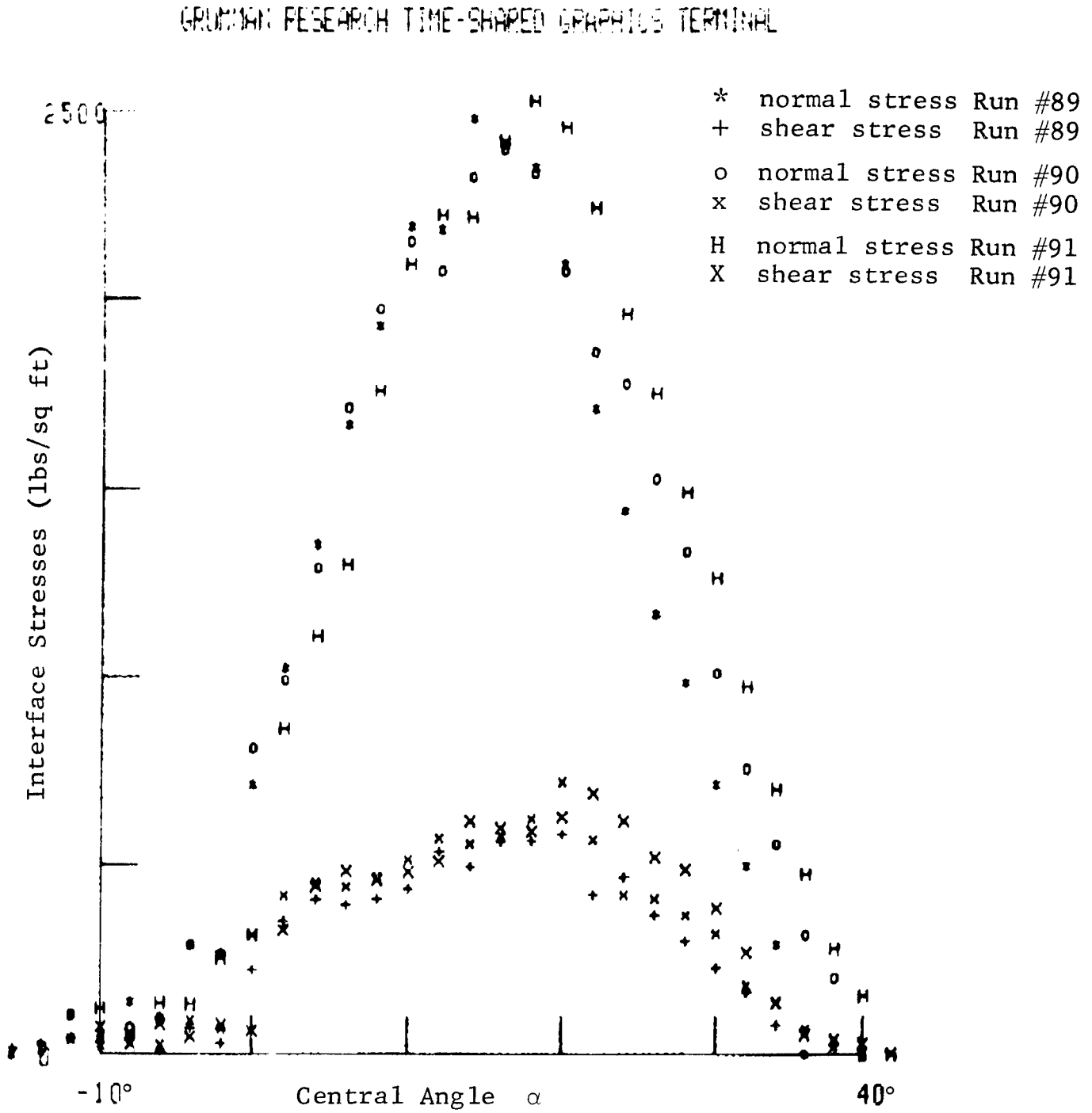

Fig. 37 Run #89-91 Average Interface Normal and Shear Stresses Measured in Loose Sand

Run #89: Load = 409 lbs, Drawbar Pull = -3 lbs, Torque = 116 ft lbs

Run #90: Load = 441 lbs, Drawbar Pull = -2 lbs, Torque = 137 ft lbs

Run #91: Load = 453 lbs, Drawbar Pull = -16 lbs, Torque = 140 ft lbs

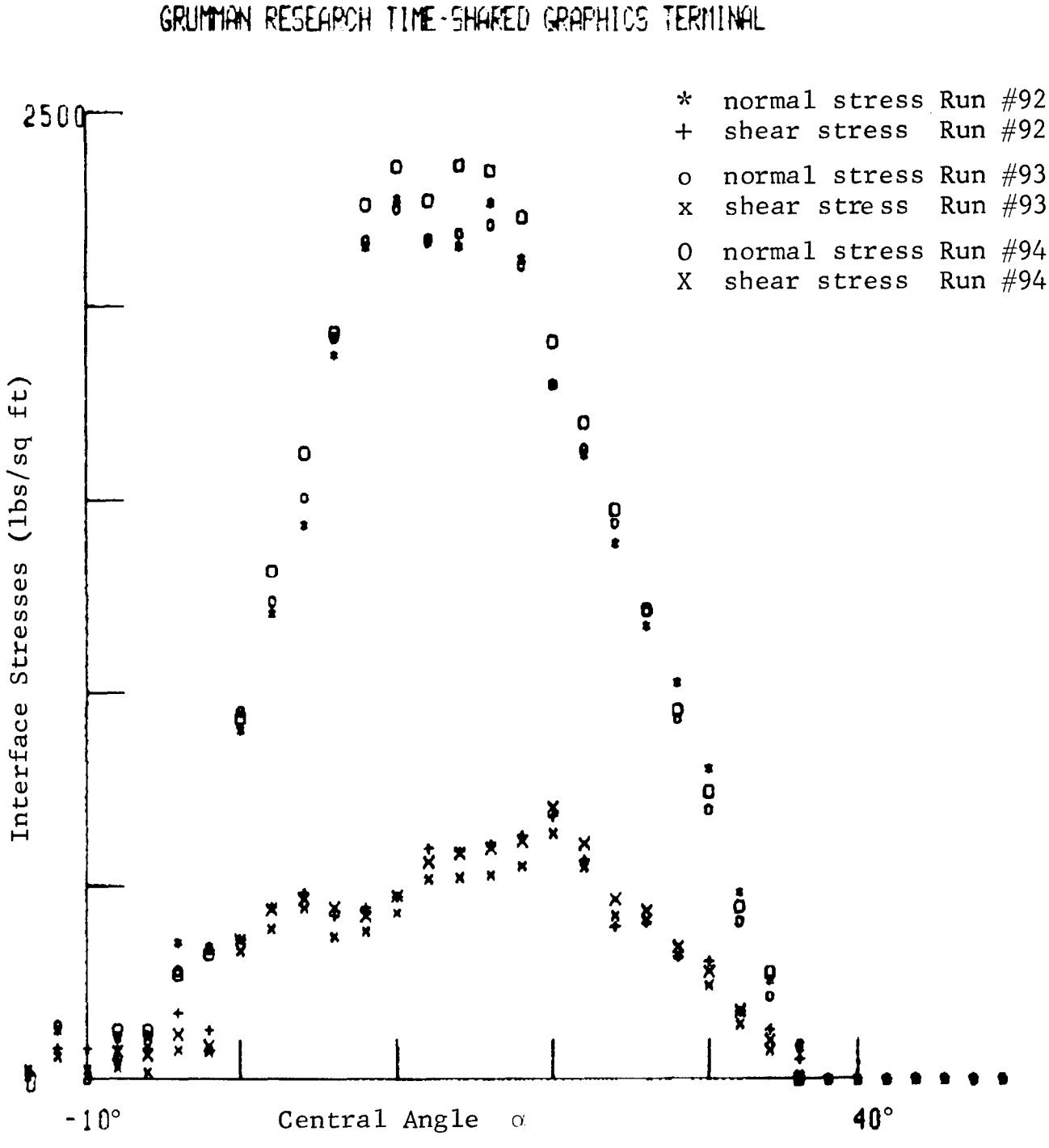

Fig. 38 Run #92-94 Average Interface Normal and Shear Stresses Measured in Loose Sand
Run #92: Load = 413 lbs, Drawbar Pull = 19 lbs, Torque = 139 ft lbs
Run #93: Load = 411 lbs, Drawbar Pull = 7 lbs, Torque = 123 ft lbs
Run #94: Load = 428 lbs, Drawbar Pull = 13 lbs, Torque = 135 ft lbs

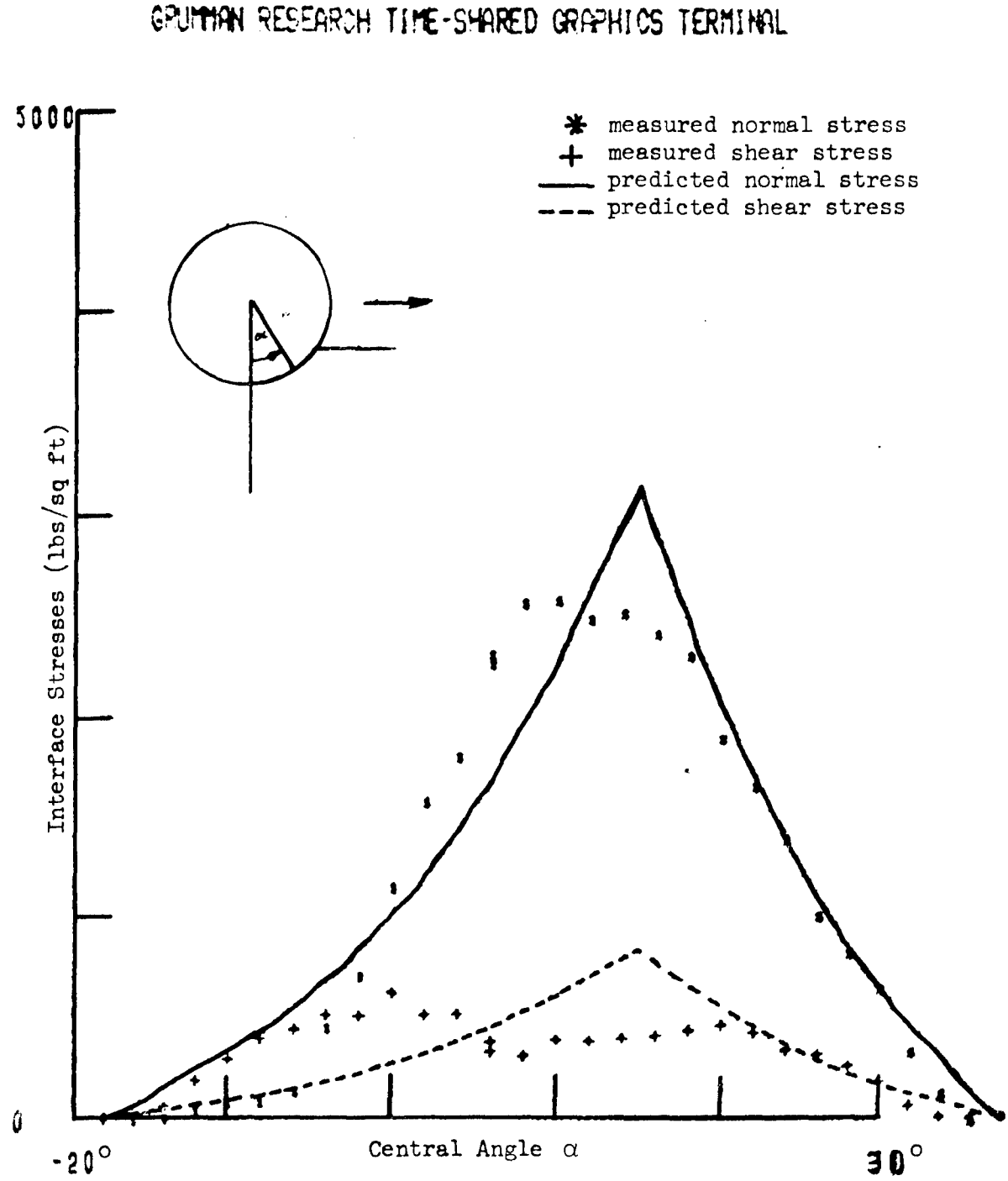

Fig. 39 Run #102 Measured and Predicted Average Interface Normal and Shear Stresses in Loose Sand
Load = 444 lbs, Drawbar Pull = 25 lbs, Torque = 145 ft lbs

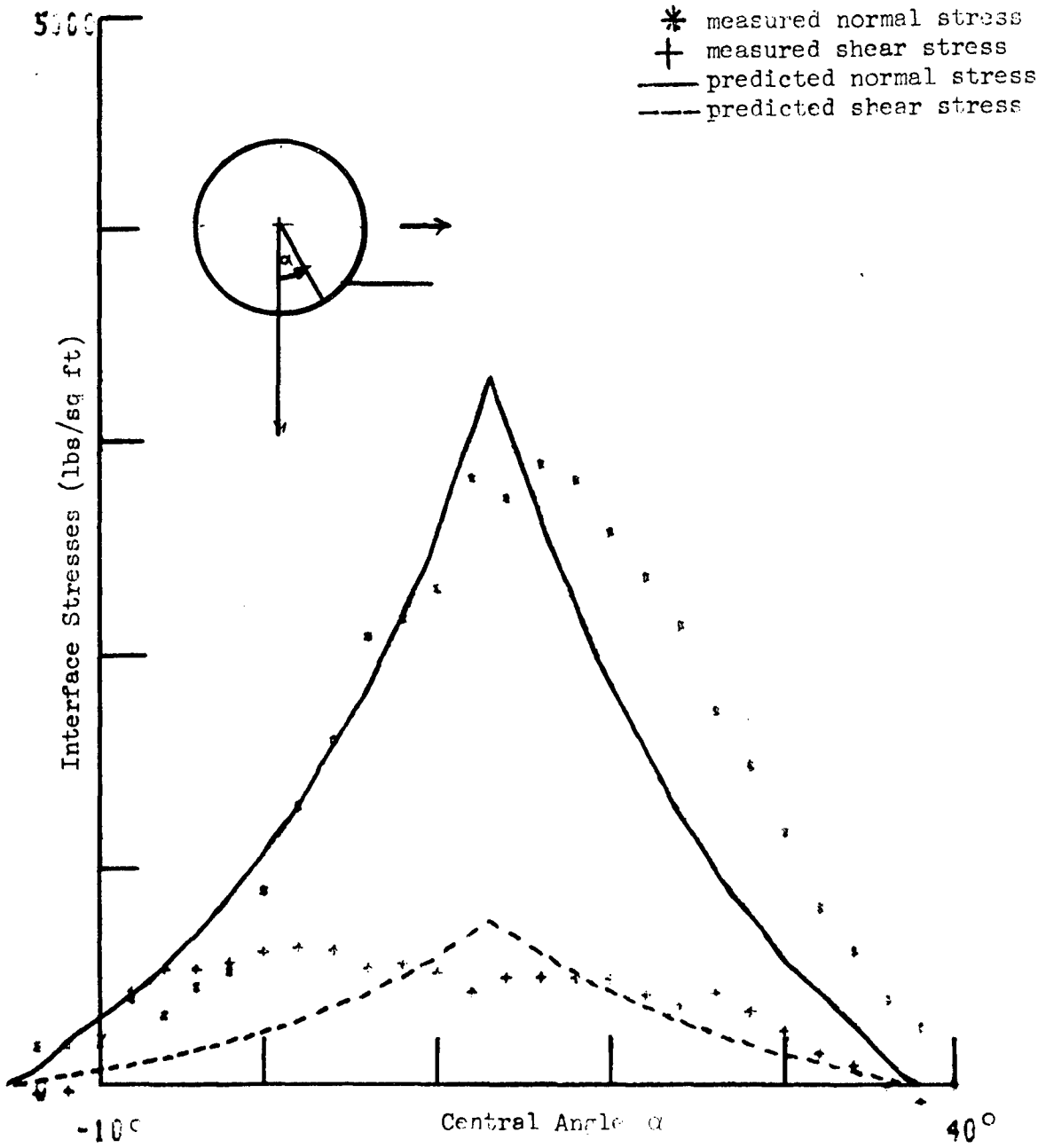

Fig. 40 Run #105 Measured and Predicted Average Interface Normal and Shear Stresses in Loose Sand
Load = 532 lbs, Drawbar Pull = 2 lbs, Torque = 164 ft lbs

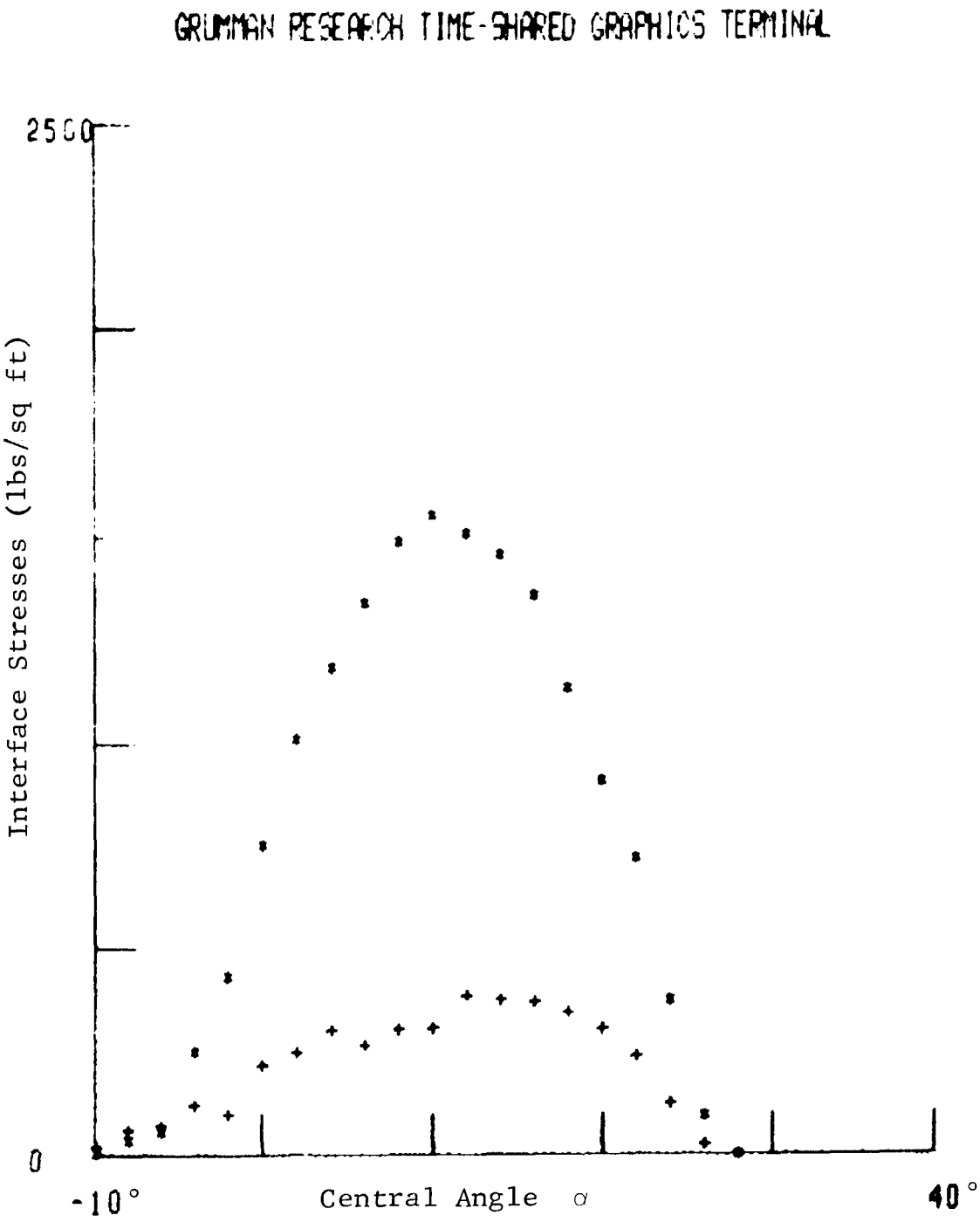

Fig. 41 Run #117 Average Interface Normal and Shear Stresses Measured in Loose Sand
Load = 229 lbs, Drawbar Pull = 17 lbs,
Torque = 68 ft lbs

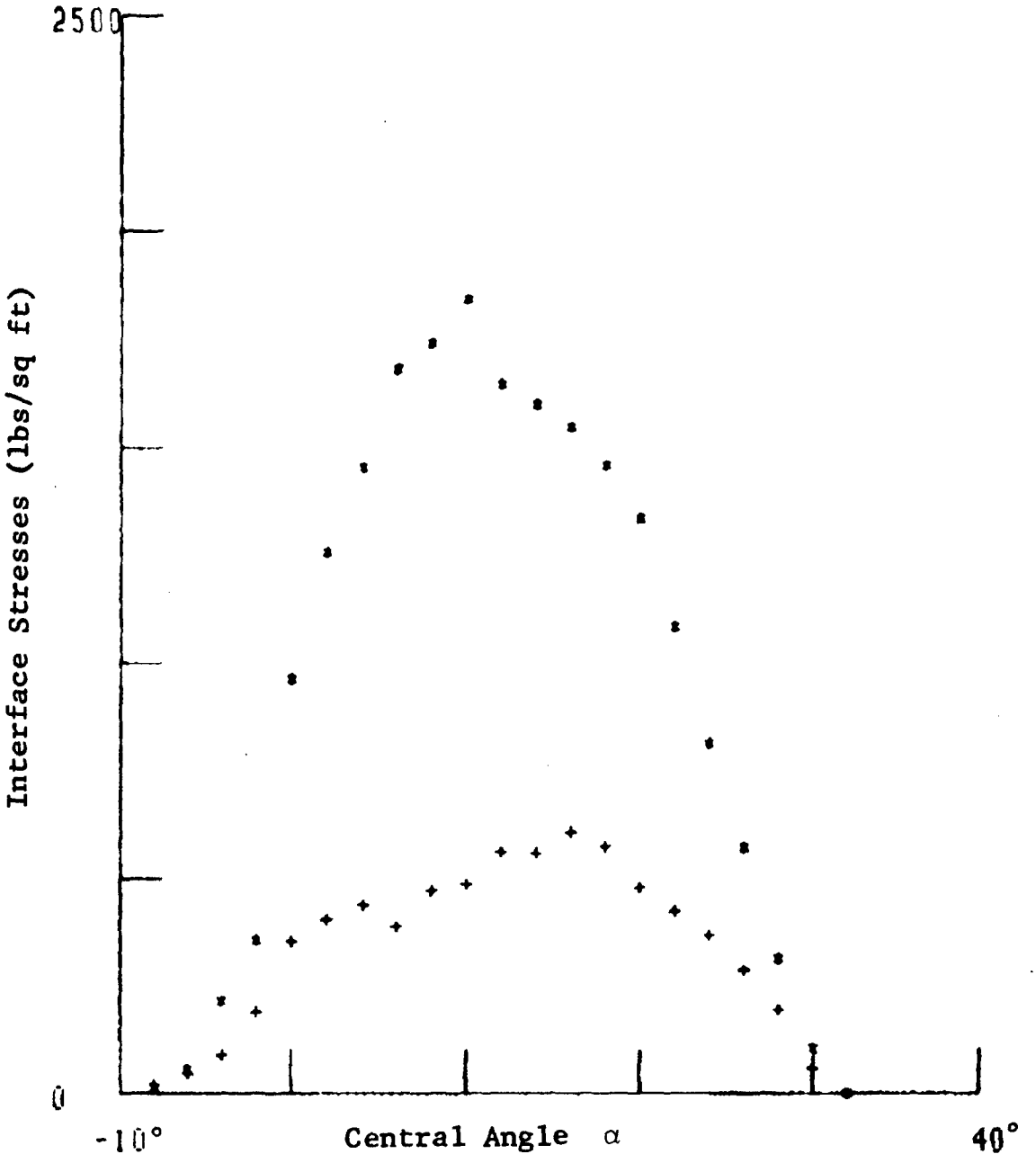

Fig. 42 Run #119 Average Interface Normal and Shear Stresses Measured in Loose Sand
Load = 299 lbs, Drawbar Pull = 37 lbs,
Torque = 113 ft lbs

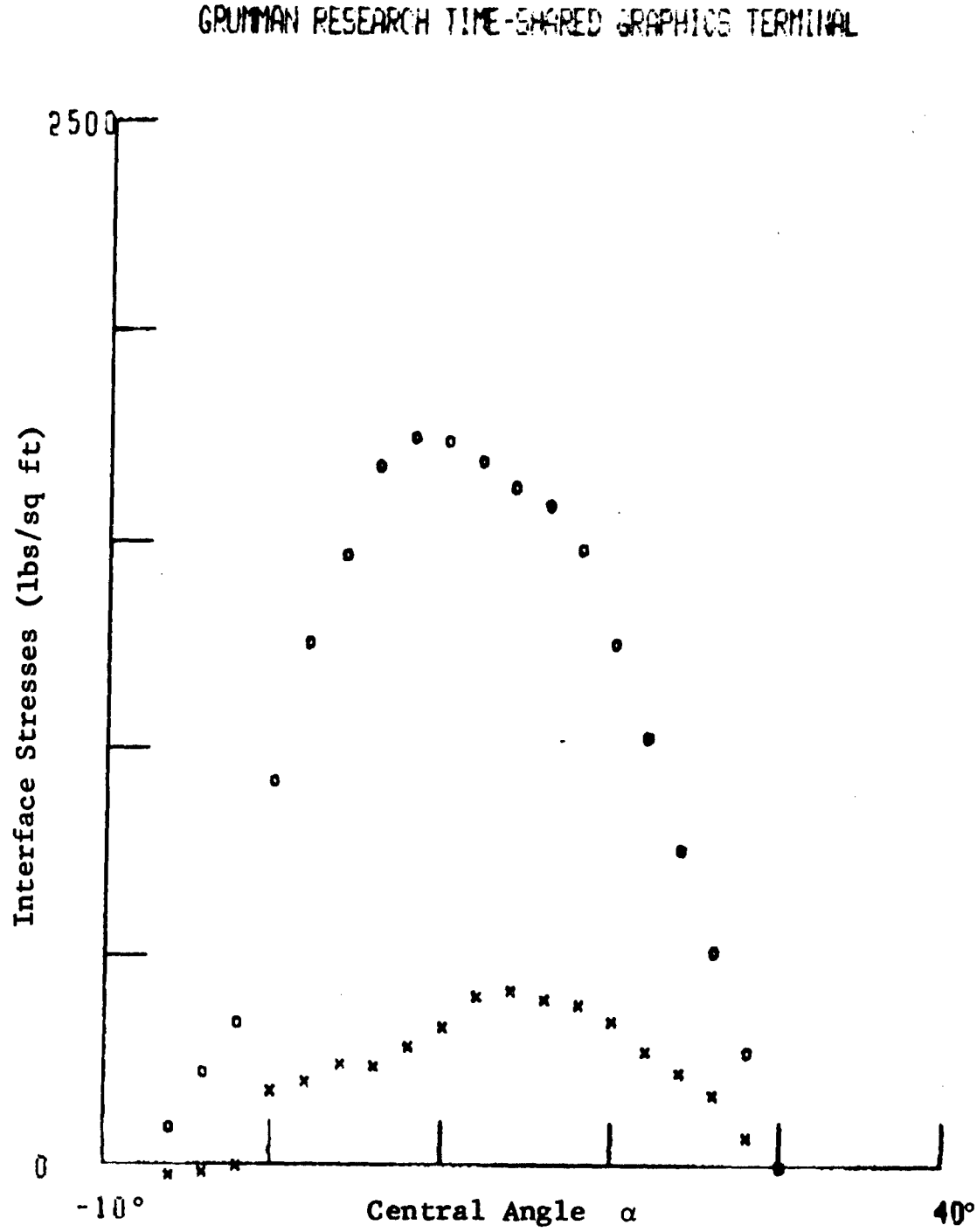

Fig. 43 Run #120 Average Interface Normal and Shear Stresses Measured in Loose Sand
Load = 286 lbs, Drawbar Pull = 0 lbs,
Torque = 67 ft lbs

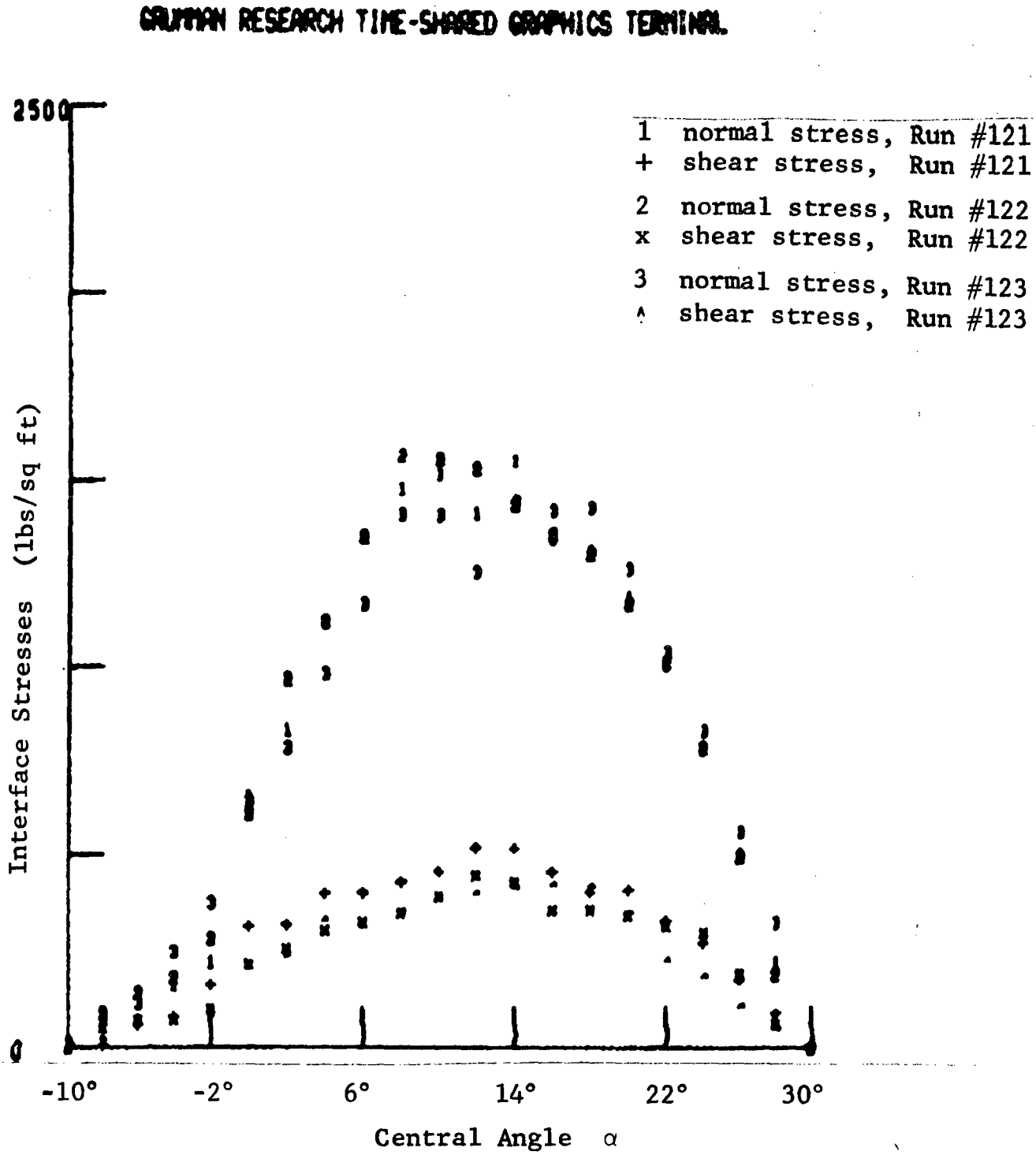

Fig. 44 Run#121-123 Average Interface Normal and Shear Stresses Measured in Loose Sand

Run #121: Load = 250 lbs, Drawbar Pull = 30 lbs, Torque = 96 ft lbs

Run #122: Load = 254 lbs, Drawbar Pull = 19 lbs, Torque = 83 ft lbs

Run #123: Load = 247 lbs, Drawbar Pull = 11 lbs, Torque = 75 ft lbs

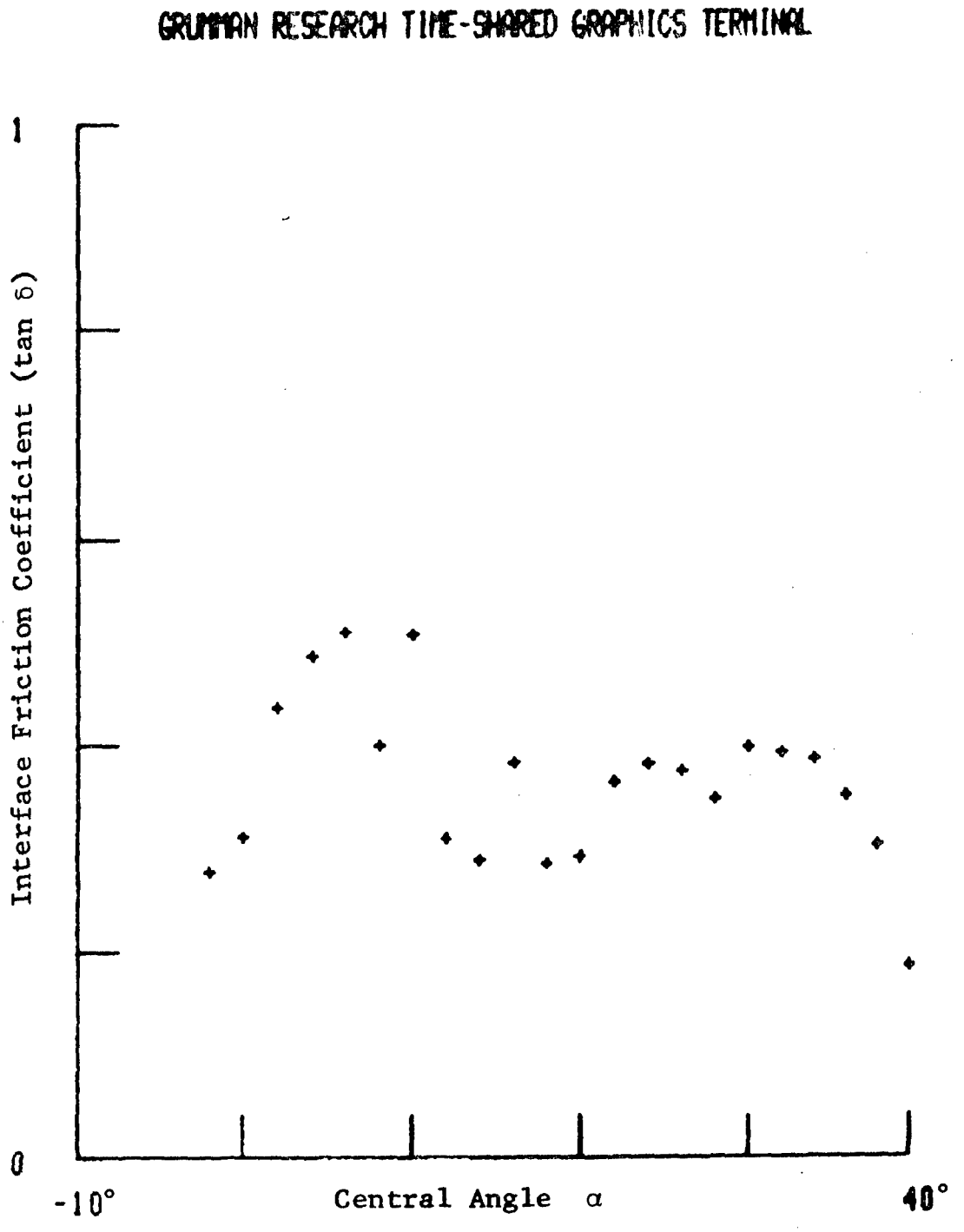

Fig. 45 Run #69 Variation of Interface Friction Coefficient (tan δ) Along the Interface in Loose Sand Load = 402 lbs, Drawbar Pull = 6 lbs, Torque = 157 ft lbs

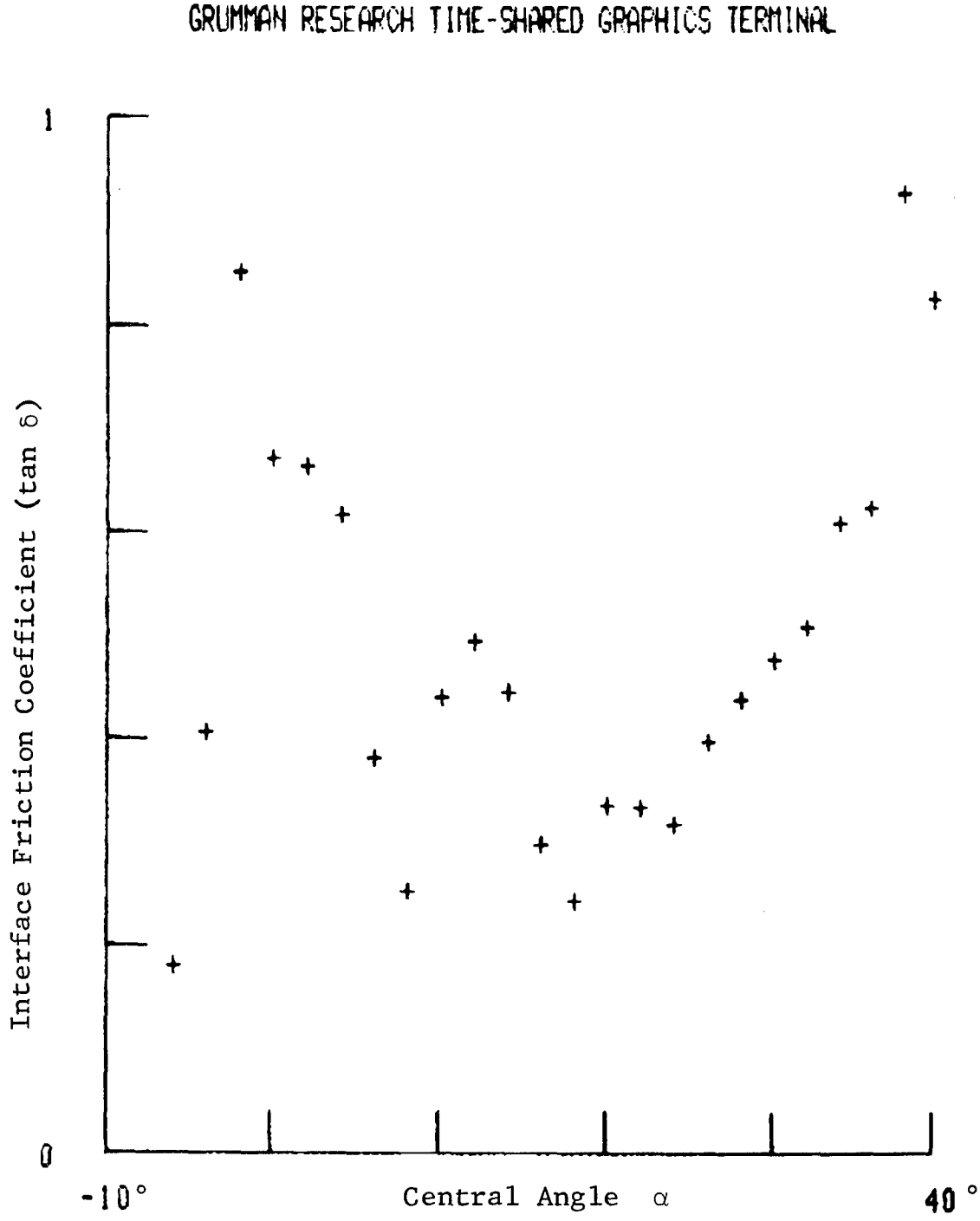

Fig. 46 Run #70 Variation of Interface Friction Coefficient (tan δ) Along the Interface in Loose Sand Load = 446 lbs, Drawbar Pull = 26 lbs, Torque = 193 ft lbs

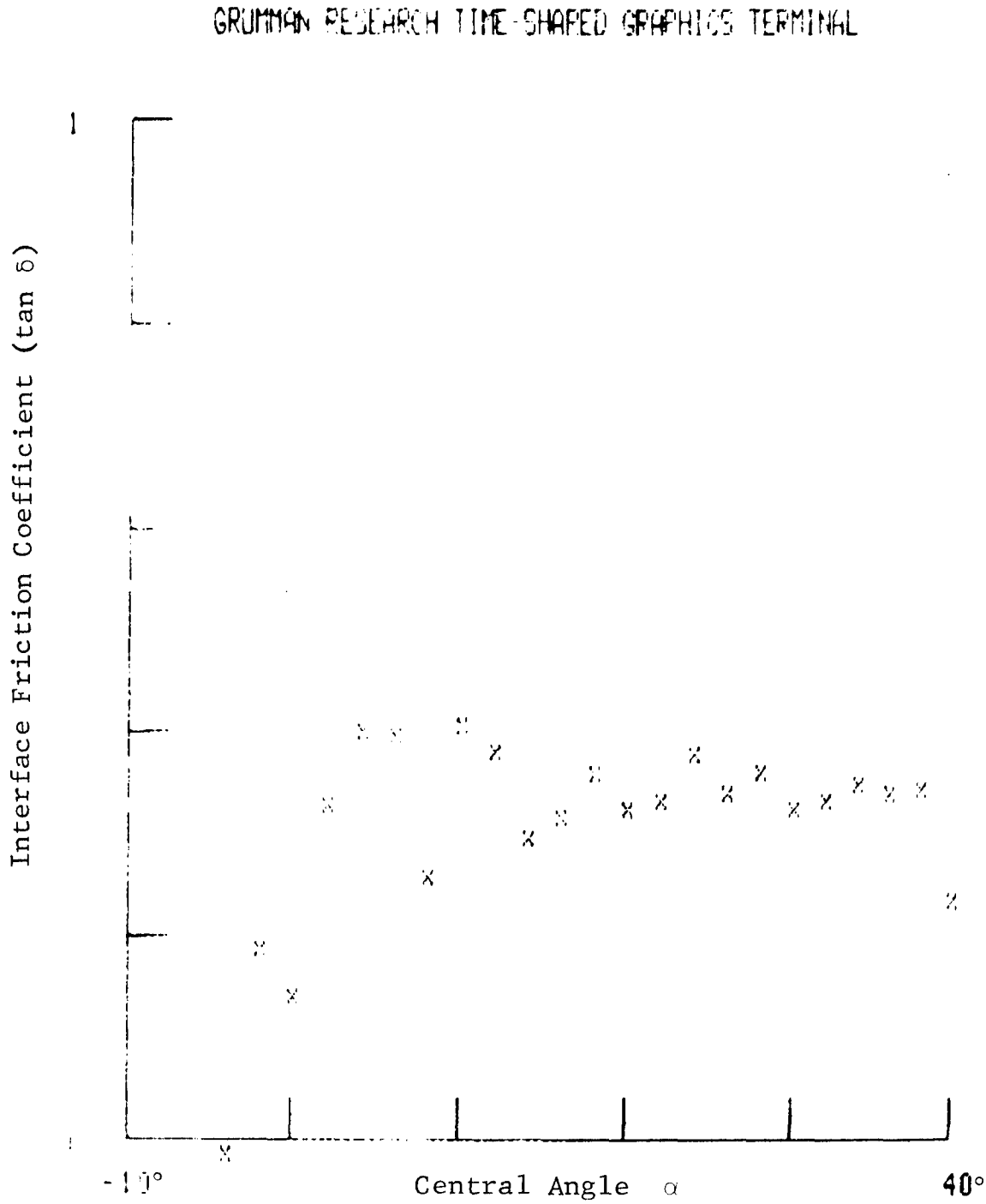

Fig. 47 Run #71 Variation of Interface Friction Coefficient (tan δ) Along the Interface in Loose Sand
Load = 417 lbs, Drawbar Pull = 6 lbs,
Torque = 156 ft lbs

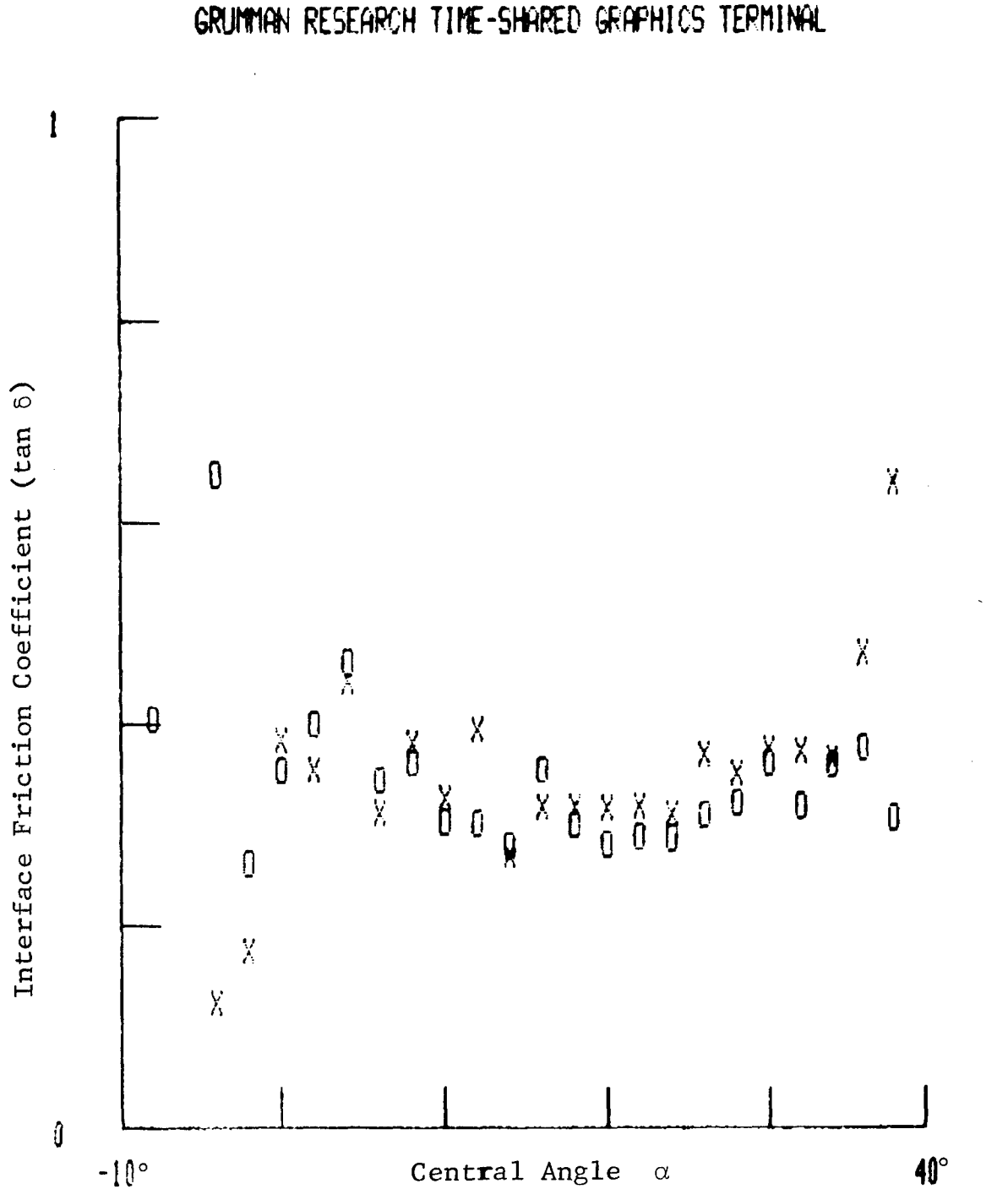

Fig. 48 Run #80-81 Variation of Interface Friction Coefficient (tan δ) Along the Interface in Loose Sand
Run #80: Load = 406 lbs, Drawbar Pull = 2 lbs, Torque = 146 ft lbs
Run #81: Load = 379 lbs, Drawbar Pull = 10 lbs, Torque = 143 ft lbs

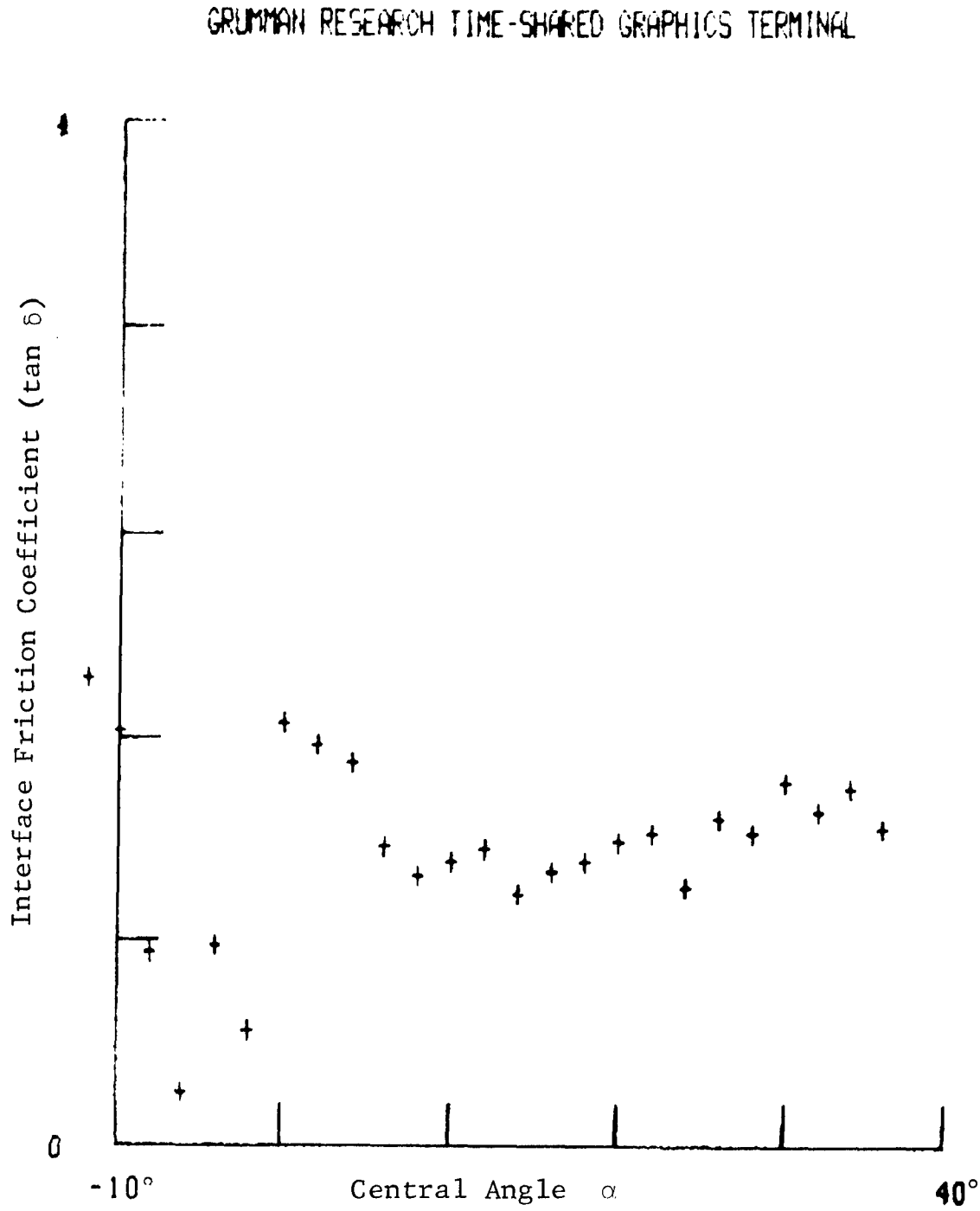

Fig. 49 Run #87 Variation of Interface Friction Coefficient (tan δ) Along the Interface in Loose Sand Load = 375 lbs, Drawbar Pull = 9 lbs, Torque = 125 ft lbs

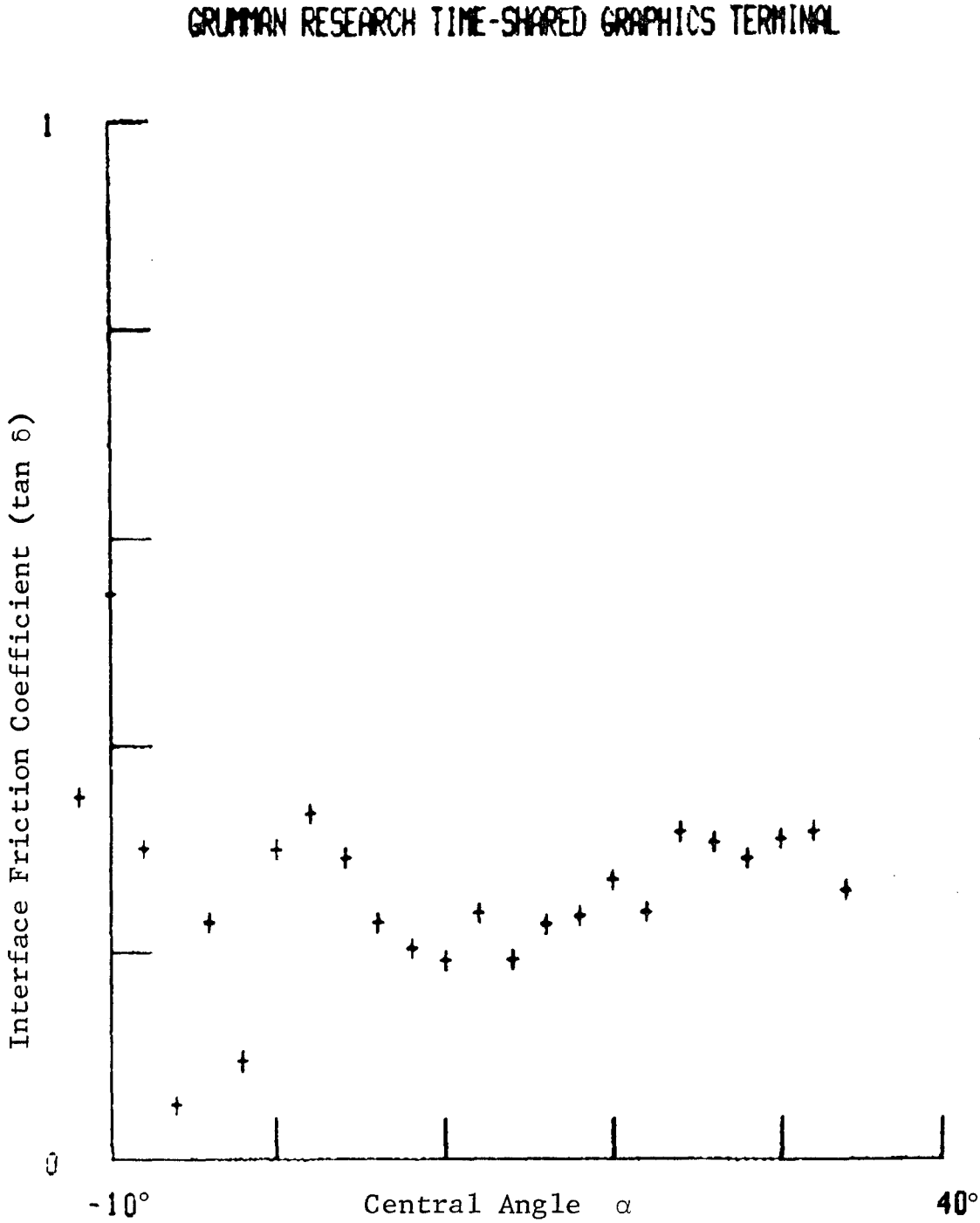

Fig. 50 Run #89 Variation of Interface Friction Coefficient (tan δ) Along the Interface in Loose Sand
Load = 409 lbs, Drawbar Pull = -3 lbs,
Torque = 116 ft lbs

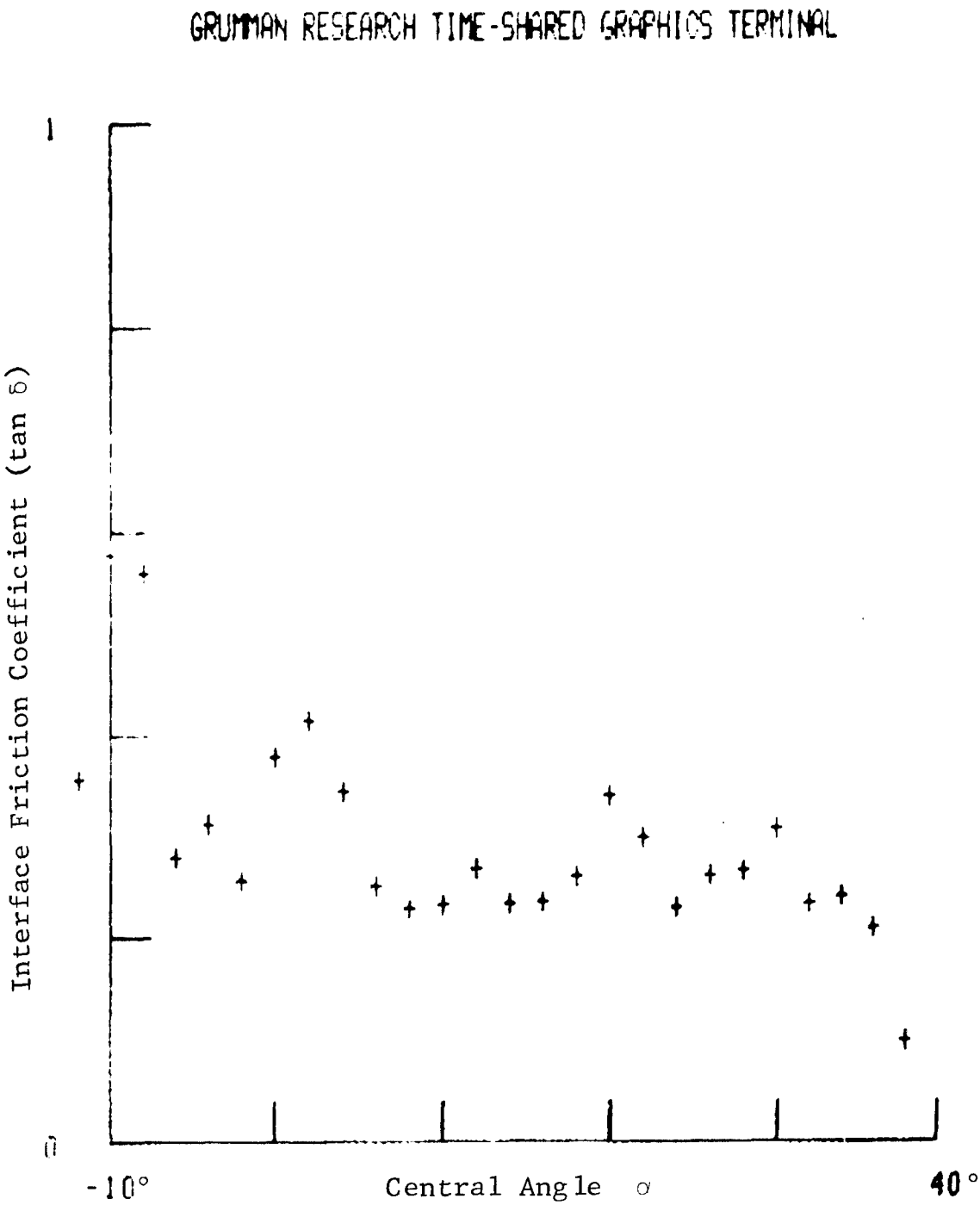

Fig. 51 Run #90 Variation of Interface Friction Coefficient (tan δ) Along the Interface in Loose Sand Load = 441 lbs, Drawbar Pull = -2 lbs, Torque = 137 ft lbs

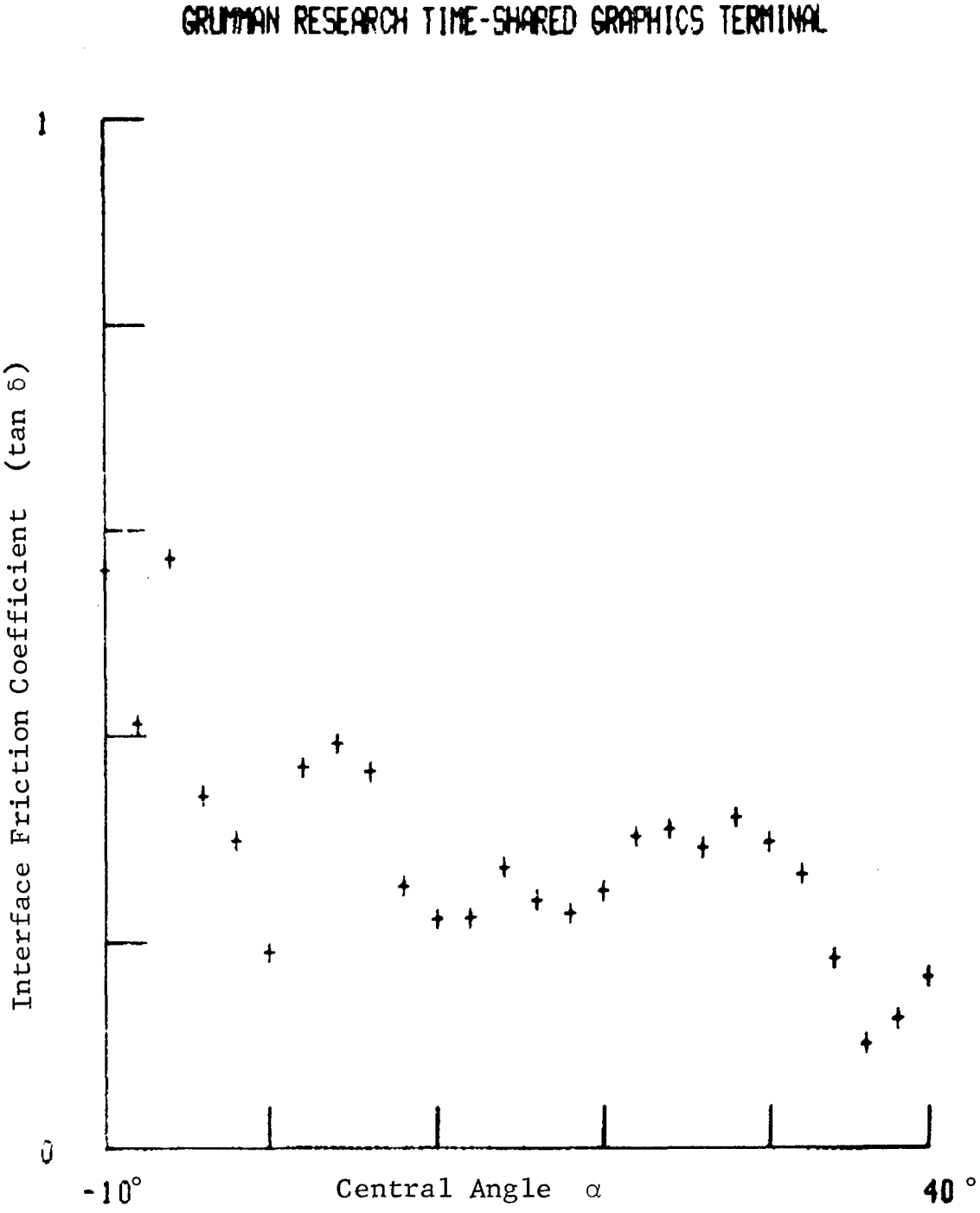

Fig. 52 Run #91 Variation of Interface Friction Coefficient (tan δ) Along the Interface in Loose Sand Load = 453 lbs, Drawbar Pull = -16 lbs, Torque = 140 ft lbs

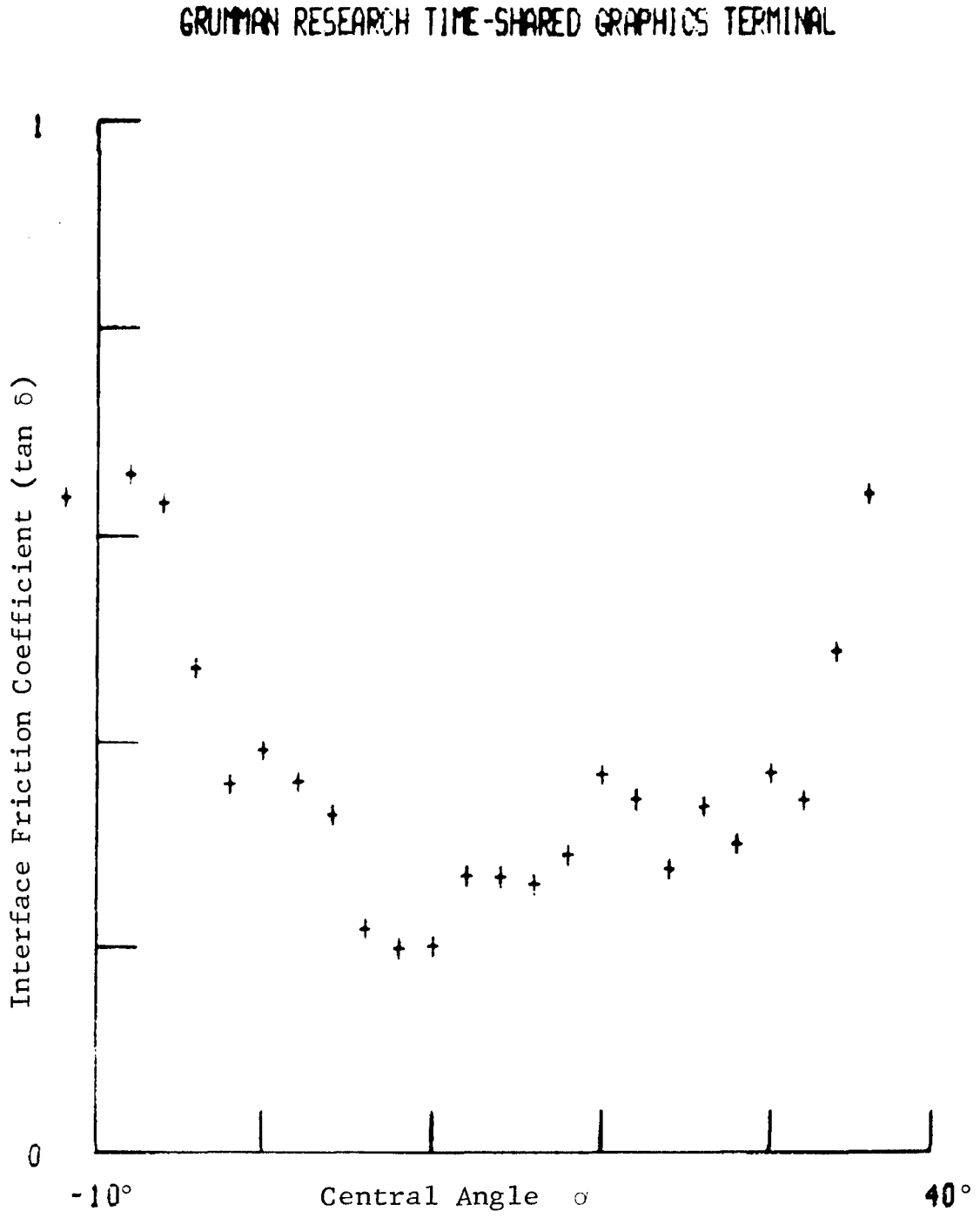

Fig. 53 Run #92 Variation of Interface Friction Coefficient (tan δ) Along the Interface in Loose Sand Load = 413 lbs, Drawbar Pull = 19 lbs, Torque = 139 ft lbs

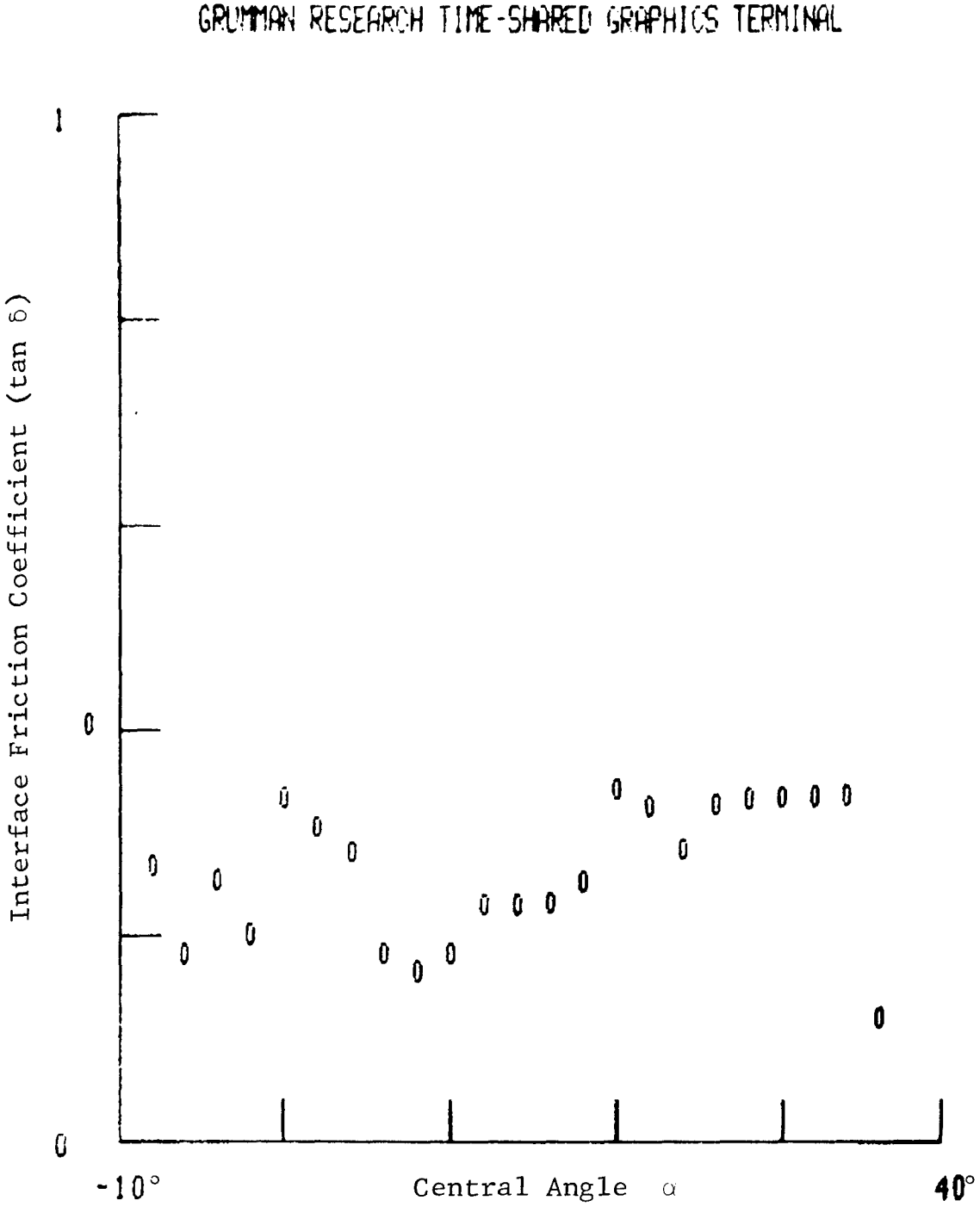

Fig. 54 Run #93 Variation of Interface Friction Coefficient (tan δ) Along the Interface in Loose Sand Load = 411 lbs, Drawbar Pull = 7 lbs, Torque = 123 ft lbs

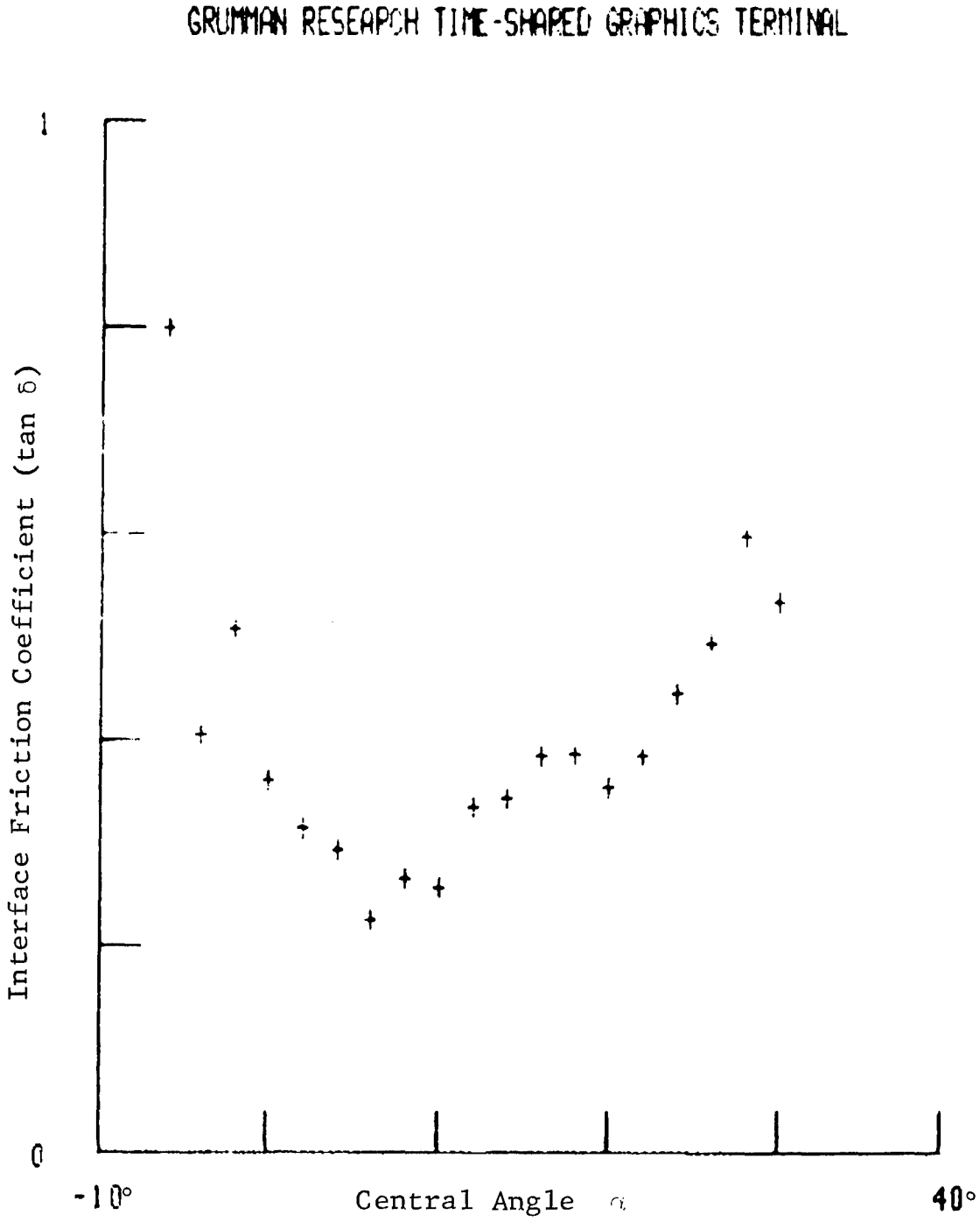

Fig. 55 Run #119 Variation of Interface Friction Coefficient (tan δ) Along the Interface in Loose Sand Load = 229 lbs, Drawbar Pull = 37 lbs, Torque = 68 ft lbs

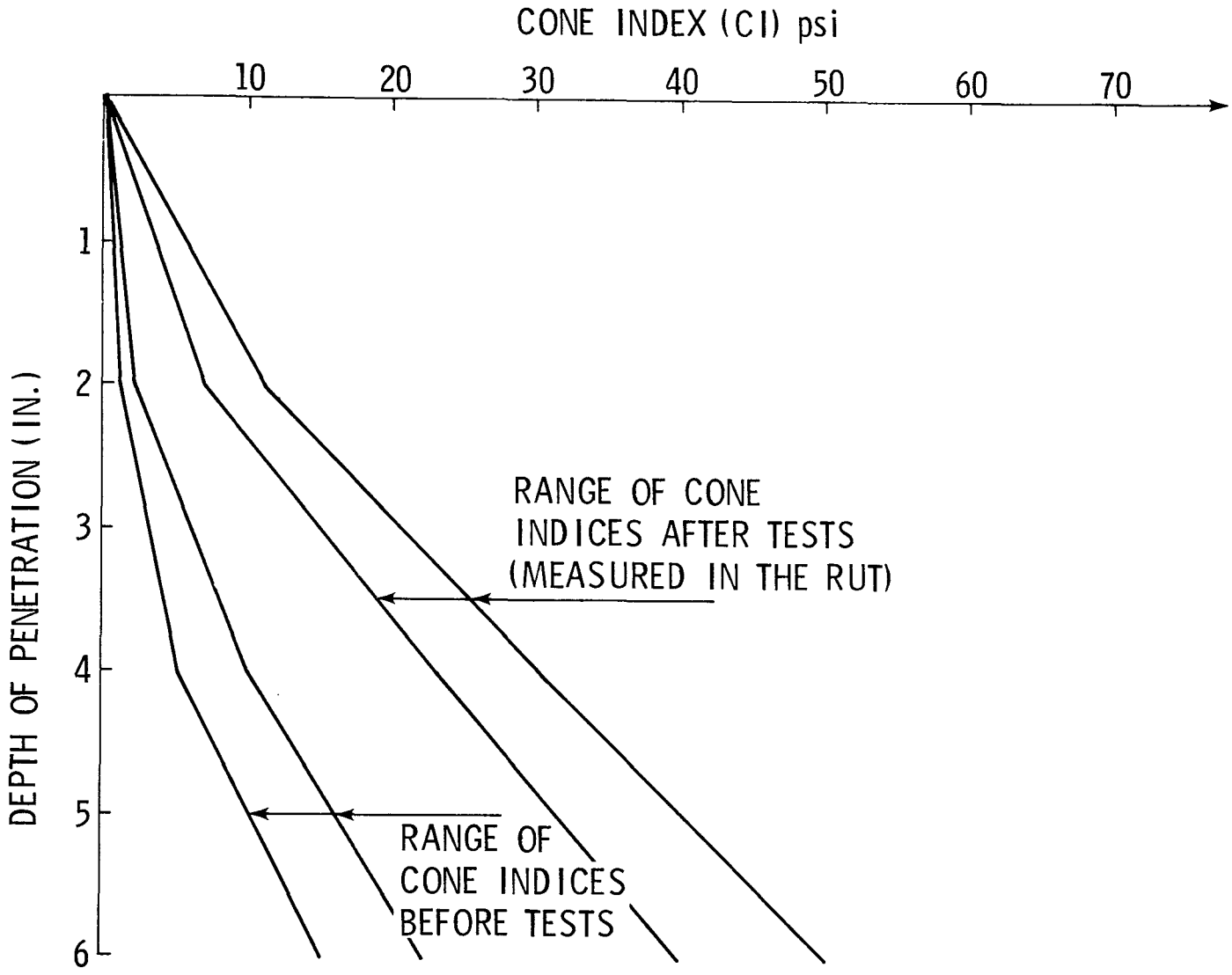

Fig. 56 Results of Cone Penetrometer Tests in Loose Sand for Runs #69-78

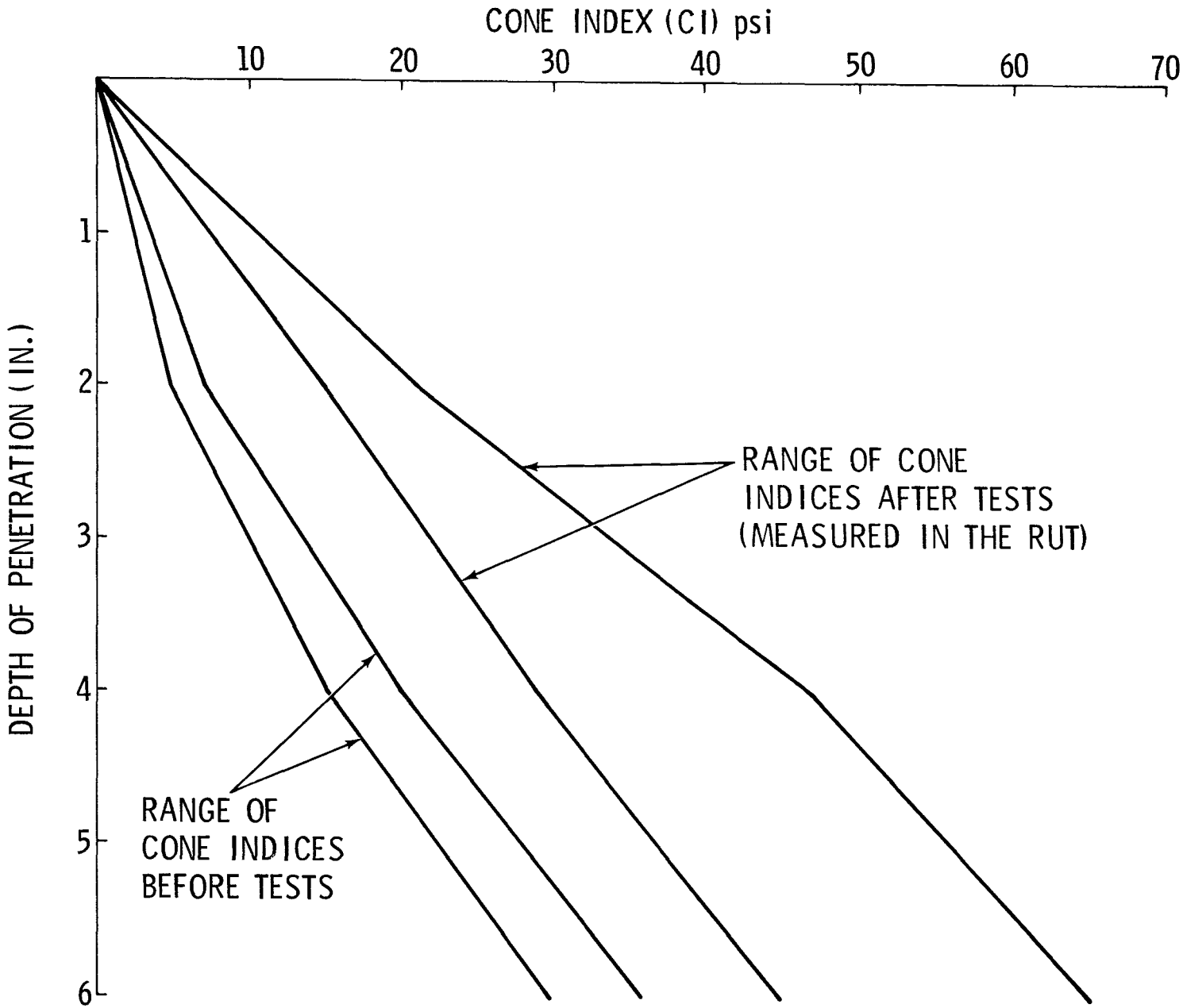

Fig. 57 Results of Cone Penetrometer Tests in Loose Sand for Runs #80-123

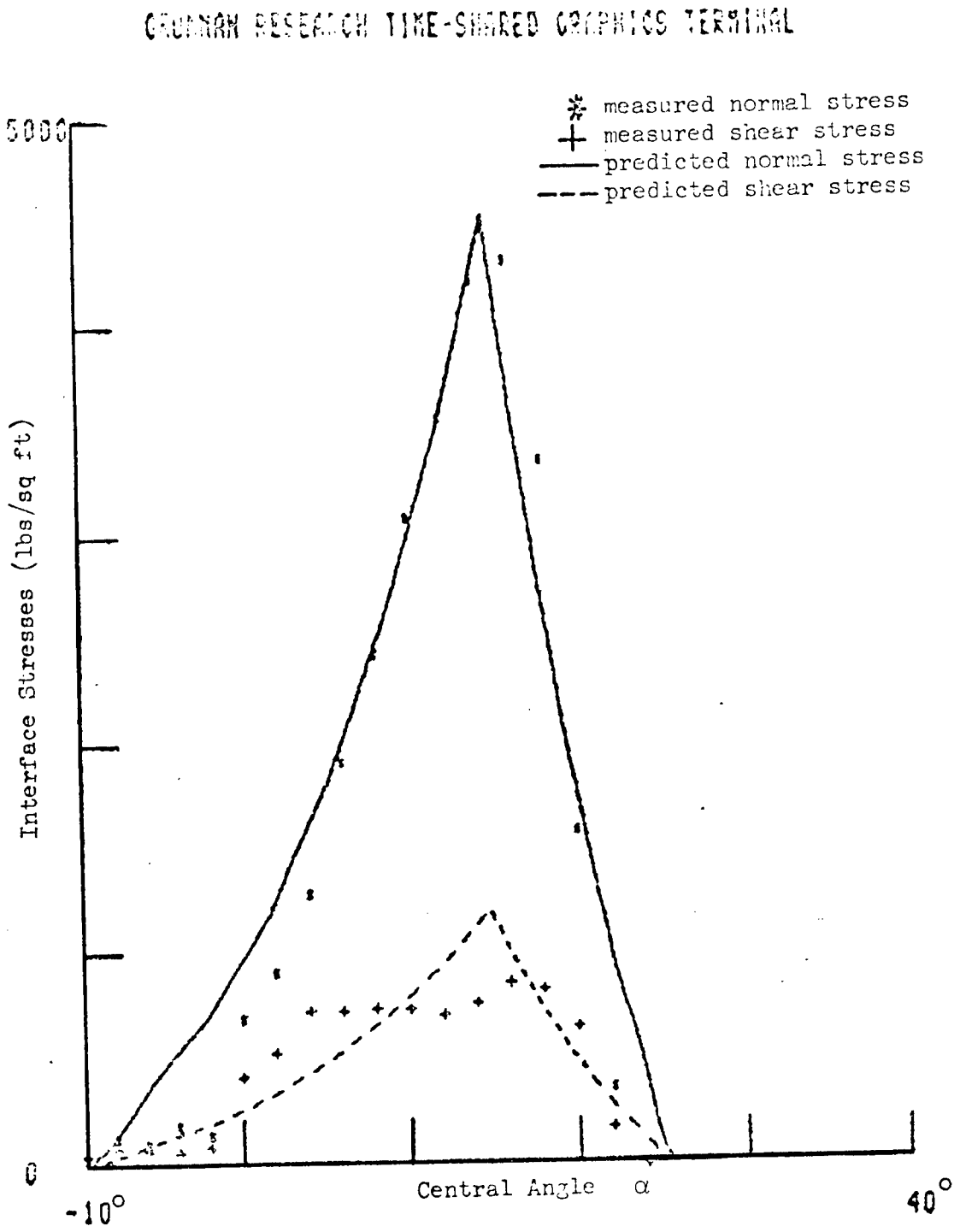

Fig. 58 Run #98 Measured and Predicted Average Interface Normal and Shear Stresses in Dense Sand Load = 426 lbs, Drawbar Pull = 32 lbs, Torque = 138 ft lbs

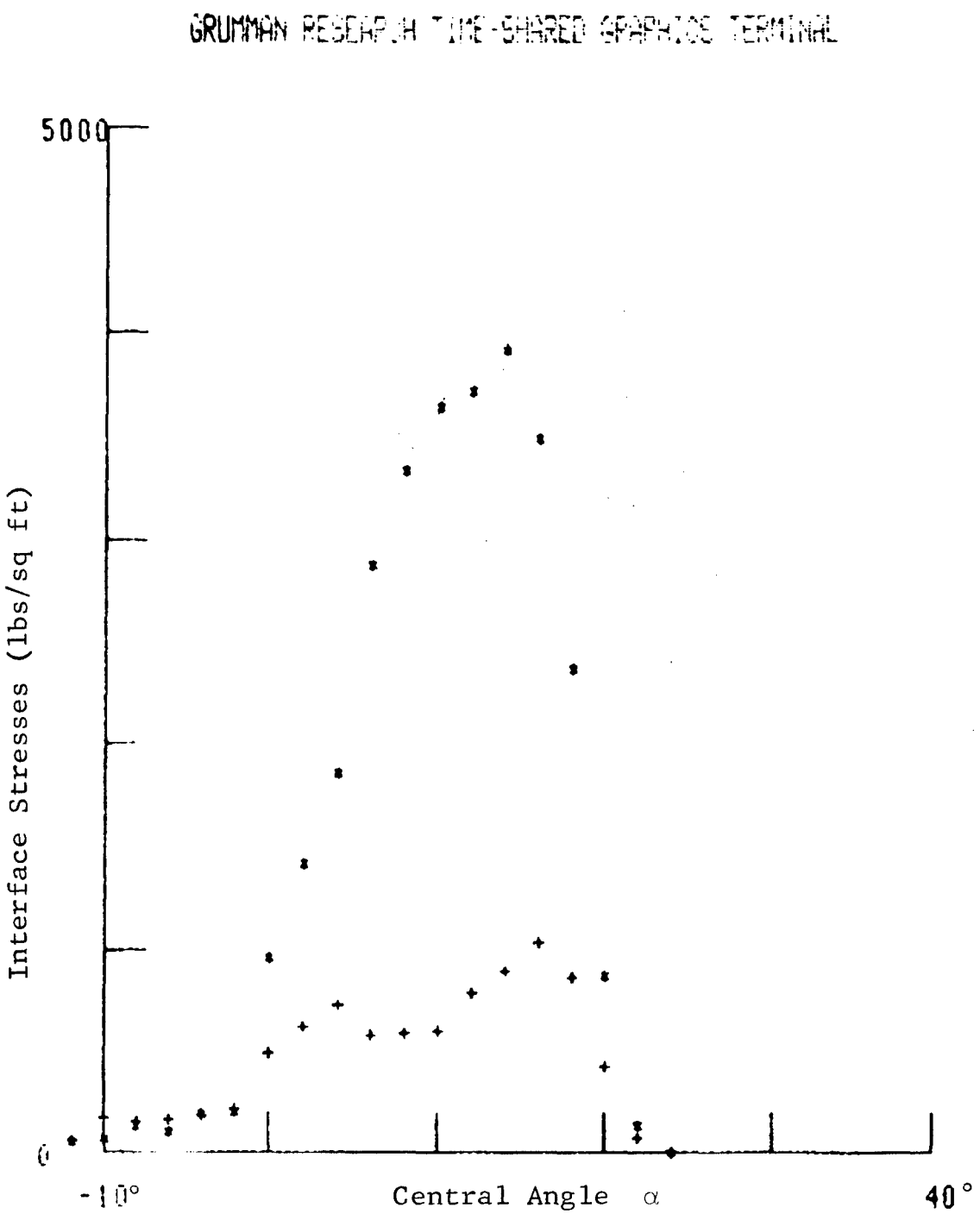

Fig. 59 Run #107 Average Interface Normal and Shear Stresses Measured in Dense Sand
Load = 486 lbs, Drawbar Pull = 51 lbs,
Torque = 158 ft lbs

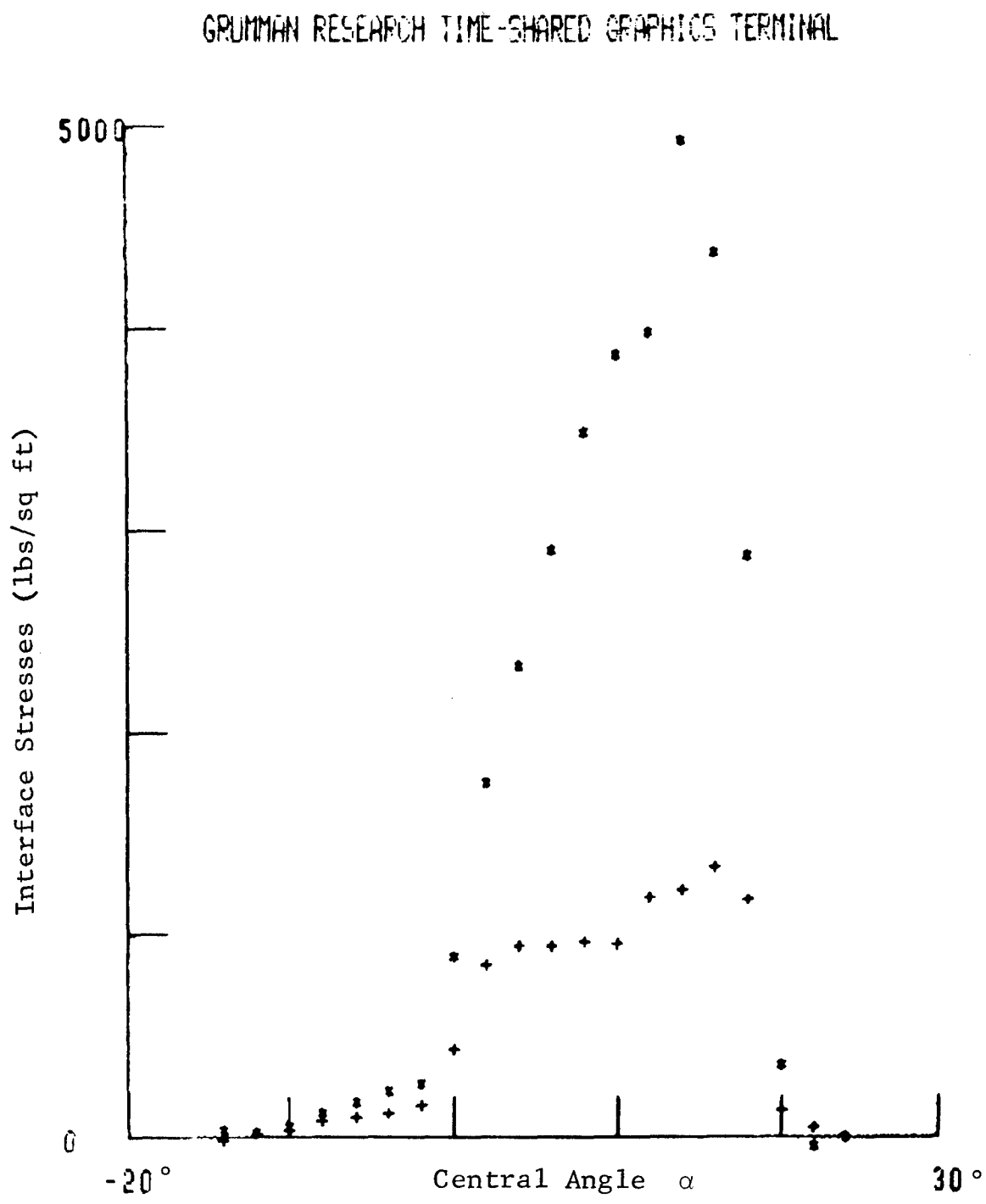

Fig. 60 Run #108 Average Interface Normal and Shear Stresses Measured in Dense Sand
Load = 487 lbs, Drawbar Pull = 67 lbs,
Torque = 177 ft lbs

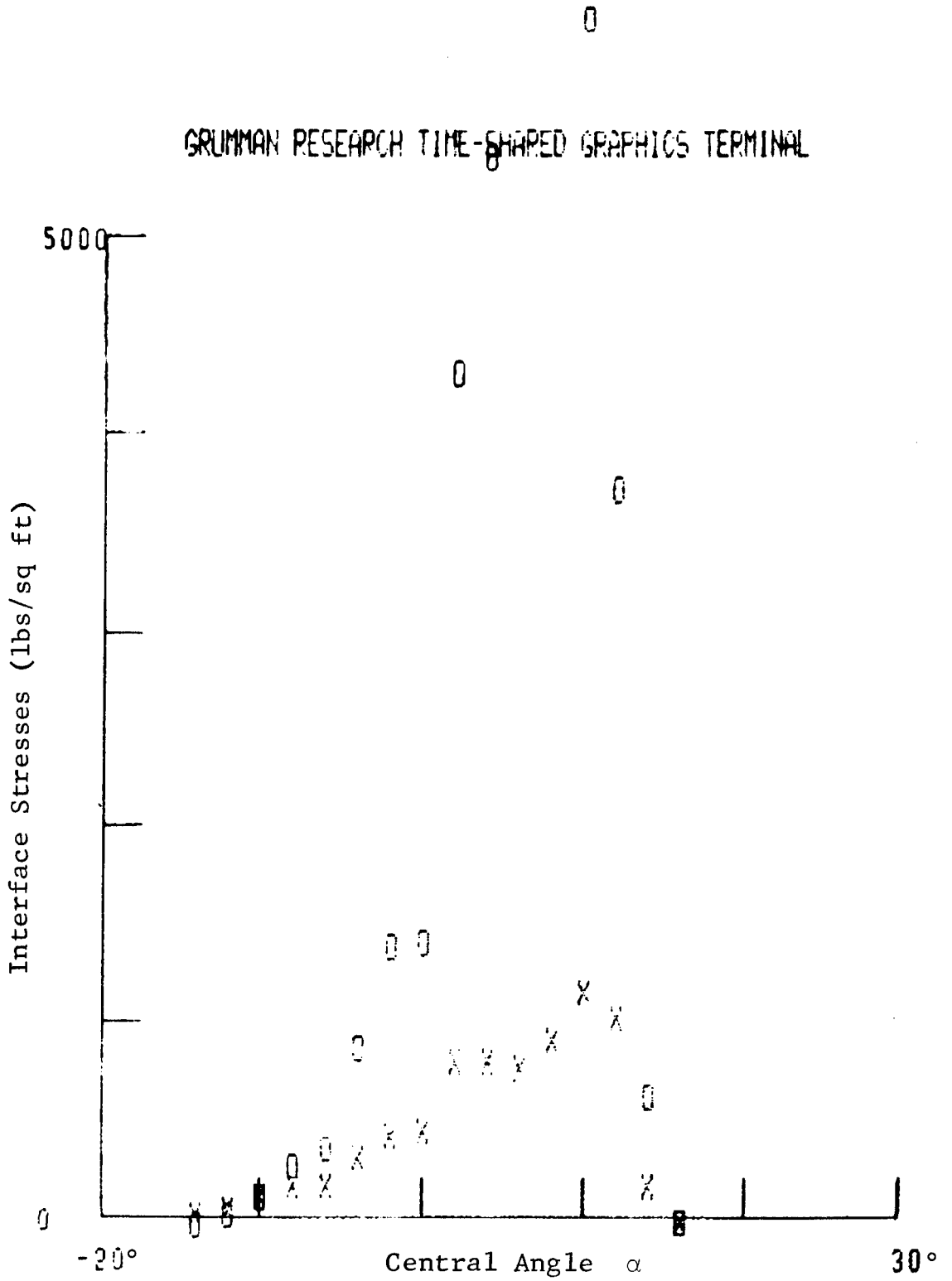

Fig. 61 Run #109 Average Interface Normal and Shear Stresses Measured in Dense Sand
Load = 561 lbs, Drawbar Pull = 51 lbs,
Torque = 127 ft lbs

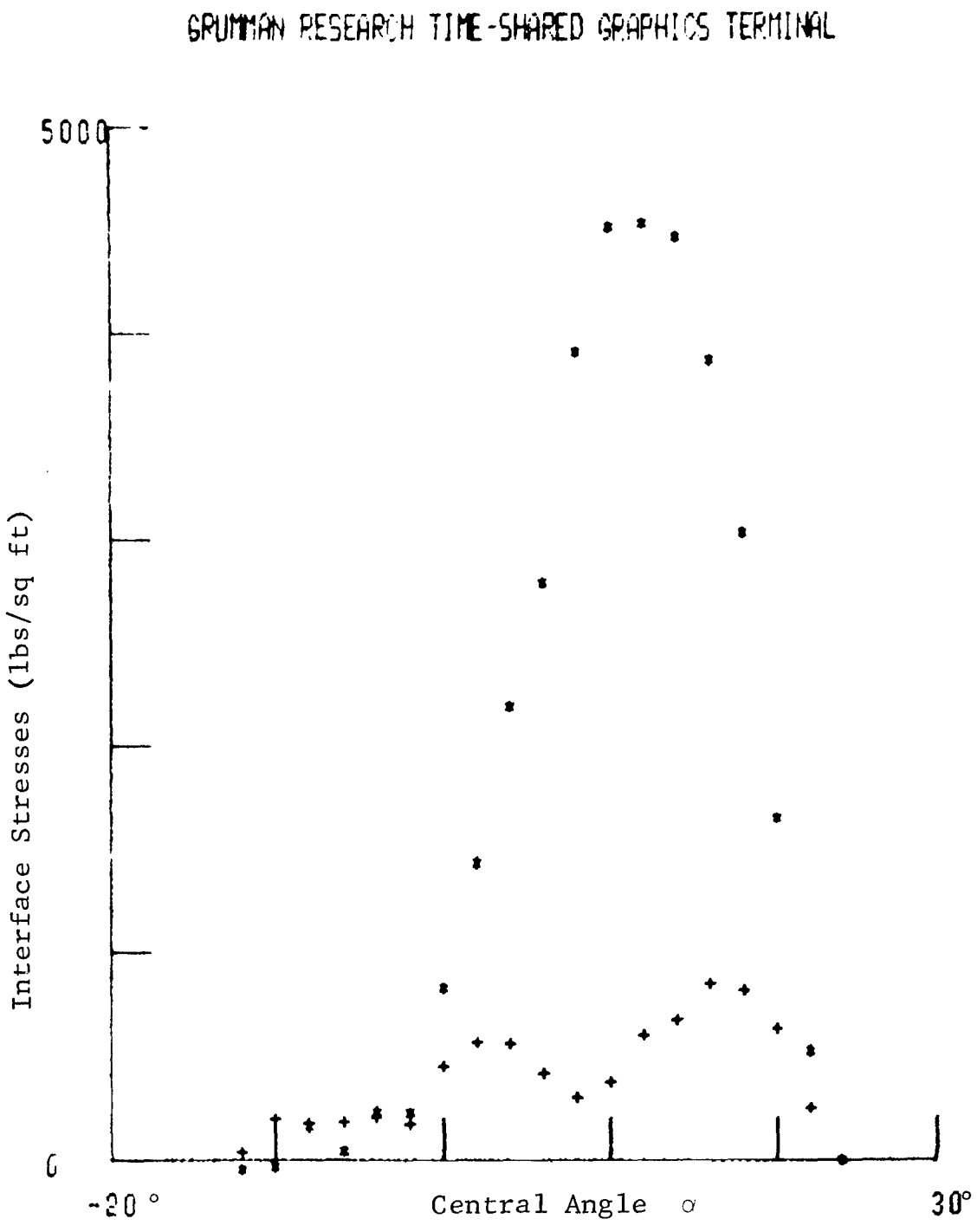

Fig. 62 Run #110 Average Interface Normal and Shear Stresses Measured in Dense Sand
Load = 481 lbs, Drawbar Pull = 10 lbs,
Torque = 118 ft lbs

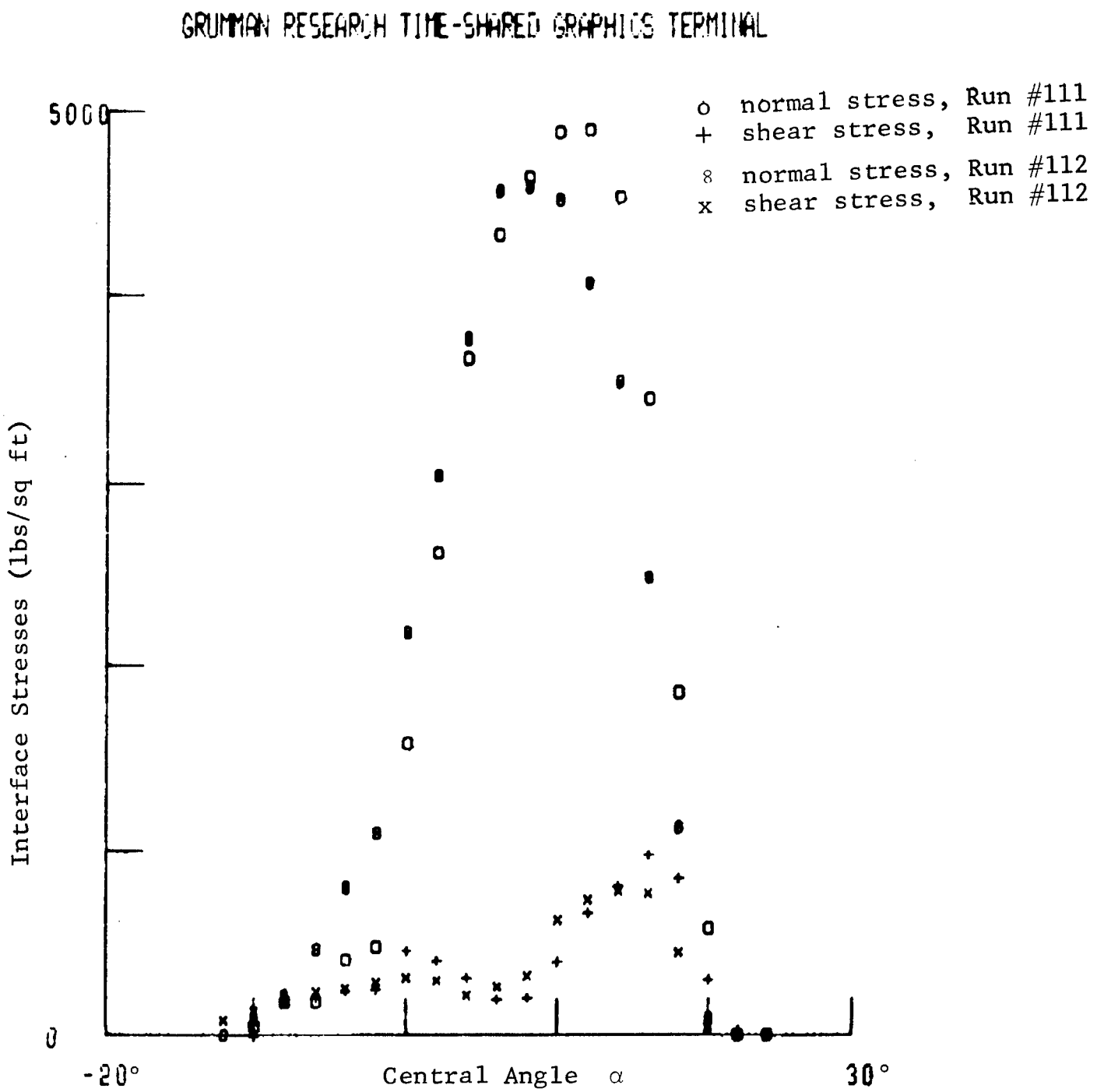

Fig. 63 Run #111-112 Average Interface Normal and Shear Stresses Measured in Dense Sand
Run #111: Load = 535 lbs, Drawbar Pull = 15 lbs, Torque = 100 ft lbs
Run #112: Load = 552 lbs, Drawbar Pull = 4 lbs, Torque = 105 ft lbs

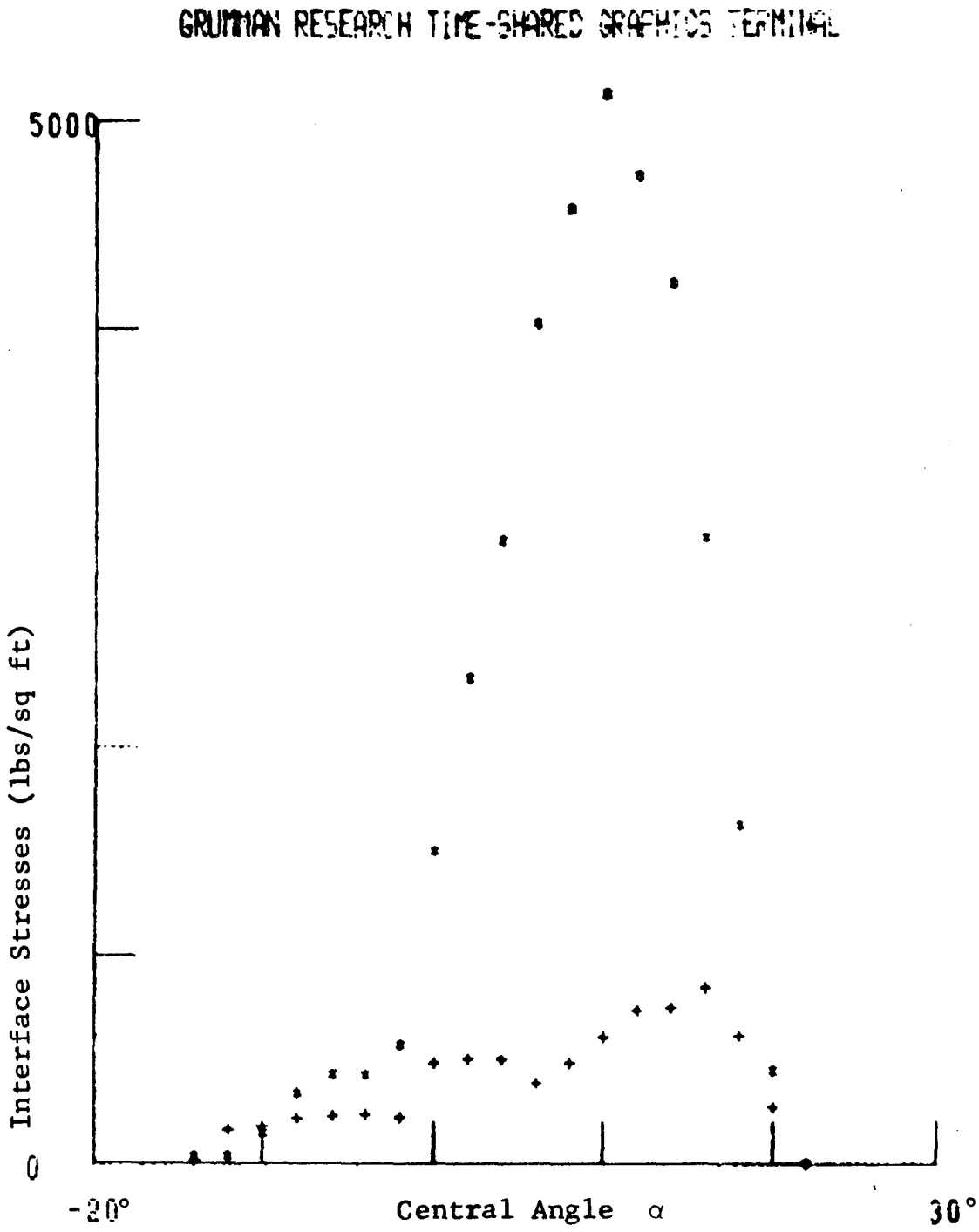

Fig. 64 Run #113 Average Interface Normal and Shear Stresses Measured in Dense Sand
Load = 535 lbs, Drawbar Pull = 25 lbs,
Torque = 124 ft lbs

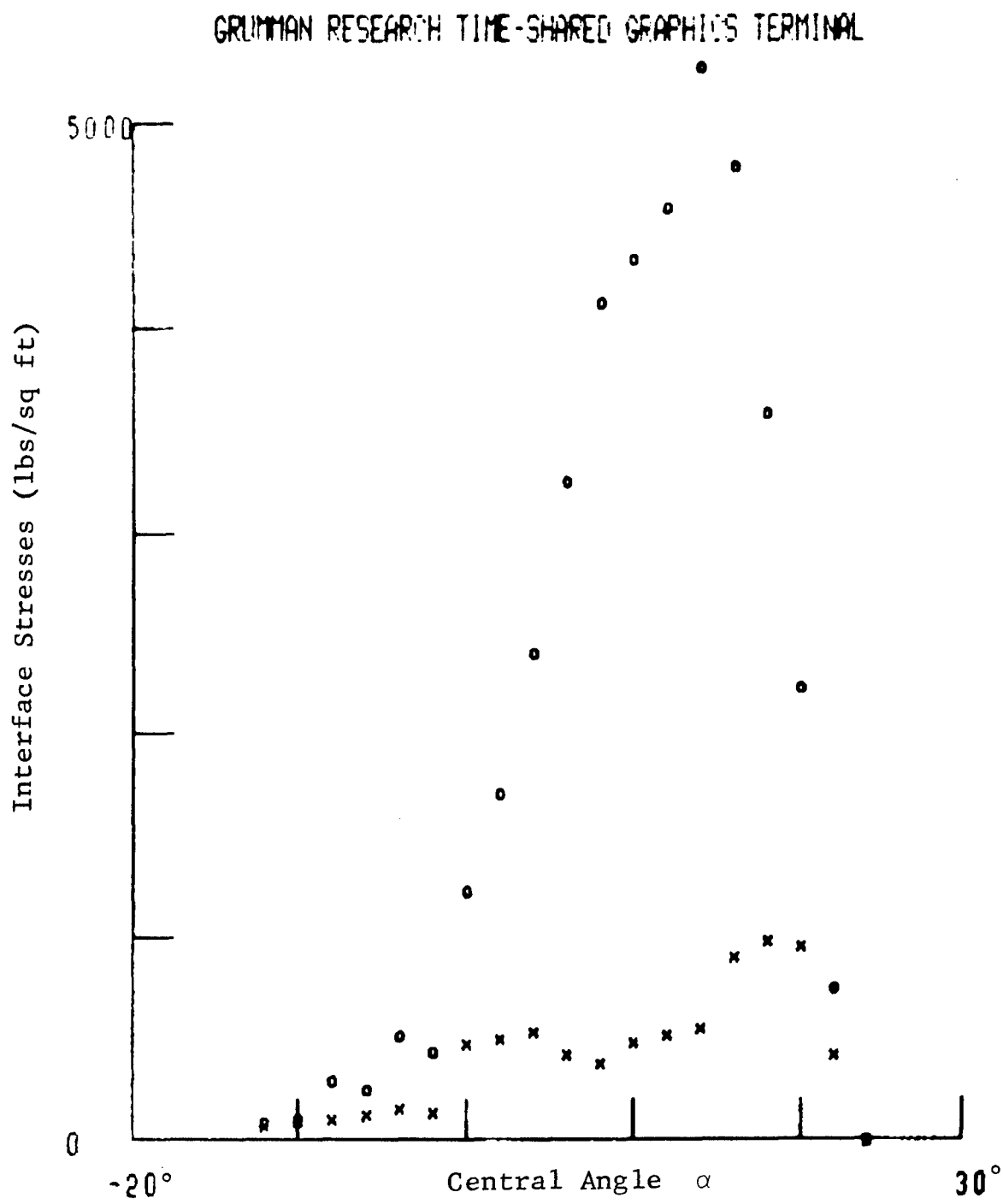

Fig. 65 Run #114 Average Interface Normal and Shear Stresses Measured in Dense Sand
Load = 576 lbs, Drawbar Pull = 2 lbs,
Torque = 127 ft lbs

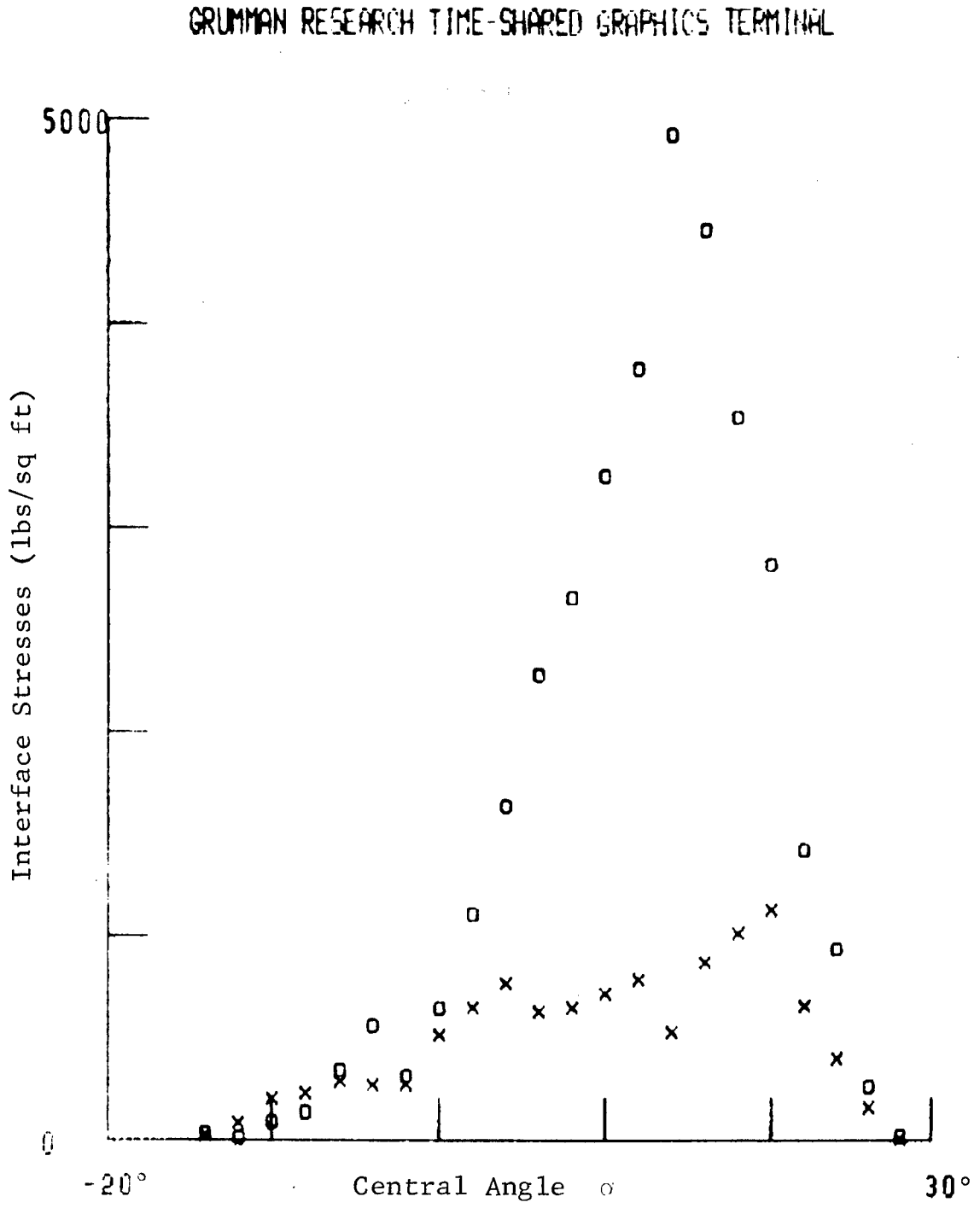

Fig. 66 Run #115 Average Interface Normal and Shear Stresses Measured in Dense Sand
Load = 513 lbs, Drawbar Pull = 41 lbs,
Torque = 174 ft lbs

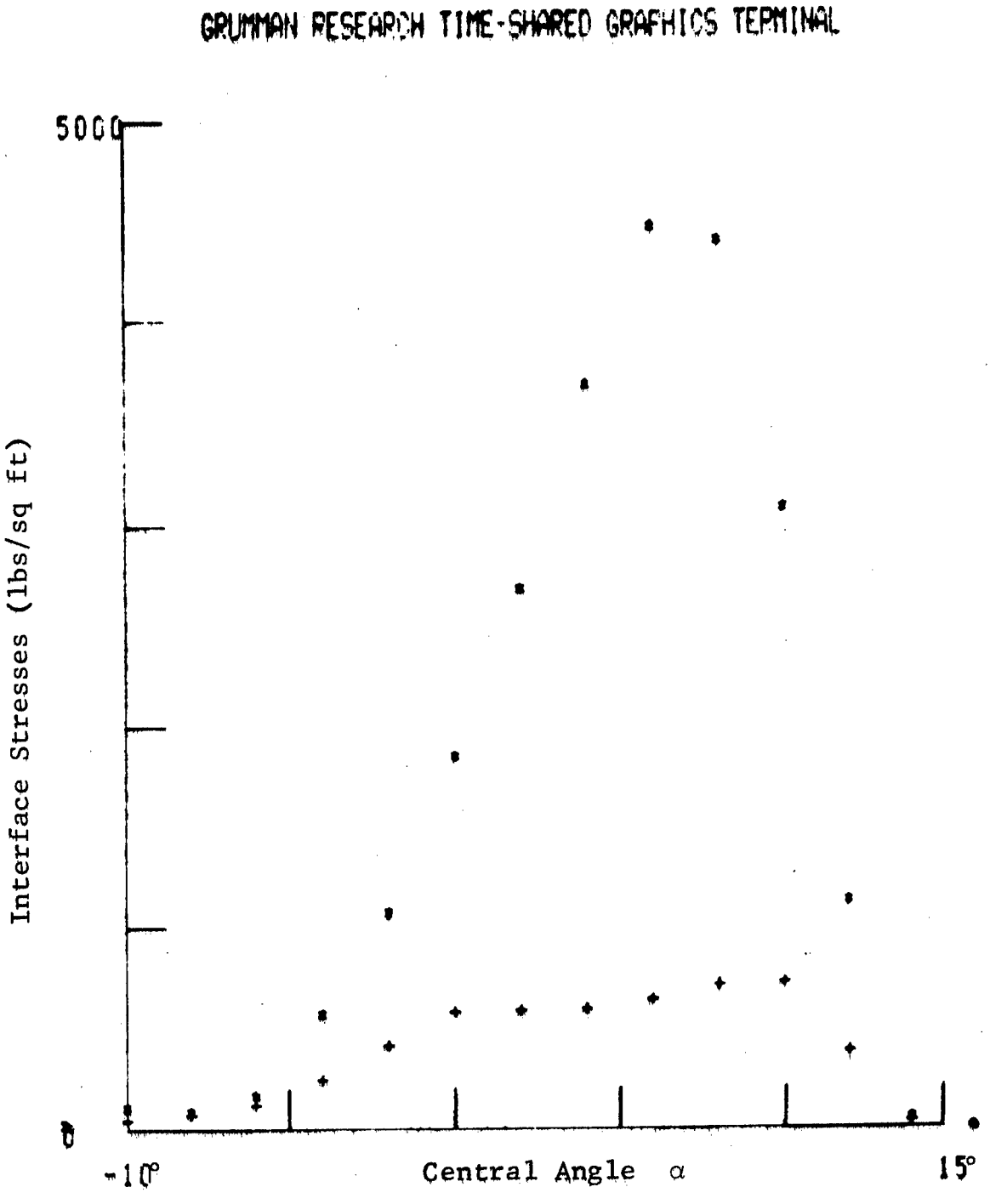

Fig. 67 Run #124 Average Interface Normal and Shear Stresses Measured in Dense Sand
Load = 336 lbs, Drawbar Pull = 42 lbs,
Torque = 83 ft lbs

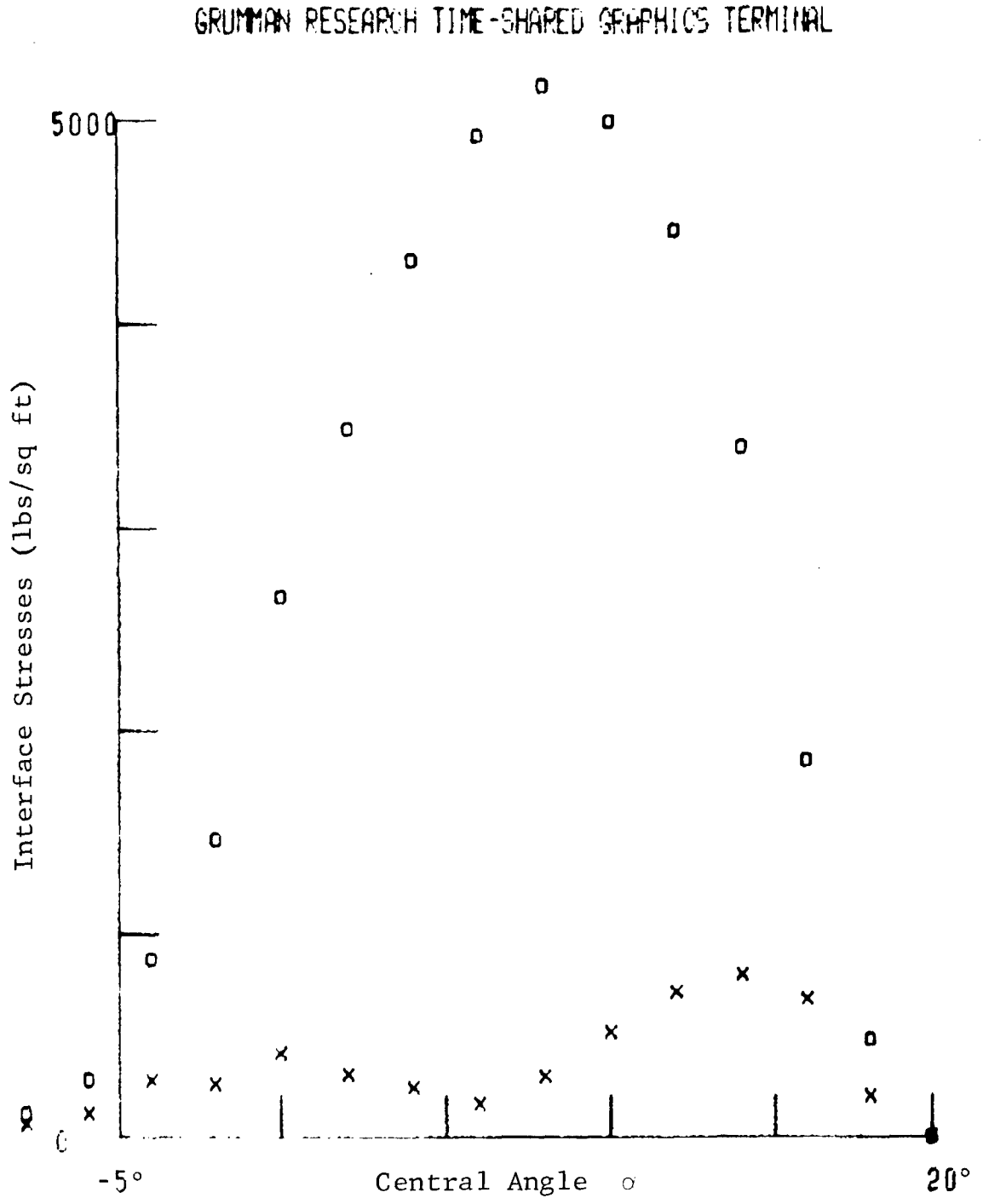

Fig. 68 Run #126 Average Interface Normal and Shear Stresses Measured in Dense Sand
Load = 550 lbs, Drawbar Pull = 1 lb,
Torque = 79 ft lbs

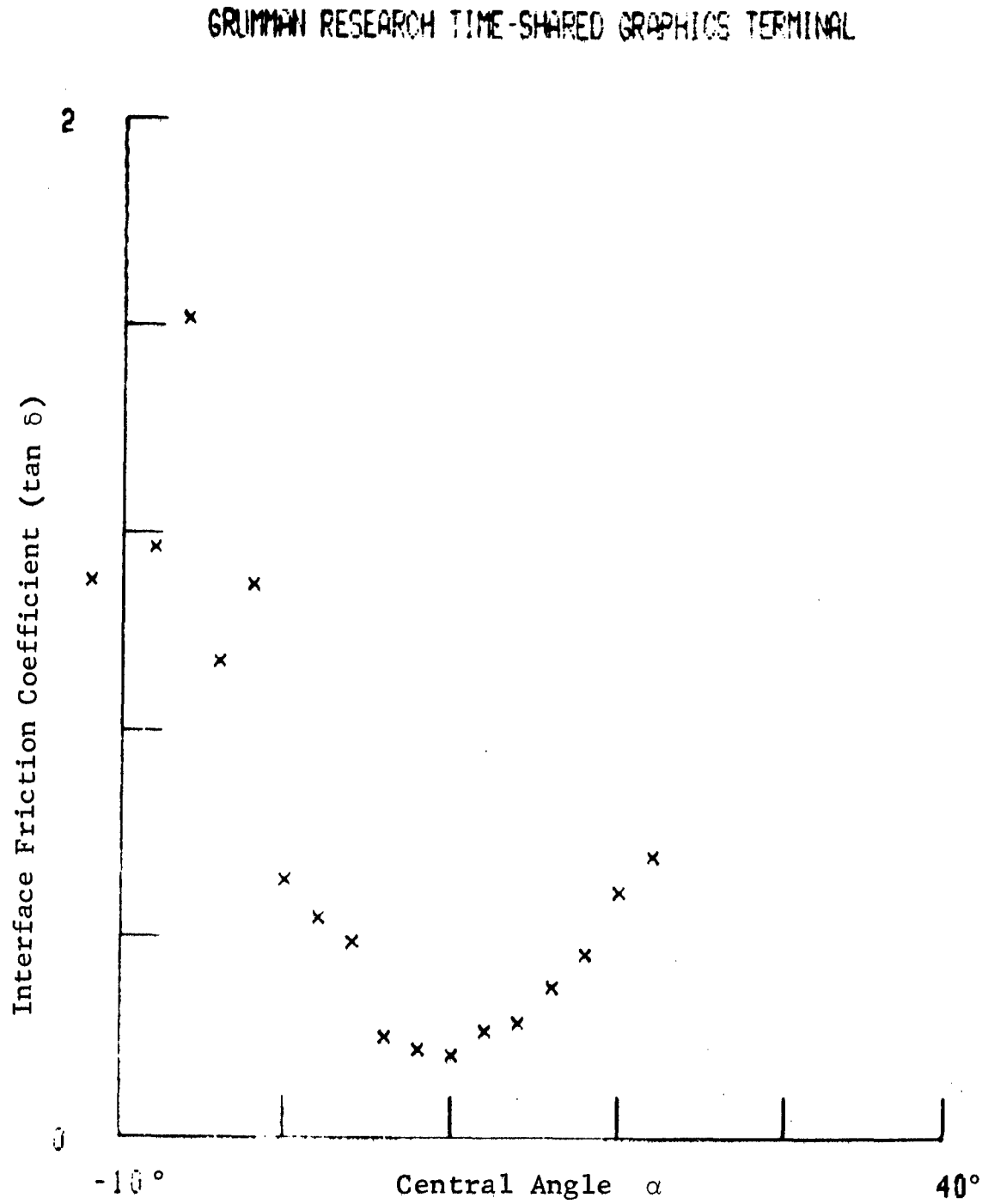

Fig. 69 Run #107 Variation of Interface Friction Coefficient (tan δ) Along the Interface in Dense Sand
Load = 480 lbs, Drawbar Pull = 51 lbs,
Torque = 158 ft lbs

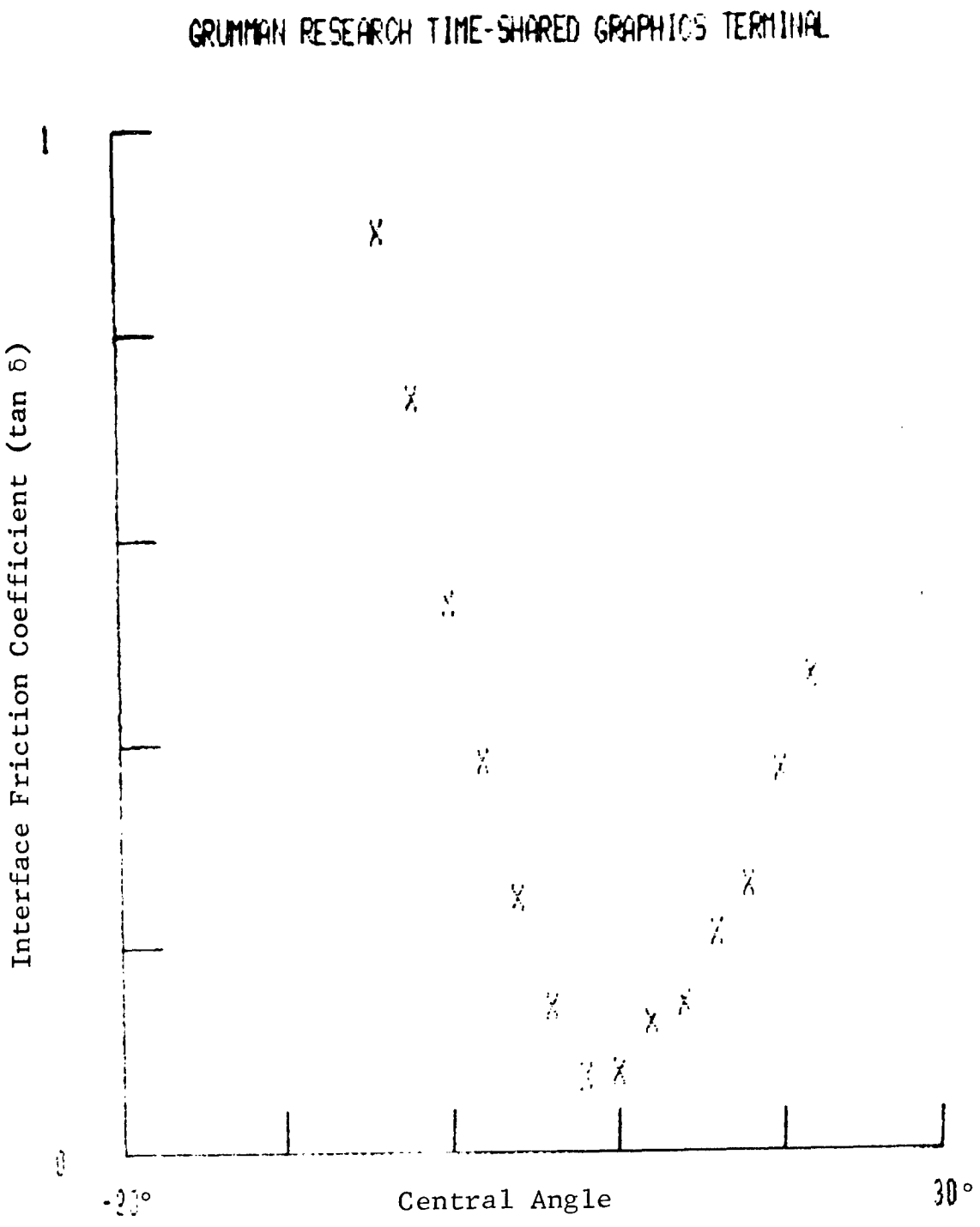

Fig. 72 Run #110 Variation of Interface Friction Coefficient (tan δ) Along the Interface in Dense Sand Load = 481 lbs, Drawbar Pull = 10 lbs, Torque = 118 ft lbs

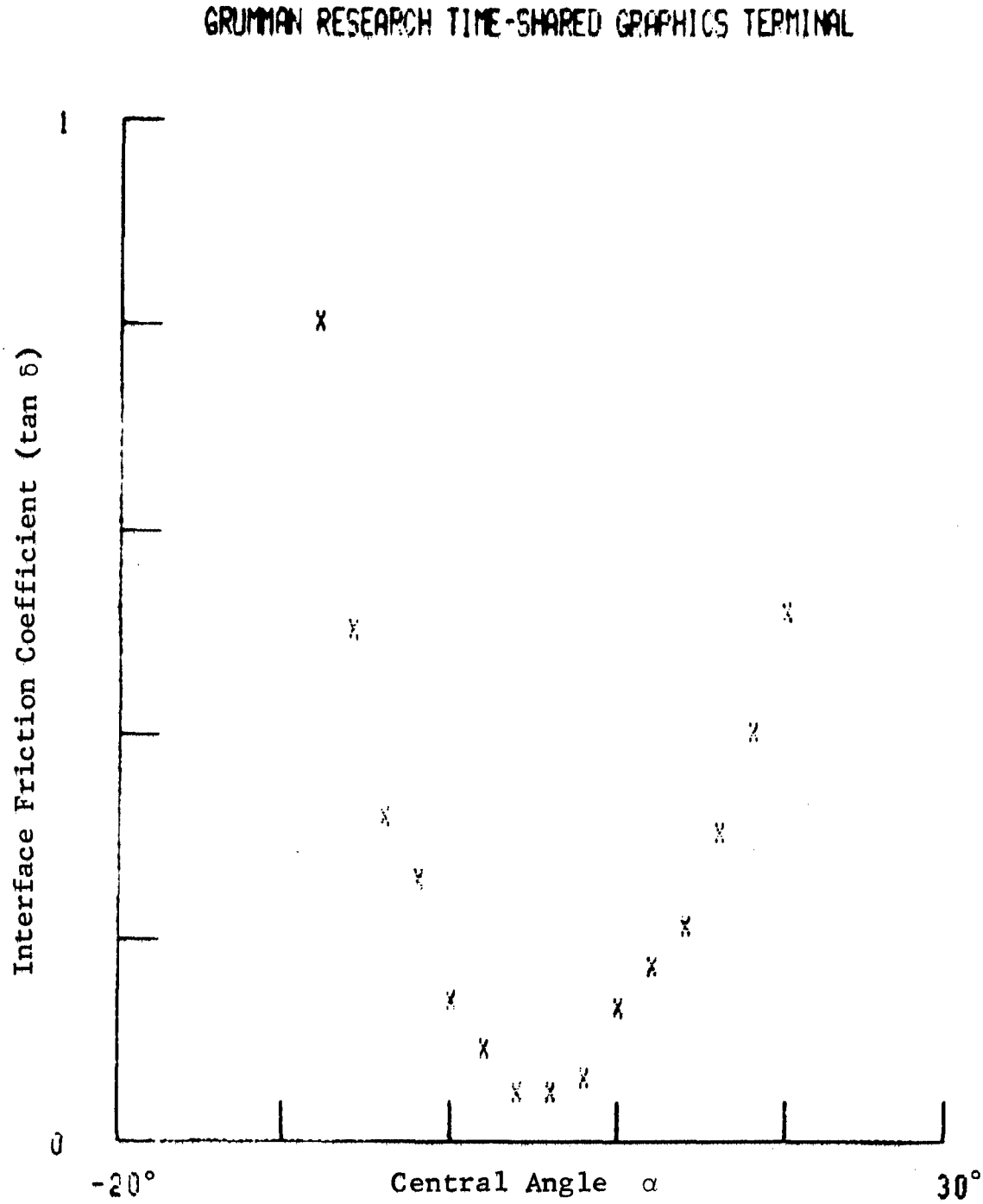

Fig. 73 Run #111 Variation of Interface Friction Coefficient (tan δ) Along the Interface in Dense Sand Load = 535 lbs, Drawbar Pull = 15 lbs, Torque = 100 ft lbs

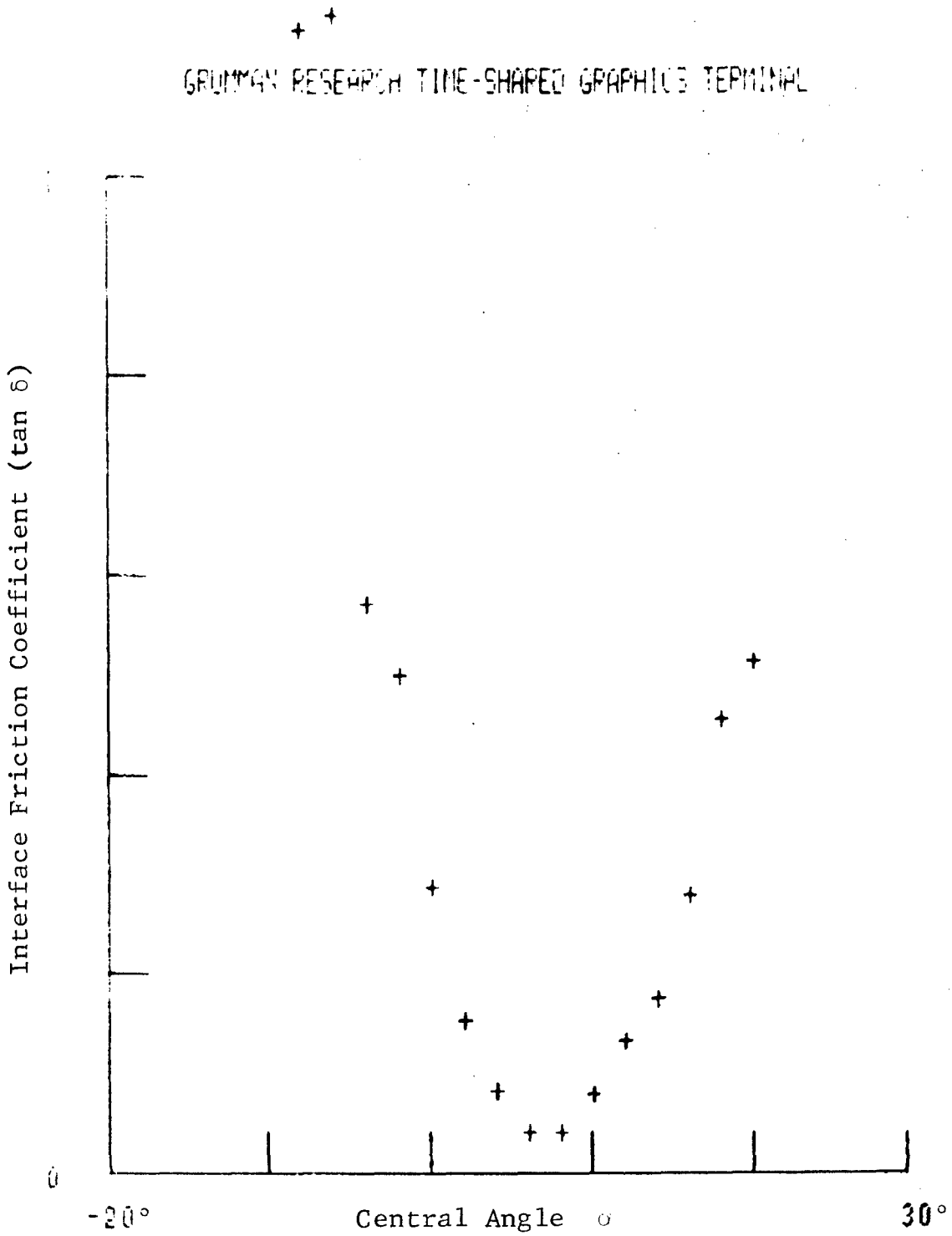

Fig. 74 Run #112 Variation of Interface Friction Coefficient (tan δ) Along the Interface in Dense Sand
Load = 576 lbs, Drawbar Pull = 2 lbs,
Torque = 105 ft lbs

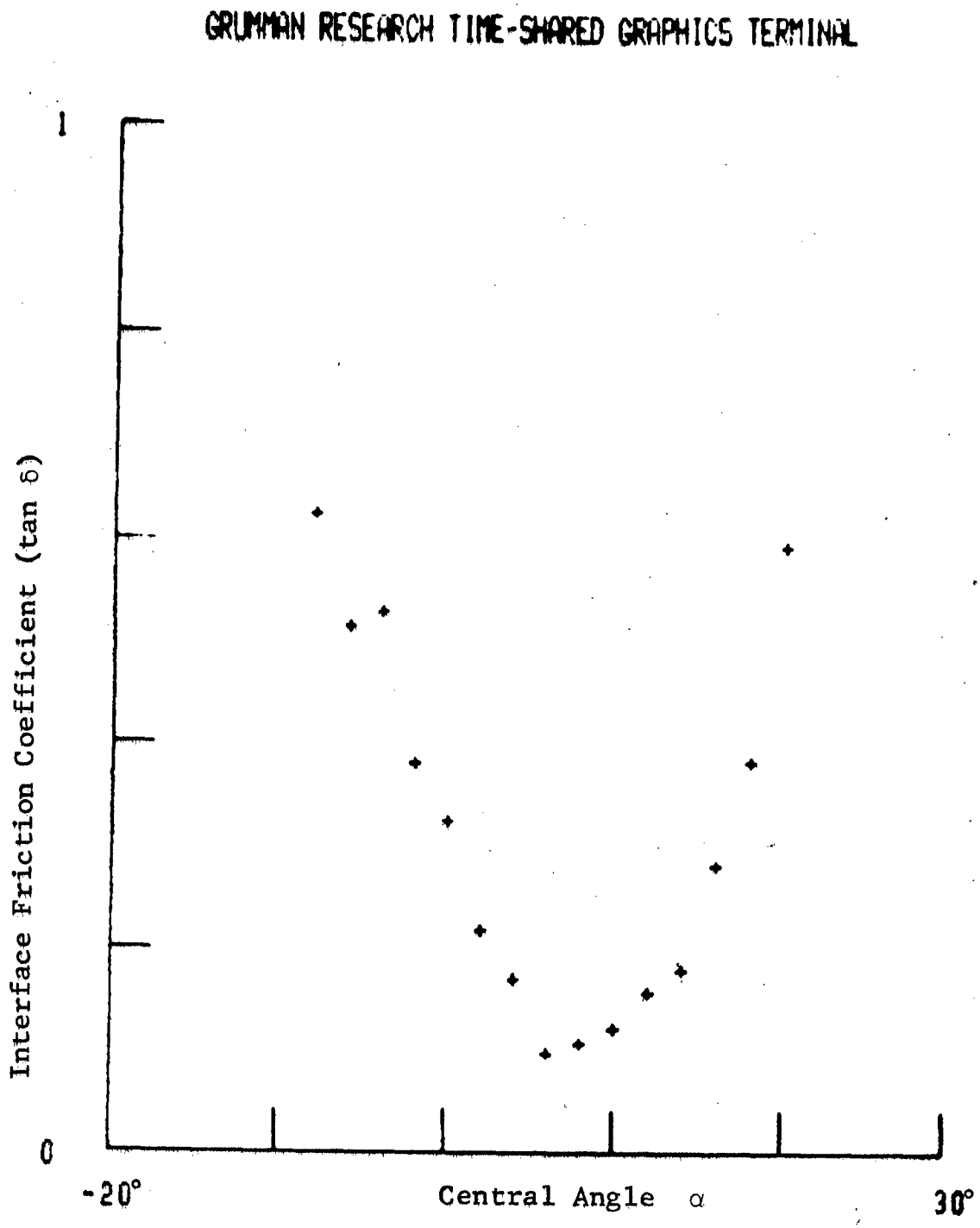

Fig. 75 Run #113 Variation of Interface Friction Coefficient (tan δ) Along the Interface in Dense Sand Load = 535 lbs, Drawbar Pull = 25 lbs, Torque = 124 ft lbs

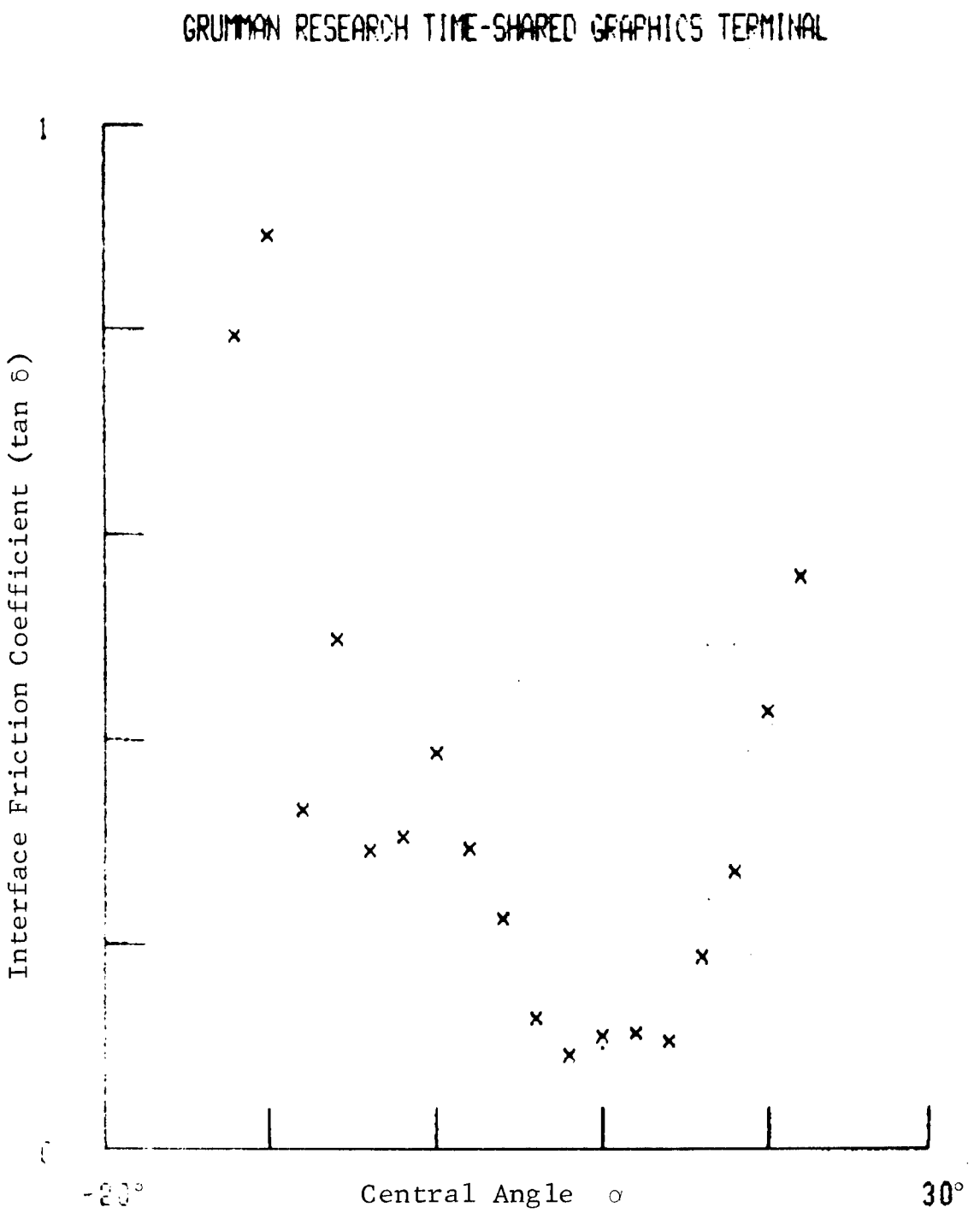

Fig. 76 Run #114 Variation of Interface Friction Coefficient (tan δ) Along the Interface in Dense Sand Load = 576 lbs, Drawbar Pull = 2 lbs, Torque = 127 ft lbs

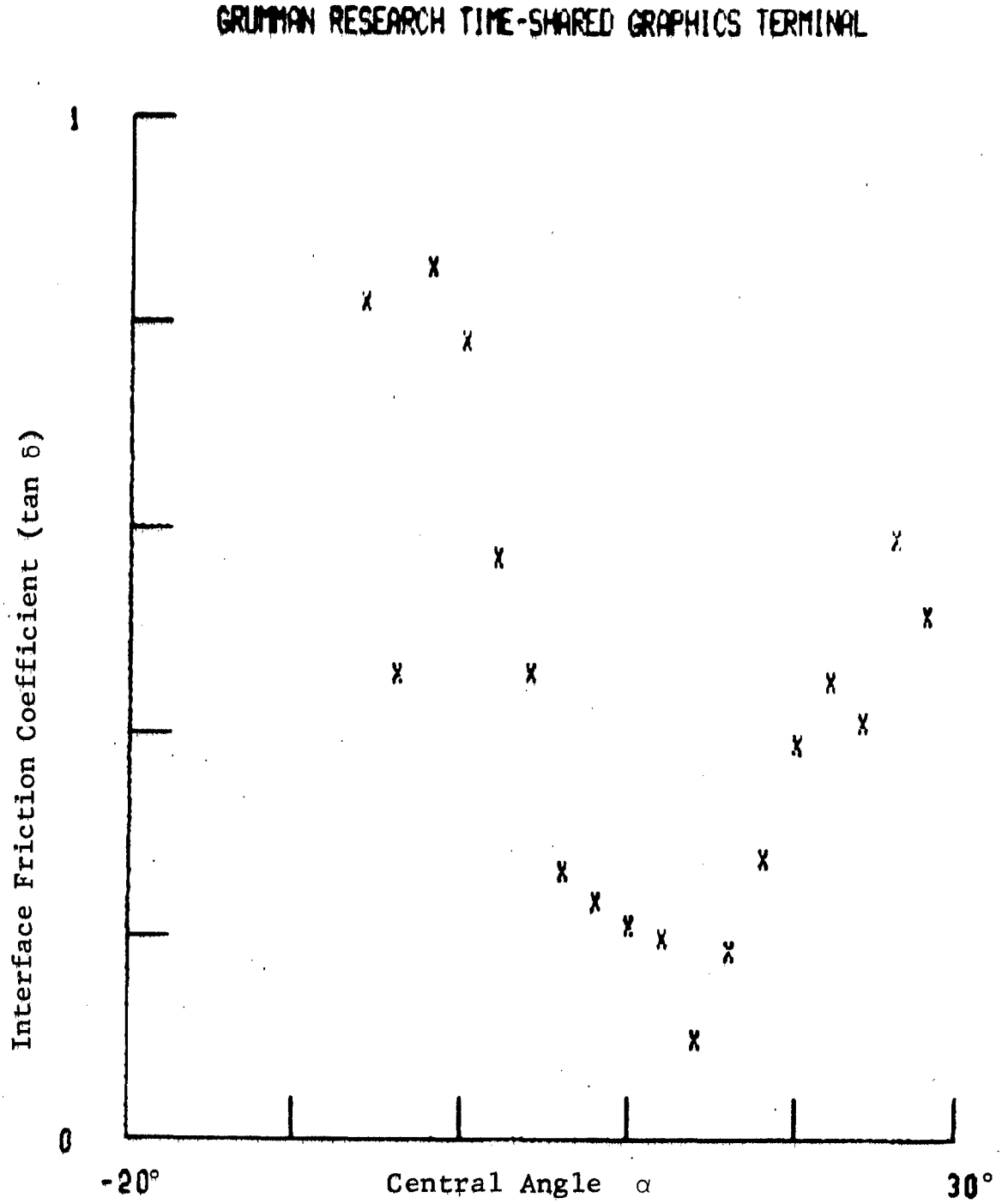

Fig. 77 Run #115 Variation of Interface Friction Coefficient (tan δ) Along the Interface in Dense Sand
Load = 513 lbs, Drawbar Pull = 41 lbs,
Torque = 174 ft lbs

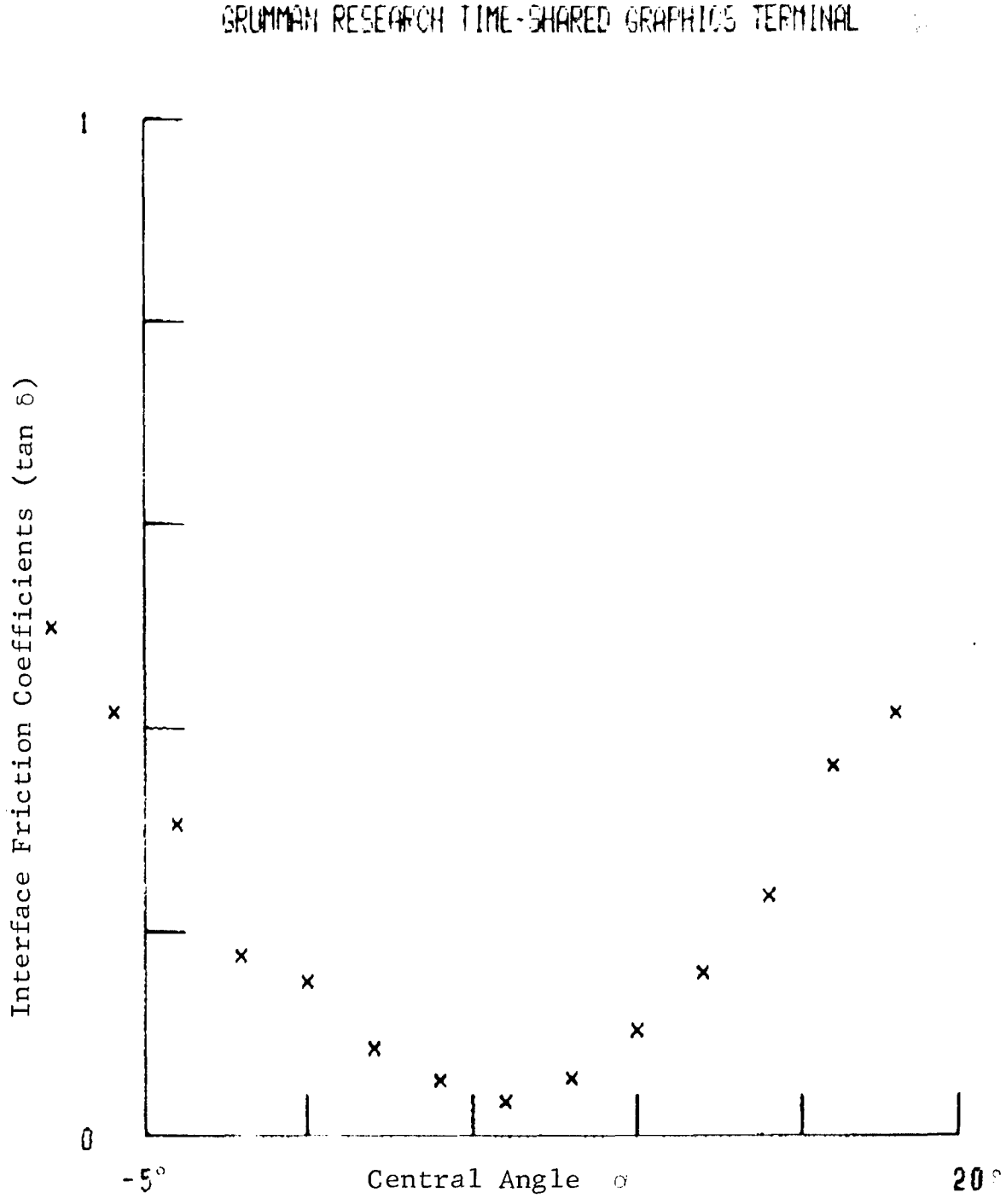

Fig. 78 Run #126 Variation of Interface Friction Coefficient (tan δ) Along the Interface in Dense Sand
Load = 550 lbs, Drawbar Pull = 1 lb,
Torque = 79 ft lbs

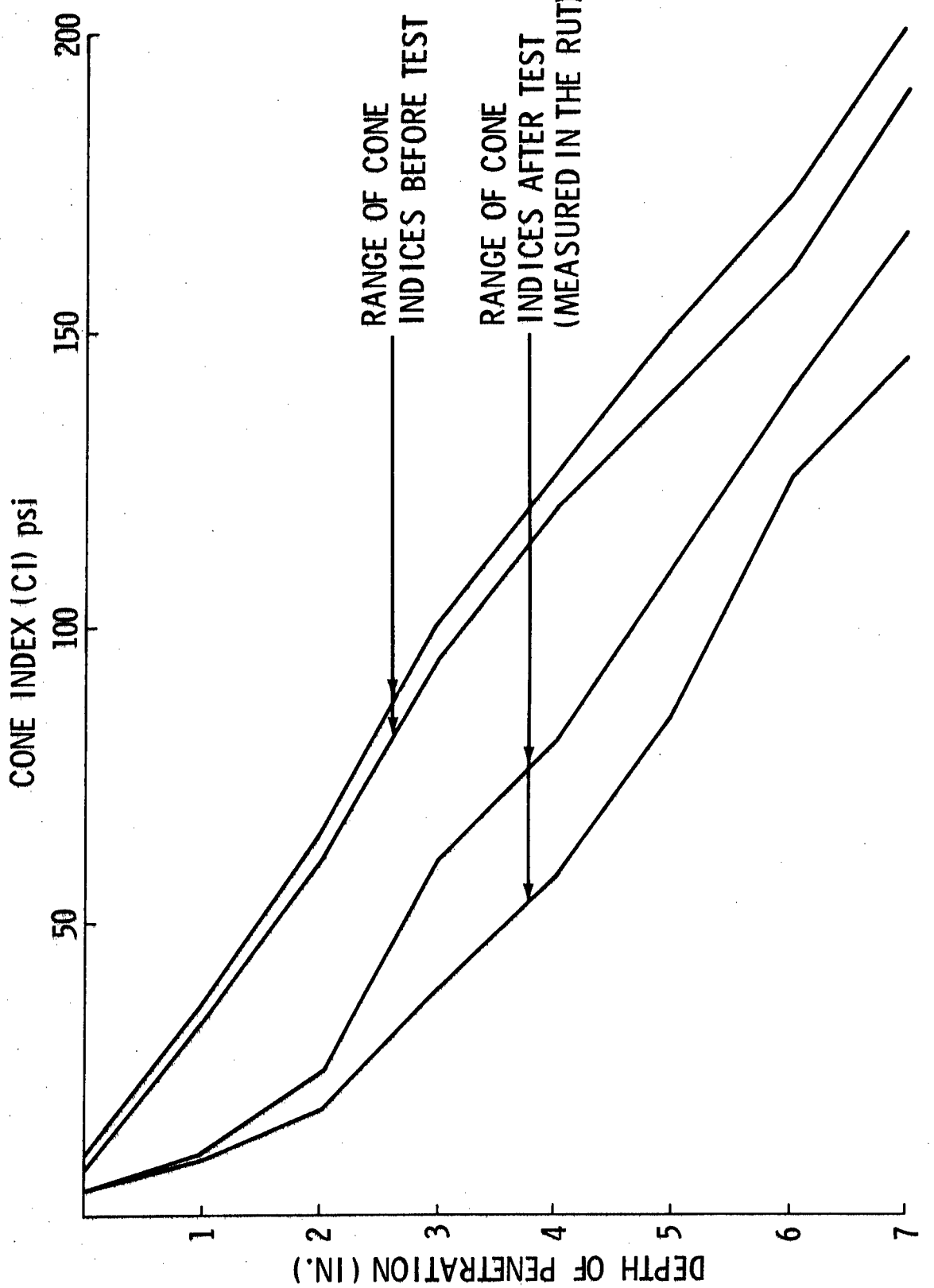

Fig. 79 Results of Cone Penetrometer Tests in Dense Sand for Run #98

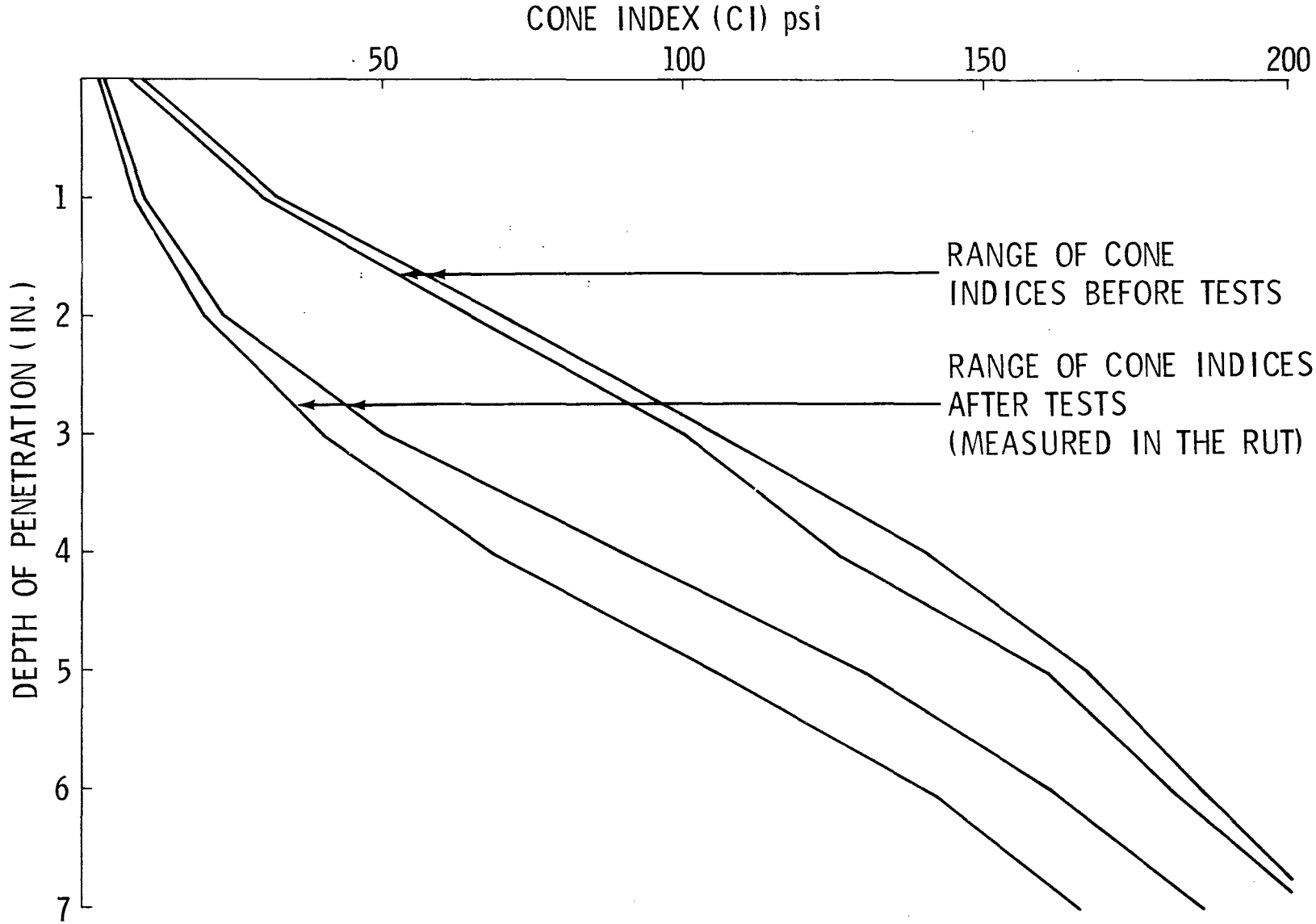

Fig. 80 Results of Cone Penetrometer Tests in Dense Sand for Runs #107-111

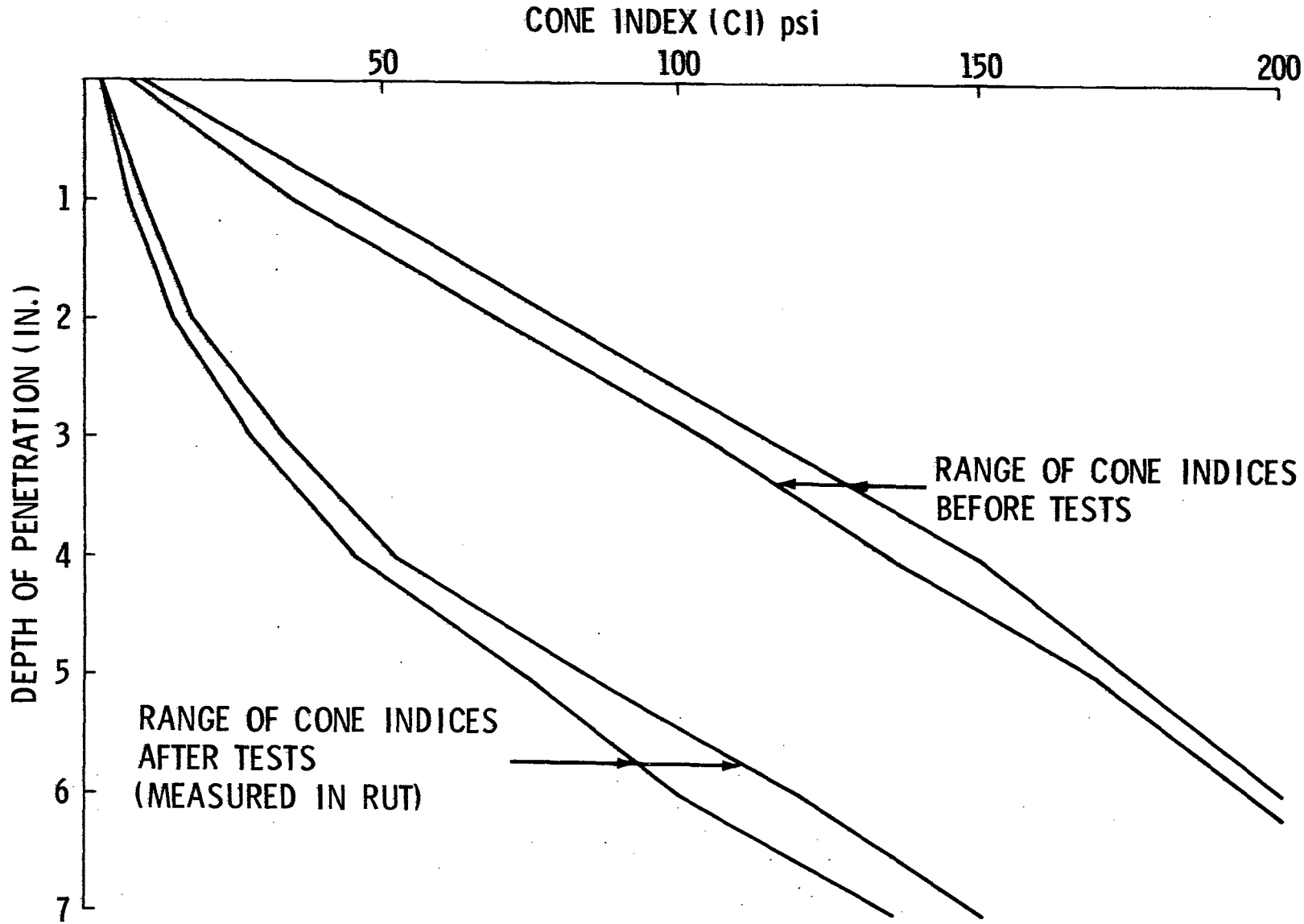

Fig. 81 Results of Cone Penetrometer Tests in Dense Sand for Runs #112-126

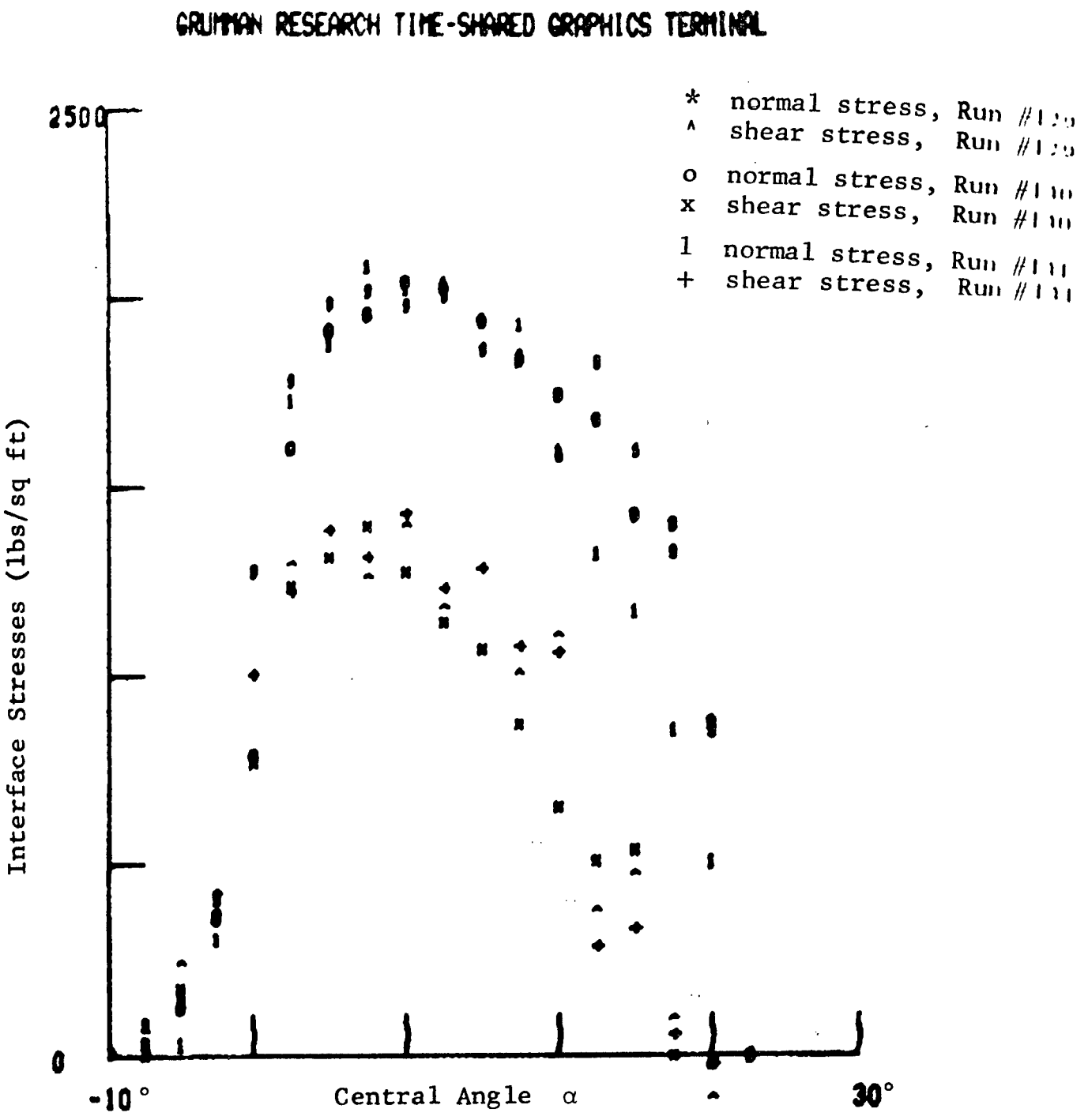

Fig. 82 Run #129-131 Average Interface Normal and Shear Stresses Measured in Loam
Run #129: Load = 336 lbs, Drawbar Pull = 126 lbs, Torque = 203 ft lbs
Run #130: Load = 322 lbs, Drawbar Pull = 111 lbs, Torque = 185 ft lbs
Run #131: Load = 310 lbs, Drawbar Pull = 130 lbs, Torque = 199 ft lbs

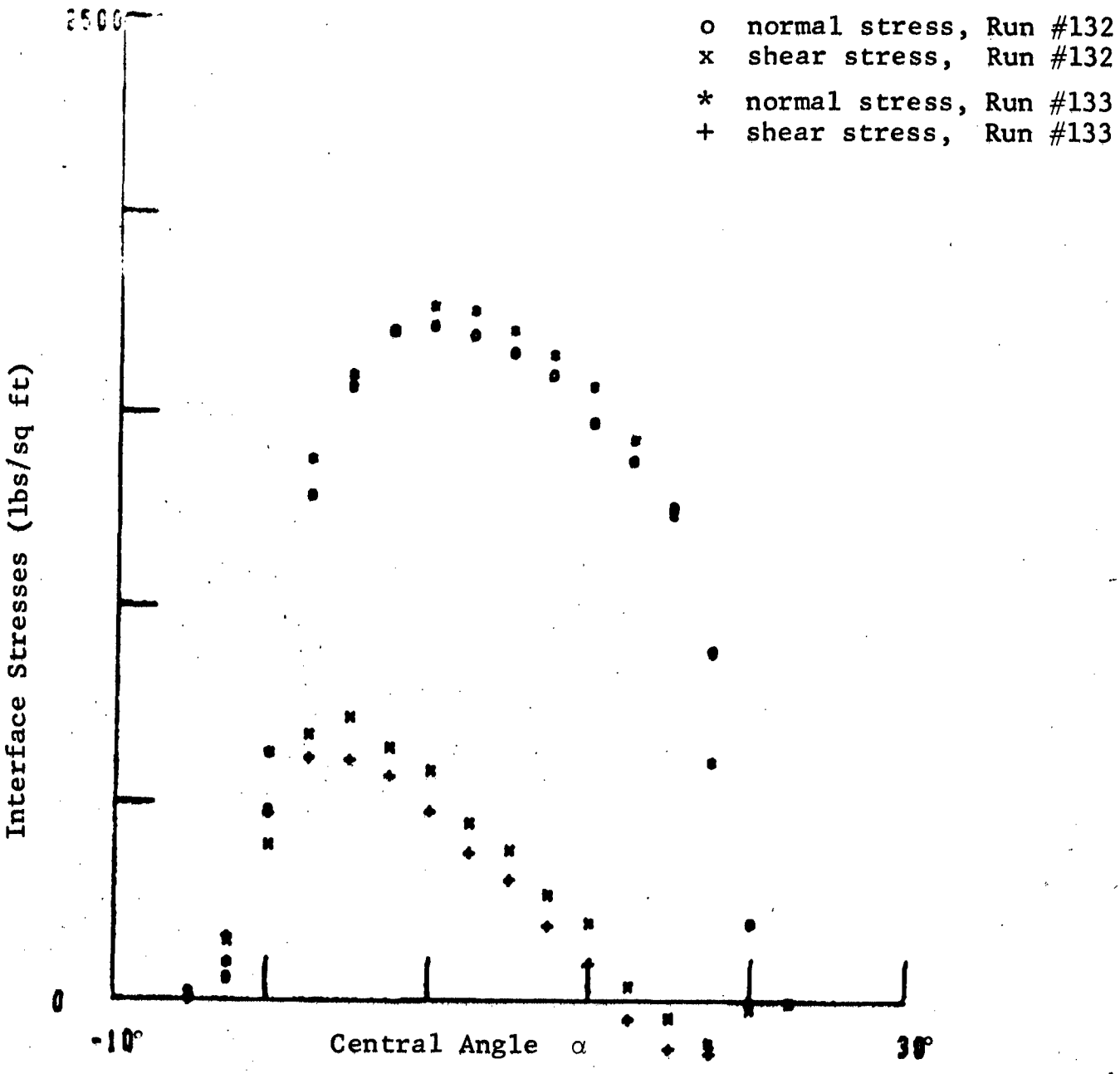

Fig. 83 Run #132-133 Average Interface Normal and Shear Stresses Measured in Loam
Run #132: Load = 244 lbs, Drawbar Pull = 24 lbs, Torque = 72 ft lbs
Run #133: Load = 244 lbs, Drawbar Pull = 14 lbs, Torque = 59 ft lbs

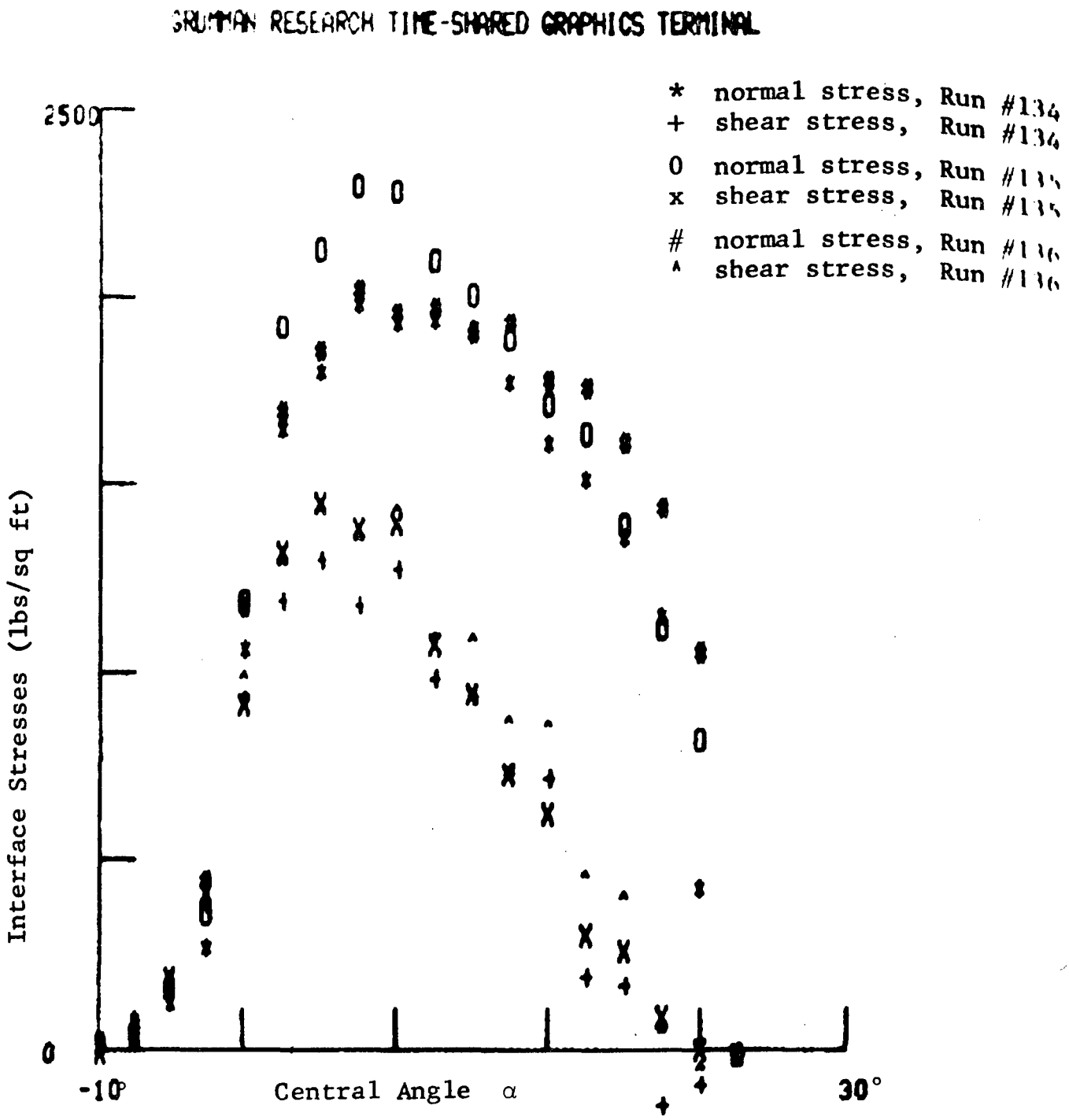

Fig. 84 Run #134-136 Average Interface Normal and Shear Stresses Measured in Loam

Run #134: Load = 303 lbs, Drawbar Pull = 100 lbs, Torque = 166 ft lbs

Run #135: Load = 340 lbs, Drawbar Pull = 111 lbs, Torque = 185 ft lbs

Run #136: Load = 336 lbs, Drawbar Pull = 114 lbs, Torque = 192 ft lbs

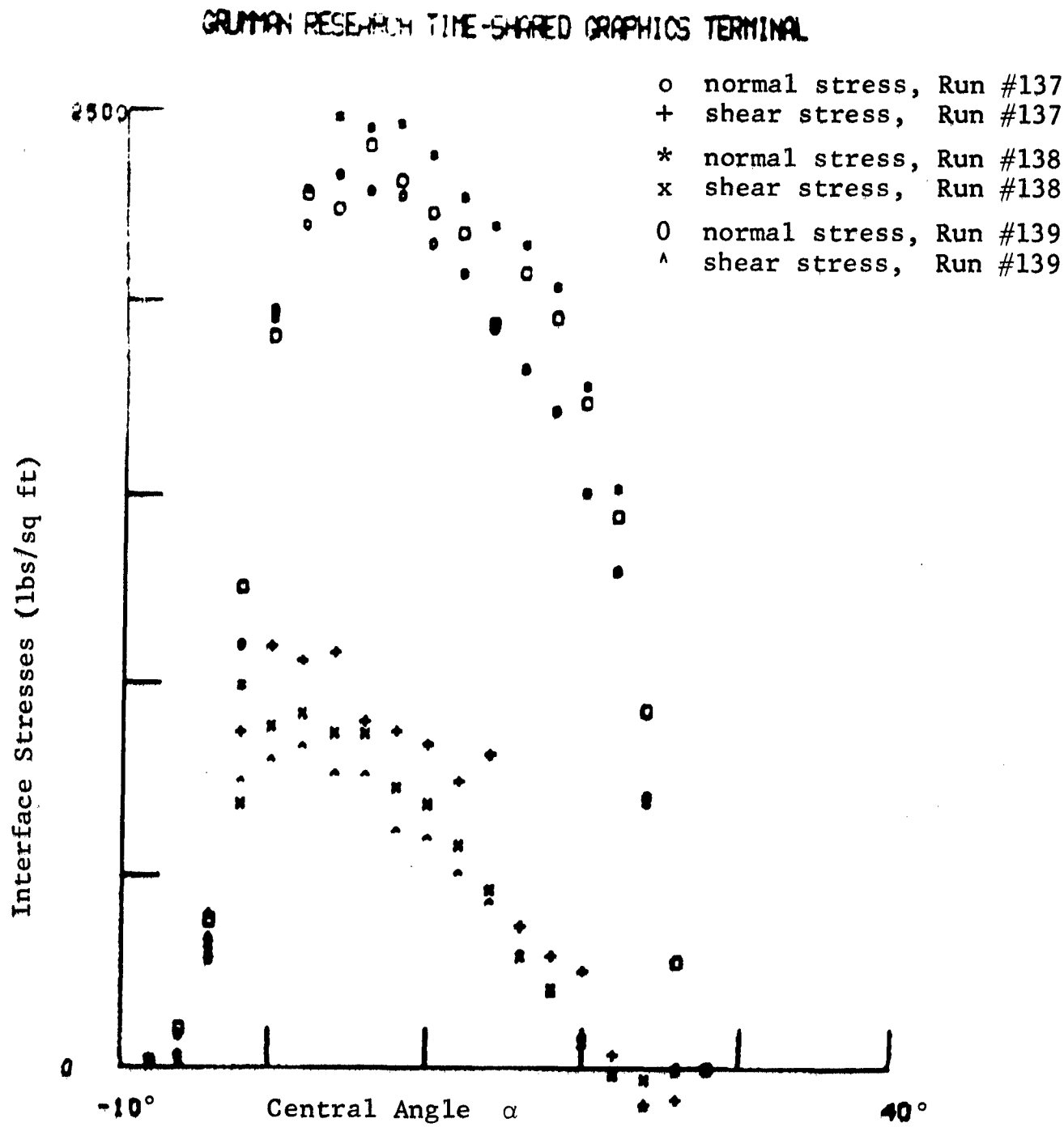

Fig. 85 Run #137-139 Average Interface Normal and Shear Stresses Measured in Loam

Run #137: Load = 401 lbs, Drawbar Pull = 66 lbs, Torque = 157 ft lbs

Run #138: Load = 404 lbs, Drawbar Pull = 39 lbs, Torque = 125 ft lbs

Run #139: Load = 370 lbs, Drawbar Pull = 34 lbs, Torque = 111 ft lbs

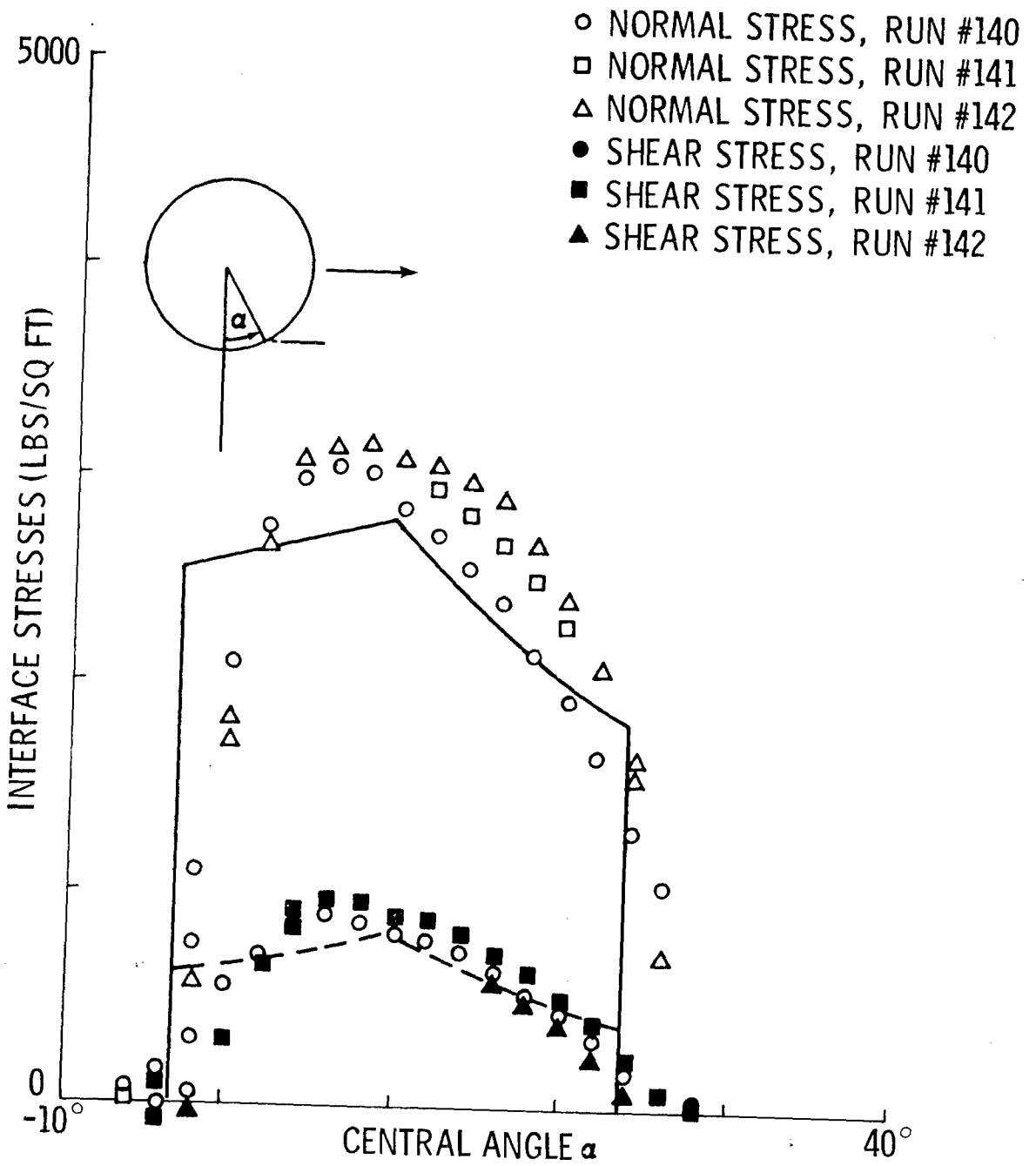

Fig. 86 Run #140-142 Measured and Predicted Average Interface Normal and Shear Stresses in Loam

Run #140: Load = 490 lbs, Drawbar Pull = 33 lbs, Torque = 141 ft lbs

Run #141: Load = 527 lbs, Drawbar Pull = 25 lbs, Torque = 149 ft lbs

Run #142: Load = 519 lbs, Drawbar Pull = 0 lb, Torque = 118 ft lbs

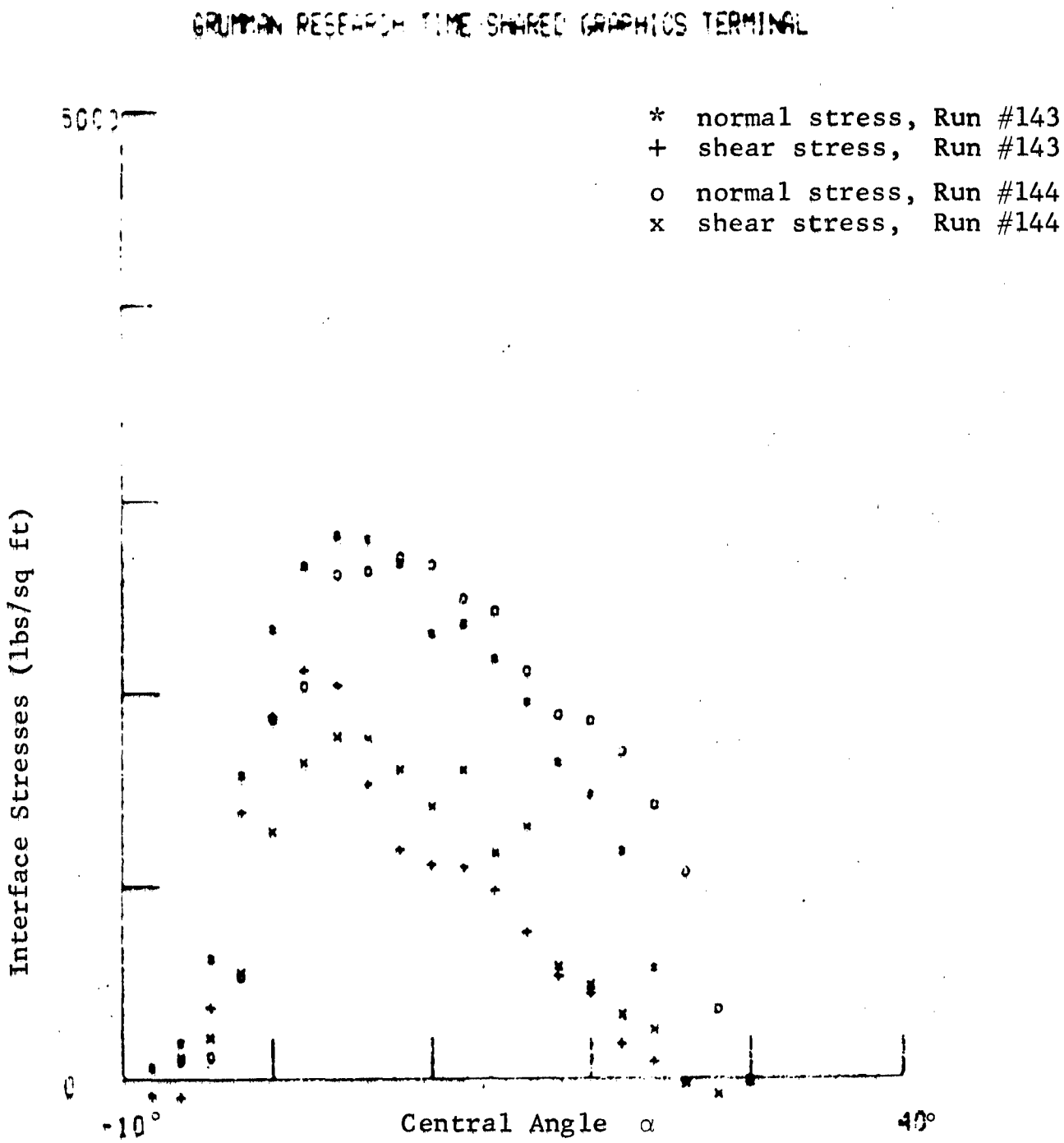

Fig. 87 Run #143-144 Average Interface Normal and Shear Stresses Measured in Loam
Run #143: Load = 441 lbs, Drawbar Pull = 158 lbs, Torque = 251 ft lbs
Run #144: Load = 461 lbs, Drawbar Pull = 140 lbs, Torque = 226 ft lbs

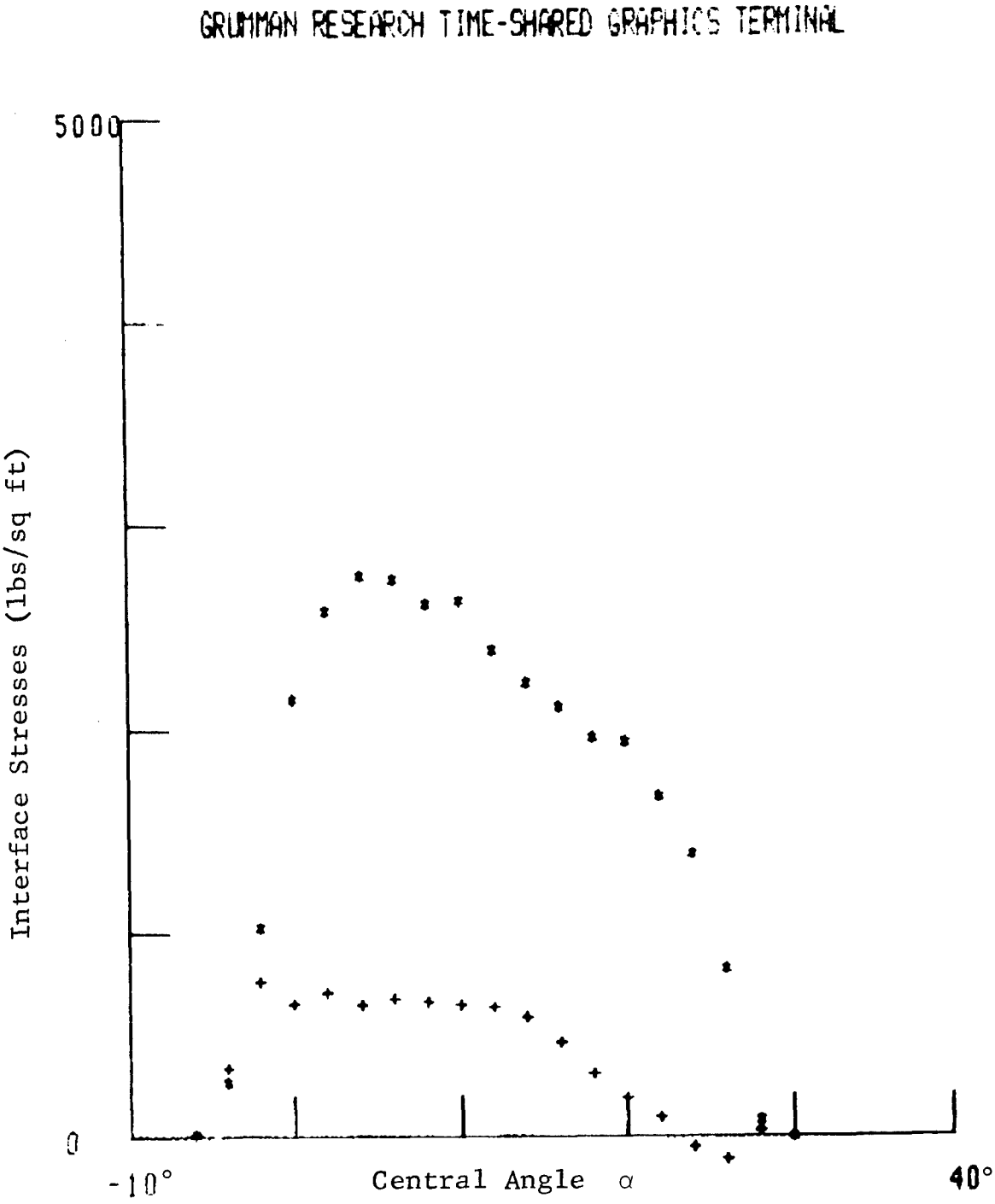

Fig. 88 Run #145 Average Interface Normal and Shear Stresses Measured in Loam
Load = 454 lbs, Drawbar Pull = 20 lbs,
Torque = 121 ft lbs

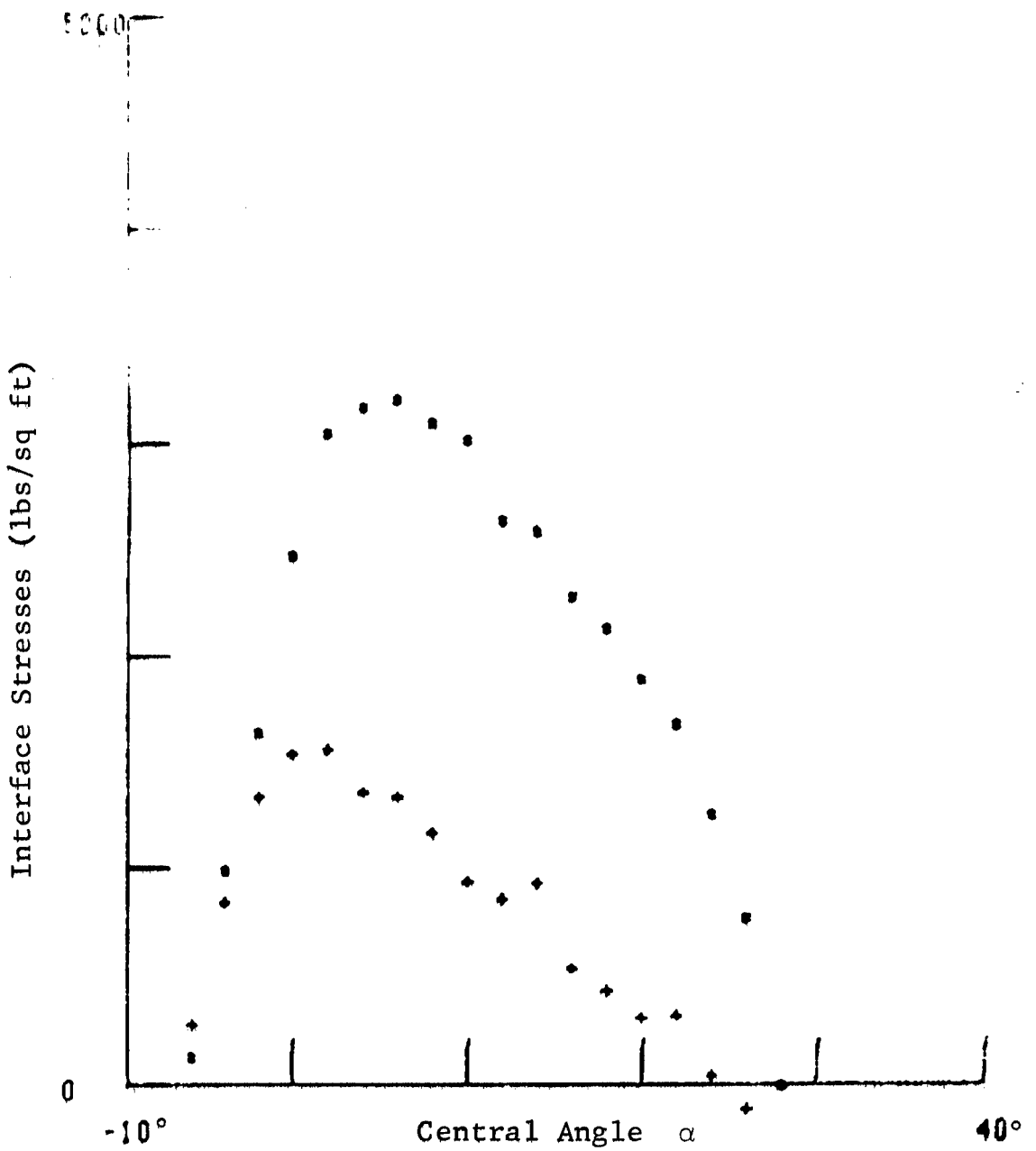

Fig. 89 Run #146 Average Interface Normal and Shear Stresses Measured in Loam
Load = 531 lbs, Drawbar Pull = 107 lbs,
Torque = 226 ft lbs

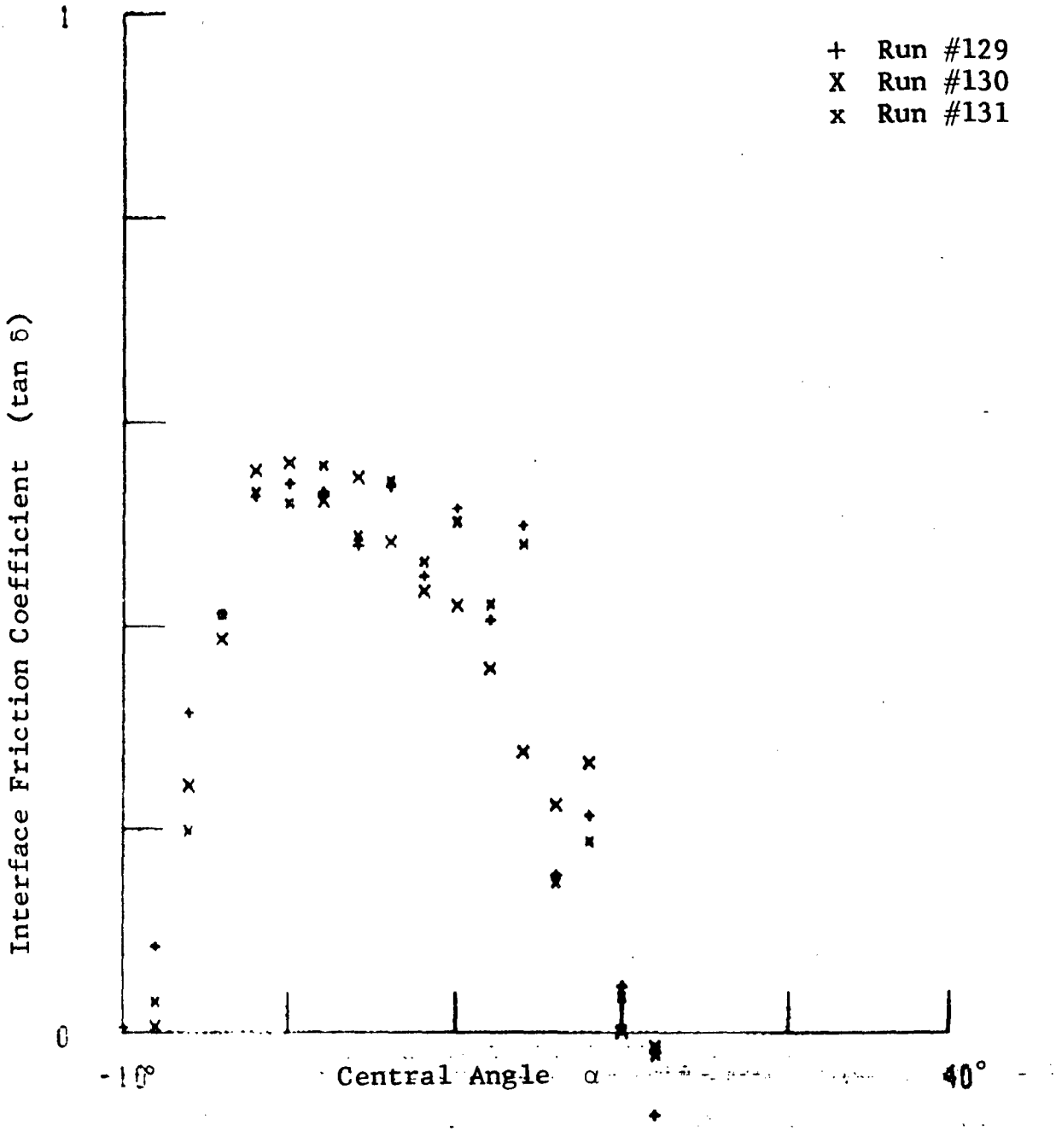

Fig. 90 Run #129-131 Variation of Interface Friction Coefficient (tan δ) Along the Interface in Loam
Run #129: Load = 336 lbs, Drawbar Pull = 126 lbs, Torque = 203 ft lbs
Run #130: Load = 322 lbs, Drawbar Pull = 111 lbs, Torque = 185 ft lbs
Run #131: Load = 310 lbs, Drawbar Pull = 130 lbs, Torque = 199 ft lbs

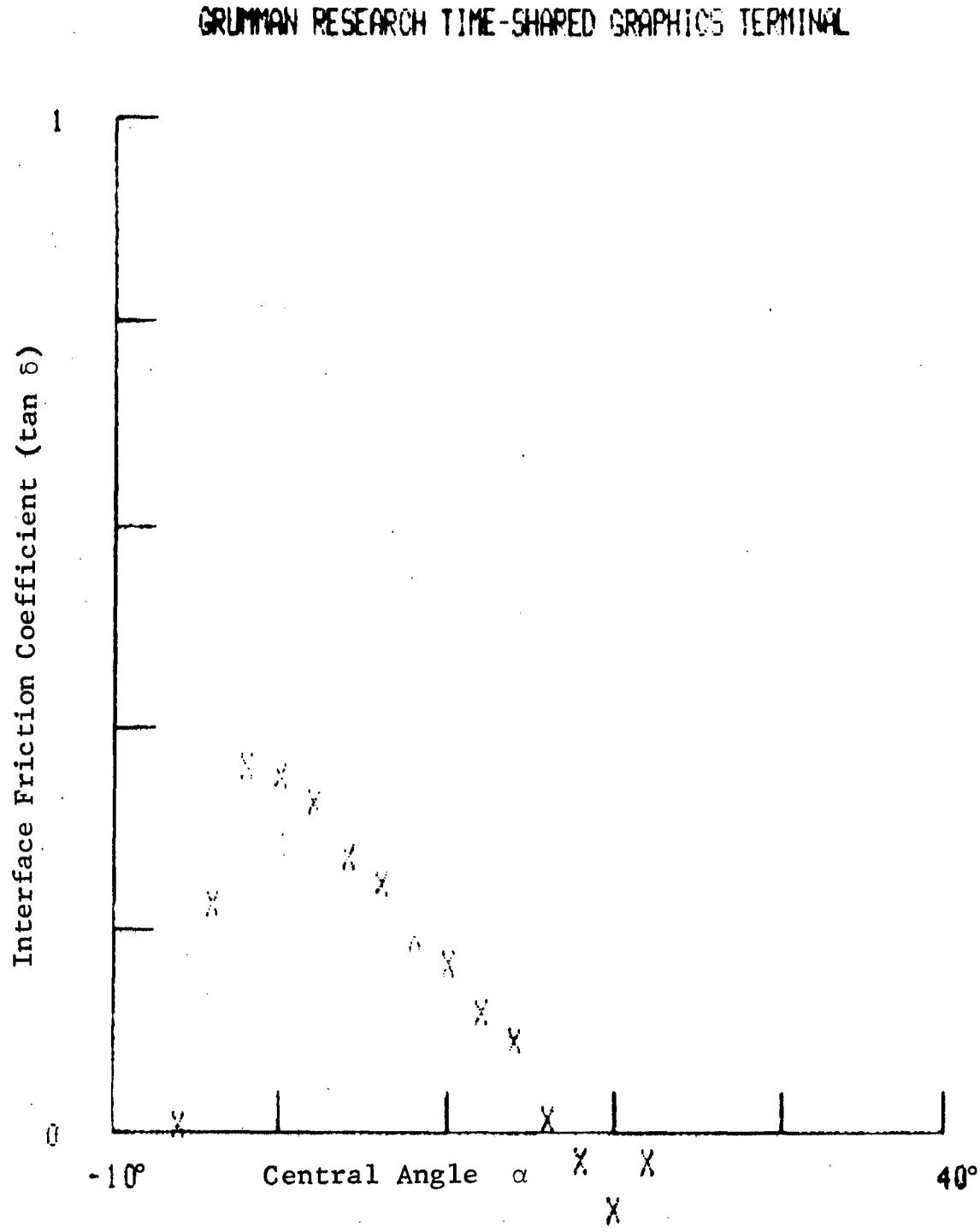

Fig. 91 Run #132 Variation of Interface Friction Coefficient (tan δ) Along the Interface in Loam
Load = 244 lbs, Drawbar Pull = 24 lbs,
Torque = 72 ft lbs

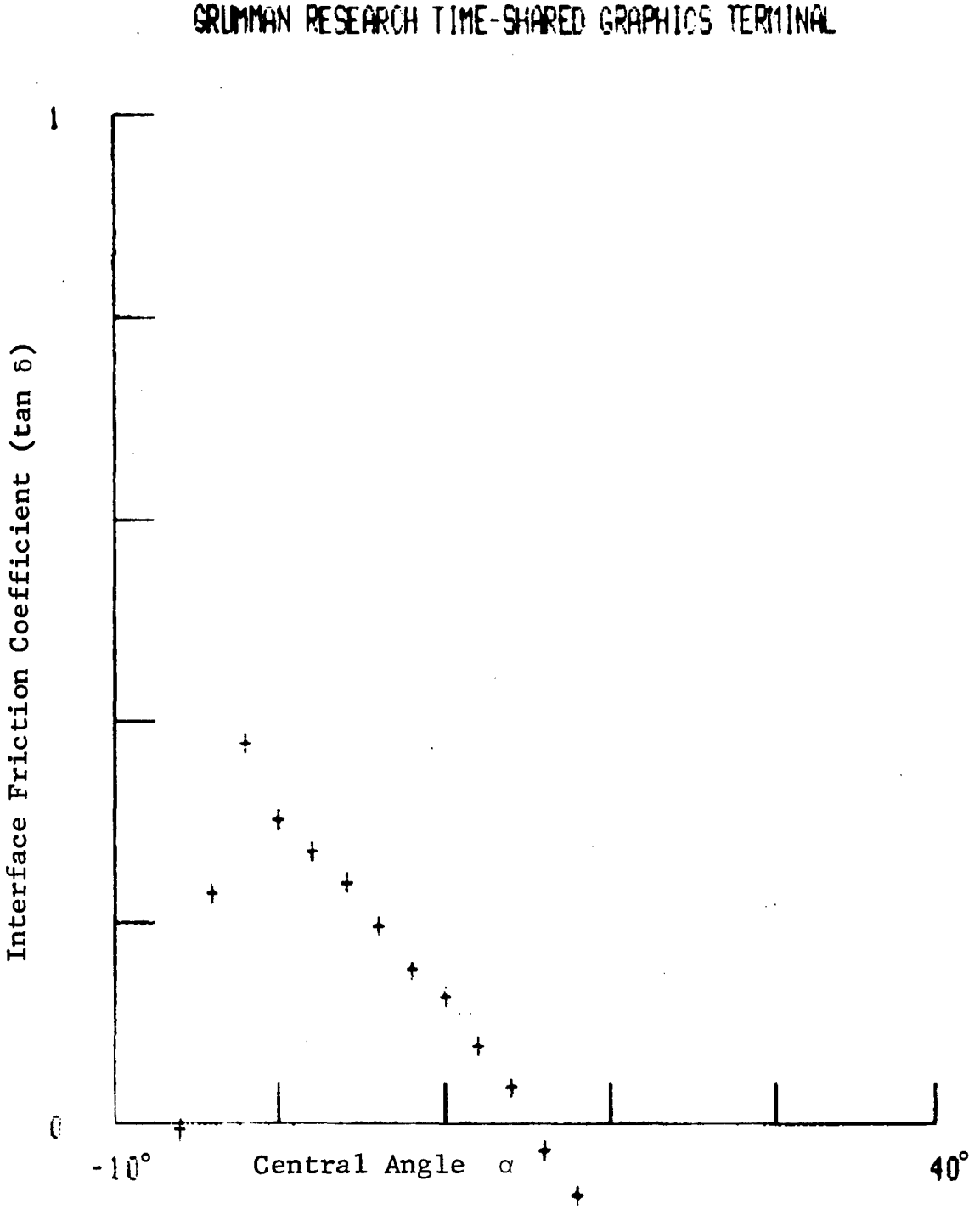

Fig. 92 Run #133 Variation of Interface Friction Coefficient (tan δ) Along the Interface in Loam
Load = 244 lbs, Drawbar Pull = 14 lbs,
Torque = 59 ft lbs

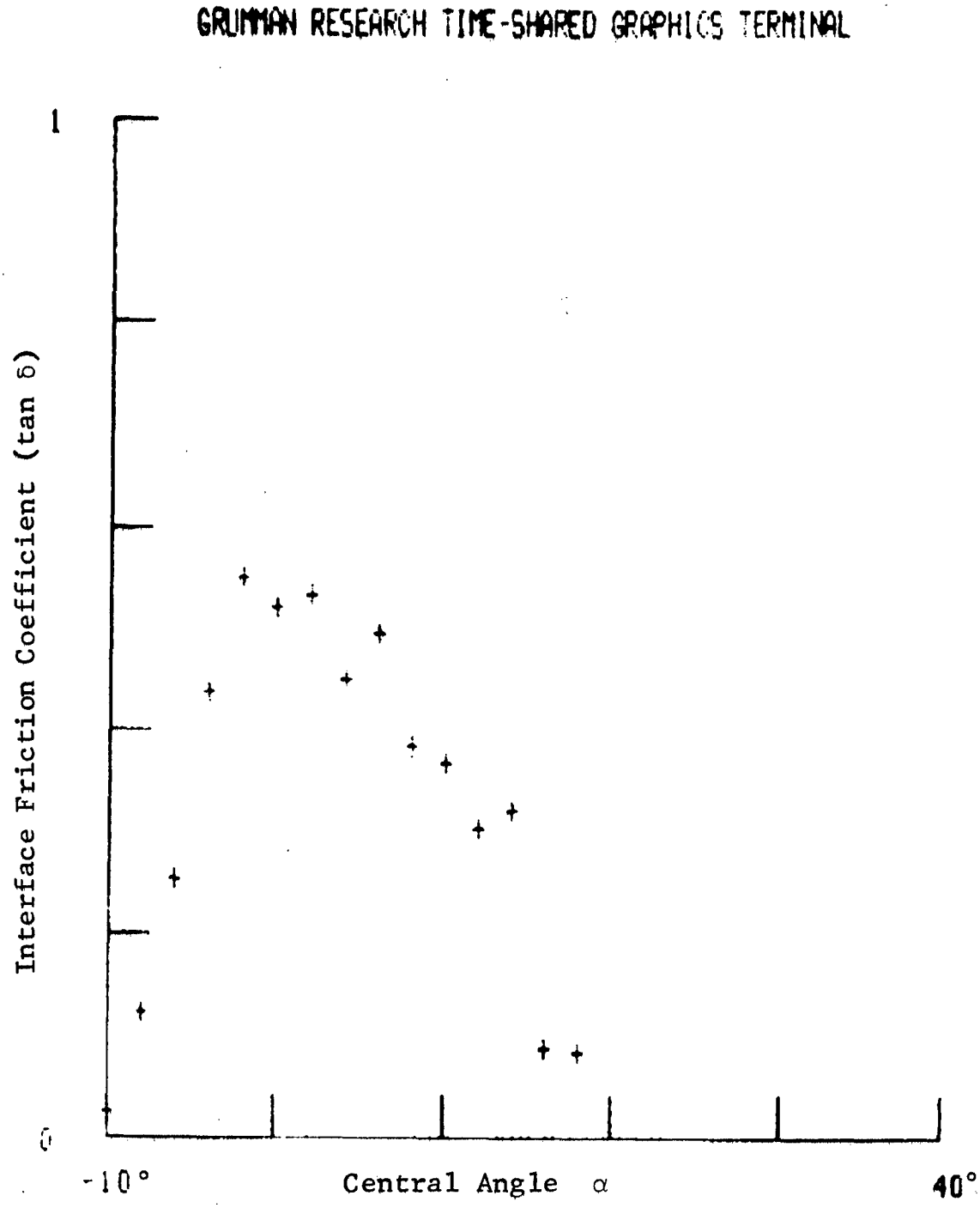

Fig. 93 Run #134 Variation of Interface Friction Coefficient (tan δ) Along the Interface in Loam
Load = 303 lbs, Drawbar Pull = 100 lbs,
Torque = 166 ft lbs

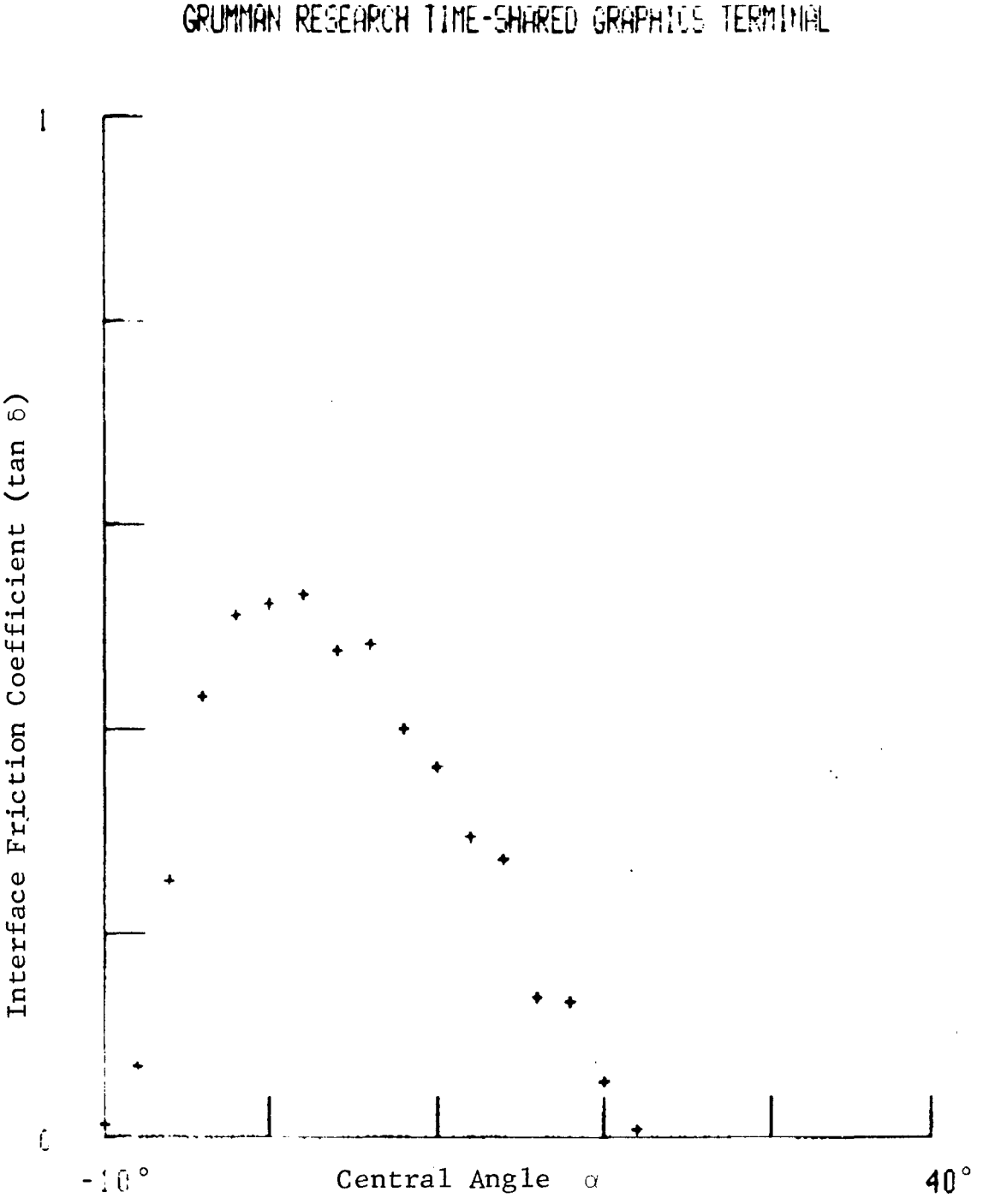

Fig. 94 Run #135 Variation of Interface Friction Coefficient (tan δ) Along the Interface in Loam
Load = 340 lbs, Drawbar Pull = 111 lbs,
Torque = 185 ft lbs

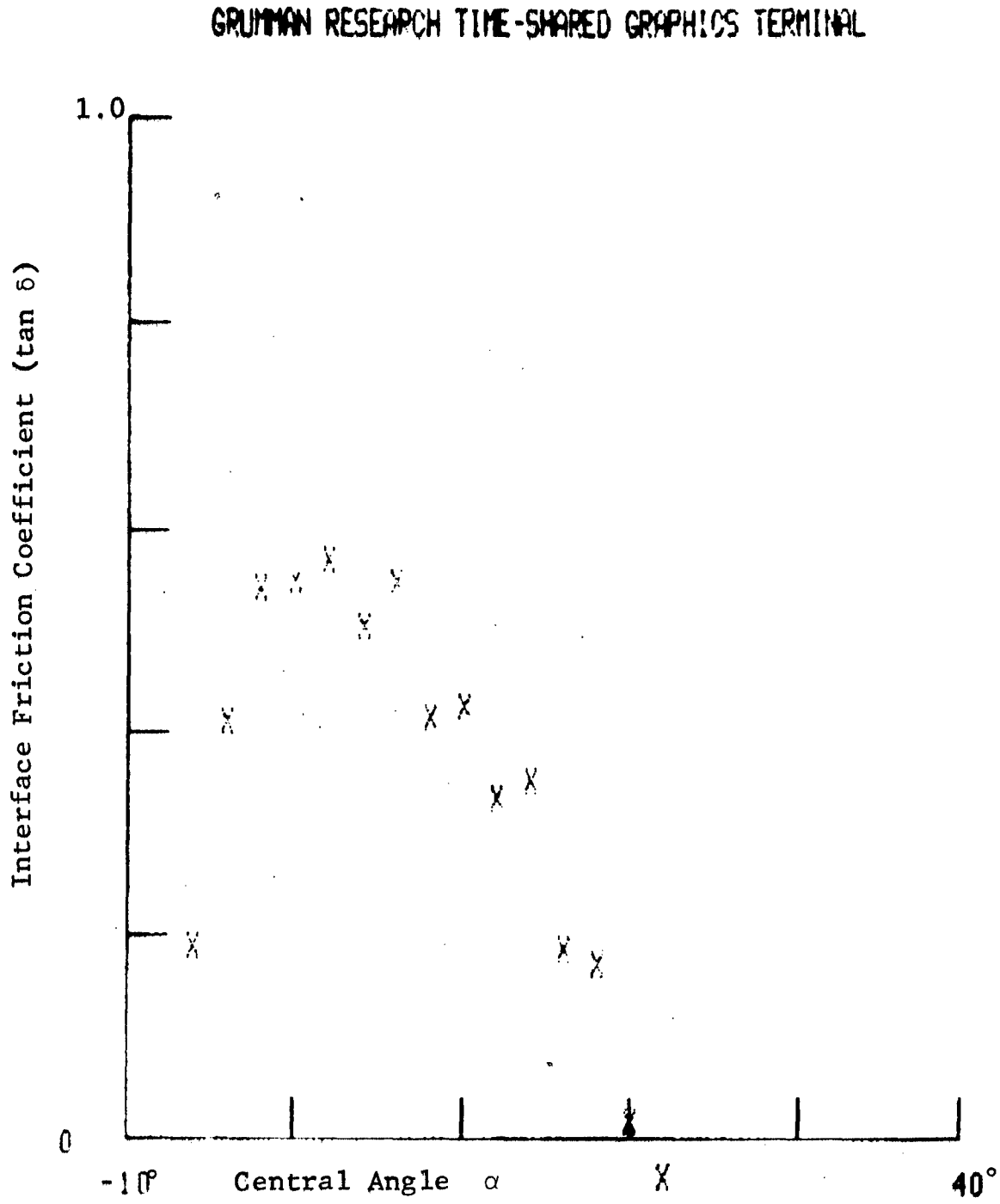

Fig. 95 Run #136 Variation of Interface Friction Coefficient (tan δ) Along the Interface in Loam
Load = 336 lbs, Drawbar Pull = 114 lbs,
Torque = 192 ft lbs

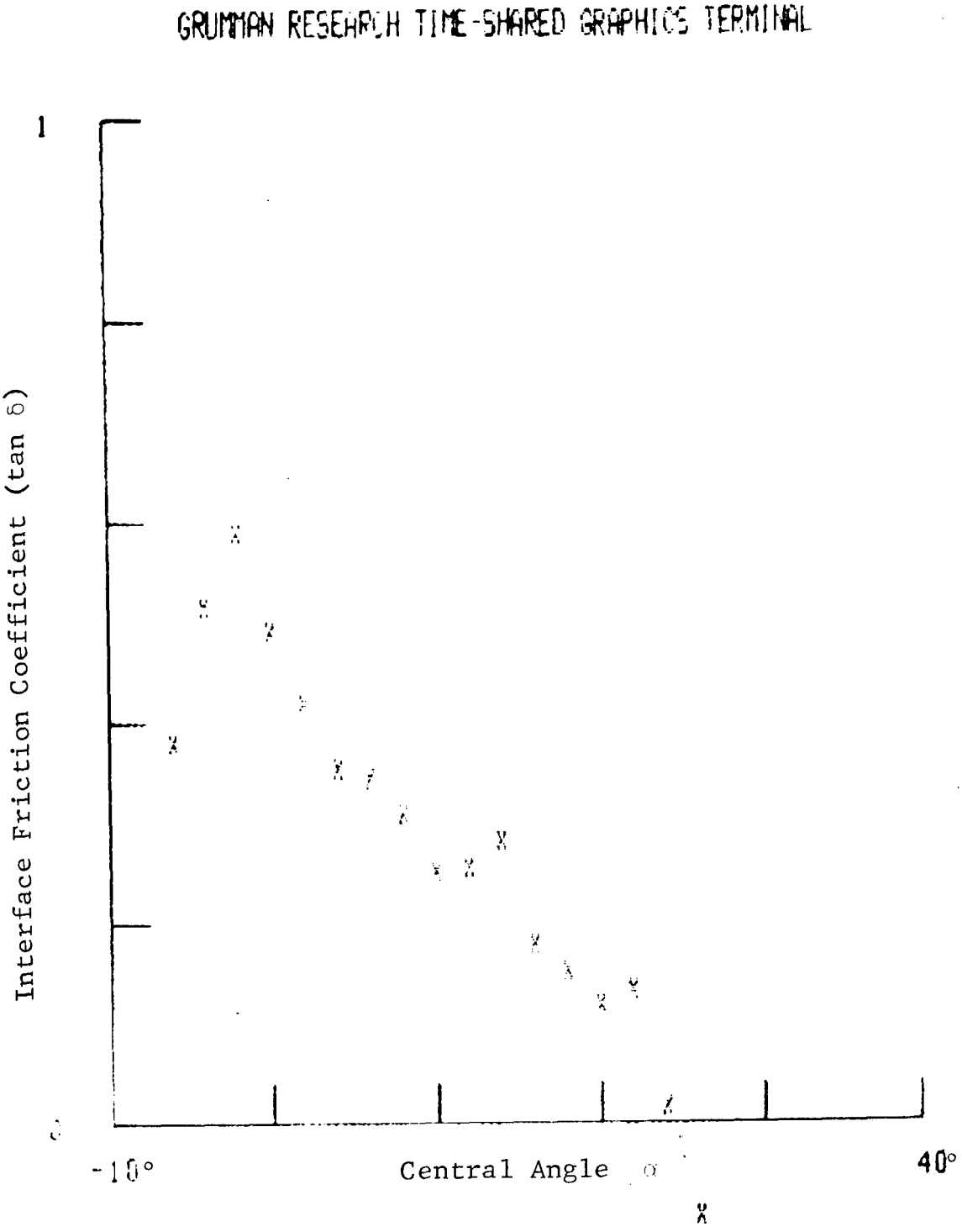

Fig. 96 Run #146 Variation of Interface Friction Coefficient (tan δ) Along the Interface in Loam
Load = 531 lbs, Drawbar Pull = 107 lbs,
Torque = 226 ft lbs

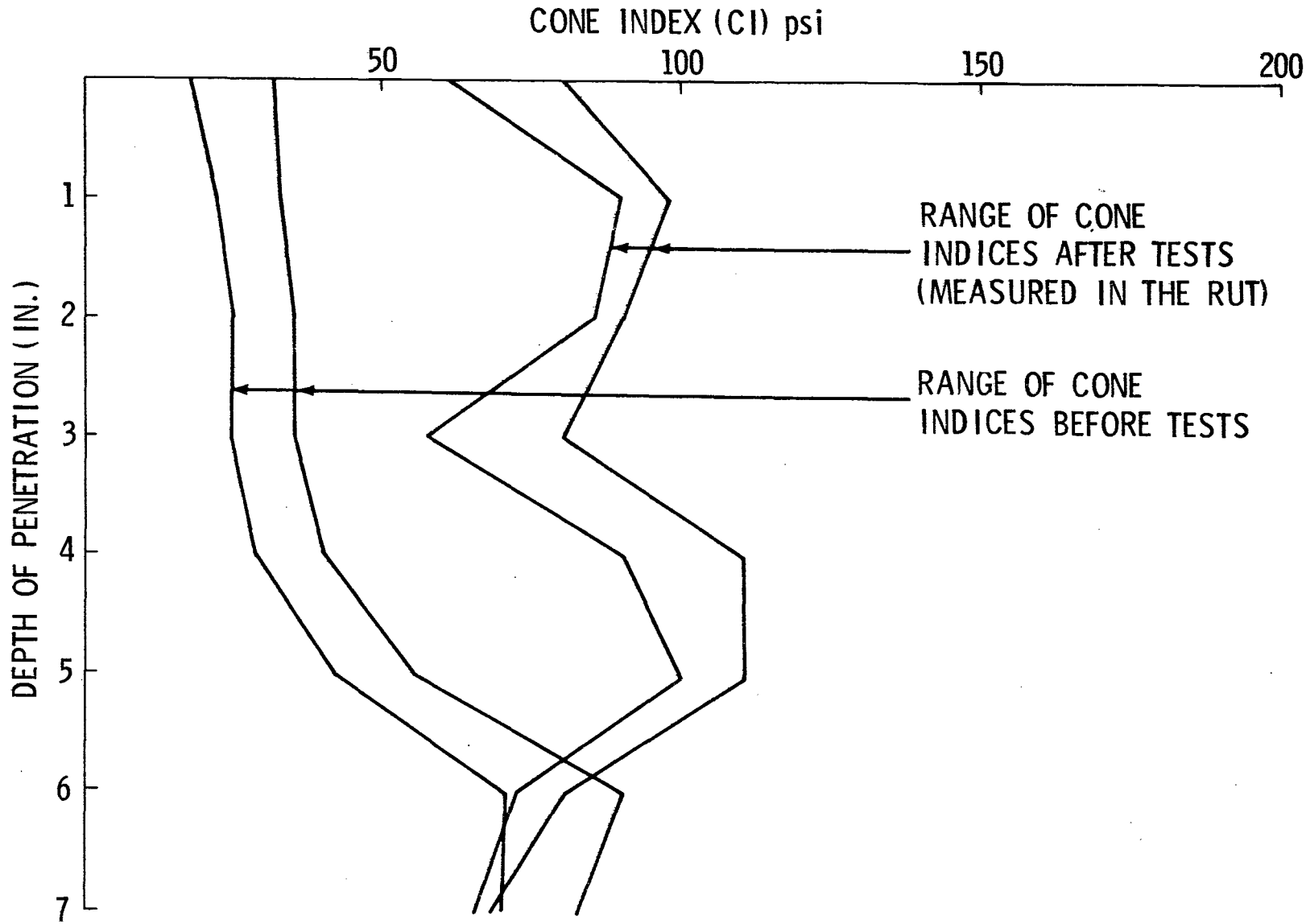

Fig. 97 Results of Cone Penetrometer Tests in Loam for Runs #129-136

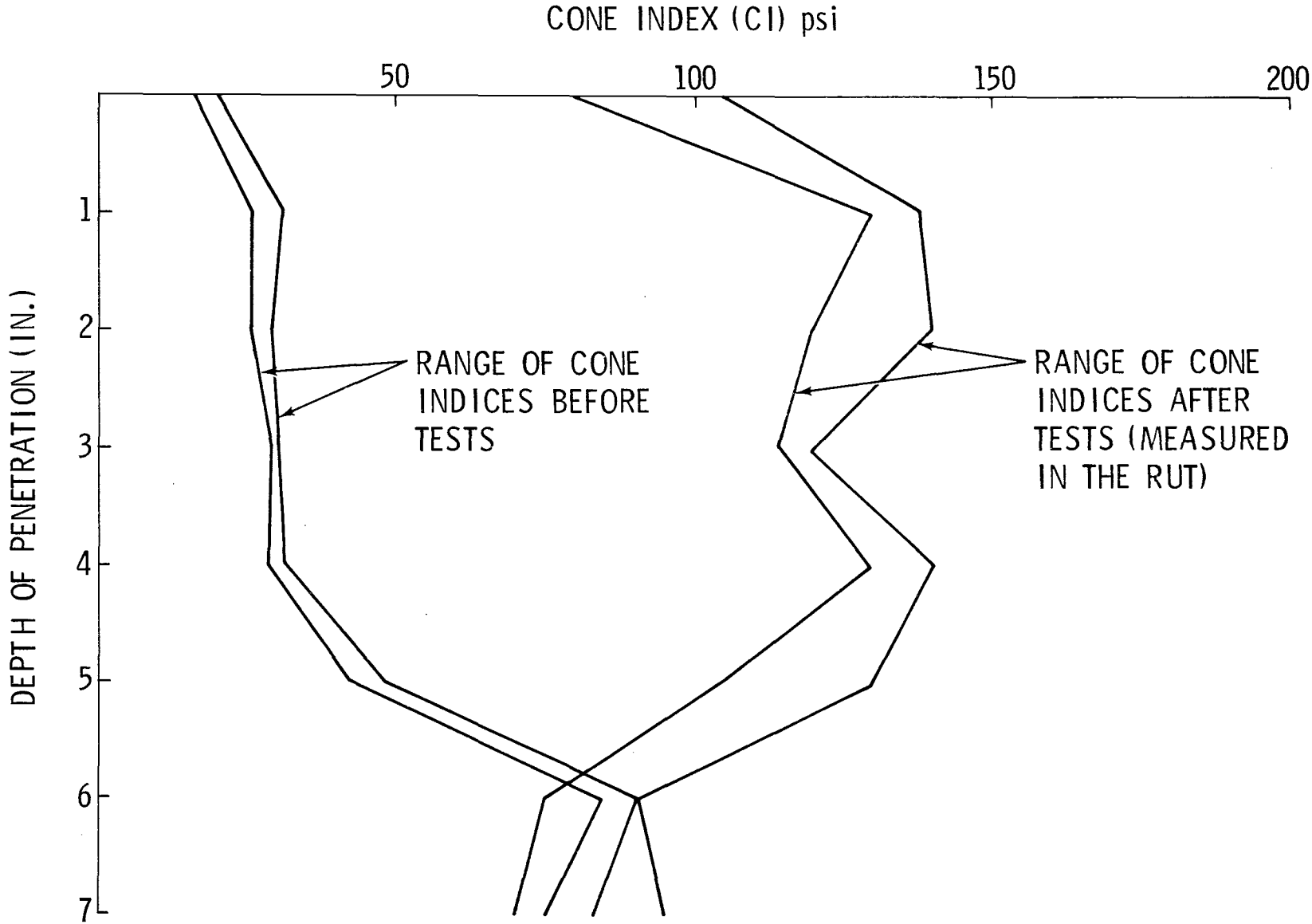

Fig. 98 Results of Cone Penetrometer Tests in Loam for Runs #137-146

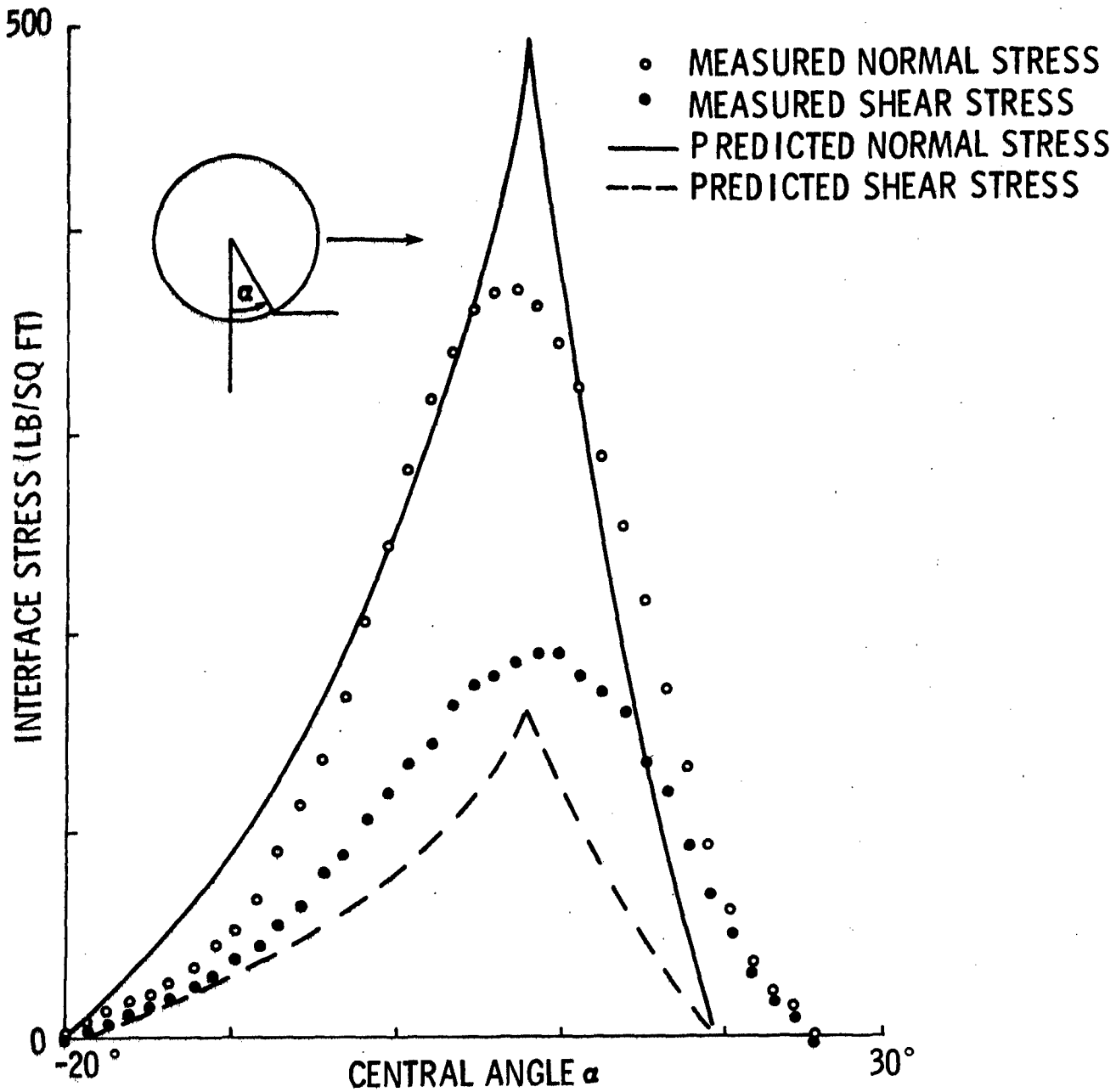

Fig. 99 Run #110102 Measured and Predicted Average Interface Normal and Shear Stresses. Wheel Diameter = 8 in., Width = 2 in. - Jones Beach Sand - Level Surface

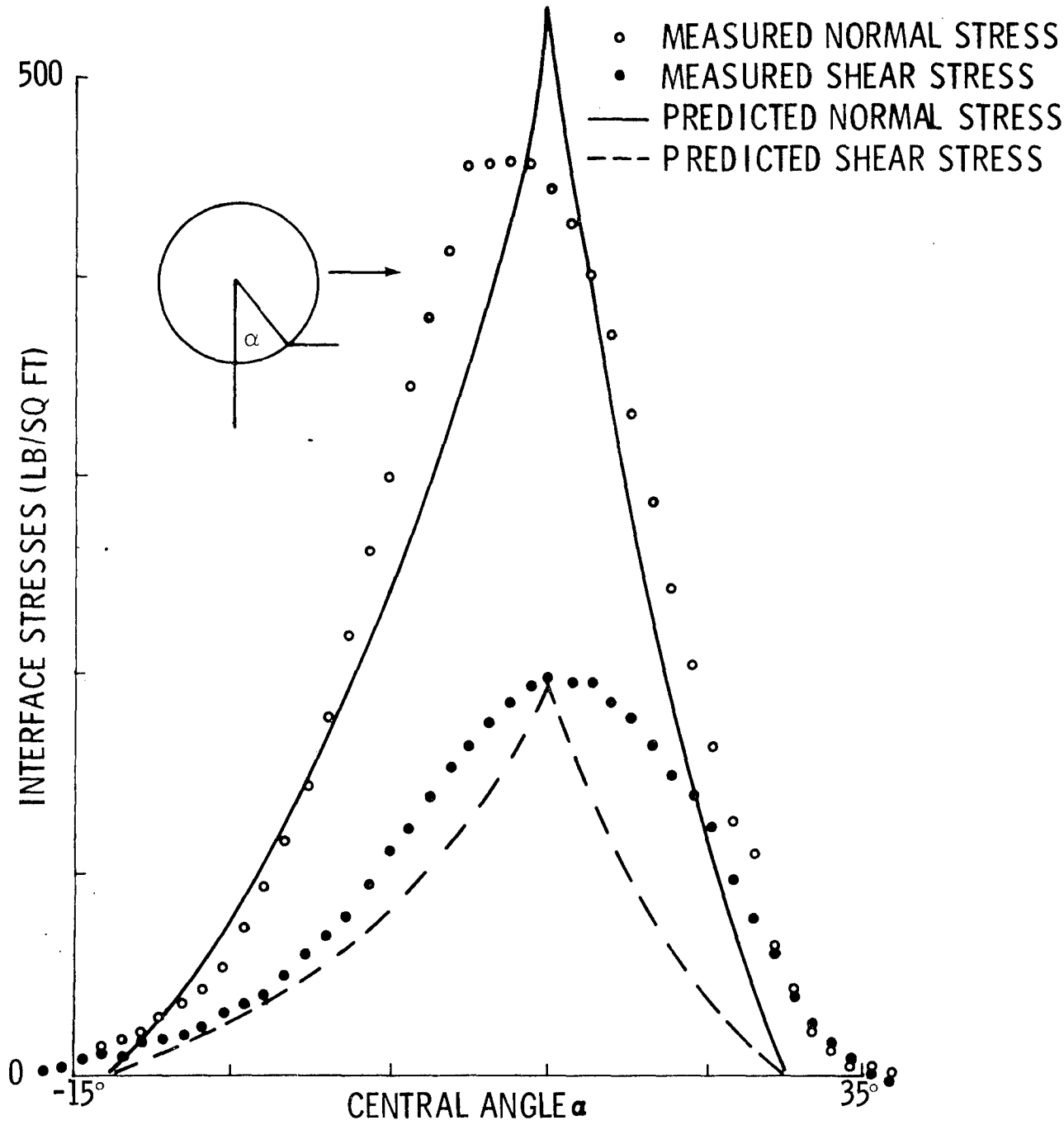

Fig. 100 Run #110602 Measured and Predicted Average Interface Normal and Shear Stresses. Wheel Diameter = 8 in., Width = 2 in. - Jones Beach Sand - 4° Slope

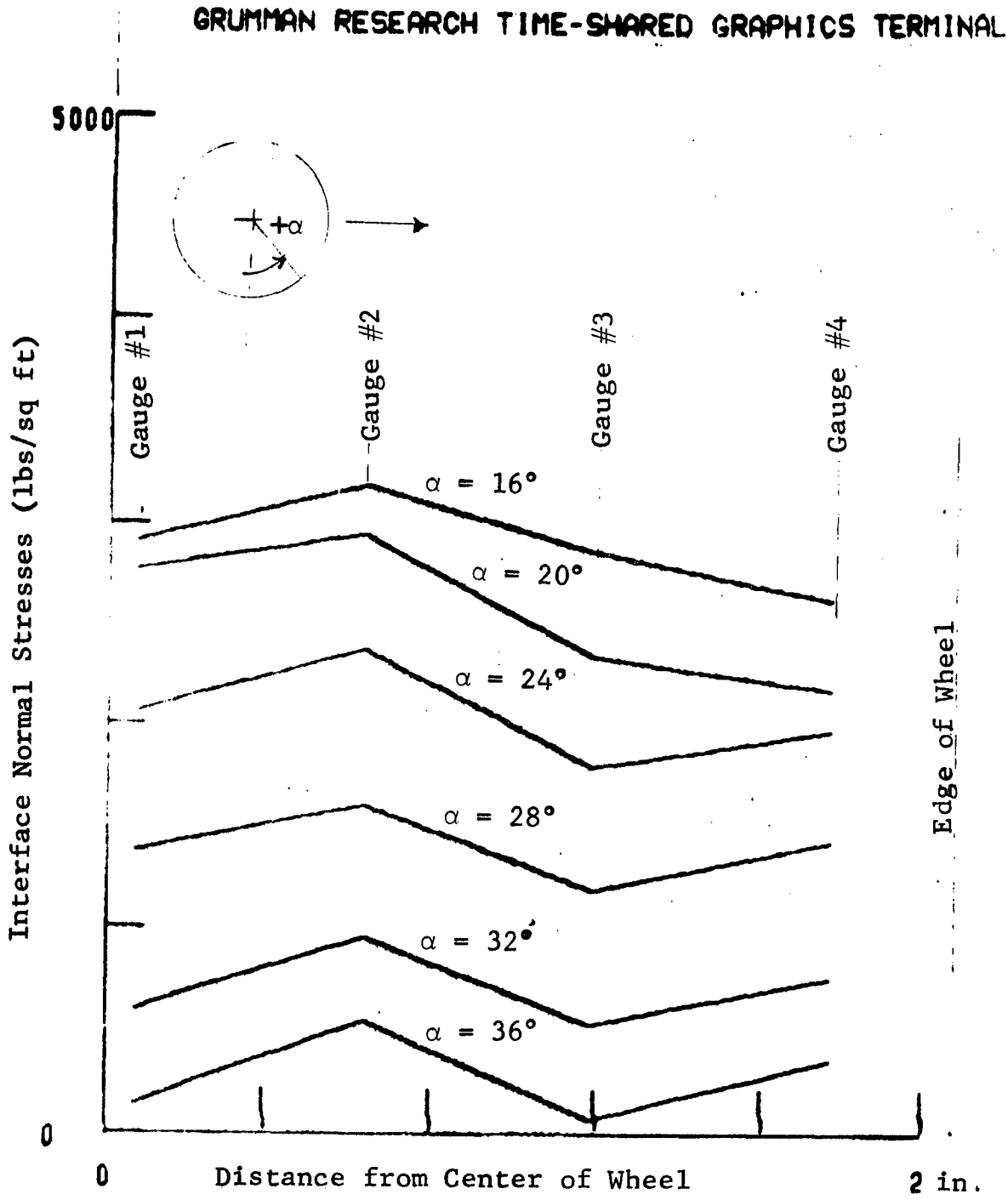

Fig. 101 Run #105 Transverse Distribution of Normal Stresses at Central Angles 16° to 36° Loose Sand

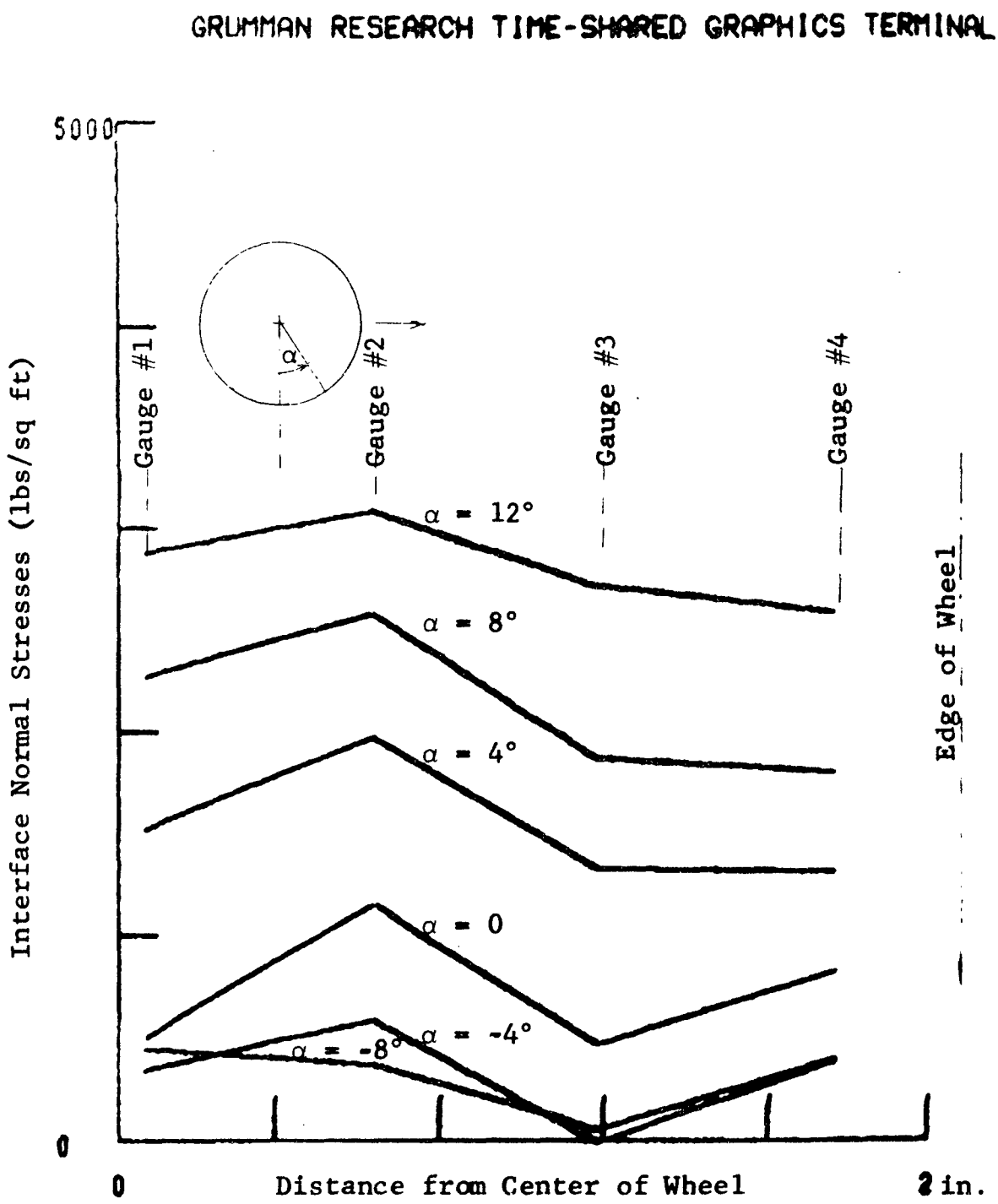

Fig. 102 Run #105 Transverse Distribution of Normal Stresses at Central Angles -8° to 12° Loose Sand

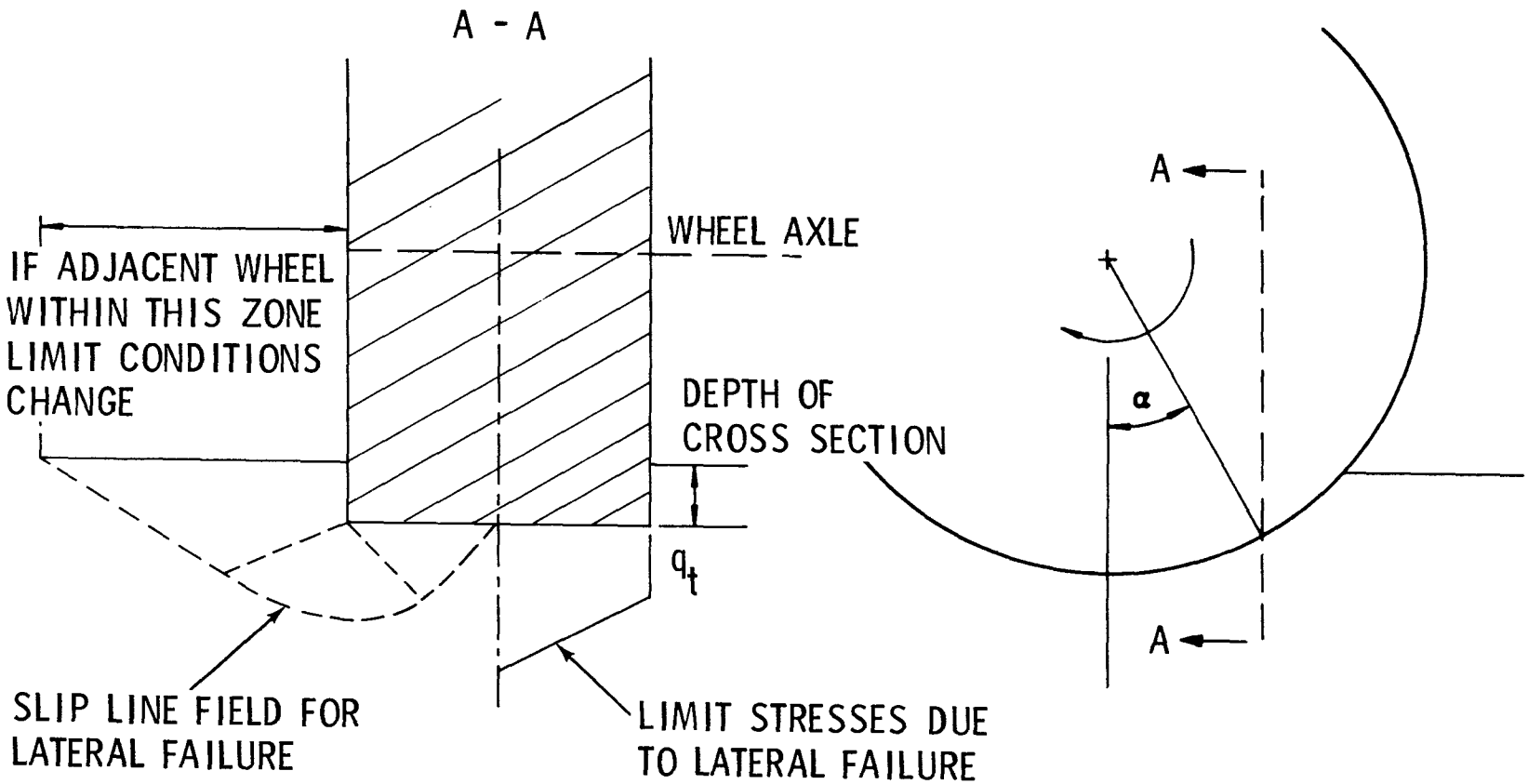

Fig. 103 Limiting Normal Stresses due to Lateral Failure

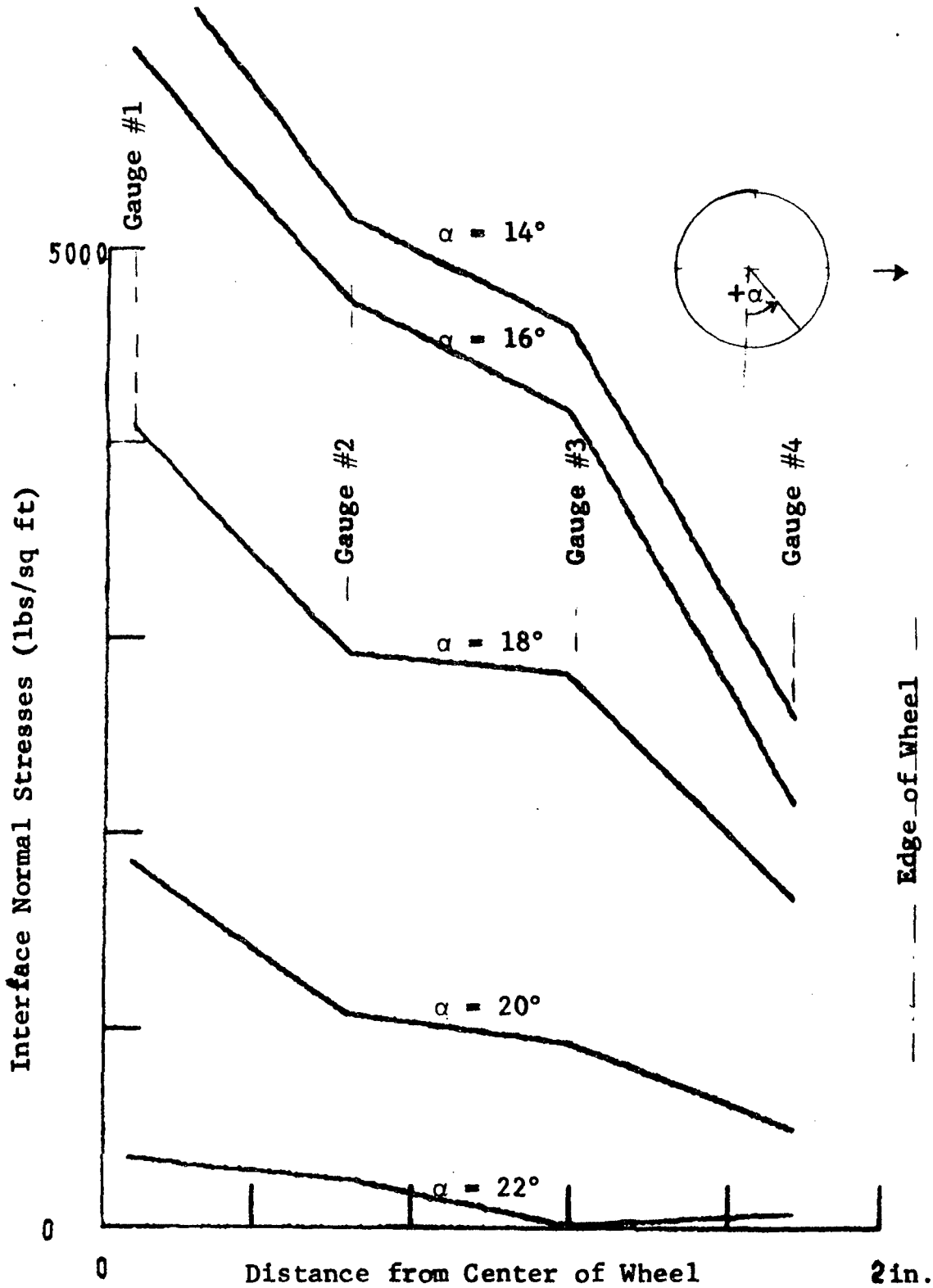

Fig. 104 Run #107 Transverse Distribution of Normal Stresses at Central Angles 14° to 22° Dense Sand

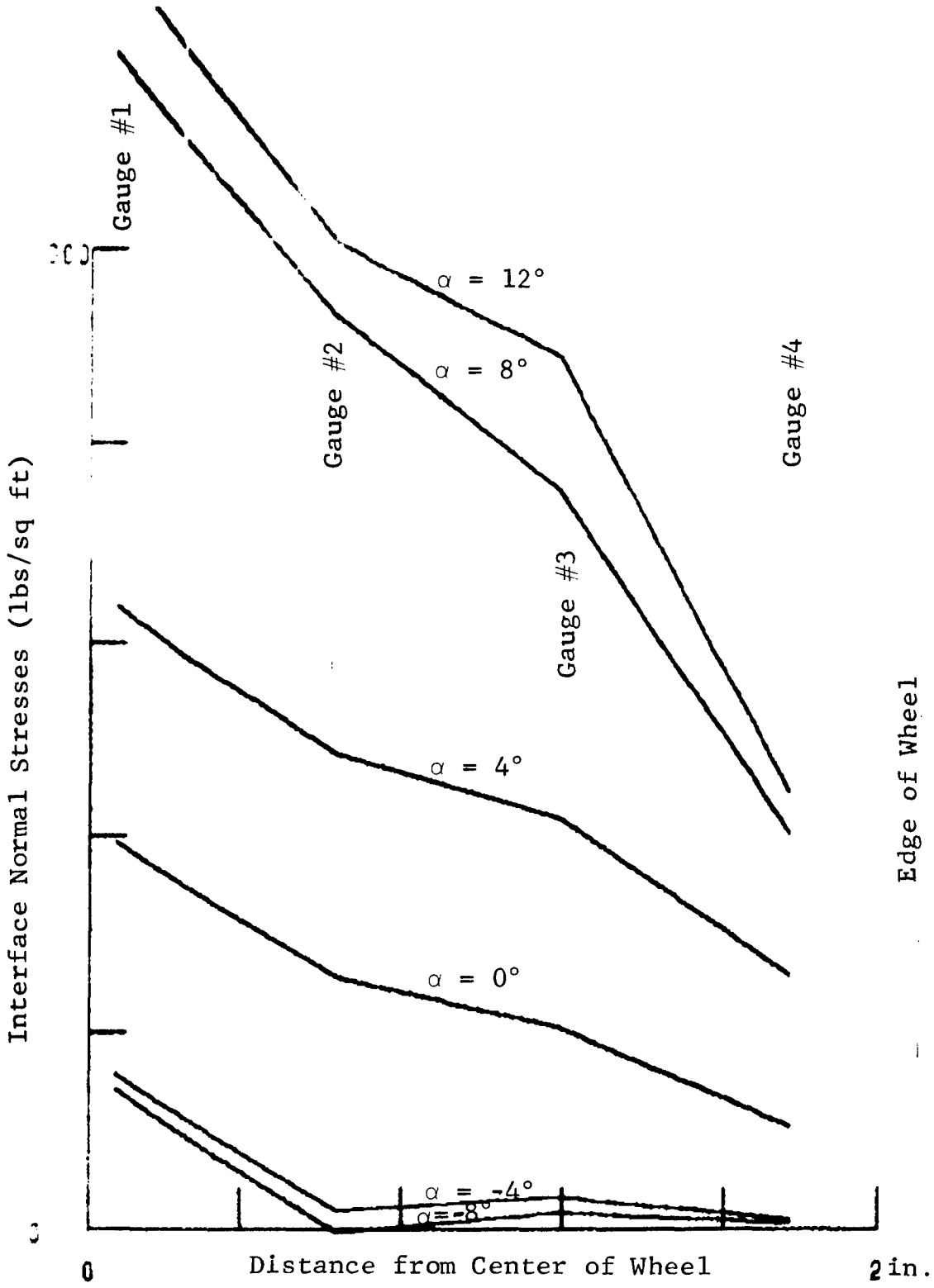

Fig. 105 Run #107 Transverse Distribution of Normal Stresses at Central Angles -8° to 12° Dense Sand

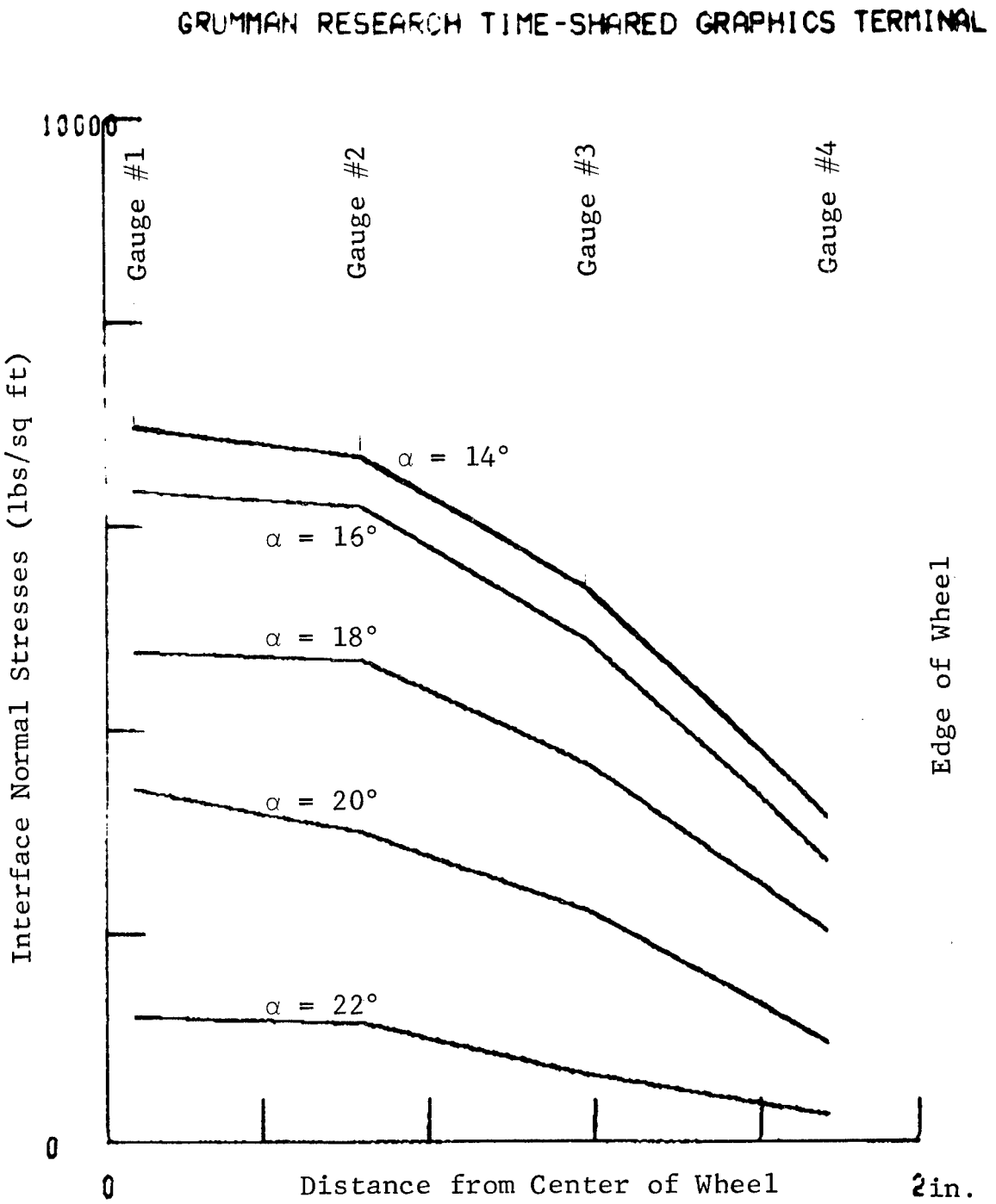

Fig. 106 Run #114 Transverse Distribution of Normal Stresses at Central Angles 14° to 22° Dense Sand

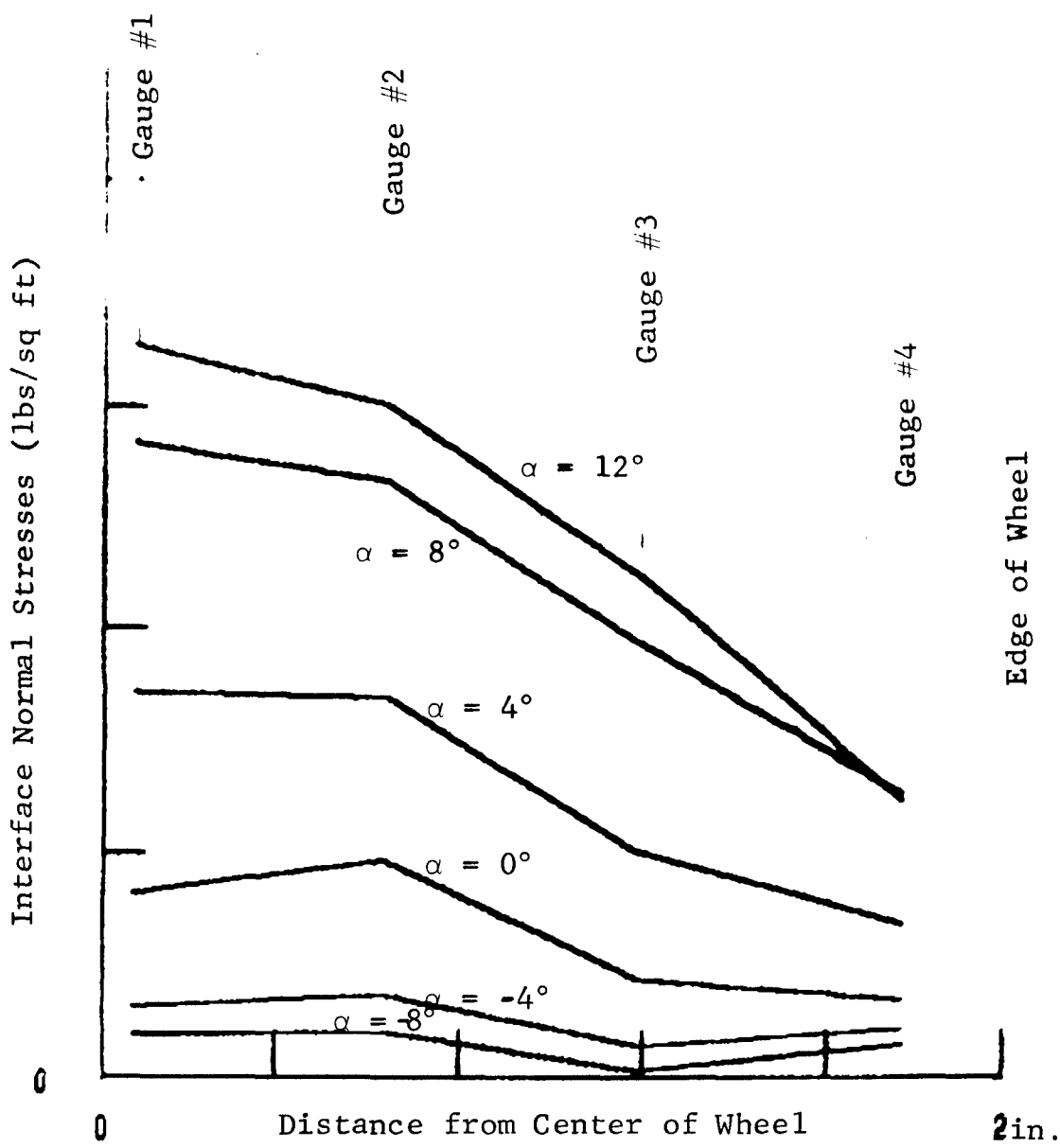

Fig. 107 Run #114 Transverse Distribution of Normal Stresses at Central Angles -8° to 12° Dense Sand

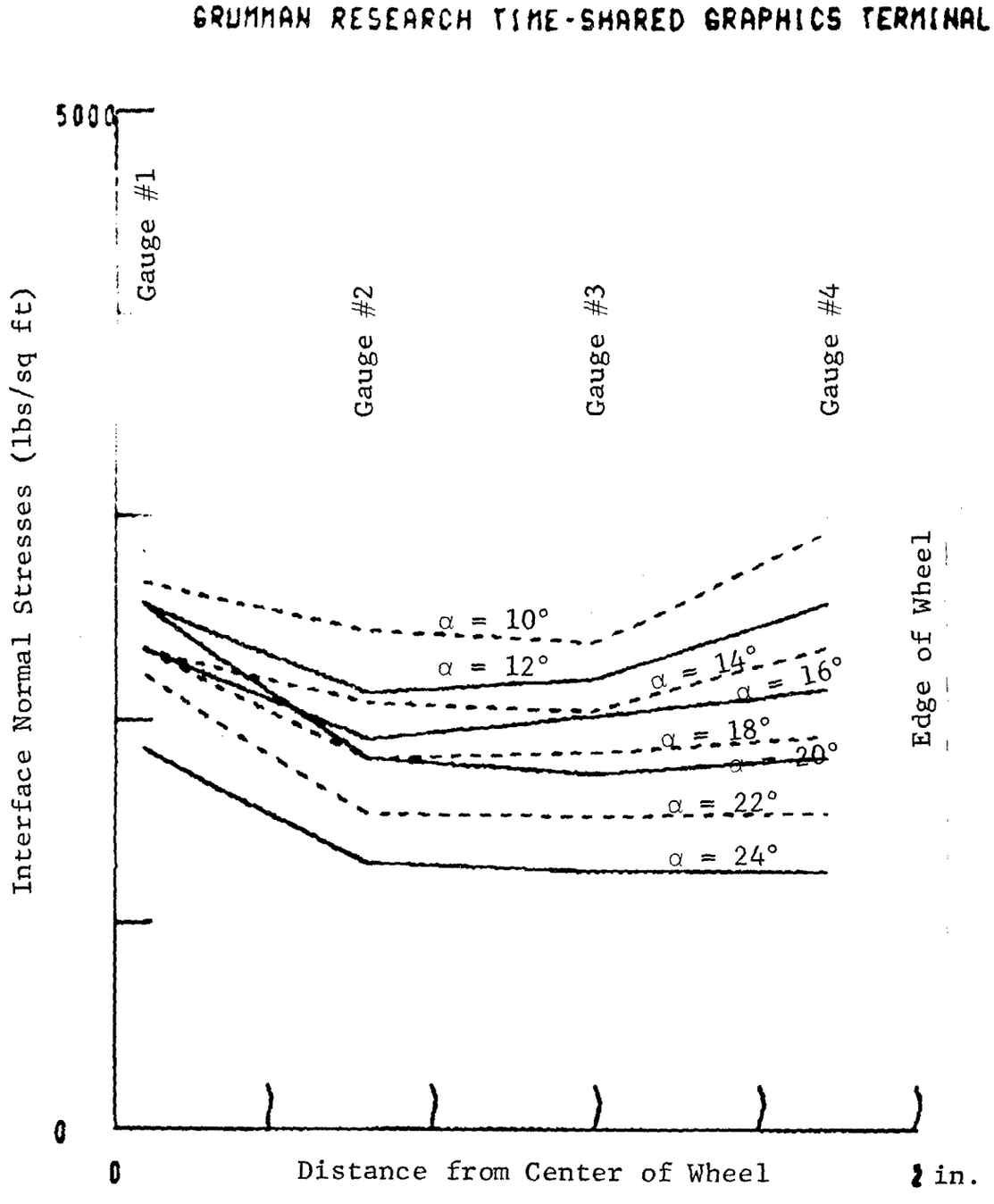

Fig. 108 Run #145 Transverse Distribution of Normal Stresses at Central Angles 10° to 24° Loam

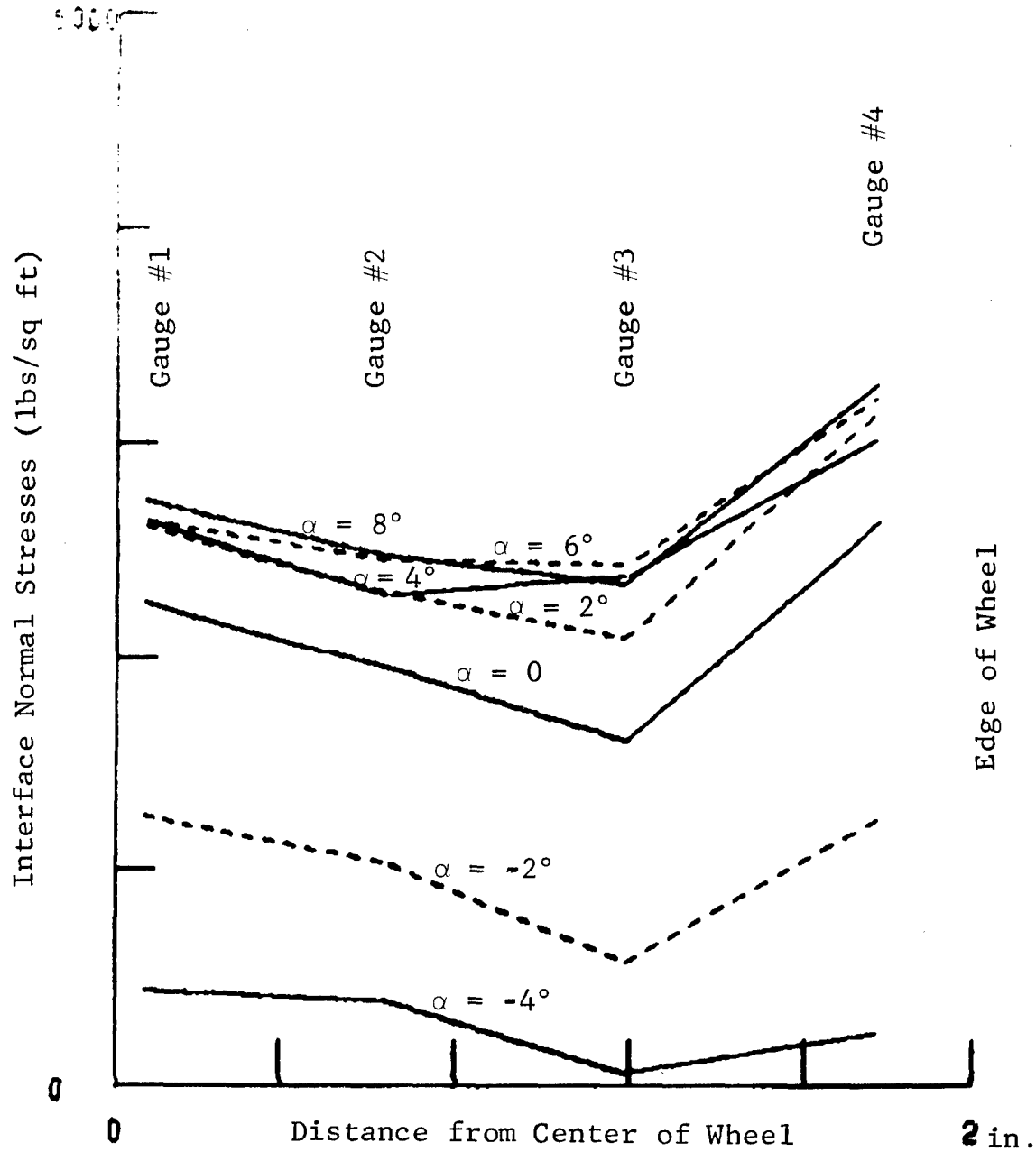

Fig. 109 Run #145 Transverse Distribution of Normal Stresses at Central Angles -4° to 8° Loam

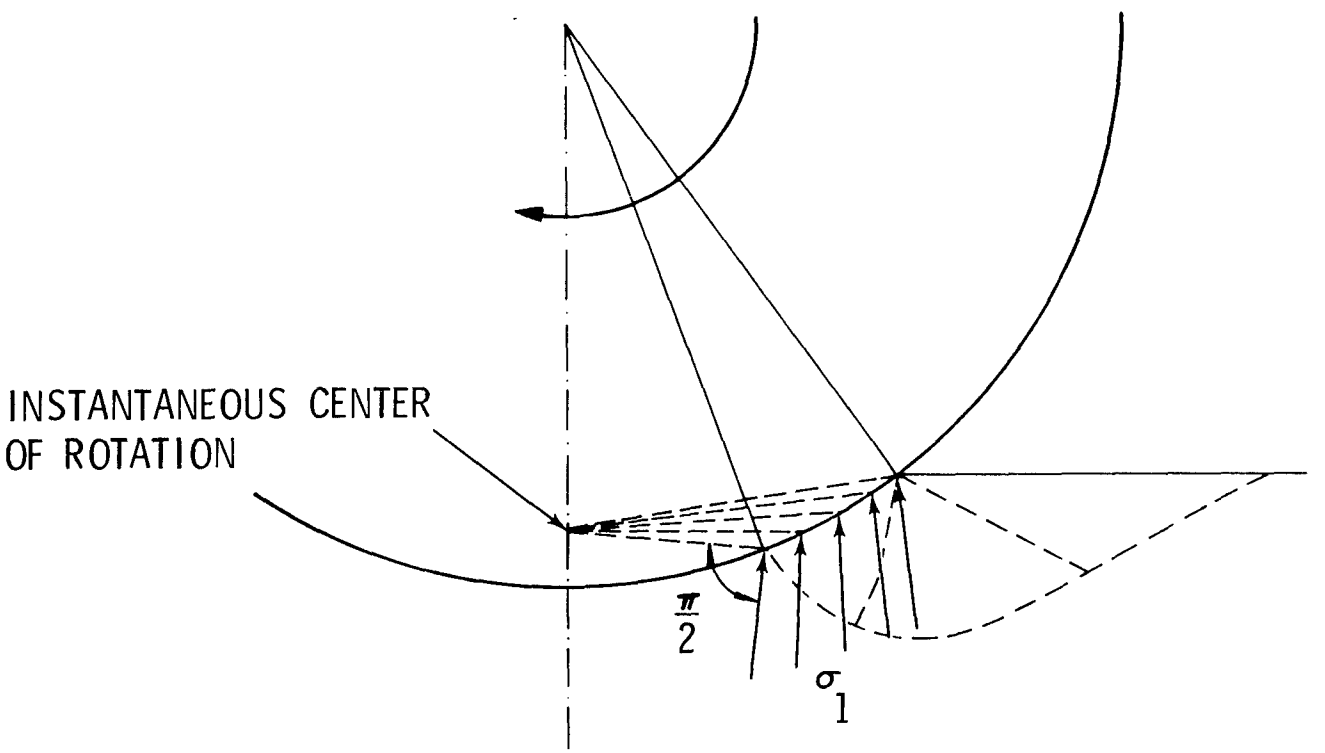

Fig. 110 Orientation of Major Principal Stress in the Front Field Approximately Corresponds to that of Instantaneous Velocity Vector

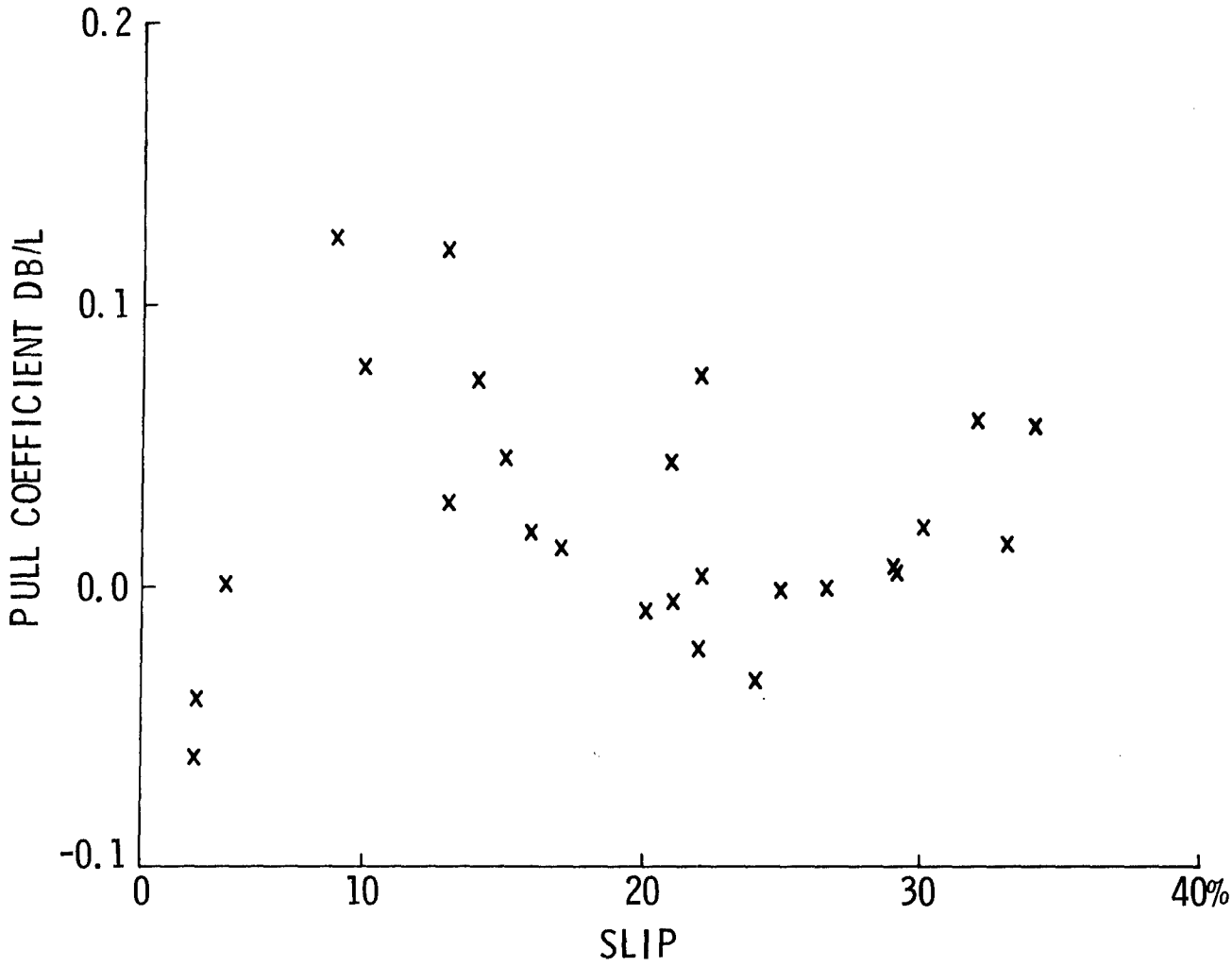

Fig. 111 Pull Coefficient Versus Measured Slip Values in Loose Sand

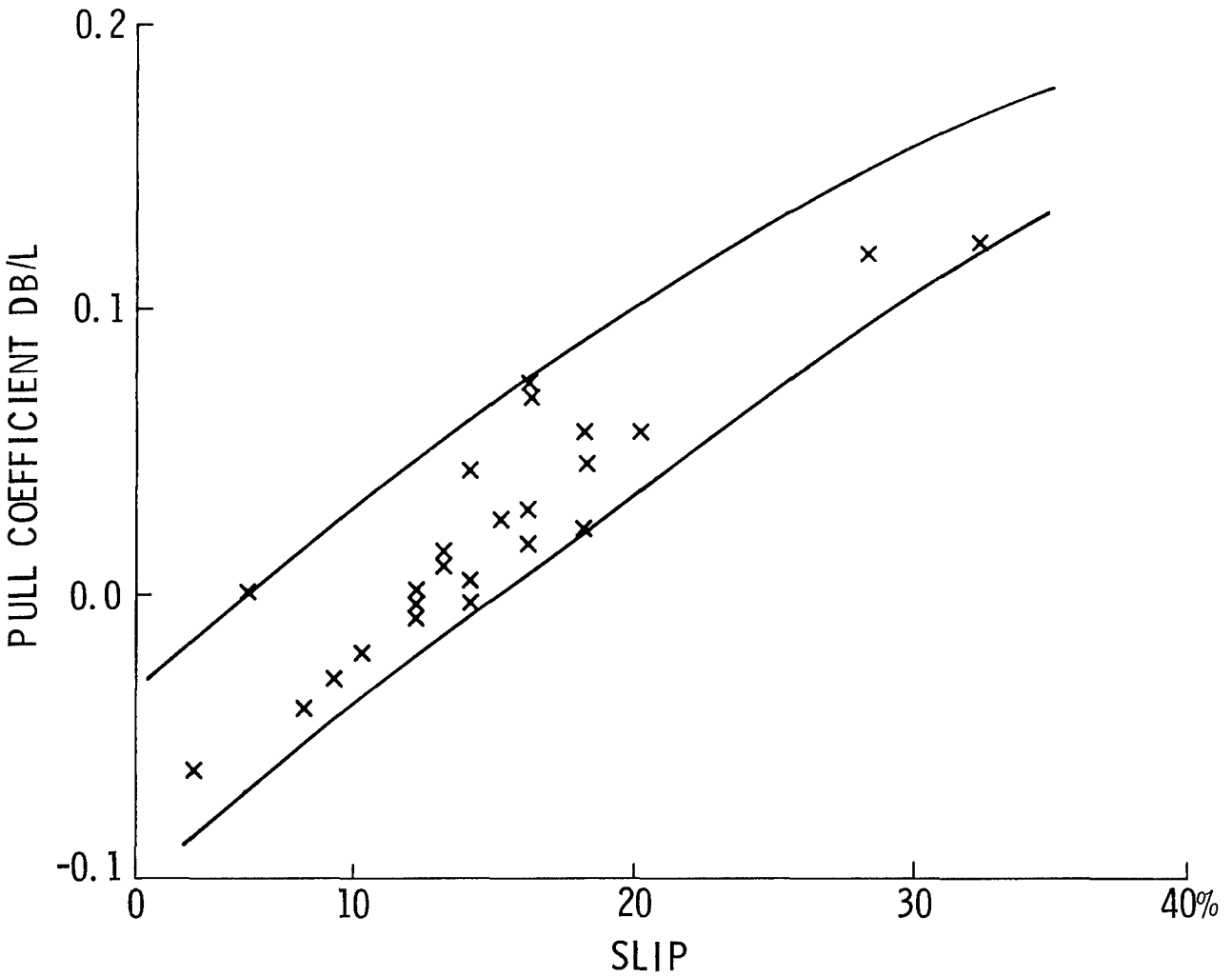

Fig. 112 Pull Coefficient Versus Predicted Slip Values in Loose Sand

```
LKWH.SRC       09-JAN-73    08:57

00100 C      THIS PROGRAM COMPUTES TORQUE,SINKAGE AND SLIP VALUES
00110 C      FOR DRIVEN RIGID WHEELS. ALL UNITS ARE IN FT. ,LBS.,
00120 C      AND DEGREES EXCEPT FOR THE SINKAGE OUTPUT WHICH IS IN
00130 C      INCHES. INPUT FILE 'SOL' CONTAINS THE FOLLOWING DATA:
00140 C      COHESION,FRICTION ANGLE,UNIT WEIGHT OF SOIL,SLOPE.
00150 C      ANGLE,SLIP PARAMETER 'J' ZERO,SLIP PARAMETER K .
00160 C      INPUT FILE 'WH1' CONTAINS THE FOLLOWING DATA:
00170 C      WHEEL RADIUS,WIDTH,DRAWBAR PULL,LOAD.
00180 C      INPUT FILE 'TOL' CONTAINS TOLERANCES AND VARIOUS
00190 C      CONSTANTS.RECOMMENDED VALUES ARE: 0.1,0.03,1.09,0.95
00200 C      20.0,2.0,2.0,0.9,0.7,16,12. THESE VALUES SHOULD BE
00210 C      CHANGED ONLY AFTER CONSULTATION WITH PROGRAM
00220 C      ORIGINATOR. SOIL STRENGTH PARAMETERS IN PROGRAM
00230 C      REFER TO STRENGT OF UNDISTURBED GROUND AS DETERMINED
00240 C      BY TRIAXIAL OR DIRECT SHEAR TESTS.PROGRAM DOES NOT
00245 C      APPLY TO BRAKED OR TOWED WHEELS WITH SIGNIFICANT
00250 C      NEGATIVE DRAWBAR PULL.
00260            DIMENSION HH(35),QQ(35),EE(35)
00270            DIMENSION WE(35),DRB(35),TRQ(35)
00280            DIMENSION LD(30),DR(30),TR(30),AR(30),DEL(30)
00290            DIMENSION PU(30),LC(30)
00300            DIMENSION AE(30)
00310            IMPLICIT REAL (L)
00320            DELT(D9,F9)=ASIN(SIN(D9)/SIN(F9))
00330            QUA(D9,F9)=COS(D9)+SQRT(COS(D9)**2-COS(F9)**2)
00340            QUP(D9,F9)=COS(D9)-SQRT(COS(D9)**2-COS(F9)**2)
00350            EPO(F9,T9,T8)=EXP(2*(T9-T8)*SIN(F9)/COS(F9))
00360            TAN(F9)=SIN(F9)/COS(F9)
00370            CALL MAXTIME (800)
00380            CALL IFILE(1,'SOL')
00390            CALL IFILE(2,'WH1')
00400            CALL IFILE(3,'TOL')
00410    10      READ (1,20) C0,F0,G0,S0,SLJ,SLK
00420    20      FORMAT (2F)
00430            IF(EOFC(1).LT.0) GO TO 50
00440            PRINT 30,C0,F0,G0
00450    30      FORMAT (1H ,'COHESION= ',F8.0,'  FR.ANG.= ',F8.2,'  GAMM

A= ',F8.2)
00460            PRINT 40,S0,SLJ,SLK
00470    40      FORMAT (1H ,'SLOPE=',F9.3,'  J ZERO=',F9.3,' K=',F9.3)
00480            GO TO 10
00490    50      READ (2,60)R0,B0,DB,L0
00500    60      FORMAT (2F)
00510            IF (EOFC(2).LT.0) GO TO 90
00520            PRINT 70,R0,B0
00530    70      FORMAT (1H ,'RADIUS= ',F8.3,'  WIDTH= ',F8.3)
00540            PRINT 80,L0,DB
00550    80      FORMAT (1H ,'LOAD= ',F10.1,'  DRAWBAR= 'F10.1)
00560            GO TO 50
00570    90      PI=3.14159
00580            MM=49
```

```
00590            NN=17
00600            READ(3,100) TOL,TOP,B1,B2,B3,B4,B5,B6,B7,B8,K3,K5
00610   100      FORMAT (10F,2I)
00620            IF (EOFC(3).LT.0) GO TO 110
00630   110      A1=D0+15
00640            A2=10
00650            A3=A2
00660            SIM=L0/(.8*R0*B0)
00670   120      IF (F0.LE.12) GO TO 950
00680            IF (C0.LE.0) GO TO 130
00690            GO TO 140
00700   130      C0=.2
00710   140      IF (C0.GT.50) GO TO 180
00720            IF(F0.GT.40) GO TO 170
00730            DMAX=56*ATAN(SIND(F0))
00740            DMIN=0.01*DMAX
00750            DB1=DB+L0*SIND(S0)
00760            D0=(.35+DB1/L0)*F0
00770            IF (D0.GT.DMAX) D0=DMAX
00780            IF(D0.LT.DMIN) D0=DMIN
00790            DE1=D0/57.3
00800            FR1=F0/57.3
00810            DE2=DELT(DE1,FR1)
00X20            TH1PI/2-.5*(DE1+DE2)
00830            DUA=QUA(DE1,FR1)
00840            DUP=QUP(DE1,FR1)
00850            DUB=EP0(FR1,TH1,0)
00860            DUC=DUA*DUB/DUP
00870            SIE=(C0+G0*R0*0.333)*DUC
00880            IF (SIE.LT.SIM) GO TO 150
00890            BA=.05
00900            GO TO 160
00910   150      BA=.1
00920   160      F2=(1+BA)*F0
00930            C2=C0
00940            G2=(1+BA)*G0
00950            GO TO 190
00960   170      F2=1.0*F0
00970            C2=C0
00980            G2=1.0*G0
00990            GO TO 190
01000   180     G2=1.1*G0
01010            F2=0.9*F0
01020            F4=F0/57.3
01030            F5=F2/57.3
01040            TA1=TAN(F4)
01050            TA2=TAN(F5)
01060            TAM=C0+SIM*TA1
01070            C2=TAM-SIM*TA2
01080   190      PRINT 200,C2,F2,G2
```

```
01090   200     FORMAT (1H ,'REAR: COH.= ',F8.2,'  FR.A.= ',F8.2,'  GAMM
A= ',F8.2)
01100           F5=F2/57.3
01110           TA2=TAN(F5)
01120           P2=C2/TA2
01130           IF (F2.LE.F0) F3=F2
01140           IF (F0.LE.F2) F3=F0
01150           DMAX=56*ATAN(SIND(F3))
01160           DMIN=0.01*DMAX
01170           DB1=DB+L0*SIND(S0)
01180           D0=(.35+DB1/L0)*F0
01190           IF (D0.GT.DMAX) D0=DMAX
01200           KA=0
01210           AEMAX=60
01220           ARE=AEMAX/57.3
01230           AMAX=21
01240           AMIN=1
01250           PULC=DB1/L0
01260           DDF=1.0
01270   210     RR0=R0
01280           EE1=S0/57.3
01290           GG0=G2
01300           FF1=F2/57.3
01310           CC0=C2
01320           AA0=A2/57.3
01330           DD1=-D0/57.3
01340           X1=0
01350           AL=DDF*DD1
01360           CALL  SLIP(RR0,EE1,AA0,GG0,DD1,FF1,CC0,DDF,AL,X1,P2,HH,Q
Q,EE,JJ1)
01370           EJ=-EE(JJ1)
01380           QJ=QQ(JJ1)
01390           AL=-(HH(JJ1))/57.3
01400           DO 220 J=(2*NN),(2*NN-JJ1+1),-1
01410           HH(J)=-HH(2*NN-J+1)
01420           QQ(J)=QQ(2*NN-J+1)
01430           EE(J)=-EE(2*NN-J+1)
01440   220     CONTINUE
01450           N1=2*NN-JJ1+1
01460           X1=1
01470           AA0=AL+.2
01480           AX=0
01490           AY=0
01500   230     GG0=G0
01510           DD1=D0/57.3
01520           FF1=F0/57.3
01530           CC0=C0
01540           CC1=CC0/TAN(FF1)
01550           D2=ATAN(W0*SIN(EE1)/(CC1+W0*COS(FF1)))
01560           D3=DELT(D2,FF1)
01570           T1=(D3-D2)/2
01580           D4=DELT(DD1,FF1)
```

```
01590            T2=PI/2+.5*(D4+DD1)-AL
01600            QU1=(W0*COS(EE1)+CC1)/COS(D2)
01610            QU2=QUP(D2,FF1)
01620            SIG=QU1/QU2
01630            EP1=EP0(FF1,T2,T1)
01640            SIG1=SIG*EP1
01650            QU3=QUA(DD1,FF1)
01660            QU4=SIG1*QU3*COS(DD1)-CC1
01670            SIG2=(QJ+CC1)/(QU3*COS(DD1))
01680            EP2=SIG2/SIG1
01690            TF1=TAN(FF1)
01700            P01=ALOG(EP2)
01710            THDEL=-P01/(2*TF1)
01720            AA1=AL+THDEL
01730            IF (QU4.GE.QJ) GO TO 340
01740            CALL SLIP(RR0,EE1,AA0,GG0,DD1,FF1,CC0,DDF,AL,X1,P2,HH,QQ
, EE,JJ1)
01750            QD=QJ-QQ(JJ1)
01760            IF (QD.LT.0) AX=AA0
01770            IF (QD.GT.0) AY=AA0
01780            IF (AX*AY) 240,250,240
01790    240     AA0=(AX+AY)/2
01800            IF (ABS(QD)-.05*QJ) 310,310,245
01810            GO TO 230
01820    245     GO TO 230
01830    250     IF (ABS(QD)-.05*QJ) 310,310,260
01840    260     IF(AA0.EQ.ARE) GO TO 270
01850            GO TO 290
01860    270     IF(QQ(JJ1).LT.(1-TOL)*SIM) GO TO 280
01870            IF(D0.EQ.DMAX) GO TO 810
01880            D0=B1*D0+QD*D0/QJ+B4
01890            IF(D0.GT.DMAX) D0=DMAX
01900            GO TO 210
01910    280     SIM=QQ(JJ1)
01920            GO TO 120
01930    290     AMD=AA0-AL
01940            QM=.5*(QJ+QQ(JJ1))
01950            IF (QD.LT.0) ADD=-.02
01960            IF(QD.GT.0) ADD=.02
01970            AAD=AMD*QD/QM
01980            AA0=AA0+AAD+ADD
01990            IF(AA0.EQ.(AL+.01)) GO TO 310
02000            IF (AA0.LT.AL) AA0=AL+.01
02010            IF (AA0.GE.ARE) GO TO 300
02020            GO TO 230
02030    300     AA0=ARE
02040            GO TO 230
02050    310     DO 320 J=(N1-1),(N1+1-JJ1),-1
02060            HH(J)=HH(J-N1+JJ1)
02070            QQ(J)=QQ(J-N1+JJ1)
02080            EE(J)=EE(J-N1+JJ1)
```

```
02090   320     CONTINUE
02100           TORQ=0
02110           LOAD=0
02120           DRAB=0
02130           DO 330 J=2*NN-1,N1+1-JJ1,-1
02140           ARC=R0*(HH(J)-HH(J+1))/57.3
02150           QAV=.5*(QQ(J+1)+QQ(J))
02160           TAV=.5*(EE(J+1)+EE(J))
02170           AAV=.5*(HH(J+1)+HH(J))/57.3
02180           LOA=(TAV*SIN(AAV)+QAV*COS(AAV))*ARC
02190           DRA=(TAV*COS(AAV)-QAV*SIN(AAV))*ARC
02200           TOR=R0*TAV*ARC
02210           LOAD=LOAD+LOA
02220           DRAB=DRAB+DRA
02230           TORQ=TORQ+TOR
02240   330     CONTINUE
02250           LOAD=B0*(LOAD*COSD(S0)+DRAB*SIND(S0))
02260           TORQB0*TORQ
02270           DRAB=B0*(DRAB-LOAD*SIND(S0))
02280           GO TO 410
02290   340     JJ1=16
02300           DALPH=57.3*(AA1-AL)/JJ1
02310           DO 350 J=(N1-1),(N1+1-JJ1),-1
02320           HH(J)=57.3*AL+DALPH
02330           QQ(J)=QJ
02340           EE(J)=EJ
02350           AL=HH(J)/57.3
02360           IF(J.LT.(N1-1)) GO TO 350
02370   350     CONTINUE
02380           AA0=HH(J)/57.3
02390           TORQ=0
02400           LOAD=0
02410           DRAB=0
02420           DO 360 J=2*NN-1,N1+1-JJ1,-1
02430           ARC=R0*(HH(J)-HH(J+1))/57.3
02440           QAV=.5*(QQ(J+1)+QQ(J))
02450           TAV=.5*(EE(J+1)+EE(J))
02460           AAV=.5*(HH(J+1)+HH(J))/57.3
02470           LOA=(TAV*SIN(AAV)+QAV*COS(AAV))*ARC
02480           DRA=(TAV*COS(AAV)-QAV*SIN(AAV))*ARC
02490           TOR=R0*TAV*ARC
02500           LOAD=LOAD+LOA
02510           DRAB=DRAB+DRA
02520           WE(J)=B0*(LOAD*COSD(S0)+DRAB*SIND(S0))
02530           DRB(J)=B0*(DRAB-LOAD*SIND(S0))
02540           TORQ=TORQ+TOR
02550           TRQ(J)=B0*TORQ
02560           IF(J.GE.(N1+1)) GO TO 360
02570           IF (WE(J).GT.L0) GO TO 370
02580           IF(J.LT.(N1+1)) GO TO 370
```

```
02590            GO TO 390
02600    360     CONTINUE
02610    370     WR=(WE(J)-L0)/(WE(J)-WE(J+1))
02620            LOAD=WE(J)-WR*(WE(J)-WE(J+1))
02630            TORQ=TRQ(J)-WR*(TRQ(J)-TRQ(J+1))
02640            DRAB=DRB(J)-WR*(DRB(J)-DRB(J+1))
02650            AA0=(HH(J)-WR*(HH(J)-HH(J+1)))/57.3
02660            IF(A2.LE.(5.73*AA0)) GO TO 380
02670            GO TO 400
02680    380     A2=A2+B6
02690            IF(A2.GT.AMAX) A2=AMAX
02700            ITAL=1
02710            GO TO 410
02720    390     LOAD=WE(J)
02730            DRAB=DRB(J)
02740            TCRQ=TRQ(J)
02750            GO TC 410
02760    400     IF(D0.EQ.DMAX) GO TO 750
02770            KFR=1
02780    410     IF(K.EQ.(K3+K5)) GO TO 830
02790            IF(K.EQ.K3) GO TO 940
02800    420     K=K+1
02810            LD(K)=LOAD
02820            TR(K)=TCRQ
02830            DR(K)=DRAB
02840            AR(K)=A2
02850            DEL(K)=D0
02860            AAE=57.3*AA0
02870            AE(K)=AAE
02880            PU(K)=DR(K)/LD(K)
02890            LC(K)=LD(K)/L0
02900            IF(KFR.EQ.1) GO TO 470
02910            IF(ITAL.EQ.1) GO TO 430
02920            GO TO 440
02930    430     ITAL=0
02940            GO TO 210
02950    440     IF(AR(K).GE.(0.8*AE(K))) GO TO 450
02960            GO TO 490
02970    450     IF(KA.EQ.1) GO TO 460
02980            AMAX=0.8*AE(K)
02990            KA=1
03000            GO TO 490
03010    460     IF(AR(K).GE.(0.9*AE(K))) GO TO 750
03020            GO TO 490
03030    470     IF(A2.EQ.AMIN) GO TO 480
03040            GO TO 490
03050    480     IF(PU(K).GE.(PULC+TOP)) GO TO 770
03060            GO TO 490
03070    490     IF(ABS(PU(K)-PULC)-TOP) 500,500,510
03080    500     IF(ABS(LC(K)-1)-TOL) 820,820,620
```

```
03090   510     IF(PU(K).GE.(PULC+TOP)) GO TO 520
03100           IF (PU(K).LE.(PULC-TOP)) GO TO 560
03110           GO TO 620
03120   520     IF (LC(K).GE.1+TOP) GO TO 540
03130           IF (LC(K).LE.(1-TOP)) GO TO 550
03140           D0=B2*D0-B3*(PU(K)-PULC)-B8
03150           IF(KFR.EQ.1) GO TO 530
03160           GO TO 650
03170   530     A2=A2-B6
03180           KFR=0
03190           GO TO 650
03200   540     D0=B2*D0-B3*(PU(K)-PULC)
03210           A2=BR*A2-B8*LC(K)-B8
03220           GO TO 650
03230   550     D0=B2*D0-B3*(PU(K)-PULC)-B8
03240           A2=B1*A2+B5*LC(K)+B4
03250           GO TO 650
03260   560     IF(KFR.EQ.1) GO TO 570
03270           IF (LC(K).GT.(1+TOL)) GO TO 600
03280           IF(LC(K).LT.(1-TOL)) GO TO 610
03290           D0=B1*D0-B3*(PU(K)-PULC)+B4
03300           IF(KFR.EQ.1) GO TO 570
03310           GO TO 650
03320   570     IF(A2.GE.(AMAX-1)) GO TO 750
03330           IF(A2.GE.43*AA0) GO TO 580
03340           GO TO 590
03350   580     D0=B1*D0-.5*B3*(PU(K)-PULC)+.5*BT
03360   590     A2=A2+B6
03370           GO TO 650
03380   600     D0=B1*D0-B3*(PU(K)-PULC)+B4
03390           A2=B2*A2-0.5*B5*LC(K)-B8
03400           GO TO 650
03410   610     D0=B1*D0-B3*(PU(K)-PULC)+B4
03420           A2=B1*A2+B5*LC(K)+B4
03430           GO TO 650
03440   620     IF(LC(K).GT.1) GO TO 630
03450           IF(LC(K).LT.1)GO TO 640
03460   630     A2=B2*A2-B5*LC(K)
03470           IF(A2.LT.AMIN) A2=AMIN
03480           GO TO 650
03490   640      A2=B1*A2+B5/LC(K)
03500           IF(A2.GT.AMAX) A2=AMAX
03510           GO TO 650
03520   650     IF (A2.LT.AMIN) A2=AMIN
03530           IF(A2.GT.AMAX) A2=AMAX
03540           IF (D0.LT.DMIN) D0=DMIN
03550           IF (D0.GT.DMAX) D0=DMAX
03560           IF(KFR.EQ.1) GO TO 660
03570           GO TO 670
03580   660     KFR=0
```

```
03590            GO TO 210
03600    670     IF(AR(K-1).EQ.AR(K)) GO TO 680
03610            GO TO 800
03620    680     IF (PU(K).GE.PULC) GO TO 690
03630            GO TO 700
03640    690     IF (PU(K-1).LE.PULC) GO TO 710
03650            GO TO 720
03660    700     IF(PU(K-1).GE.PULC) GO TO 710
03670            GO TO 720
03680    710     D0=(DEL(K)+DEL(K-1))/2
03690            IF (D0.LT.DMIN) D0=DMIN
03700            IF (D0.GT.DMAX) D0=DMAX
03710            GO TO 800
03720    720     IF (DEL(K-1).EQ.DEL(K)) GO TO 730
03730            GO TO 800
03740    730     IF(A2.EQ.AMAX) GO TO 740
03750            IF(A2.EQ.AMIN) GO TO 760
03760            IF(D0.EQ.DMAX) GO TO 780
03770            IF (D0.EQ.DMIN) GO TO 790
03780            GO TO 800
03790            GO TO 820
03800    740     IF (LC(K).LE.(1-TOL)) GO TO 750
03810            GO TO 820
03820    750     SLP=1.0
03830            GO TO 960
03840    760     IF(LC(K).GT.(1+TOL)) GO TO 770
03850            GO TO 820
03860    770     SNK=0
03870            GO TO 960
03880            GO TO 820
03890    780     IF(PU(K).LE.(PULC-TOP)) GO TO 750
03900            GO TO 820
03910            GO TO 820
03920    790     IF(PU(K).GE.(PULC+TOP)) GO TO 770
03930            GO TO 820
03940            GO TO 820
03950    800     GO TO 210
03960    810     F5=F2/57.3
03970            TA2=TAN(F5)
03980            PSI=C2/TA2
03990            F2=B7*F2
04000            F5=F2/57.3
04010            TA2=TAN(F5)
04020            C2=PSI*TA2
04030            IF(KOC.GE.3) SNK=0
04040            GO TO 960
04050            KOC=KOC+1
04060            GO TO 190
04070    820     GO TO 942
04080    830     K6=K3+K5
```

```
04090           DO 840 K=1,K6
04100           IF(LC(K).GT.1.0) GO TO 850
04110   840     CONTINUE
04120           GO TO 900
04130   850     K1=K
04140           LMX=LC(K1)
04150   860     DO 870 K=1,K6
04160           IF(LC(K).LT.1.0) GO TO 880
04170   870     CONTINUE
04180           DO 875 K=1,K6
04190           IF(LC(K).EQ.1.0) GO TO 885
04200   875     CONTINUE
04210   880     K2=K
04220           LMN=LC(K2)
04230           GO TO 905
04240   885     K4=K
04250           IF(K1.EQ.0) GO TO 890
04260           IF(K2.EQ.0)  GO TO 895
04270           GO TO 905
04280   890     LMX=LC(K4)
04290           K1=K4
04300           GO TO 905
04310   895     LMN=LC(K4)
04320           K2=K4
04330           GO TO 905
04340   900     GO TO 750
04350           GO TO 940
04360   905     DO 915 K=1,K6
04370           IF(LC(K).LT.LMX) GO TO 910
04380           GO TO 915
04390   910     LMX=LC(K)
04400   915     CONTINUE
04410           DO 920 K=1,K6
04420           IF(LC(K).EQ.LMX) GO TO 925
04430   920     CONTINUE
04440   925     KM=K
04450           DO 930 K=1,K6
04460           IF (LC(K).GT.LMN) GO TO 98
04470           GO TO 930
04480   928     LMN=LC(K)
04490   930     CONTINUE
04500           DO 932 K=1,K6
04510           IF (LC(K).EQ.LMN) GO TO 934
04520   932     CONTINUE
04530   934     KN=K
04540           IF(PU(KN).LE.PULC) GO TO 936
04550           GO TO 980
04560   936     IF(PU(KM).GE.PULC) GO TO 938
04570           GO TO 986
04580   938     PUR=(PU(KN)-PULC)/(PU(KN)-PU(KM))
```

```
04590            K=K6+1
04600            LD(K)=LD(KN)+PUR*(LD(KM)-LD(KN))
04610            TR(K)=TR(KN)+PUR*(TR(KM)-TR(KN))
04620            DR(K)=DR(KN)+PUR*(DR(KM)-DR(KN))
04630            AAE=AE(KN)+PUR*(AE(KM)-AE(KN))
04640            A2=AR(KN)+PUR*(AR(KM)-AR(KN))
04650            D0=DEL(KN)+PUR*(DEL(KM)-DEL(KN))
04660            LC(K)=LD(K)/L0
0T670            IF(LC(K).GE.(1+TOP)) GO TO 984
04680            IF(LC(K).LE.(1-TOP)) GO TO 980
04690            GO TO 820
04700    940     B1=1.03
04710            B3=15
04720            B4=0.5
04730            B5=1
04740            B6=1
04750            GO TO 420
04760    942     SNK=R0*(1-COS(AA0))*12
04770            SP=(1-D0/DMAX)
04780            IF(SP.EQ.0) GO TO 944
04790            SLP=SLJ-SLK*ALOG(SP)
04800            GO TO 960
04810    944     SLP=1.0
04820            GO TO 980
04830    950     F1=F0/57.3
04840            TA3=TAN(F1)
04850            C0=C0+0.5*SIM*TA3
04860            RR=R0
04870            BB=B0
04880            LA=L0
04890            DB0=DB
04900            SS=S0
04910            CC=C0
04920            GG=G0
04930            ZJ=SLJ
04940            ZK=SLK
04950            CALL LKWC(RR,BB,LA,DB0,SS,CC,GG,ZJ,ZK,TOL,TOP,LL,DP,TQ,S
L,SL)
04960            K=1
04970            LD(K)=LL
04980            DR(K)=DP
04990            TR(K)=TQ
05000            SNK=SI
05010            SLP=SL
05020            GO TO 960
05030    960     IF(SLP.EQ.1.0) GO TO 980
05040            IF(SNK.EQ.0) GO TO 984
05050            PRINT 965,LD(K),DR(K)
05060    965     FORMAT (1H ,'LOAD= ',F10.2,'  DRAWBAR PULL = ',F10.2)
05070            PRINT 970, TR(K)
05080    970     FORMAT (1H ,'TORQUE= ',F10.2)
```

```
          LKWH.SRC       09-JAN-73    08:57

05090               PRINT 975,SNK,SLP
05100     975       FORMAT (1H ,'SINKAGE= ',F10.2,' IN   SLIP= ',F10.3)
05110               GO TO 999
05120     980       PRINT 982
05130     982       FORMAT (1H ,' NO GO  :  100 % SLIP ' )
05140               GO TO 999
05150     984       PRINT 986
05160     986       FORMAT (1H ,'USE HARD SURFACE FORMULA OR VARIABLE DELTA'

)
05170     990        CALL RTIME (I1)
05180               PRINT 994,I1
05190     994       FORMAT (1H0,'TIME= ',I10)
05200     999       STOP
```

```
SYSTEM?..
.
```

```
SLIP.SRC       08-JAN-73   17:05

00100            SUBROUTINE SLIP(R0,E1,A0,G0,D1,F1,C0,DF,AM,XX,PL,H,Q,E,J
1)
00110            DIMENSION X(49,17),Z(49,17),S(49,17),T(49,17)
00120            DIMENSION A(35),B(35),C(35)
00130            DIMENSION D(35)
00140            DIMENSION H(35),Q(35),E(35)
00150            IMPLICIT REAL (L)
00160            DEL(D9,F9)=ASIN(SIN(D9)/SIN(F9))
00170            QUA(D9,F9)=COS(D9)+SQRT(COS(D9)**2-COS(F9)**2)
00180            QUP(D9,F9)=COS(D9)-SQRT(COS(D9)**2-COS(F9)**2)
00190            EPO(F9,T9,T8)=EXP(2*(T9-T8)*SIN(F9)/COS(F9))
00200            TAN(F9)=SIN(F9)/COS(F9)
00210            DIS(A9,D9,T9,T8,F9)=R0*(A9-D9)*EXP((T9-T8)*SIN(F9)/COS(F
9))
00220            M=49
00230            N=17
00240            PI=3.14159
00250    16      W0=0
00260            TF=TAN(F1)
00270            DAF=TAN(D1)
00280            I1=2*N-1
00290            C1=C0/TF
00300            U1=PI/4-F1/2
00310            F3=1-SIN(F1)
00320            V3=SIN(E1-F1)/COS(F1)
00330            V4=COS(E1-F1)/COS(F1)
00340            V5=SIN(E1+F1)/COS(F1)
00350            V6=COS(E1+F1)/COS(F1)
00360            D2=ATAN(W0*SIN(E1)/(C1+W0*COS(F1)))
00370            D3=DEL(D2,F1)
00380            T1=(D3-D2)/2
00390            D5=D1*(1+DF)/2
00400            D4=DEL(D5,F1)
00410            T2=PI/2+.5*(D4+D1)-A0
00420            W1=(W0*COS(E1)+C1)/COS(D2)
00430            W2=QUP(D2,F1)
00440            S1=W1/W2
00450            T3=.75*PI+.5*F1-T2+T1-A0
00460            L1=DIS(A0,AM,T2,T1,F1)
00470            L2=2.5*L1*COS(U1)*COS(T3-F1)/COS(F1)
00480            L=L2
00490    20      DO 40 J=1,N
00500            I=N+1-J
00510            AJ=J
00520            AN=N
00530            Z(I,J)=0
00540            S(I,J)=S1
00550            T(I,J)=T1
00560            X(I,J)=(AJ-2)*L/(AN-2)
00570            X(N,1)=0
00580            X(N-1,2)=.5*L/(AN-2)
00590    40      CONTINUE
00600    50      DO 70 I=N,(2*N-1)
00610            J=1
```

```
00630            AI=FLOAT(I)
00640            AN=FLOAT(N)
00650            X(I,J)=0
00660            Z(I,J)=0
00670            T(I,J)=T1+(T2-T1)*(AI-AN)/(AN-1)
00680            POW=EPO(F1,T(I,J),T1)
00690            S(I,J)=POW*S(N,1)
00700    70      CONTINUE
00710            Q2=QUA(D1,F1)
00720            Q(1)=Q2*S(2*N-1,1)*COS(D1)-C1
00730            E(1)=(Q(1)+C1)*DAF
00740            H(1)=57.3*A0
00750            DO 200 J=2,N
00760    80      DO 180 I=(N+2-J),(J+2*(N-1))
00770            IF (I.EQ.(J+2*(N-1))) GO TO 130
00780            K=0
00790            TH1=T(I,J-1)+U1
00800            TH2=T(I-1,J)-U1
00810            SI1=S(I,J-1)
00820            SI2=S(I-1,J)
00830            V7=2*S(I-1,J)*S(I,J-1)
00840            U9=S(I-1,J)+S(I,J-1)
00850            V8=(T(I,J-1)-T(I-1,J))*TF
00860            V9=2*S(I-1,J)*S(I,J-1)*V8
00870            U6=2*TF*(S(I,J-1)*T(I,J-1)+S(I-1,J)*T(I-1,J))
00880    90      V1=TAN(TH1)
00890            V2=TAN(TH2)
00900            XI=V1*X(I,J-1)
00910            XJ=V2*X(I-1,J)
00920            V12=1/(V1-V2)
00930            X(I,J)=V12*(Z(I-1,J)-Z(I,J-1)+XI-XJ)
00940            Z(I,J)=Z(I-1,J)+(X(I,J)-X(I-1,J))*V2
00950            AA=V3*(X(I,J)-X(I-1,J))+V4*(Z(I,J)-Z(I-1,J))
00960            BB=V5*(X(I,J)-X(I,J-1))+V6*(Z(I,J)-Z(I,J-1))
00970            U5=S(I,J-1)-S(I-1,J)
00980            IF (U9.LE.0) GO TO 110
00990            GO TO 120
01000    110     PRINT 112
01010    112     FORMAT(1H-,'CANT COMPUTE CASE : CHECK INPUT')
01040    120     S(I,J)=(V7+V9+G0*(SI1*AA+SI2*BB))/U9
01050            T(I,J)=(U5+U6+G0*(BB-AA))/(2*TF*U9)
01060            IF ( K.EQ.1) GO TO 180
01070            TH1=.5*(T(I,J-1)+T(I,J))+U1
01080            TH2=.5*(T(I-1,J)+T(I,J))-U1
01090            SI1=.5*(S(I,J-1)+S(I,J))
01100            SI2=.5*(S(I-1,J)+S(I,J))
01110            U6=2*TF*(SI1*T(I,J-1)+SI2*T(I-1,J))
01120            V7=SI1*S(I-1,J)+SI2*S(I,J-1)
01130            V9=2*SI1*SI2*V8
01140            U9=SI1+SI2
01150            K=1
01160            GO TO 90
```

```
01170   130     CH=R0*SIN(A0)
01180           CH1=CH+X(J+2*N-3,J-1)
01190           A(J)=ASIN(CH1/R0)
01200           D(J)=D1*(1-(1-DF)*(A(J)-A(2))/(AM-A(2)))
01210           DAJ=TAN(D(J))
01220           B1=DEL(D(J),F1)
01230           B2=.5*(D(J)+B1)
01240           T(I,I-2*(N-1))=PI/2+B2-A(J)
01250           TH3=.5*(T(I,I-2*(N-1))+T(I-1,I-2*(N-1)))
01260           TH4=TH3-U1
01270           TH5=TAN(TH4)
01280           TAJ=TAN(A(J))
01290           Z1=1/TH5
01300           Z2=Z1*TAJ
01310           Z3=1/(1+Z2)
01320           Z4=Z1*(Z(I-1,J-1)-Z(I-1,J))
01330           X(I,J)=Z3*(X(I-1,J)+Z2*X(I-1,J-1)+Z4)
01340           Z(I,J)=Z(I-1,J-1)+TAJ*(X(I-1,J-1)-X(I,J))
01350           AA=V3*(X(I,J)-X(I-1,J))+V4*(Z(I,J)-Z(I-1,J))
01360           U3=2*S(I-1,J)*TF*(T(I,J)-T(I-1,J))
01370           S(I,J)=S(I-1,J)+U3+G0*AA
01380           Q1=QUA(D(J),F1)
01390           Q(J)=Q1*S(I,J)*COS(D(J))-C1
01400           E(J)=(Q(J)+C1)*DAJ
01410           CH2=CH+X(I,I-2*(N-1))
01420           CH3=ASIN(CH2/R0)
01430           H(J)=57.3*CH3
01440           IF (XX.EQ.1) GO TO 155
01450           AM=DF*ATAN((Q(J)+PL)*DAJ/Q(J))
01460   155     IF(CH3.GE.(AM+.002)) GO TO 176
01470           IF (CH3.LE.(AM-.002)) GO TO 160
01480           IF(J.LE.7) GO TO 165
01490           GO TO 220
01500   160     IF( J.GE.7) GO TO 170
01510   165     L=.5*L+.05
01520           GO TO 20
01530   170     H1=H(J)-H(J-1)
01540           H2=57.3*AM-H(J-1)
01550           H3=H2/H1
01560           H4=H3*(X(N+1-J,J)-X(N-J+2,J-1))
01570           X(N+1-J,J)=X(N-J+2,J-1)+H4
01580           GO TO 80
01590   176     IF (J.LT.N) GO TO 180
01600           L=1.5*L+.1
01610           GO TO 20
01620   180     CONTINUE
01630   200     CONTINUE
01640   220     J1=J
01650           RETURN
01660   1000    END
```

```
          LKWC.SRC       08-JAN-73    16:57

00100           SUBROUTINE LKWC(R0,B0,L0,DB,S0,C0,G0,SJ,SK,TL,TP,LL,DP,T

Q,SI,SL)
00110           DIMENSION HH(35),QQ(35),EE(35)
00120           DIMENSION WE(35),DRB(35),TRQ(35)
00130           DIMENSION LD(15),DR(15),TR(15),AR(15),DEL(15)
00140           DIMENSION PU(15),LC(15)
00150           DIMENSION AE(15)
00160           IMPLICIT REAL (L)
00170           TAN(F9)=SIN(F9)/COS(F9)
00180           PI=3.14159
00190           DEAMAX=1.57
00200           DEAMIN=.02
00210           DB1=DB+L0*SIND(S0)
00220           PULC=DB1/L0
00230           DEA=ASIN(2*PULC+.1)
00240           IF (DEA.GT.DEAMAX) DEA=DEAMAX
00250           IF(DEA.LT.DEAMIN) DEA=DEAMIN
00260    10     AMAX=21
00270           AMIN=1
00280           ARMIN=-AMIN/57.3
00290    20     ALF=DEA/2
00300           A2=-ALF/3
00310    30     DO 60 J=1,35
00320           IF (J.GT.11) GO TO 40
00330           HH(J)=A2+(J-1)*4*ALF/30
00340           QQ(J)=C0*(1+COS(DEA)+PI-ALF+HH(J))
00350           EE(J)=C0*SIN(DEA)
00360           IF (J.LE.11) GO TO 50
00370    40     HH(J)=ALF+(J-11)*2/57.3
00380           QQ(J)=C0*(1+COS(DEA)+PI+ALF-HH(J))
00390           EE(J)=C0*SIN(DEA)
00400    50     AL=57.3*HH(J)
00410    60     CONTINUE
00420    70     TORQ=0
00430           LOAD=0
00440           DRAB=0
00450           DO 65 J=2,35
00460           ARC=R0*(HH(J)-HH(J-1))
00470           QAV=.5*(QQ(J-1)+QQ(J))
00480           TAV=.5*(EE(J-1)+EE(J))
00490           AAV=.5*(HH(J-1)+HH(J))
00500           LOA=(TAV*SIN(AAV)+QAV*COS(AAV))*ARC
00510           DRA=(TAV*COS(AAV)-QAV*SIN(AAV))*ARC
00520           TOR=R0*TAV*ARC
00530           LOAD=LOAD+LOA
00540           DRAB=DRAB+DRA
00550           WE(J)=B0*(LOAD*COSD(S0)+DRAB*SIND(S0))
00560           DRB(J)=B0*(DRAB-LOAD*SIND(S0))
00570           TORQ=TORQ+TOR
00580           TRQ(J)=B0*TORQ
00590           IF (WE(J).GT.L0) GO TO 80
00600    65     CONTINUE
```

```
00610            IF (WE(J).LT.(1-TL)*L0) GO TO 150
00620            GO TO 80
00630    80      IF(HH(J).LT.(-2*A2)) GO TO 90
00640            GO TO 100
00650    90      IF (A2.GE.ARMIN) GO TO 130
00660            A2=A2+.02
00670            IF(A2.GE.ARMIN) A2=ARMIN
00680            GO TO 30
00690    100     WR=(WE(J)-L0)/(WE(J)-WE(J-1))
00700            LOAD=WE(J)-WR*(WE(J)-WE(J-1))
00710            TORQ=TRQ(J)-WR*(TRQ(J)-TRQ(J-1))
00720            DRAB=DRB(J)-WR*(DRB(J)-DRB(J-1))
00730            AA0=(HH(J)-WR*(HH(J)-HH(J-1)))
00740    110     IF(K.EQ.15) GO TO 200
00750            K=K+1
00760            LD(K)=LOAD
00770            TR(K)=TORQ
00780            DR(K)=DRAB
00790            AR(K)=A2
00800            ARK=57.3*A2
00810            DEL(K)=DEA
00820            AAE=57.3*AA0
00830            AE(K)=AAE
00840            PU(K)=DR(K)/LD(K)
00850            LC(K)=LD(K)/L0
00860            IF(ABS(PU(K)-PULC)-TP) 120,120,150
00870    120     LL=LD(K)
00880            DP=DR(K)
00890            TQ=TR(K)
00900            SI=R0*(1-COS(AA0))*12
00910            SP=(1-DEA/DEAMAX)
00920            IF(SP.EQ.0) GO TO 140
00930            SL=SJ-SK*ALOG(SP)
00940            GO TO 200
00950    130     SI=0
00960            SL=0
00970            GO TO 200
00980    140     SL=1.0
00990            GO TO 200
01000    150     IF(PU(K).GE.(PULC+TP)) GO TO 160
01010            IF (PU(K).LE.(PULC-TP)) GO TO 170
01020    160     IF(DEA.EQ.DEAMIN) GO TO 130
01030            DEA=DEA+(PULC-PU(K))-0.05
01040            IF(DEA.LT.DEAMIN) DEA=DEAMIN
01050            GO TO 10
01060    170     IF (DEA.EQ.DEAMAX) GO TO 140
01070            DEA=DEA+(PULC-PU(K))+0.05
01080            IF(DEA.GT.DEAMAX) DEA=DEAMAX
01090            GO TO 10
01100    200     RETURN
01110            STOP
```

DISTRIBUTION LIST

Please notify USATACOM, AMSTA-RUR, Warren, Michigan 48090 of corrections and/or changes in address.

No. of Copies

74 Commander
U.S. Army Tank-Automotive Command
Warren, Michigan 48090

ATTENTION:

Chief Scientist, AMSTA-CL	(1)
Director of RD&E, AMSTA-R	(1)
Deputy Director of RD&E, AMSTA-R	(1)
Foreign Intelligence Office, AMSTA-RI	(1)
Systems Development Division, AMSTA-RE	(6)
Concept & Technology Division, AMSTA-RH	(6)
Vehicular Components Division, AMSTA-RK	(4)
Surface Mobility Division, AMSTA-RU	(5)
Research & Analysis Functions, AMSTA-RUR	(20)
Propulsion Systems Division, AMSTA-RG	(6)
Canadian Forces Liaison Office, CDLS-D	(1)
U.S. Marine Corps Liaison Office, USMC-LNO	(5)
CDC Liaison Office, CDCLN-A	(5)
Project Manager ARSV, AMCPM-RSV	(3)
Project Manager MICV, AMCPM-MICV	(3)
Project Manager M561, AMCPM-GG	(2)
Project Manager M60, AMCPM-M60	(1)
Project Manager XM1, AMCPM-GCM	(3)

4 Office, Chief Research & Development
Department of the Army
ATTN: Dr. O'Connor, LTC M. Remus, Mr. M.V. Kreipke,
Dr. V. Zadnik
Washington, D.C. 20310

2 Commander
U.S. Army Weapons Command
ATTN: AMSWE-SY (Dr. Hung, Mr. Rankine)
Rock Island, Illinois 61201

2 Director
U.S. Army Corps of Engineers
Waterways Experiment Station
PO Box 631
Vicksburg, Mississippi 39180

No. of
Copies

6 Director
U.S. Army Corps of Engineers
Waterways Experiment Station
ATTN: Mobility & Environmental Laboratory
PO Box 631
Vicksburg, Mississippi 39180

1 Superintendant
U.S. Military Academy
ATTN: Professor of Ordnance
West Point, New York 10996

1 Director
U.S. Army Natick Laboratories
ATTN: Technical Library
Natick, Massachusetts 01760

2 Commander
U.S. Army Material Command
AMC Building, Room 8S56
ATTN: Mr. R. Navarin, AMCRD-TV
Washington, D.C. 20315

1 Commander
U.S. Army Material Command
ATTN: AMCRD-GV, Mr. J. Carr
Washington, D.C. 20315

1 President
U.S. Army Arctic Test Center
ATTN: STEAC-IT (Mr. Dufendach)
APO 409
Seattle, Washington 98733

2 Commander
U.S. Army Test & Evaluation Command
ATTN: AMSTE-BB and AMSTE-TA
Aberdeen Proving Ground, Maryland 21005

2 Director
U.S. Army Ballistic Research Laboratory
Aberdeen R&D Center
Aberdeen Proving Ground, Maryland 21005

No. of
Copies

3 Director
U.S. Army Cold Regions Research & Engineering Laboratory
ATTN: Dr. W. Harrison, Dr. Freitag, Mr. R. Liston
PO Box 282
Hanover, New Hampshire 03755

1 Commander
U.S. Army Combat Development Command
ATTN: Mr. E. Hurford
Ft. Lee, Virginia 23801

1 Director
U.S. Army Human Engineering Laboratory
ATTN: Mr. Eckels
Aberdeen Proving Ground, Maryland 21005

2 Grumman Aerospace Corporation
ATTN: Dr. L. Karafiath, Mr. E. Markow
Plant 35
Bethpage, Long Island, New York 11714

1 Dr. Bruce Liljedahl
Agricultural Engineering Department
Purdue Univefsity
Lafayette, Indiana 46207

1 Mr. T. Andrisan
Brown Engineering Corporation
Huntsville, Alabama 35804

1 Director
U.S. Army Advanced Material Concepts Agency
ATTN: Mr. Rymiszewski
2461 Eisenhower Avenue
Hoffman Building
Alexandria, Virginia 22314

1 Dr. W. G. Baker
Civil Engineering Department
University of Detroit
4001 W. McNichols
Detroit, Michigan 48221

1 Director
U.S. Army Transportation Agency
ATTN: CDCT-M (Mr. Betts)
Ft. Eustis, Virginia 23604

No. of
Copies

1 Professor E. Niemi
Keweenaw Field Station
Rural Route 1
PO Box 94D
Calumet, Michigan 49913

3 Director
U.S. Army Material Systems Analysis Agency
ATTN: Messrs D. Woomert, W. Niemeyer, W. Criswell
Aberdeen Proving Ground, Maryland 21005

2 Library
Cornell Aeronautical Laboratory
Box 235
4455 Genessee St.
Buffalo, New York 14221

2 Director
National Tillage Machinery Laboratory
Box 792
Auburn, Alabama 36830

2 Chrysler Corporation
Mobility Research Laboratory, Defense Engineering
ATTN: Dr. B. Van Deusen, Mr. J. Cohren
Dept. 6100
PO Box 751
Detroit, Michigan 48231

1 Dr. N. C. Costes
George C. Marshall Space Flight Center
Code SSE-SSL-N
Huntsville, Alabama 35809

20 Director
Defense Documentation Center
Cameron Station
Alexandria, Virginia 22314

2 President
U.S. Armor Board
Ft. Knox, Kentucky 40121

1 Food Machinery Corporation
1105 Coleman Avenue
PO Box 267
Technical Library
San Jose, California 95103

No. of
Copies

1 Commander
HQ, U.S. Air Force (SAGT)
ATTN: Major Goodel
Washington, D.C. 20330

1 Southwest Research Institute
ATTN: Mr. R. C. Hemion
8500 Culebra Road
San Antonio, Texas 78228

1 U.S. Marine Corps
Mobility & Support Division
Development and Education Command
ATTN: Mr. Hickson
Quantico, Virginia 22134

1 Mr. H. C. Hodges
Nevada Automotive Test Center
Box 234
Carson City, Nevada 89701

1 Mr. W. S. Hodges
Lockheed Missile andSpace Corporation
R&D Division
Sunnyvale, California 94088

2 Commander
Yuma Proving Ground
ATTN: STEYP-RPT, STEYP-TE
Yuma, Arizona 85364

1 Mr. A. M. Wooley
West Coast Test Branch
Mobility and Support Division
Marine Corps Base
Camp Pendleton, California 92055

1 Mr. R. D. Wismer
Deere & Company
Engineering Research
3300 River Drive
Moline, Illinois 61265

1 U.S. Forest Service
Division of Engineering
ATTN: Mr. B. Y. Richardson
1621 N. Kent Street
Arlington, Virginia 22209

No. of
Copies

1 Mr. Irja Johnsson
SFM, Forsvaretsforskningsanstalt
Avd 2
Stockholm 80, Sweden

1 Oregon State University
Library
Corvallis, Oregon 97331

1 Mr. Sven E. Lind
SFM, Forsvaretsforskningsanstalt
Avd 2
Stockholm 80, Sweden

1 Mr. Robert W. Forsyth
Lockheed Aircraft Service Company
PO Box 33
Ontario, California 91764

1 Engineering Societies Library
345 East 47th Street
New York, New York 11017

1 Dr. M. G. Bekker
224 East Islay Drive
Santa Barabra, California 93101

2 Dr. I. R. Ehrlich
Stevens Institude of Technology
Davidson Laboratory
Castle Point Station
Hoboken, New Jersey 07030

Unclassified
Security Classification

DOCUMENT CONTROL DATA - R & D

(Security classification of title, body of abstract and indexing annotation must be entered when the overall report is classified)

1. ORIGINATING ACTIVITY (Corporate author)	2a. REPORT SECURITY CLASSIFICATION
Grumman Aerospace Corporation - Research Department Stevens Institute of Technology	Unclassified
	2b. GROUP

3. REPORT TITLE

AN APPLICATION OF PLASTICITY THEORY TO THE SOLUTION OF THE RIGID WHEEL-SOIL INTERACTION PROBLEM

4. DESCRIPTIVE NOTES (Type of report and inclusive dates)

Final Report

5. AUTHOR(S) (First name, middle initial, last name)

Leslie L. Karafiath, Edward A. Nowatzki
I. Robert Ehrlich, J. Capin

6. REPORT DATE	7a. TOTAL NO. OF PAGES	7b. NO. OF REFS
March 1973	191	13

8a. CONTRACT OR GRANT NO.	9a. ORIGINATOR'S REPORT NUMBER(S)
Contract No. DAAE07-72-C-0033	RE_-448
b. PROJECT NO.	
c.	9b. OTHER REPORT NO(S) (Any other numbers that may be assigned this report)
d.	TACOM Report No. 11758 (LL 141)

10. DISTRIBUTION STATEMENT

Distribution of this document is unlimited

11. SUPPLEMENTARY NOTES	12. SPONSORING MILITARY ACTIVITY
	Land Locomotion Division U.S. Army Tank Automotive Command (TACOM), Warren, Michigan

13. ABSTRACT

Plasticity theory is applied to the analysis of soil-wheel interaction. The problem is reduced to the determination of stresses at the interface of the rigid wheel and the soil. Once these stresses are known, the wheel load, torque, pull and drag are obtained by integrating the stresses along the wheel perimeter. To find the distribution of interface stresses, the basic differential equations of equilibrium are combined with the Coulomb-Mohr yield criterion for soils and the equations are solved by a numerical procedure. The numerical solution scheme and the computer program which accomplishes the solution are described in detail.

Tests performed with the soil bin dynamometer facilities of Stevens Institute of Technology are discussed. Test results show good agreement with prediction. The validity of assumptions introduced in the computational scheme is examined. It is found that refinement in the assumptions regarding the distribution of interface friction and the magnitude of the "separation angle" would further improve the accuracy of the method.

Finally, it is concluded that the proposed theory for predicting rigid wheel performance is fundamentally correct and is practical from

DD FORM 1 NOV 65 1473

Unclassified
Security Classification

14. KEY WORDS	LINK A		LINK B		LINK C	
	ROLE	WT	ROLE	WT	ROLE	WT
the viewpoint of required computer time. This report represents an essential first step toward the establishment of a rigorous simulation of the soft soil performance of wheeled vehicles.						